TU Graz

Graz University of Technology

PhD Thesis

Generalized Noncoherent Ultra-Wideband Receivers

conducted at the
Signal Processing and Speech Communications Laboratory
Graz University of Technology, Austria

by
Dipl.-Ing. Andreas Pedroß-Engel

Supervisor:
Assoc.Prof. Dipl.-Ing. Dr. Klaus Witrisal
Graz University of Technology, Austria

Assessors/Examiners:
Assoc.Prof. Dipl.-Ing. Dr. Klaus Witrisal
Graz University of Technology, Austria

Prof. Dipl.-Ing. Dr.-Ing. Lutz Lampe
University of British Columbia, Vancouver, Canada

Graz, June 2014

To my wonderful wife!
Thank you for everything!

Abstract

This thesis investigates noncoherent multi-channel ultra-wideband receivers. Noncoherent ultra-wideband receivers promise low power consumption and low processing complexity as they, in contrast to coherent receiver architectures, relinquish the need of complex carrier frequency and phase recovering. Unfortunately, their peak data rate is limited by the delay spread of the multipath radio channel. Noncoherent *multi-channel* receivers can break this rate limit due to their capability to demodulate multi-carrier signals. Such receivers use an analog front-end to separate the received signals into their sub-channels.

In this work, the modeling and optimization of realistic front-end components is addressed and their impact on the system performance of noncoherent multi-channel ultra-wideband receivers is analyzed. With a proposed generalized mathematical framework, it is shown that there exists a variety of noncoherent multi-channel receiver types with similar system performance which differ only in their front-end filters. It is also shown that analog multipliers introduce strong interference due to higher-order mixing products. To analyze the impact of such interference on the performance of the receiver system, a Wiener-Hammerstein system model is introduced for the multiplication device. It is shown that the receiver performance strongly depends on the input power of the nonideal multiplier devices. A proposed mixed-signal integration device is able to suppress nonlinear cross-products between data carriers. Passive filter structures are analyzed for this purpose. It is shown that the optimized filter outperforms the reference system using an ideal sliding window integrator because it is able to mitigate more system noise. Additionally, an enhanced signal detection is introduced which is able to mitigate undesired nonlinear effects and hereby reduces the bit-error rate. Finally, a hardware example of a noncoherent multi-channel receiver is presented which proves the feasibility to design and manufacture such receivers with today's technologies.

Kurzfassung

Diese Arbeit untersucht inkoheränte, mehrkanalige Ultra-Breitbandempfängerstrukturen. Im Gegensatz zu koheränten Empfängern, müssen inkoheränte Empfänger Frequenz und Phase des empfangenen Signals nicht wiederherstellen. Sie versprechen daher einen geringeren Stromverbrauch und weniger komplexe Verarbeitung der empfangenen Signale. Die maximale Datenrate ist jedoch durch die Dauer der Impulsantwort des Mehrwege-Funkkanals limitiert. *Mehrkanalige* inkoheränte Empfänger sind in der Lage parallele Mehrträgersignale zu dekodieren und können daher diese Limitierung umgehen. Sie verwenden eine analoge Eingangsstufe um die empfangenen Signale in die jeweiligen Teilbänder zu separieren.

Diese Arbeit behandelt die Modellierung und Optimierung von realistischen Systemkomponenten der Eingansstufe und analysiert deren Einfluss auf die Gesamtleistung von mehrkanaligen Ultra-Breitbandempfängern. Mit Hilfe eines allgemeinen mathematischen Modells wird gezeigt, dass eine Vielfalt von inkoheränten mehrkanaligen Empfängern mit ähnlicher Systemleistung möglich sind, welche sich nur in deren Eingangsfilter unterscheiden. Es wird auch gezeigt, dass analoge Multiplizierer durch Mischprodukte höherer Ordnung starke Interferenz verursachen. Um den Einfluss dieser Interferenz auf die Gesamtleistung zu untersuchen, wird ein Wiener-Hammerstein Systemmodell für reale analoge Multiplizierer vorgestellt. Mit Hilfe eines vorgeschlagenen gemischt analog-digitalen Integrators ist es möglich, nichtlineare Kreuzprodukte der Datenträger zu unterdrücken. Dafür werden passive Filterstrukturen untersucht. Es wird gezeigt, dass es ein optimierter gemischt analog-digitaler Filter ermöglicht mehr Rauschen zu unterdrücken und daher ein Referenzsystem mit idealem Integrator zu übertreffen. Zusätzlich wird eine verbesserte Signaldetektion vorgeschlagen, welche nichtlineare Effekte unterdrückt und dadurch die Bitfehlerwahrscheinlichkeit reduzieren. Schlussendlich wird ein Prototyp eines inkoheränter mehrkanaliger Ultra-Breitbandempfänger vorgestellt. Dieses Gerät beweist die Machbarkeit solcher Empfängerstrukturen mit Hilfe der heute verfügbaren Technologien.

Statutory Declaration

I declare that I have authored this thesis independently, that I have not used other than the declared sources/resources, and that I have explicitly marked all material which has been quoted either literally or by content from the used sources.

—————————————————
date

—————————————————
(signature)

Contents

The evolution of a PhD thesis in four simple steps. Told by four extraordinary examples of human beings:

Motivation:
"Science is the most exciting and sustained enterprise of discovery in the history of our species. It is the great adventure of our time."

– Michael Crichton

Methods:
"A learning experience is one of those things that says, 'You know that thing you just did? Don't do that.'"

– Douglas Adams

Results:
"God was always invented to explain mystery. God is always invented to explain those things that you do not understand." – Richard Feynman

Conclusions:
"If this does not appeal to you sufficiently to recognize in me a discoverer of principles, do me, at least, the justice of calling me an inventor of some beautiful pieces of electrical apparatus." – Nikola Tesla

1

Introduction

Modern society is built on fast accessibility of digital information. Examples include the world wide web, digital audio and video broadcast, or electronic banking and trading. The amount of data increases each second[1] and the need to transport it as fast as possible from one point to another is more crucial than ever, especially for systems which require real-time interaction as traffic control and tracking [3], disaster control [4, 5], or surgical support systems [6].

Another desire of modern society is the demand of easy accessibility to any digital information or data from every possible location using wireless technology. This need was the main driver for the rapid evolution of modern mobile cellular multimedia platforms[2], wireless communication standards with high spectral efficiency, as LTE [7] or WiMax [8], and low-power wireless sensor network protocols, as Bluetooth [9], ZigBee [10], or ANT [11, 12].

A big issue is the limited battery capacity all mobile devices have in common, hence low-power consumption is a must for any of its components, including computing power and communications. In this thesis the modeling and optimization of noncoherent multi-channel ultra-wideband (UWB) receivers and their impact on the receiver performance is studied. These receivers are most suitable for mobile short range high rate applications as they promise low-complexity, low-power devices but still maintaining reasonable data rates [13].

---

[1]   More than 90 % of all the data in the world has been generated over the last three years [1]. E.g. the Large Hadron Collider (LHC) in CERN alone produced in its first full year (2010) 13 PByte of data, on average, 412 MByte data per seconds [2].

[2]   The term "phone" seems to be an understatement for the computational power of current devices as Apple's iPhone or Google's Nexus series.

1.1 History of Ultra-Wideband Communications

Ultra-Wideband communications have a long history. The cornerstone of any applied wireless communications lies in the experiments of David Edward Hughes in 1879 [14]. He was successful in producing radio signals using an electric spark generator which could be detected by a telephone receiver. Due to the lack of band selection filters, these generated sparks were inherently ultra-wideband. The zenith of this early UWB communication age marked the commercialization of the spark-gap transmitters for wireless telegraphy – to transmit Morse codes – by Nikola Tesla [15,16] and Guglielmo Marconi [17]. Those wireless transmission systems got much attention in media due to the patent battles [18] between Marconi and Tesla on the one hand and due to the rescue of 710 survivors of the *RMS Titanic* catastrophe on the other hand. Before the Titanic sunk completely, a wireless distress call was sent by its spark-gap wireless telegraphs, owned and operated by the Marconi Company, which got intercepted by the *RMS Carpathia* [19].

The end of the spark-gap transmitters and the early UWB communication age was sealed when in 1904 Otto Nußbaumer transmitted a first audio broadcast within the premises of (which is nowadays known as) Graz University of Technology[3] and when 1906 Reginald Fessenden transmitted the first amplitude modulated audio broadcast using an alternator-transmitter [20].

During the 1960's to 1990's the US department of defense restricted UWB for classified UWB radar programs and secure military communications. Therefore, little effort was put into public UWB research [21]. Nevertheless, Gerald F. Ross proposed the first modern UWB patent in 1971 [22]. But still UWB had been fallen into oblivion for a very long time, until modern UWB was revived for the public by the works of Charles Fowler et al. about the first public UWB radar [23] in 1990. In 1997 the first works in public UWB impulse radio for communications were published by Moe Z. Win and Robert A. Scholtz [24].

Due to the emerging interests in UWB, the Federal Communications Commission (FCC) has defined emission rules regarding UWB transmission systems in 2002 as *Revision of Part 15 of the Commission's Rules Regarding Ultra-Wideband Transmission Systems* [25]. IEEE followed the specifications of the FCC and specified the standard *IEEE 802.15.4a* on low data rate UWB communications [26] in 2006. The draft standard *IEEE 802.15.3a* on high data rate UWB communications was withdrawn in 2006 after the IEEE 802.15.3a Task Group failed to agree on a single system specification [27]. In 2007, ISO adopted parts of the the withdrawn IEEE 802.15.3a as *ISO/IEC 26907* and *ISO/IEC 26908* [28, 29]. These standards specify a physical layer (PHY) for UWB based on multi-band orthogonal-frequency-division multiplexing (MB-OFDM) which requires complex coherent demodulation of the data at the receiver.

Until today there exist no commercially successful high-rate UWB systems, although MB-OFDM UWB was considered for wireless transmission of USB [30] and Bluetooth 3.0 [31]. The promise of the UWB technology to maintain low-power low-complexity transceiver systems could not be met by coherent MB-OFDM UWB which turned out to be a very complex power hungry technology. New approaches as noncoherent high rate UWB schemes need to be considered and studied.

---

[3] Note that this thesis was written 110 years after this remarkable experiment, in which Nußbaumer transmitted the Styrian anthem "Dachsteinlied"!

1.2 The Ultra-Wideband Channel

In narrowband and wideband wireless communications fading is a severe problem [32]. Fading communication links appear when the radio waves travel, due to reflections, over more than one way from the transmitter to the receiver. Depending on the phases of the received signals, constructive or destructive interference may appear. For constructive interference the signal gets boosted, but for destructive interference no signal can be received at all. This phenomenon is frequency dependent, so that in the same scenario a destructive interference can be resolved for a different frequency. Hence, those multipath channels are frequency selective.

A multipath channel can be described, using a tapped delay line model, as

$$c(t,\tau) = \sum_{n=0}^{N-1} \alpha_n(t)\delta(\tau - \tau_n(t)), \tag{1.1}$$

where N is the number of paths a signal propagates, $\alpha_n(t)$ is the complex gain of the nth ray, $\delta(\cdot)$ is the Dirac delta function [33], and τ_n is the time the signal needs to propagate via the nth path. The parameters of the multipath channel can be modeled as stochastic processes and can be statistically described (cf. Appendix A).

In general the channel $c(t,\tau)$ is time-variant, given that receivers, transmitters, or reflectors may move. For the time-variant channel $c(t,\tau)$, t is the time parameter whereas τ is the delay parameter. The received signal $r(t)$ is therefore given as

$$r(t) = c(t,\tau) * s(t) + n(t) \tag{1.2}$$

$$= \int_{\tau=-\infty}^{+\infty} c(t,\tau) s(t-\tau) d\tau + n(t), \tag{1.3}$$

where $*$ denotes the convolution operator, $s(t)$ is the sent signal, and $n(t)$ is noise.

(a) Absolute value of the channel impulse response. (b) Magnitude response.
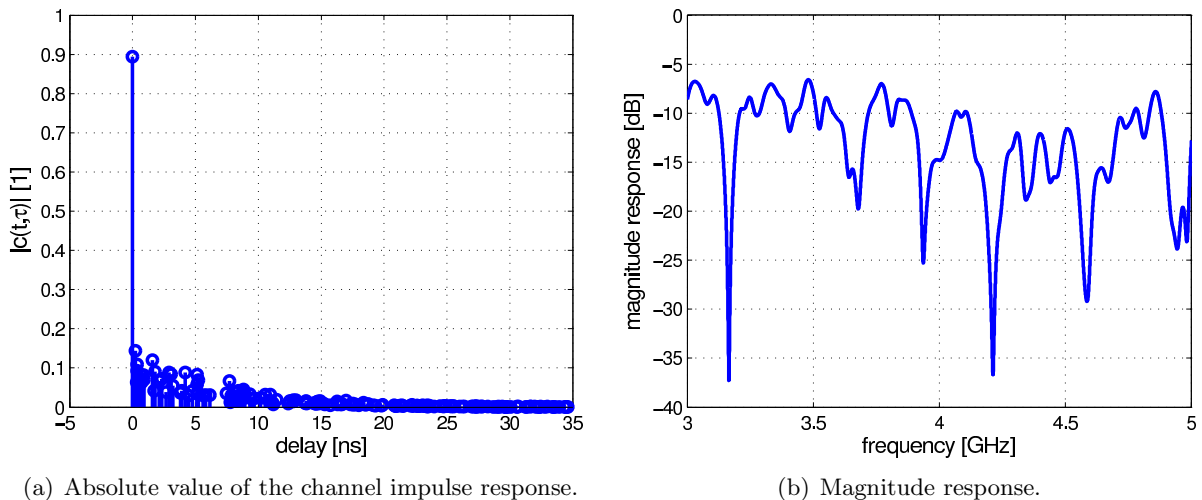
Figure 1.1: Example of a time-variant multipath channel at given time t.

In Fig. 1.1 a sample function of such a time-variant UWB channel response is depicted[4]. The first peak in the impulse response represents the *line-of-sight* (LOS) ray. It can be seen that it is strong in contrast to all the other rays which arrive later. This scenario is hence a LOS scenario where there exists a line of sight between the transmitter and receiver. All other components

---

[4] The channel parameters can be found in Tab. 2.2

are *non-line-of-sight* (NLOS) rays that travel along paths due to reflections. The magnitude response shows clearly the deep fading dips which are caused by those reflections.

To conquer those narrowband fading-dips, the bandwidth of the signal can be expanded so that it becomes more robust to this phenomena. When expanding the signal bandwidth to

1. at least 20 % of its center frequency, or

2. at least 500 MHz

the signal is called an ultra-wideband signal (according to FCC regulations [25]).

In impulse radio, the UWB signals utilize short pulses in the range of one nanosecond to transmit data [24]. Short pulses always result in large bandwidths. To assure that those signals do not interfere with other radio systems, the transmit power of UWB transmitters needs to be reduced [25]. On the contrary, UWB communication systems must be robust to interfering signals themselves, which might result in the need for interference mitigation schemes [34, 35].

The big advantage of UWB communication is its ability to resolve multipath [36, 37] and, hence, a strong reduction of fading [38, 39]. This allows for reduction of fading margins in the link power budget and thus allows low-power signal transmissions [24].

(a) Normalized pulse shape in time-domain.

(b) Power spectral density.
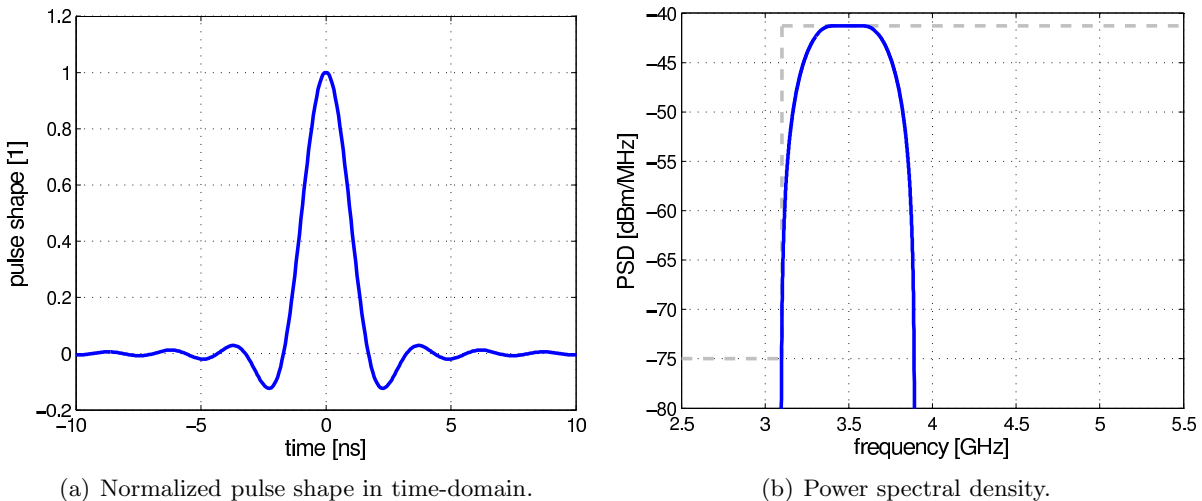
Figure 1.2: *The IEEE 802.15.4a reference pulse. The pulse shape is a root raised-cosine pulse with a pulse width of $T_p = 2$ ns and $\beta = 0.6$.*

In Fig. 2.2 an exemplary UWB pulse is shown. The pulse shape is a root raised-cosine pulse with a pulse width of $T_p = 2$ ns and $\beta = 0.6$ which resembles the IEEE 802.15.4a reference pulse [40]. Also the power spectral density (PSD) of such a pulse is shown. It can be seen that the width of the pulse is 499.2 MHz. It has a center frequency of 3.4944 GHz which represents the channel 1 specified in IEEE 802.15.4a and complies with the FCC PSD emission limit for UWB communications [25]. FCC permits a PSD of maximal -41.3 dBm/MHz in the frequency range between 3.1 GHz and 10.6 GHz and limits the emission in the rest of the spectrum to -75 dBm/MHz.

1.3 Noncoherent Ultra-Wideband Receivers

Noncoherent UWB receivers are potentially low-complexity UWB receiver architectures as they, in contrast to coherent receiver architectures, relinquish the need for complex carrier frequency and phase recovery. But they are suboptimum as they only exploit the signal envelope.

There are two basic noncoherent receiver classes that perform signal processing in analog and thus avoid analog-to-digital converters (ADC) with high sampling rate: energy detectors (ED) and autocorrelation receivers (AcR) [13].

Energy Detector

In Fig. 1.3 a signal flow diagram of an energy detector is depicted. This receiver computes the energy of a received signal pulse by integrating the instantaneous received signal power over the symbol period T_{sym}, which can mathematically expressed for a single transmitted data symbol d as

$$y = \int_{t=0}^{T_{\text{sym}}} (f(t) * c(t) * s(t) + f(t) * n(t))^2 \, dt \tag{1.4}$$

where $s(t) = d\varphi(t)$ is the transmitted signal, $\varphi(t)$ is the bandlimited shape of the transmitted pulse, $c(t)$ is the time-invariant channel, $f(t)$ is a bandpass filter, and $n(t)$ is noise. The equation (1.4) can be expanded to

$$y = \underbrace{\int_{t=0}^{T_{\text{sym}}} (f(t) * c(t) * s(t))^2 \, dt}_{\text{signal-by-signal term}}$$

$$+ 2 \underbrace{\int_{t=0}^{T_{\text{sym}}} (f(t) * c(t) * s(t)) \times (f(t) * n(t)) \, dt}_{\text{signal-by-noise term}}$$

$$+ \underbrace{\int_{t=0}^{T_{\text{sym}}} (f(t) * n(t))^2 \, dt}_{\text{noise-by-noise term}}, \tag{1.5}$$

where the first line is the signal-by-signal term, the second line is the signal-by-noise term, and the third line is the noise-by-noise term.
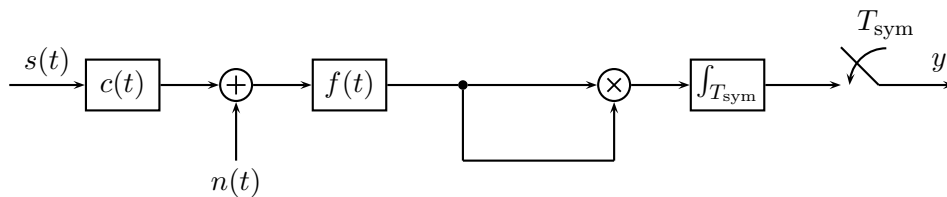
Figure 1.3: Signal flow diagram of an energy detector.

Because only the pulse energy is computed in detection, only noncoherent signal modulation schemes as on-off keying (OOK) or pulse-position modulation (PPM) can be considered, so that $d \in \{0, 1\}$. Detection for OOK simplifies to a threshold comparison, hence

$$\hat{d} = \begin{cases} 1 & \text{, for } y \geq \gamma \\ 0 & \text{, for } y < \gamma. \end{cases} \tag{1.6}$$

The choice of an appropriate decision threshold γ is based on input noise and signal power [41]. In comparison to coherent receivers, synchronization simplifies for noncoherent receivers to determine the start of a symbol period at fractions of the symbol interval instead of fractions of a pulse duration [42, 43].

Autocorrelation Receiver

A different noncoherent architecture is the autocorrelation receiver (see Fig. 1.4). A typical modulation for AcR is a transmitted reference scheme [44] where for a single symbol two consecutive pulses $\varphi(t+\tau)$ and $(2d-1)\varphi(t)$ are transmitted. The pulse spacing τ is chosen so that both pulses are aligned by the delay line τ. The autocorrelation in the receiver front-end leads to an instantaneous phase comparison of the two transmitted pulses [13], which is given as

$$y = \int_{t=0}^{T_{\text{sym}}} (f(t) * c(t) * s(t-\tau) + f(t) * n(t-\tau)) \times (c(t) * f(t) * s(t) + f(t) * n(t)) \, dt,$$
(1.7)

where $s(t) = \varphi(t+\tau) + (2d-1)\varphi(t)$. For instance, if both pulses have the same phase, that is for $d = 1$, the output y of the AcR simplifies to

$$y = \int_{t=0}^{T_{\text{sym}}} (c(t) * f(t) * \varphi(t))^2 \, dt + \nu,$$
(1.8)

which resembles a simple energy detection of the pulse shape. The term ν accumulates all signal-by-noise and noise-by-noise terms. For $d = 0$, the sign of the second pulse is inverted. For this case the output y of the AcR is given as

$$y = \int_{t=0}^{T_{\text{sym}}} - (c(t) * f(t) * \varphi(t))^2 \, dt + \nu$$
(1.9)

Detection is reduced to a simple sign estimation, hence

$$\hat{d} = \begin{cases} 1 & \text{, for } y \geq 0 \\ 0 & \text{, for } y < 0. \end{cases}$$
(1.10)

Note that no recovery of the absolute carrier phase is needed while the phase information of the pulses is still exploited. Synchronization complexity is comparable to the synchronization of energy detectors.
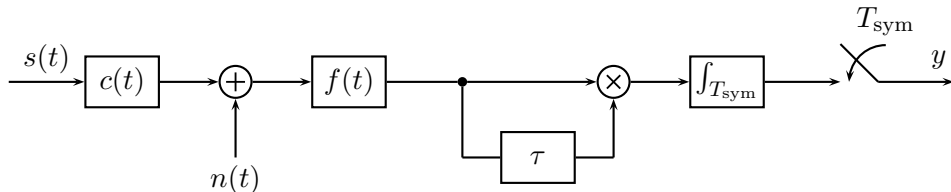
Figure 1.4: Signal flow diagram of an autocorrelation receiver.

The simplicity of noncoherent UWB receivers comes at the cost of reduced robustness in presence of noise and multipath interference in comparison to coherent UWB receivers. For instance, to achieve high data rate using an energy detection receiver, a rather hard limit is set by the excess delay of the multipath channel. Equalization schemes achieve limited gains only [45].

Multi-Channel Receivers

An approach for increasing the data rate without the drawbacks of complex coherent MB-OFDM UWB is noncoherent multi-carrier transmission [46], where an analog front-end is used to separate the received signal into its subcarriers[5].

E.g. [47] presents a noncoherent multi-channel transceiver system based on a 0.35 μm CMOS technology. The transmitter is able to generate four subcarriers using OOK. The pulse shapes are obtained by quasi-elliptic microstrip filters [48] and have a bandwidth of 190 MHz. The signaling has a overall bandwidth of 1.15 GHz with a center frequency of 3.675 GHz. The subcarriers can be sampled and processed at the receiver with much lower bandwidth; typically at symbol rate. A fixed implementation of a suitable filter bank results in a very robust high-rate receiver, but it requires highly selective front-end filters [49]. The authors of [47] suggest low-temperature co-fired ceramic (LTCC) filters as receiver front-end filters for future revisions of their transceiver system.

In [50] an approach to optimize the signaling parameters for multi-carrier UWB transmission is shown by maximizing the channel capacity for given channel parameters (e.g. delay spread[6] of the multipath channel) and system constraints (e.g. maximal signaling bandwidth, maximal number of subcarriers, and duty circle). It was shown that a maximal bit rate of 1.435 Gbit/s is possible for a multipath channel with a delay spread of 9 ns. The found solution utilizes 16 subcarriers with bandwidths of 464 MHz each and a duty circle of 19.3 %. As can be seen, this solution exploits the full UWB bandwidth which is designated by FCC. An analysis of how the channel capacity changes for noncoherent multi-channel UWB receivers due to fading is presented in [51]. It has been shown that for high signal-to-noise ratio (SNR) scenarios, a high number of subcarriers is preferable in order to increase the data rate.

In [52] a coexistance-based channel coding for noncoherent multi-channel UWB receivers is studied. Algorithms based on the nonlinear Teager-Kaiser operator and on the Otsu method combined with BCH and Reed-Solomon codes were derived. These algorithms show significant improvement in bit-error rate (BER) in presence of interference while preserving high data rate communication in comparison to methods which use simple thresholds only.

The impact of narrowband interference on noncoherent multi-channel UWB receivers were analyzed in [53] and [54]. Interference mitigation methods were derived and it has been shown, that those methods result in processing gain. Possible options to reduce the impact of narrowband interference on the receiver performance are the variation of symbol duration and pulse shaping. It was also shown, that modified energy detection schemes based on the Teager-Kaiser operator and high-pass filtering are able to mitigate multiple narrowband interferers, but at the cost of receiver performance.

The aforementioned studies proof the benefit of noncoherent multi-carrier signaling schemes for high data rate UWB communication systems. However, a fixed implementation of suitable highly selective front-end filters of the aforementioned multi-channel receivers lacks any flexibility concerning the band selection. The flexibility improves with the receiver architecture described in [55], which performs an autocorrelation operation in the analog front-end and leaves the band-selection to a digital back-end running at moderately slow symbol rate. This receiver is discussed in more detail within this thesis.

---

[5]   This signaling scheme is also called multi-band impulse radio UWB (MB-IR-UWB).
[6]   The delay spread is the difference between the time of arrival of the earliest significant and the latest significant multipath component.

1.4 Research Questions and Thesis Outline

The aim of this thesis is to answer following research questions:

> ***How can front-end components of noncoherent multi-channel UWB receivers be modeled and optimized?***

> ***Which impact do realistic front-end components have on the performance of noncoherent multi-channel UWB receivers?***

These two questions were investigated within the *NOFDM - Noncoherent Orthogonal Frequency Division Multiplexing* project funded by the Autrian Research Promotion Agency (FFG) under grant 825899. Goal of this project was to develop and evaluate a noncoherent multi-channel UWB receiver demonstrator.

According to the aforementioned research questions, this thesis is organized as follows: In Chapter 2 a mathematical framework is derived for generalized noncoherent multi-channel receivers and a proper noncoherent multi-carrier modulation scheme is introduced. Performance metrics are defined and the used system simulation framework is described. Additionally three reference receivers are introduced whose performance metrics will be used for comparison in the rest of this work.

Chapter 3 analyzes the impact of nonideal front-end components, as front-end filters, multiplication devices, or integration devices, on the system performance of the reference receivers.

In Chapter 4, a method for enhanced signal detection is proposed for noncoherent multi-channel receivers to mitigate undesired nonlinear effects.

A hardware example of an actual, realized noncoherent multi-channel UWB receiver is presented in Chapter 5. The receiver power-budged and the actually used components devices are discussed.

Finally, conclusions are drawn in Chapter 6.

2

The Generalized Noncoherent Multi-Channel Receiver

This chapter describes a generalized analytical framework for noncoherent multi-channel receiver systems. Investigating the mathematical framework will lead us to the conclusion that many different receiver flavors are possible including multi-channel energy detectors and multichannel autocorrelation receivers. Also a possible signaling scheme will be introduced, namely noncoherent orthogonal frequency-division multiplexing (NOFDM). To ensure high receiver performance, design rules will be stated for the receiver front-end filters. Finally, some receiver performance metrics are defined and the used simulation framework is described.

2.1 The Noncoherent Multi-Channel Receiver in a Nutshell

Let us assume an inter-symbol-interference (ISI) free scenario. By introduction of a sufficiently long zero guard interval, our analysis can concentrate on a single transmitted symbol with period T_{sym}. Considering a linear orthogonal pulse amplitude modulation (OPAM) signaling scheme [56] the most generic transmitted signal $s(t)$ can be written as

$$s(t) = \sum_{k=1}^{K} d_k \phi_k(t), \tag{2.1}$$

where $\phi_k(t)$ is the kth basis of the K-dimensional signal space and $d_k \in \mathbb{R}$ is the kth element of a K-dimensional symbol vector $\mathbf{d}$. The transmitted signal $s(t)$ gets altered by a communication channel $c(t, \tau)$. This channel is a concatenation of the transmit filter, the actual transmission channel, and the receiver front-end filter. Assuming that $c(t, \tau)$ is time-invariant within the symbol interval T_{sym}, the received signal $r(t)$ is given as

$$r(t) = c(t) * s(t) + n(t), \tag{2.2}$$

where $n(t)$ is a white Gaussian noise process at the antenna of the receiver.
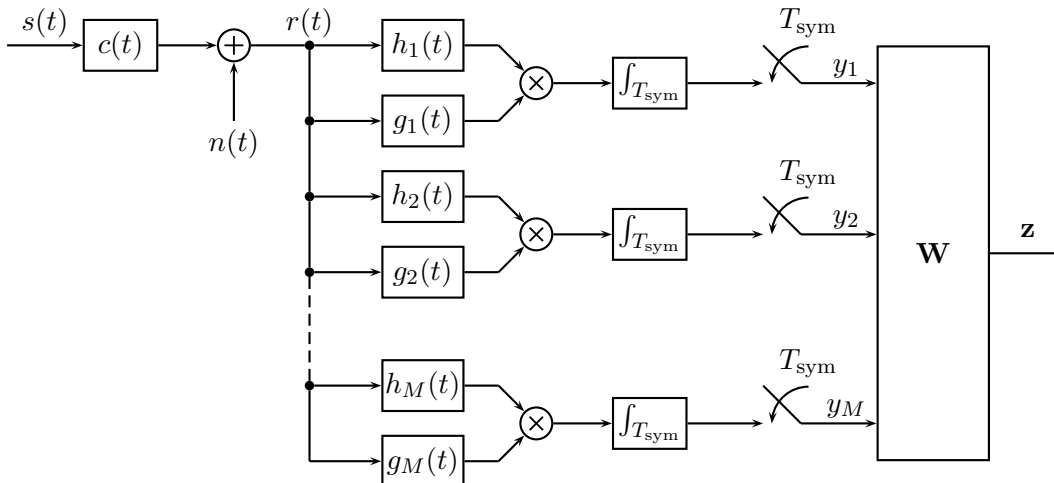
Figure 2.1: Signal flow diagram of a Generalized Noncoherenz Multi-Channel Receiver.

In Fig. 2.1 the signal flow diagram is depicted of a generalized noncoherent multi-channel receiver with M parallel receiver channels. An output sample y_m of the mth receiver channel is given as

$$y_m = \int_{\lambda=0}^{T_{\mathrm{sym}}} (h_m(t) * r(t)) \times (g_m(t) * r(t)) \, dt, \tag{2.3}$$

where $m = 1, \ldots, M$, $h_m(t)$ and $g_m(t)$ are linear time-invariant filters called *projection filters*[7].

---

[7] The reason for this nomenclature will come clear in subsequent paragraphs.

The output of the mth front-end channel can be expanded to

$$
y_m = \underbrace{\int_{t=0}^{T_{\text{sym}}} \left(h_m(t) * c(t) * s(t) \right) \times \left(g_m * c(t) * s(t) \right) dt}_{\text{signal-by-signal term}}
$$

$$
+ \underbrace{\int_{t=0}^{T_{\text{sym}}} \left(h_m(t) * c(t) * s(t) \right) \times \left(g_m * n(t) \right) dt}_{\text{signal-by-noise term}}
$$

$$
+ \underbrace{\int_{t=0}^{T_{\text{sym}}} \left(h_m(t) * n(t) \right) \times \left(g_m * c(t) * s(t) \right) dt}_{\text{noise-by-signal term}}
$$

$$
+ \underbrace{\int_{t=0}^{T_{\text{sym}}} \left(h_m(t) * n(t) \right) \times \left(g_m * n(t) \right) dt,}_{\text{noise-by-noise term}} \tag{2.4}
$$

where the first line is the desired *signal-by-signal* term, the second and the third line are undesired *signal-by-noise* and *noise-by-signal* terms, and the fourth line represents the undesired *noise-by-noise* term.

Given that we only consider the strictly ISI-free case and that the signal pulse duration $T_{\text{p}} < T_{\text{sym}}$, where T_{sym} is the symbol period, we can expand the integration interval for the signal-by-signal term to infinity and get

$$
y_m = \int_{t=-\infty}^{+\infty} \left(h_m(t) * c(t) * s(t) \right) \times \left(g_m * c(t) * s(t) \right) dt + \nu_m, \tag{2.5}
$$

which represents the correlation of two signals. The additive term ν_m accumulates all undesired terms. Due to the fact that the Fourier transform is unitary, and with use of the Parseval theorem, (2.5) can be rewritten as

$$
y_m = \frac{1}{2\pi} \int_{\omega=-\infty}^{+\infty} \left(H_m(j\omega) C(j\omega) S(j\omega) \right) \times \left(G_m(j\omega) C(j\omega) S(j\omega) \right) dt + \nu_m, \tag{2.6}
$$

which can further be represented as

$$
y_m = \frac{1}{2\pi} \left\langle H_m(j\omega) G_m^*(j\omega); |C(j\omega) S(j\omega)|^2 \right\rangle + \nu_m, \tag{2.7}
$$

where $\langle \cdot; \cdot \rangle$ is the scalar product operator. In (2.7) the intrinsic functionality of any noncoherent multi-channel receiver becomes clear: the power spectral density (PSD) $|R(j\omega)|^2 = |C(j\omega) S(j\omega)|^2$ of the received signal gets projected onto M different basis functions. The receiver basis is hence represented by the set $\{ X_m(j\omega) = H_m(j\omega) G_m^*(j\omega) \}$ of its respective projection filter *cross-spectra*.

When considering a linear signaling scheme (cf. (2.1)), we can further expand (2.7) and obtain for the mth front-end channel

$$
y_m = \underbrace{\frac{1}{2\pi} \sum_{k=1}^{K} |d_k|^2 \left\langle X_m(j\omega); |C(j\omega)\Phi_k(j\omega)|^2 \right\rangle}_{\text{signal co-terms}}
$$

$$
+ \underbrace{\frac{1}{2\pi} \sum_{k=1}^{K} \sum_{\substack{l=1 \\ l \neq k}}^{K} d_k d_l^* \left\langle X_m(j\omega); |C(j\omega)|^2 \Phi_k(j\omega)\Phi_l^*(j\omega) \right\rangle}_{\text{signal cross-terms}}
$$

$$
+ \nu_m, \tag{2.8}
$$

where the first line represents the so called *signal co-terms*, the second line represents the so-called *signal cross-terms*.

For easy representation, the output of the M receiver channels can be merged and written in vector notation as

$$
\mathbf{y} = \mathbf{P} \left(\mathbf{d} \odot \mathbf{d}^*\right) + \mathbf{Q} \left(\mathbf{d}\tilde{\otimes}\mathbf{d}^*\right) + \boldsymbol{\nu}, \tag{2.9}
$$

where $\odot$ is the element wise multiplication, $\tilde{\otimes}$ is the reduced Kronecker product where the squared terms are excluded [33], $\mathbf{P}$ is the *co-term projection matrix* (cf. the signal co-terms in (2.8)) of size $M \times K$, $\mathbf{Q}$ is the *cross-term projection matrix* (cf. the signal cross-terms in (2.8)) of size $M \times K(K-1)$, and $\boldsymbol{\nu}$ is a vector which collects all undesired terms.

As we will see in Section 2.2 and Section 2.4, a simple way to obtain the submitted data vector $\mathbf{d}$ from the sample vector $\mathbf{y}$ is to use a linear transformation matrix $\mathbf{W}$ which inverts $\mathbf{P}$ previous to detection, i.e., $\mathbf{WP} = \mathbf{I}_{K \times K}$ where $\mathbf{I}_{K \times K}$ is the $K \times K$ identity matrix. The so obtained decision variable $\mathbf{z}$ (cf. Fig. 2.1) is, hence, given as

$$
\mathbf{z} = \mathbf{Wy} \tag{2.10}
$$

$$
= \left(\mathbf{d} \odot \mathbf{d}^*\right) + \mathbf{WQ} \left(\mathbf{d}\tilde{\otimes}\mathbf{d}^*\right) + \mathbf{W}\boldsymbol{\nu}. \tag{2.11}
$$

2.2 Noncoherent Orthogonal Frequency-Divison Multiplexing

The derivation of the vector representation of the receiver channels gives valuable insight how the signaling for noncoherent multi-channel receivers needs to look like. As it can be seen in (2.9), the model unfortunately does not represent a linear system like

$$\mathbf{y} = \mathbf{P}\mathbf{s} + \boldsymbol{\nu} \tag{2.12}$$

which would be preferred for easier signal detection [57]. To obtain such a linear system, the cross-term projection matrix $\mathbf{Q}$ needs to vanish[8], i.e.

$$\left\langle X_m(j\omega); |C(j\omega)|^2 \, \Phi_k(j\omega)\Phi_l^*(j\omega) \right\rangle = 0, \tag{2.13}$$

for $k, l = 1, \ldots, K$, and $k \neq l$. This can be ensured by design of the transmitter signaling. E.g. if $\{\phi_k(t)\}$ is *separated in frequency domain*, that is

$$\Phi_k(j\omega)\Phi_l^*(j\omega) = 0, \tag{2.14}$$

for $\omega \in \mathbb{R}$, $k, l = 1, \ldots, K$, and $k \neq l$, it will hold independently of the channel response $C(j\omega)$. This constraint also ensures *orthogonality* between all $\{\phi_k(t)\}$, which is required by (2.1).

It needs also to be noted that $\mathbf{s} = (\mathbf{d} \odot \mathbf{d}^*)$. Thus to ensure appropriate and unique symbols and a bijective mapping from $\{s_k\}$ to $\{d_k\}$, the elements d_k of the symbol vector $\mathbf{d}$ need to be

$$d_k \in \mathbb{R}^+, \tag{2.15}$$

hence, amplitude-shift keying (ASK) would be a proper modulation. With $d_k \in \{0, 1\}$, so that $\{s_k\} = \{d_k\}$, *noncoherent* modulation schemes as on-off keying (OOK) or pulse position modulation (PPM) are supported and an inverse mapping from $\{s_k\}$ to $\{d_k\}$ is not needed. Each data symbol d_k might be modulated with a random equiprobable sign $\in \{+, -\}$ to ensure a zero-mean data vector and thus avoiding spurs in the PSD.

These constraints, the orthogonality and frequency separation of the basis signals $\{\phi_k(t)\}$, and the restriction of the symbol vector elements to OOK or PPM, lead to the *noncoherent orthogonal frequency-division multiplexing* (NOFDM) modulation scheme [46] defined as

$$s(t) = \Re\left\{\sum_{k=1}^{K} d_k\varphi(t)e^{+j\left(k-\frac{K+1}{2}\right)\omega_{\text{sc}}t}e^{+j\omega_{\text{c}}t}\right\}, \tag{2.16}$$

where $\Re\{\cdot\}$ resembles the real value operator. This signal consists of K subcarriers with a frequency spacing of ω_{sc} rad/s, a center frequency of ω_{c} rad/s, and the pulse shape of the transmitted signal $\varphi(t)$. To ensure frequency separation, the bandwidth B_{p} of the pulse shape $\varphi(t)$ needs to be $B_{\text{p}} \leq \omega_{\text{sc}}$. To ensure ISI-free condition, the pulse duration T_{p} of the pulse shape $\varphi(t)$ needs to be $T_{\text{p}} < T_{\text{sym}}$.

In this entire work an NOFDM signal is used with $K = 7$ subcarriers with a frequency spacing of 250 MHz and a center frequency of 4 GHz. The used pulse shape $\varphi(t)$ is a root raised-cosine pulse with a roll-off factor of $\beta = 0.5$ which has been truncated at its first zero-crossings next to the main lobe. The pulse duration is 10.6 ns. An additional minimal zero guard interval is added to end up with a symbol period of $T_{\text{sym}} = 16$ ns. Depending on the maximal channel excess delay of the NLOS multipath components, a longer zero guard interval can be used but extends the symbol period.

The pulse shape and the PSD of the subcarriers are depicted in Fig. 2.2. Using a proper trans-

---

[8] Note that in practice it is typically not possible to get the cross-terms to vanish, but it is possible to get them insignificant.

mitter filter, the NOFDM signaling complies with the FCC PSD emission limit for UWB communications [25], which permit a PSD of maximal -41.3 dBm/MHz in the frequency range between 3.1 GHz and 10.6 GHz and limits the emission in the rest of the spectra to -75 dBm/MHz.

In Fig. 2.3 the correlation matrix of the different subcarriers is illustrated. It can be seen that the pulses are almost orthogonal to each other, with a maximal correlation coefficient of $1.73 \cdot 10^{-3}$.

In [58, 59] different orthogonal basis signals have been studied, e.g discrete prolate spheroidal sequences, an orthogonal pulse amplitude modulation scheme based on code-division multiple access (CDMA) spreading codes, shift-added noise waveforms, and signals obtained by genetic optimization. It was shown that the NOFDM signaling is superior to all the other studied signals in terms of system performance metrics (cf. Section 2.5).
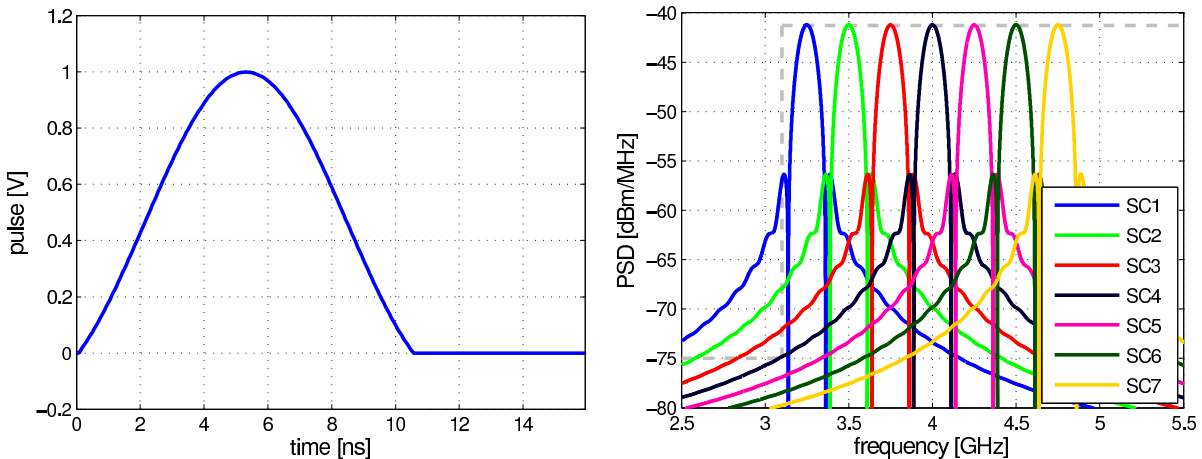
(a) Normalized pulse shape $\varphi(t)$ in time-domain.

(b) Power spectral density with $K = 7$ subcarriers.

Figure 2.2: *The NOFDM signaling scheme. The pulse shape $\varphi(t)$ is a root raised-cosine pulse truncated at its first zero-crossing next to the main lobe. The symbol period is 16 ns with a pulse duration of approximately 10.6 ns. The last 5.4 ns represent a zero guard-interval. The frequency spacing between the subcarriers is 250 MHz and the center frequency is 4 GHz. The average power of the signaling is -9 dBm.*
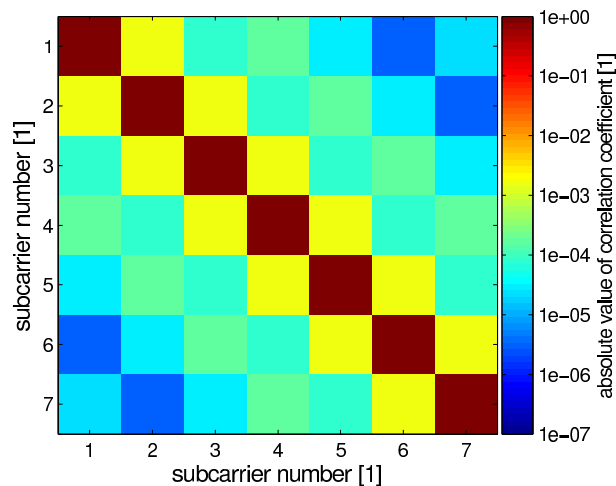
Figure 2.3: *Correlation matrix of $K = 7$ NOFDM subcarriers.*

2.3 Design Rules for Ideal Projection Filters

For optimal receiver performance, the receiver projection filters need to be designed to enable the receiver to detect the transmitted signals as good as possible. Within this section some design rules will be stated. Let's begin with a very general and trivial rule:

1. The impulse responses of the projection filters need to be short enough to ensure ISI free detection, hence the impulse responses need to be shorter than $T_{\text{sym}} - T_{\text{p}} - T_{\text{max}}$, accounting for the maximal channel excess delay T_{max} and the pulse duration T_{p}.

For ISI free transmission we can then consider a single symbol interval $[0, T_{\text{sym}})$ without loss of generality. By expanding this symbol period periodically, the sent signal $s(t)$ can be represented by the Fourier series

$$s(t) = \sum_{i=-\infty}^{+\infty} s_i e^{j\omega_0 it}, \tag{2.17}$$

where $\omega_0 = \frac{2\pi}{T_{\text{sym}}}$. The Fourier coefficients s_i are given as

$$s_i = \frac{1}{T_{\text{sym}}} \int_{t=0}^{T_{\text{sym}}} s(t) e^{-j\omega_0 it} dt \tag{2.18}$$

$$= \sum_{k=1}^{K} d_k \varphi_{k,i}, \tag{2.19}$$

where $\varphi_{k,i} = \Phi_k(j\omega_0 i)$ are the Fourier coefficients of the basis functions defined in (2.1).

The received signal $r(t)$ is (as in (2.2)) given as

$$r(t) = c(t) * s(t) + n(t),$$

where $c(t)$ is the transmission channel and $n(t)$ is a band-limited Gaussian noise process with a flat power density spectrum. Using Fourier series expansion, the received signal $r(t)$ can be represented in the integration interval T_{sym} by the Fourier coefficients r_i given as

$$r_i = c_i s_i + n_i, \tag{2.20}$$

with $c_i = C(j\omega_0 i)$ and $\{n_i\}$ being the Fourier coefficients of $n(t)$.

Each receiver channel output

$$y_m = \int_{t=0}^{T_{\text{sym}}} (h_m(t) * r(t)) \times (g_m(t) * r(t)) \, dt \tag{2.21}$$

is further given (for $h_m(t)$ and $g_m(t)$ being real valued and using the Fourier series expansion) as

$$
y_m = \underbrace{T_{\mathrm{sym}} \sum_{i=-\infty}^{+\infty} h_{m,i} g_{m,i}^* c_i c_i^* \sum_{k=1}^{K} d_k d_k^* \varphi_{k,i} \varphi_{k,i}^*}_{\text{signal co-terms}}
$$

$$
+ \underbrace{T_{\mathrm{sym}} \sum_{i=-\infty}^{+\infty} h_{m,i} g_{m,i}^* c_i c_i^* \sum_{k=1}^{K} \sum_{\substack{l=1 \\ l \neq k}}^{K} d_k d_l^* \varphi_{k,i} \varphi_{l,i}^*}_{\text{signal cross-terms}}
$$

$$
+ \underbrace{T_{\mathrm{sym}} \sum_{i=-\infty}^{+\infty} h_{m,i} g_{m,i}^* c_i \left(\sum_{k=1}^{K} d_k \varphi_{k,i} \right) n_i^*}_{\text{signal-by-noise terms}}
$$

$$
+ \underbrace{T_{\mathrm{sym}} \sum_{i=-\infty}^{+\infty} h_{m,i} g_{m,i}^* c_i^* n_i \left(\sum_{l=1}^{K} d_l^* \varphi_{l,i}^* \right)}_{\text{noise-by-signal terms}}
$$

$$
+ \underbrace{T_{\mathrm{sym}} \sum_{i=-\infty}^{+\infty} h_{m,i} g_{m,i}^* n_i n_i^*}_{\text{noise-by-noise terms}} \tag{2.22}
$$

where $h_{m,i} = H_m(j\omega_0 i)$, and $g_{m,i} = G_m(j\omega_0 i)$. In Appendix B.1 this and all following steps to derive the signal-to-interference-and-noise ration (SINR) are illustrated in more detail.

In matrix representation, the mth receiver output can be written as

$$
y_m = \underbrace{T_{\mathrm{sym}} \mathbf{g}_m^H \mathbf{H}_m \mathbf{C}^H \mathbf{C} \mathbf{\Psi}}_{=\mathbf{P}} (\mathbf{d} \odot \mathbf{d}^*)
$$

$$
+ \underbrace{T_{\mathrm{sym}} \mathbf{g}_m^H \mathbf{H}_m \mathbf{C}^H \mathbf{C} \tilde{\mathbf{\Psi}}}_{=\mathbf{Q}} (\mathbf{d} \tilde{\otimes} \mathbf{d}^*) \tag{2.23}
$$

$$
+ T_{\mathrm{sym}} \mathbf{g}_m^H \mathbf{H}_m \mathbf{C} \mathbf{N}^H \mathbf{\Phi} \mathbf{d}
$$

$$
+ T_{\mathrm{sym}} \mathbf{g}_m^H \mathbf{H}_m \mathbf{C}^H \mathbf{N} \mathbf{\Phi}^* \mathbf{d}^*
$$

$$
+ T_{\mathrm{sym}} \mathbf{g}_m^H \mathbf{H}_m \mathbf{n}', \tag{2.24}
$$

where the elements of the vectors $\mathbf{g}_m$ and $\mathbf{n}'$ are given as $[\mathbf{g}_m]_i = g_{m,i}$ and $[\mathbf{n}']_i = n_i n_i^*$. The matrices $\mathbf{H}_m$, $\mathbf{C}$, and $\mathbf{N}$, are diagonal matrices with $[\mathbf{H}_m]_{i,i} = h_{m,i}$, $[\mathbf{C}]_{i,i} = c_i$, and $[\mathbf{N}]_{i,i} = n_i$. The elements of the matrices $\mathbf{\Phi}$ and $\mathbf{\Psi}$ are given as $[\mathbf{\Phi}]_{i,k} = \varphi_{k,i}$ and $[\mathbf{\Psi}]_{i,k} = \varphi_{k,i} \varphi_{k,i}^*$. The columns of $\tilde{\mathbf{\Psi}}$ consist of $\boldsymbol{\varphi}_k \odot \boldsymbol{\varphi}_l^*$ for $k = 1, \ldots, K$, $l = 1, \ldots, K$, but $l \neq k$, where the elements of the vector $\boldsymbol{\varphi}_k$ are given as $[\boldsymbol{\varphi}_k]_i = \varphi_{k,i}$.

If defining a projection filter cross-spectra matrix $\mathbf{X}$ with $[\mathbf{X}]_{i,m} = g_{m,i}h_{m,i}^*$, the receiver output vector $\mathbf{y}$ can be represented as

$$
\begin{aligned}
\mathbf{y} = T_{\mathrm{sym}}\mathbf{X}^H\mathbf{C}^H\mathbf{C}\boldsymbol{\Psi}\left(\mathbf{d}\odot\mathbf{d}^*\right) &\quad \} =: \boldsymbol{\alpha} \\
+ T_{\mathrm{sym}}\mathbf{X}^H\mathbf{C}^H\mathbf{C}\tilde{\boldsymbol{\Psi}}\left(\mathbf{d}\tilde{\otimes}\mathbf{d}^*\right) &\quad \} =: \boldsymbol{\beta} \\
+ T_{\mathrm{sym}}\mathbf{X}^H\mathbf{C}\mathbf{N}^H\boldsymbol{\Phi}\mathbf{d} & \\
+ T_{\mathrm{sym}}\mathbf{X}^H\mathbf{C}^H\mathbf{N}\boldsymbol{\Phi}^*\mathbf{d}^* &\quad \Big\} =: \boldsymbol{\nu} \\
+ T_{\mathrm{sym}}\mathbf{X}^H\mathbf{n}'. &
\end{aligned}
\tag{2.25}
$$

With $\mathbf{W}$ being the pseudo inverse of $\mathbf{P} = T_{\mathrm{sym}}\mathbf{X}^H\mathbf{C}^H\mathbf{C}\boldsymbol{\Psi}$, the decision variable vector $\mathbf{z}$ is given as

$$
\begin{aligned}
\mathbf{z} = \left(\mathbf{d}\odot\mathbf{d}^*\right) & \\
+ T_{\mathrm{sym}}\mathbf{W}\mathbf{X}^H\mathbf{C}^H\mathbf{C}\tilde{\boldsymbol{\Psi}}\left(\mathbf{d}\tilde{\otimes}\mathbf{d}^*\right) & \\
+ T_{\mathrm{sym}}\mathbf{W}\mathbf{X}^H\mathbf{C}\mathbf{N}^H\boldsymbol{\Phi}\mathbf{d} & \\
+ T_{\mathrm{sym}}\mathbf{W}\mathbf{X}^H\mathbf{C}^H\mathbf{N}\boldsymbol{\Phi}^*\mathbf{d}^* & \\
+ T_{\mathrm{sym}}\mathbf{W}\mathbf{X}^H\mathbf{n}'. &
\end{aligned}
\tag{2.26}
$$

In Fig. 2.4 two alternative signal flow diagrams of this equation are depicted. When inspecting this equation, it becomes clear that maximizing the SINR means in any case that the projection filters need to feature two properties: 1) they need to maximize the signal power while minimizing noise and self-interference, and 2) they need to maintain the orthogonality of the transmitted basis-functions. Maintaining the orthogonality is given by a low condition number[9] of $\mathbf{P}$.

Note that instead of finding the best filters $\mathbf{h}_m$ and $\mathbf{g}_m$, the best cross-spectra $\mathbf{x}_m$ need to be found. The found cross-spectra $\mathbf{x}_m$ can be split into the two filters $\mathbf{h}_m$ and $\mathbf{g}_m$ after optimization. Alternatively only one filter, $\mathbf{h}_m$ or $\mathbf{g}_m$, might be synthesized while the second filter might resemble an allpass filter. It is also possible to synthesize zero-phase cross-spectra by choosing $\mathbf{h}_m = \mathbf{g}_m$.

2.3.1 Maximization of the Signal-to-Interference-and-Noise Ratio

To derive the SINR, we focus on a single decision variable z_k at first. The decision variable z_k is given as

$$
\begin{aligned}
z_k = T_{\mathrm{sym}}\mathbf{w}_k^T\mathbf{X}^H\mathbf{C}^H\mathbf{C}\boldsymbol{\Psi}\left(\mathbf{d}\odot\mathbf{d}^*\right) & \\
+ T_{\mathrm{sym}}\mathbf{w}_k^T\mathbf{X}^H\mathbf{C}^H\mathbf{C}\tilde{\boldsymbol{\Psi}}\left(\mathbf{d}\tilde{\otimes}\mathbf{d}^*\right) & \\
+ T_{\mathrm{sym}}\mathbf{w}_k^T\mathbf{X}^H\mathbf{C}\mathbf{N}^H\boldsymbol{\Phi}\mathbf{d} & \\
+ T_{\mathrm{sym}}\mathbf{w}_k^T\mathbf{X}^H\mathbf{C}^H\mathbf{N}\boldsymbol{\Phi}^*\mathbf{d}^* & \\
+ T_{\mathrm{sym}}\mathbf{w}_k^T\mathbf{X}^H\mathbf{n}', &
\end{aligned}
\tag{2.27}
$$

where $\mathbf{w}_k^T$ is the kth row of $\mathbf{W}$. When we consider ideal NOFDM, that is the subcarriers are not overlapping and, hence, are mutually orthogonal, we know that $\tilde{\boldsymbol{\Psi}} = \mathbf{0}$. Hence, the SINR of ideal NOFDM is represented by its SNR.

---

[9] The condition number also gives a measure how sensitive the inverse is to small input errors [60].

(a)

(b)
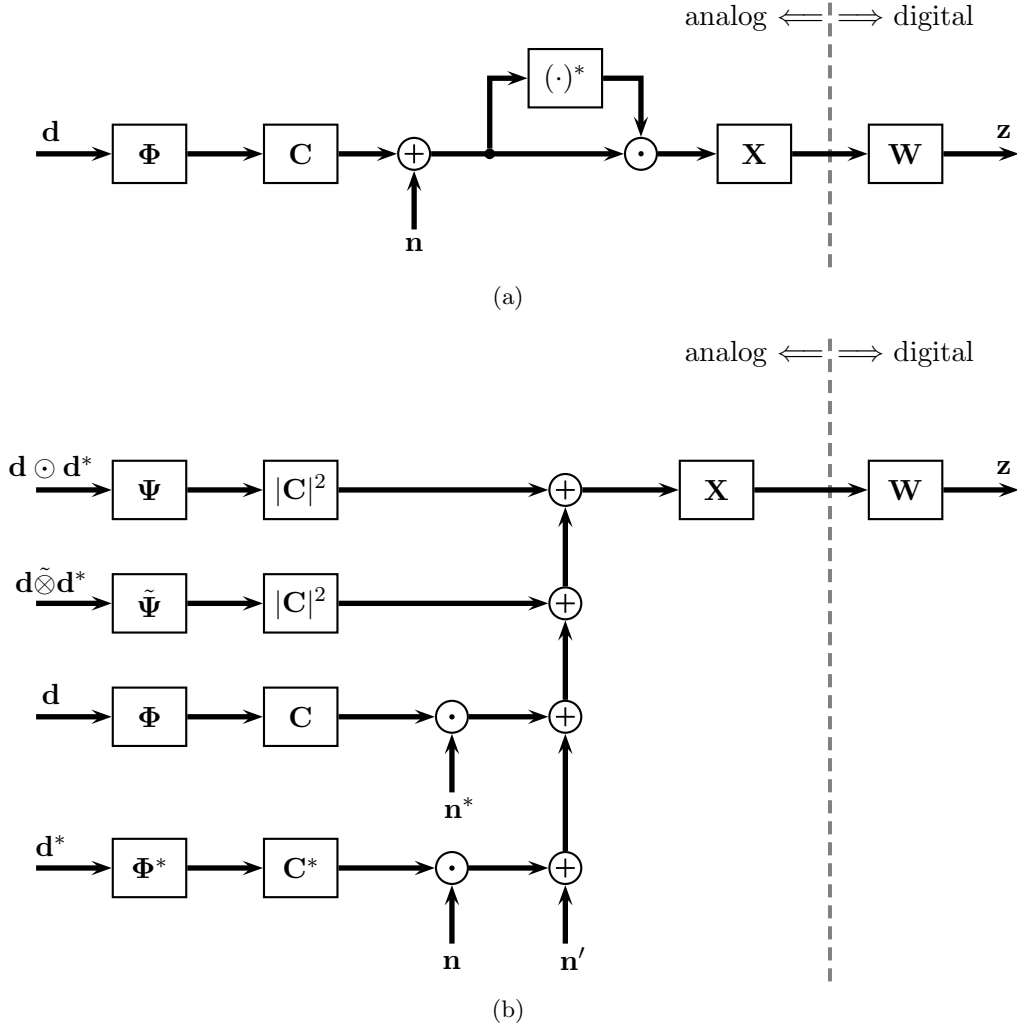
Figure 2.4: Two equivalent matrix signal flow diagrams of the generalized noncoherent multi-channel receiver.

We consider $\mathbf{W}$ being the pseudo-inverse of $\mathbf{P} = T_{\mathrm{sym}}\mathbf{X}^H\mathbf{C}^H\mathbf{C}\boldsymbol{\Psi}$, so that $T_{\mathrm{sym}}\mathbf{W}\mathbf{X}^H\mathbf{C}^H\mathbf{C}\boldsymbol{\Psi} = \mathbf{I}_{K\times K}$. A pseudo-inverse is only given for $T_{\mathrm{sym}}\mathbf{X}^H\mathbf{C}^H\mathbf{C}\boldsymbol{\Psi}$ being full rank, i.e. we can formulate the following rules:

2. The passbands of the projection filter cross-spectra $\{X_m(j\omega)\}$ need to be within the signal bandwidth to ensure $\mathbf{P}$ being full rank.

3. The set of the filter cross-spectra $\{X_m(j\omega)\}$ needs to be linearly independent to ensure $\mathbf{P}$ being full rank.

Additionally, when considering $T_{\mathrm{sym}}\mathbf{W}\mathbf{X}^H\mathbf{C}^H\mathbf{C}\boldsymbol{\Psi} = \mathbf{I}_{K\times K}$, we find out that

$$\hat{\boldsymbol{\psi}}_k' := T_{\mathrm{sym}}\mathbf{w}_k^T\mathbf{X}^H \approx \frac{\boldsymbol{\psi}_k'^H}{||\boldsymbol{\psi}_k'||^2}, \tag{2.28}$$

where $\boldsymbol{\psi}_k'$ is the kth column of $\boldsymbol{\Psi}' = \mathbf{C}^H\mathbf{C}\boldsymbol{\Psi}$. As can be seen, $\mathbf{w}_k^T\mathbf{X}^H$, which is a linear combination of the cross-spectra $\{X_m(j\omega)\}$, resembles an approximation of the normalized PSD of the kth basis signal. This means that each term in (2.27) gets projected onto $\{\mathbf{w}_k^T\mathbf{X}^H\}$. The terms $\{\mathbf{w}_k^T\mathbf{X}^H\}$ can be interpreted as the spectra of the inverse. Therefore, we define

$\hat{\psi}'_k = T_{\text{sym}} \mathbf{w}_k^T \mathbf{X}^H$ and simplify (2.27) to

$$z_k = \hat{\psi}'^H_k \boldsymbol{\Psi}' \left(\mathbf{d} \odot \mathbf{d}^* \right) + \hat{\psi}'^H_k \mathbf{N}^H \boldsymbol{\Phi}' \mathbf{d} + \hat{\psi}'^H_k \mathbf{N} \boldsymbol{\Phi}'^* \mathbf{d}^* + \hat{\psi}'^H_k \mathbf{n}', \tag{2.29}$$

where $\boldsymbol{\Phi}' = \mathbf{C}\boldsymbol{\Phi}$. With $\hat{\psi}'^H_k \boldsymbol{\Psi}' \left(\mathbf{d} \odot \mathbf{d}^* \right) = |d_k|^2$ we obtain

$$z_k = \underbrace{|d_k|^2}_{=:\alpha_k} + \underbrace{\hat{\psi}'^H_k \mathbf{N}^H \boldsymbol{\Phi}' \mathbf{d} + \hat{\psi}'^H_k \mathbf{N} \boldsymbol{\Phi}'^* \mathbf{d}^* + \hat{\psi}'^H_k \mathbf{n}'}_{=:\nu_k}, \tag{2.30}$$

where we can see that the signal-by-noise, noise-by-signal, and noise-by-noise terms are projected onto the detection space spanned by $\left\{ \hat{\psi}'_k \right\}$.

Note that for an ideal NOFDM signal where the subcarriers are ideally separated in frequency domain, $\frac{\psi'^H_k}{||\psi'_k||^2} \boldsymbol{\Phi}' \mathbf{d} = \frac{\psi'^H_k}{||\psi'_k||^2} d_k \boldsymbol{\varphi}'_k$, where $\boldsymbol{\varphi}'_k$ is the kth column of $\boldsymbol{\Phi}'$, we obtain with (2.28)

$$z_k \approx |d_k|^2 + d_k \frac{\psi'^H_k}{||\psi'_k||^2} \mathbf{N}^H \boldsymbol{\varphi}'_k + d_k^* \frac{\psi'^H_k}{||\psi'_k||^2} \mathbf{N} \boldsymbol{\varphi}'^*_k + \frac{\psi'^H_k}{||\psi'_k||^2} \mathbf{n}', \tag{2.31}$$

where $\boldsymbol{\varphi}'_k$ is the kth column of $\boldsymbol{\Phi}'$. In this ideal case the signal-by-noise and noise-by-signal terms are only dependent on their respective subcarrier $\boldsymbol{\varphi}'_k$ but not on other subcarriers. It can also be seen that these terms only exist, if the transmitted data symbol $d_k = 1$.

The SNR of the decision vector $\mathbf{z}$ for an ideal NOFDM signalling is defined as

$$\text{SNR} = \frac{\sum_{k=1}^{K} \text{E} \left\{ |d_k|^4 \right\}}{\sum_{k=1}^{K} \text{E} \left\{ \nu_k \nu_k^* \right\}} \tag{2.32}$$

where the expectation operator $\text{E} \left\{ \cdot \right\}$ is taken with respect to the noise $\{n_i\}$ and data $\{d_k\}$.

The conditioned correlation $\text{E} \left\{ \nu_k \nu_l^* | \mathbf{d} \right\}$ is derived in Appendix B.1.2. It is given for non-overlapping subcarriers, so that $\varphi^*_{p,i} \varphi_{q,i} = 0$ for $p \neq q$, and $\left\{ \hat{\psi}'_k \right\}$ being mutually orthogonal, which can be assumed due to (2.28) and $\{\psi'_k\}$ being mutually orthogonal, as

$$\text{E} \left\{ \nu_k \nu_l^* | \mathbf{d} \right\} = 2\delta_{k-l} \frac{\sigma_n^2}{T_{\text{sym}}} \sum_{p=1}^{K} |d_p|^2 \sum_{i=-\infty}^{+\infty} |\hat{\psi}'_{k,i}|^2 |\varphi'_{p,i}|^2$$
$$+ \frac{\sigma_n^4}{T_{\text{sym}}^2} \sum_{i=-\infty}^{+\infty} \hat{\psi}'^*_{k,i} \sum_{j=-\infty}^{+\infty} \hat{\psi}'_{l,j} + \delta_{k-l} \frac{\sigma_n^4}{T_{\text{sym}}^2} \sum_{i=-\infty}^{+\infty} |\hat{\psi}'_{k,i}|^2. \tag{2.33}$$

If we further assume that $\left(\hat{\psi}'_k \odot \hat{\psi}'^*_k \right)$ is orthogonal to $\left(\boldsymbol{\varphi}'_p \odot \boldsymbol{\varphi}'^*_p \right)$ for $p \neq k$, e.g. if $\hat{\psi}'_k$ does not overlap with $\boldsymbol{\varphi}_p$ for $p \neq k$,we get

$$\text{E} \left\{ \nu_k \nu_l^* | \mathbf{d} \right\} = 2\delta_{k-l} \frac{\sigma_n^2}{T_{\text{sym}}} |d_k|^2 \sum_{i=-\infty}^{+\infty} |\hat{\psi}'_{k,i}|^2 |\varphi'_{k,i}|^2$$
$$+ \frac{\sigma_n^4}{T_{\text{sym}}^2} \sum_{i=-\infty}^{+\infty} \hat{\psi}'^*_{k,i} \sum_{i=-\infty}^{+\infty} \hat{\psi}'_{l,i} + \delta_{k-l} \frac{\sigma_n^4}{T_{\text{sym}}^2} \sum_{i=-\infty}^{+\infty} |\hat{\psi}'_{k,i}|^2. \tag{2.34}$$

With $\hat{\psi}'_k \approx \frac{\psi'^H_k}{||\psi'_k||^2}$ and ideal NOFDM signaling we can approximate $\hat{\psi}'_k$ as in (2.28) and, obtain

$$\mathrm{E}\left\{\nu_k \nu_l^*|\mathbf{d}\right\} \approx 2\delta_{k-l}\frac{\sigma_n^2}{T_{\mathrm{sym}}}|d_k|^2\frac{\sum_{i=-\infty}^{+\infty}|\varphi'_{k,i}|^6}{||\psi'_k||^4}$$
$$+ \frac{\sigma_n^4}{T_{\mathrm{sym}}^2}\frac{||\varphi'_k||^2}{||\psi'_k||^2}\frac{||\varphi'_l||^2}{||\psi'_l||^2} + \delta_{k-l}\frac{\sigma_n^4}{T_{\mathrm{sym}}^2}\frac{1}{||\psi'_k||^2}. \tag{2.35}$$

The first lines in (2.33) – (2.35) represent the signal-by-noise and noise-by-signal terms. The second lines represent the noise-by-noise terms. Note that the first terms in the second line of (2.33) – (2.35) resemble the product of means $\mathrm{E}\left\{\nu_k|\mathbf{d}\right\}\mathrm{E}\left\{\nu_l^*|\mathbf{d}\right\}$. Using PPM, this product of means can be mitigated [13].

In (2.33) it can be seen that $\mathrm{E}\left\{\nu_k\nu_l^*|\mathbf{d}\right\}$ depends on all data $\{d_p\}$ whose respective subcarriers φ'_p overlap with $\hat{\psi}_k$. In (2.34) and (2.35), where the subcarriers do not overlap with $\hat{\psi}_k$, it can be seen that $\mathrm{E}\left\{\nu_k\nu_l^*|\mathbf{d}\right\}$ only depends on the data d_k. I.e. if d_k is equal to zero, the signal-by-noise and noise-by-signal terms do not contribute to the conditioned correlation. It also can bee seen in (2.33) and (2.34) that selective cross-spectra result in less noise. It becomes clear that maximizing the SNR means also to minimize the overlap of the spectra of the inverse $\mathbf{w}_k^T\mathbf{X}^H$ with subcarriers where $p \neq k$. This translates into the following design rule:

4. The spectrum of the inverse $\mathbf{w}_k^T\mathbf{X}^H$ of the kth subcarrier, which is a linear combination of the projection filter cross-spectra $\{X_m(j\omega)\}$, should not overlap with other subcarriers.

For an ideal front-end as in (2.35), it can bee seen that the SNR does not depend on the projection filter $\mathbf{X}$. But it can be seen that the SNR depends on the channel, due to $||\psi'_k||^2 = \sum_{i=-\infty}^{+\infty}|\varphi_{k,i}|^4|c_i|^4$ and $||\varphi'_k||^2 = \sum_{i=-\infty}^{+\infty}|\varphi_{k,i}|^2|c_i|^2$.

2.3.2 Conservation of Orthogonality

For OOK or PPM signals, where $d_k \in \{0,1\}$, the detection variable $\mathbf{z}$ can be represented as

$$\mathbf{z} = \mathbf{WPd} + \mathbf{WQ}\left(\mathbf{d}\tilde{\otimes}\mathbf{d}\right) + \mathbf{W}\boldsymbol{\nu}. \tag{2.36}$$

Let us assume that the chosen signaling causes the elements of $\mathbf{Q}$ to become insignificant. We know that $\mathbf{W}$ needs to resemble an inverse operator to $\mathbf{P}$, hence

$$\mathbf{W} = \mathbf{P}^\dagger, \tag{2.37}$$

where $\mathbf{P}^\dagger = \left(\mathbf{P}^H\mathbf{P}\right)^{-1}\mathbf{P}^H$ represents the Moore-Penrose pseudo inverse [33] of $\mathbf{P}$.

Matrix inversion of $\mathbf{P}$ is only possible for $M \geq K$, so that the rank of the matrix $\mathbf{P}$ is K. As aforementioned (cf. Rule 3.), the set of the filter cross-spectra $\{X_m(j\omega)\}$ needs to be linearly independent.

To ensure conservation of orthogonality due to $\mathbf{P}$, we require that the condition number of $\mathbf{P}$ converges to unity as close as possible [61], that is

$$\mathrm{cond}\left\{\mathbf{P}\right\} = \frac{\sigma_{\mathrm{max}}}{\sigma_{\mathrm{min}}} \approx 1, \tag{2.38}$$

where σ_{max} and σ_{min} are the maximal and minimal singular values of $\mathbf{P}$, respectively.

In the ideal case, the matrix $\mathbf{P}$ fulfills $\mathrm{cond}\left\{\mathbf{P}\right\} = 1$. If $\mathbf{P}$ fulfills $\mathrm{cond}\left\{\mathbf{P}\right\} = 1$ and is quadratic, $\mathbf{P}$ is called *unitary* and does hence have orthonormal column vectors[10] [61]. For a case where $\mathbf{P}$

---

[10] For sake of simplicity we assume that the singular values $\{\sigma_i\}$ of $\mathbf{P}$ are $\sigma_i = 1$ for $i = 1, \ldots, K$.

is rectangular, that is $M > K$, and cond $\{\mathbf{P}\} = 1$ is fulfilled, $\mathbf{P}$ will have orthonormal column vectors too and will be called *quasi-unitary*, so that

$$\mathbf{P}^H \mathbf{P} = \mathbf{I}_{K \times K}, \tag{2.39}$$

where $\mathbf{P}^H$ is the conjugate transpose of $\mathbf{P}$, and $\mathbf{I}_{K \times K}$ is the identity matrix of dimension K. (A proof for the relationship between a quasi-unitary matrix and its condition number is given in Appendix B.2.)

The projection filter cross-spectra $X_m(j\omega)$ needs to be designed so that the elements of the matrix $\mathbf{P}$, given as

$$[\mathbf{P}]_{m,k} = \left\langle X_m(j\omega); |C(j\omega)|^2 |\Phi_k(j\omega)|^2 \right\rangle, \tag{2.40}$$

do result in a quasi-unitary matrix, at least for a flat channel assumption, where $|C(j\omega)|^2$ is constant within the signal bandwidth. For this, we can see the following:

5. The elements of $\mathbf{P}$ need to be real valued, hence the impulse responses $h_m(j\omega)$ and $g_m(j\omega)$ need to be real valued. A proof is given in Appendix B.3.

6. The columns of $\mathbf{P}$ must be orthogonal to each other to fulfill the quasi-unitarity constraint. The projection filters need to have the same energy and their cross-spectra $\{X_m(j\omega)\}$ need to be mutually orthogonal, so that

$$\langle X_m(j\omega); X_n(j\omega) \rangle = \delta_{m-n}, \tag{2.41}$$

for all $m, n = 1, \cdots, M$, where δ_i represents the Kronecker delta. A proof is given in Appendix B.4.

7. The spectra of the basis signals $|\Phi_k(j\omega)|^2$ must be mutually orthogonal in the space spanned by the set of the projection filter cross-spectra $\{X_m(j\omega)\}$. A proof is given in Appendix B.4.

The stated constraints on designing the projection filters are not tight, so many different noncoherent multi-channel receiver versions are possible. A selection of different receiver *flavors* is shown in Section 2.6.

2.4 ZF and MMSE Linear Detection

To understand how a noncoherent multi-channel receiver is performing its operation, a singular value decomposition (SVD) [62] can be used. Applying SVD, the quasi-unitary co-term matrix $\mathbf{P}$ can be expressed as

$$\mathbf{P} = \mathbf{U}\boldsymbol{\Sigma}\mathbf{V}^H, \tag{2.42}$$

where $\mathbf{U}$ and $\mathbf{V}$ are M-dimensional and K-dimensional unitary matrices, respectively, and $\boldsymbol{\Sigma}$ is an $M \times K$ rectangular diagonal matrix with the singular values of $\mathbf{P}$ as diagonal elements. For $M \geq K$ and $\mathbf{P}$ to be quasi-unitary, the singular value matrix $\boldsymbol{\Sigma}$ needs to fulfill

$$\boldsymbol{\Sigma} = \begin{bmatrix} \mathbf{I}_{K \times K} \\ \mathbf{0}_{M-K \times K} \end{bmatrix}, \tag{2.43}$$

where $\mathbf{0}_{M-K \times K}$ is the zero matrix with $M-K$ rows and K columns. Further, using the matrices obtained using SVD, $\mathbf{P}$ can be represented equivalently as

$$\mathbf{P} = \left[\mathbf{U}_{\mathrm{M \times K}}\mathbf{V}^H, \mathbf{B}\right] \boldsymbol{\Sigma}\mathbf{I}_{K \times K}, \tag{2.44}$$

where $\mathbf{U}_{\mathrm{M \times K}}$ consists of the first K columns of the matrix $\mathbf{U}$, and $\mathbf{B}$ is a size $M \times M - K$ matrix which consists of any $M-K$ orthonormal basis column vectors which extend the space[11] spanned by the orthonormal basis column vectors of $\mathbf{U}_{\mathrm{M \times K}}\mathbf{V}^H$. The equation (2.44) represents and alternative SVD of $\mathbf{P}$, where $\left[\mathbf{U}_{\mathrm{M \times K}}\mathbf{V}^H, \mathbf{B}\right]$ and $\mathbf{I}_{K \times K}$ are its unitary matrices and $\boldsymbol{\Sigma}$ is the $M \times K$ matrix with the singular values of $\mathbf{P}$ in its diagonal.

This SVD representation of $\mathbf{P}$ in (2.44) explains the very functionality of noncoherent multi-channel receivers, namely to perform a rotation of the K-dimensional symbol vector $\mathbf{d}$ in an M-dimensional space (with constraint that $M \geq K$). Inversion of $\mathbf{P}$ can be done by the receiver post processing matrix $\mathbf{W}$, which is given, due to (2.44), as

$$\mathbf{W} = \mathbf{I}_{K \times K}\boldsymbol{\Sigma}^H \left[\mathbf{U}_{\mathrm{M \times K}}\mathbf{V}^H, \mathbf{B}\right]^H \tag{2.45}$$

or equivalently

$$\mathbf{W} = \mathbf{P}^H, \tag{2.46}$$

which resembles a back-rotation of the sample vector $\mathbf{y}$, and downsampling into the space of the symbol vector $\mathbf{d}$.

2.4.1 ZF Linear Detection

As aforementioned, $\mathbf{P}^H\mathbf{P} = \mathbf{I}_{K \times K}$ holds only for quasi-unitary matrices, while

$$\mathbf{W} = \left(\mathbf{P}^H\mathbf{P}\right)^{-1}\mathbf{P}^H \tag{2.47}$$

holds for the general case when $M \geq K$.

---

[11] In other words: the column vectors of $\mathbf{B}$ span the nullspace.

The matrix $\mathbf{W}$ resembles, besides to the Moore-Penrose pseudo inverse, the so called *zero-forcing* (ZF) linear detector [56] which chooses $\mathbf{W}$ to eliminate interference completely, regardless of noise enhancement[12] which might occur. The matrix $\mathbf{W}$ is also the unique solution to the least-square error problem $\arg\min_{\mathbf{d}} ||\mathbf{y} - \mathbf{P}\mathbf{d}||^2$ for $\mathbf{y} = \mathbf{P}\mathbf{d} + \mathbf{n}$.

2.4.2 MMSE Linear Detection

An alternative to the ZF detector is the *minimum-mean-squared-error* (MMSE) linear detector [56] which chooses $\mathbf{W}$ so that the MSE problem $\mathrm{MSE} = \arg\min_{\mathbf{d}} \mathrm{E}\left\{(||\mathbf{y} - \mathbf{P}\mathbf{d}||^2)\right\}$ gets minimized for $\mathbf{y} = \mathbf{P}\mathbf{d} + \mathbf{n}$. The MMSE detector achieves an optimum balance of noise enhancement and interference suppression with $\mathbf{W}$ which is obtained as

$$\mathbf{W} = \left(\mathbf{P}^H\mathbf{P} + \sigma_n^2\mathbf{I}_{K\times K}\right)^{-1}\mathbf{P}^H \tag{2.48}$$

for $\mathbf{d}$ being uncorrelated with unit energy [56].

2.4.3 Estimation of the Co-Term Matrix

When transmitting an arbitrary sequence $\mathbf{T}$, where $\mathbf{T}$ is a size $K \times L$ matrix with L being the number of sent symbols, the receiver front-end output sequence $\mathbf{Y}$ for an ISI-free scenario is given as

$$\mathbf{Y} = \mathbf{P}\mathbf{T} + \mathbf{Q}\bar{\mathbf{T}} + \mathbf{N}, \tag{2.49}$$

where $\mathbf{N}$ is the noise sequence, and the columns $\{\bar{\mathbf{t}}_k\}$ of $\bar{\mathbf{T}}$ are given as $\bar{\mathbf{t}}_k = \mathbf{t}_k\tilde{\otimes}\mathbf{t}_k$. To apply a ZF or MMSE linear detector, the co-term matrix $\mathbf{P}$ needs to be known. To estimate $\mathbf{P}$, the sequence $\mathbf{T}$ can be used if known a priory. The co-term matrix $\mathbf{P}$ can be obtained in a least-square sense as

$$\hat{\mathbf{P}} = \mathbf{Y}\mathbf{T}^\dagger \tag{2.50}$$
$$= \mathbf{P} + \mathbf{Q}\bar{\mathbf{T}}\mathbf{T}^\dagger + \mathbf{N}\mathbf{T}^\dagger. \tag{2.51}$$

When choosing $\mathbf{T} = \mathbf{I}_{K\times K}$, the errors caused by the cross-term matrix vanish since $\mathbf{e}_k\tilde{\otimes}\mathbf{e}_k = \mathbf{0}$ and hence $\bar{\mathbf{T}} = \mathbf{0}$. The estimated co-term matrix $\hat{\mathbf{P}}$ then simplifies to

$$\hat{\mathbf{P}} = \mathbf{P} + \mathbf{N}. \tag{2.52}$$

2.4.4 Detection of OOK and Binary PPM Symbols

To detect OOK symbols, the elements of the decision variable vector $\mathbf{z}$ need to be compared to a threshold γ. The threshold γ needs to be chosen to minimize the detection error [13]. The detection rule is hence given as

$$\left[\hat{\mathbf{d}}\right]_k = \begin{cases} 1 & \text{, for } [\mathbf{z}]_k \geq \gamma \\ 0 & \text{, for } [\mathbf{z}]_k < \gamma, \end{cases} \tag{2.53}$$

for $k = 1, \ldots, K$.

---

[12] This is related to the condition number of $\mathbf{P}$.

In binary PPM (BPPM), two consecutive symbol vectors $\mathbf{d}_0$ and $\mathbf{d}_1$ are transmitted for a single data vector $\mathbf{d}$, where $\mathbf{d}_1$ is the binary compliment of $\mathbf{d}_0$, hence $\mathbf{d}_1 = \mathbf{1} - \mathbf{d}_0$. The detection rule is therefore given as

$$\left[\hat{\mathbf{d}}\right]_k = \begin{cases} 1 & , \text{ for } [\mathbf{z}_0]_k - [\mathbf{z}_1]_k \geq 0 \\ 0 & , \text{ for } [\mathbf{z}_0]_k - [\mathbf{z}_1]_k < 0, \end{cases} \tag{2.54}$$

for $k = 1, \ldots, K$. As can be seen, there is no need of choosing a threshold γ.

2.5 Performance Metrics and the System Simulation Framework

To compare such noncoherent multi-channel receiver architectures and the influence of system components as realistic projection filters, multiplication devices or integration filters, various performance metrics need to be considered. In this section standard metrics are defined which are used in this entire work. In addition the system simulation framework and the system simulation parameters are defined.

2.5.1 Definition of Performance Metrics

The most important metric is the bit-error rate (BER) which shows the ability for the basic objective of receivers: the detection of data bits with as little errors as possible. Related to the BER are signal power metrics as the signal-to-interference-and-noise ratio (SINR), the signal-to-noise ratio (SNR), and the signal-to-interference ratio (SIR).

SINR

The SINR shows the performance of the receiver to mitigate signal cross-term interference and noise and is defined as (cf. Section 2.3 and Appendix B.1)

$$\mathrm{SINR} = \frac{\mathrm{tr}\left\{\mathbf{W}\mathrm{E}\left\{\boldsymbol{\alpha}\boldsymbol{\alpha}^H\right\}\mathbf{W}^H\right\}}{\mathrm{tr}\left\{\mathbf{W}\left(\mathrm{E}\left\{\boldsymbol{\beta}\boldsymbol{\beta}^H\right\} + \mathrm{E}\left\{\boldsymbol{\nu}\boldsymbol{\beta}^H\right\} + \mathrm{E}\left\{\boldsymbol{\beta}\boldsymbol{\nu}^H\right\} + \mathrm{E}\left\{\boldsymbol{\nu}\boldsymbol{\nu}^H\right\}\right)\mathbf{W}^H\right\}}. \tag{2.55}$$

SIR

The SIR shows the performance of the receiver to mitigate signal cross-term interference and is defined as

$$\mathrm{SIR} = \frac{\mathrm{tr}\left\{\mathbf{W}\mathrm{E}\left\{\boldsymbol{\alpha}\boldsymbol{\alpha}^H\right\}\mathbf{W}^H\right\}}{\mathrm{tr}\left\{\mathbf{W}\mathrm{E}\left\{\boldsymbol{\beta}\boldsymbol{\beta}^H\right\}\mathbf{W}^H\right\}}. \tag{2.56}$$

SNR

The SNR shows the performance of the receiver to minimize noise terms and is defined as

$$\mathrm{SNR} = \frac{\mathrm{tr}\left\{\mathbf{W}\mathrm{E}\left\{\boldsymbol{\alpha}\boldsymbol{\alpha}^H\right\}\mathbf{W}^H\right\}}{\mathrm{tr}\left\{\mathbf{W}\mathrm{E}\left\{\boldsymbol{\nu}\boldsymbol{\nu}^H\right\}\mathbf{W}^H\right\}}. \tag{2.57}$$

2.5.2 System Simulation Framework

The receiver system simulation framework supports time domain simulations and does consist of a set of MATLAB scripts, functions, and objects. The framework was designed to support object-oriented simulation of receiver devices and designs. This has the advantage that a device, e.g. a specific integrator realization, can be derived from a super-class so that it shares the same properties and methods interface[13]. Hence the different realizations of those devices are interchangeable without any effort, which makes the whole framework very flexible.

---

[13] In object-oriented programming the characteristic to derive a class from a super-class and hence sharing the same properties and methods is called *inheritance*. The characteristic that the call of the same method of a super-class or its derived class executing different code commands is called *polymorphism* [63].

In Fig. 2.5 the signal flow diagram of the simulation framework is depicted to obtain system metrics as BER, SINR, SNR, and SIR. The sampling rate R_s has been set to $R_s = 16$ GHz to be able to model the most important nonlinearities. Due to the nonlinear multiplication device a baseband simulation is not feasible without high effort. The simulation framework has proven to give results within adequate runtime.

The signaling scheme was chosen to be an NOFDM scheme (see Tab. 2.1) with $K = 7$ subcarriers which is generated by an NOFDM signal generator (SG). The pulse shape is a root-raised-cosine pulse with $\beta = 0.5$ which is truncated at its first zero-crossings next to its main lobe. The pulse duration is 10.6 ns. The symbol period was chosen to be $T_{\text{sym}} = 16$ ns, hence includes a zero-guard interval of 5.4 ns. The pulse energies were normalized to 1 Joule. The subcarrier spacing is 250 MHz with a center frequency of 4 GHz. For the simulation the signal is generated in baseband and then upconverted. Binary PPM was chosen for easier demodulation. The data stream has a length of 1000 symbols per UWB channel instantiation, therefore the data payload is 7000 bits. To ensure separability of signal co- and cross-terms, the signal generator generates distinct signal sequences per subcarrier.

Table 2.1: NOFDM signal scheme parameter.

Parameter Name	Parameter	Value
Number of subcarriers	K	7
Symbol period	T_{sym}	16 ns
Subcarrier spacing	$\frac{\omega_{\text{sc}}}{2\pi}$	250 MHz
Center frequency	$\frac{\omega_{\text{c}}}{2\pi}$	4 GHz
Pulse shape	$\varphi(t)$	root-raised-cosine pulse, truncated at first zero-crossings next to main lobe, $\beta = 0.5$
Pulse duration	T_{p}	10.6 ns
Zero-guard interval		5.4 ns
Modulation		Binary pulse position (BPPM)

The UWB channel $c[k]$ is modeled for short-range indoor communication (see Tab. 2.2). It has an RMS delay spread of 2 ns, a Ricean K-factor of 4, a Nakagami factor of the multipath components of 2, and an average number of multipath components of 5 per ns (cf. Appendix A and [64]). The simulations were in general performed over 100 UWB channel instantiations.

Table 2.2: UWB channel parameters.

Parameter Name	Parameter	Value
RMS delay spread	τ_{rms}	2 ns
Ricean K-factor	K_{LOS}	4
Nakagami m-factor	m_{Nakagami}	2
Average number of multipath components	λ	5 ns^{-1}

The noise generator (NG) generates a complex additive white Gaussian noise (AWGN) process with noise power spectral density of $N_0/2$.

After filtering with a root-raised-cosine front-end filter $f[k]$ with $\beta = 0.2$ and a pulse width of 462.32 ps the subcarrier signals and the noise get up-converted to a center frequency of 4 GHz.

From here on the simulation is split into three parallel signal paths: the first signal path processes the subcarrier signals independently; the second signal path processes the summed

subcarrier signals, hence the changes in the signal co- and cross-terms can be studied; the third signal path processes the summed subcarrier signals with the added noise so that the changes of all signal co- and cross-terms, signal-by-noise, noise-by-signal, and noise-by-noise terms can be studied.

In each signal path the associated signal gets filtered by $2M$ projection filters $\{h_m[k]\}$ and $\{g_m[k]\}$, respectively, to obtain the signals for the M receiver channels.

For a realistic modeling of hardware multiplication devices the signals need to be conditioned by the gains g_1 and g_2 to match the desired input range of the given multiplier model.

After the multiplication device, the subcarrier signals get summed so that in each channel the signal co-term is obtained.

After the multiplication operation, the signals get integrated over the symbol period T_{sym} and down-sampled with a factor of $R_s T_{\text{sym}}$ to obtain the receiver output vector sequence.

The standard method of determining the co-term matrix $\mathbf{P}$ is done using a training sequence where each subcarrier gets switched on sequentially. The equalizer matrix $\mathbf{W}$ is computed using MMSE optimization (cf. Section 2.4.2). The received output vector sequence gets multiplied with the equalizer matrix $\mathbf{W}$.

To obtain estimates of the BER a decision device (DD) decides on the transmitted symbols (cf. Section 2.4.4). The estimated symbols are compared to the sent ones. For each error an error counter gets increased.

To obtain an estimate of SINR, SNR, and SIR the output signals of the system simulation, which are a co-terms-only signal, a co-terms-plus-cross-terms signal, and a complete signal with co, cross, and noise terms, need to be linearly combined (see Fig. 2.5) to obtain a cross-terms only for the SIR estimator, noise-terms only signal for the SNR estimator, and a cross-terms-plus-noise-term signal for the SINR estimator.
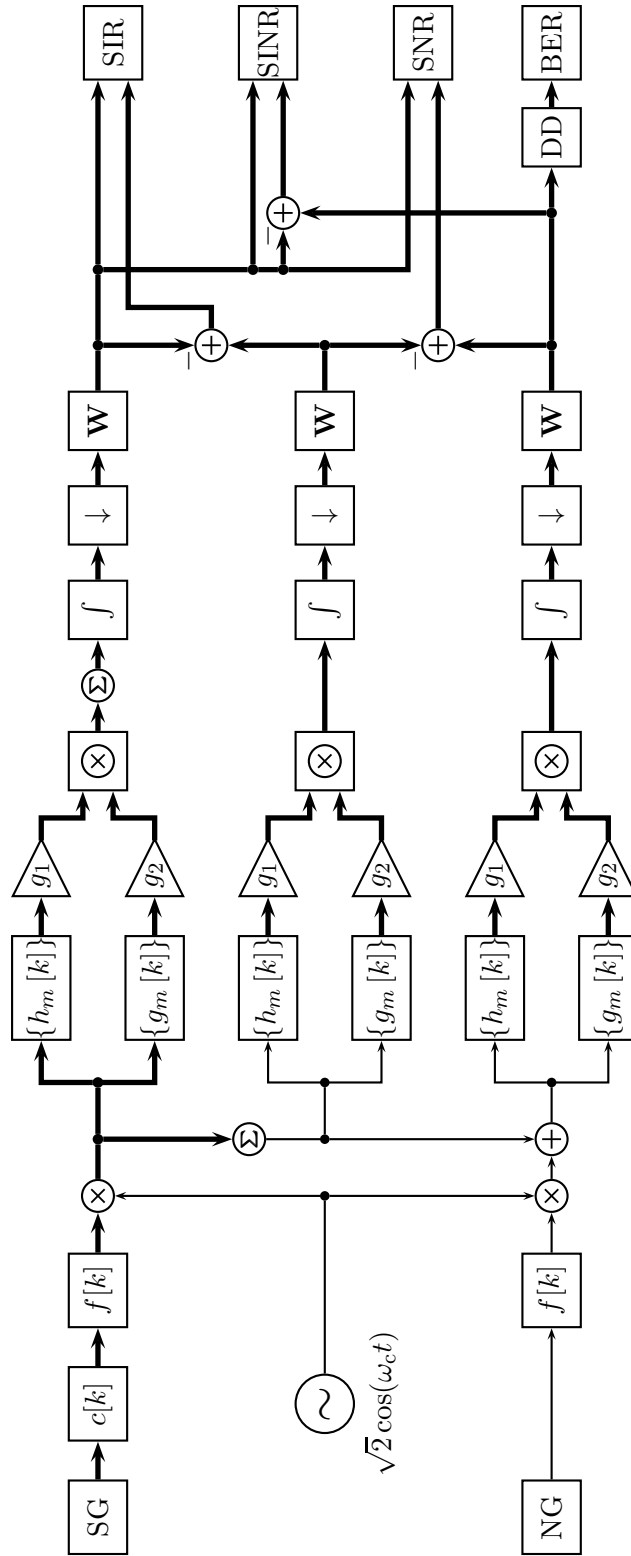
Figure 2.5: Signal flow diagram of the simulation framework.

2.6 A Variety of Noncoherent Multi-Channel Receivers

In this section three examples of noncoherent multi-channel receivers with ideal projection filters are presented and compared. These receivers act as reference receivers for the rest of the work.

2.6.1 Multi-Channel Energy Detector

A possible receiver system is the multi-channel energy detector (MC-ED) for NOFDM signaling [46, 49], which utilizes projection filters given as

$$X_m(j\omega) = \Pi_m(j\omega), \tag{2.58}$$

where $\{\Pi_m(j\omega)\}$ represent ideal rectangular passband filters. The filter cross-spectra $\{\Pi_m(j\omega)\}$ are depicted in Fig. 2.7(a) and Fig. 2.7(b). It can be seen that they let pass the ideal m^{th} subcarrier band, from $\omega_{\text{c}} + \omega_{\text{sc}} \left(m - \frac{K+2}{2}\right) \leq |\omega| < \omega_{\text{c}} + \omega_{\text{sc}} \left(m - \frac{K}{2}\right)$. So only K receiver channels are needed. This receiver computes for each receiver channel the energy within the respective ideal subcarrier bands. The signal flow diagram of the MC-ED is depicted in Fig. 2.6.
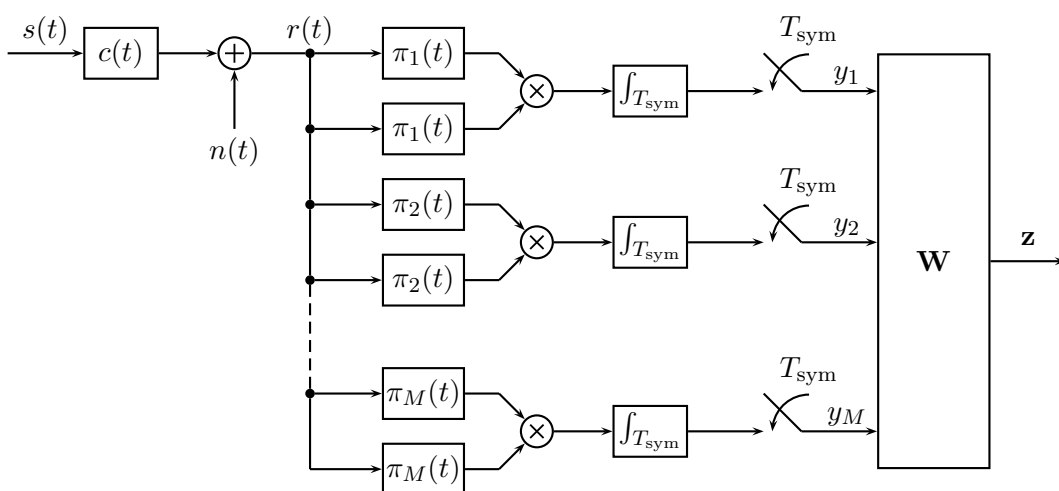
Figure 2.6: Signal flow diagram of the Multi-Channel Energy Detector.

In Fig. 2.7(c), the correlation matrix of the projection filter cross-spectra is depicted. It can be seen that the filters are orthogonal to each other, as expected. In Fig. 2.7(d) the co-term matrix $\mathbf{P}$ using the NOFDM signaling is depicted. It can be seen that $\mathbf{P}$ does have a dominant main diagonal but non-zero elements otherwise to the main diagonal due to the overlapping subcarrier spectra. Nevertheless, $\mathbf{P}$ is almost orthogonal with a condition number of $\text{cond}\{\mathbf{P}\} = 1.0187$

In Fig. 2.7(e), the spectra of the inverse $\{\mathbf{w}_k^T \mathbf{X}^H\}$ are depicted. It can be seen that the spectra let pass the subcarriers within the ideal rectangular passbands. In Fig. 2.7(f) the detection correlation matrix $\mathbf{W}\mathbf{X}^H\mathbf{\Psi}$ is shown. The detection correlation matrix is an estimation of the identity matrix $\mathbf{I}_{K \times K}$. It can be seen that due to the condition number of $\mathbf{P}$, of approximately one, the estimate is not perfect but does show some minor content with a maximum of $1.79 \cdot 10^{-2}$ in the non-main diagonals.

(a) Cross-spectra magnitude response

(b) Cross-spectra phase response

(c) Cross-spectra correlation matrix

(d) Signal co-term matrix

(e) Magnitude response of the inverse

(f) Detection correlation matrix
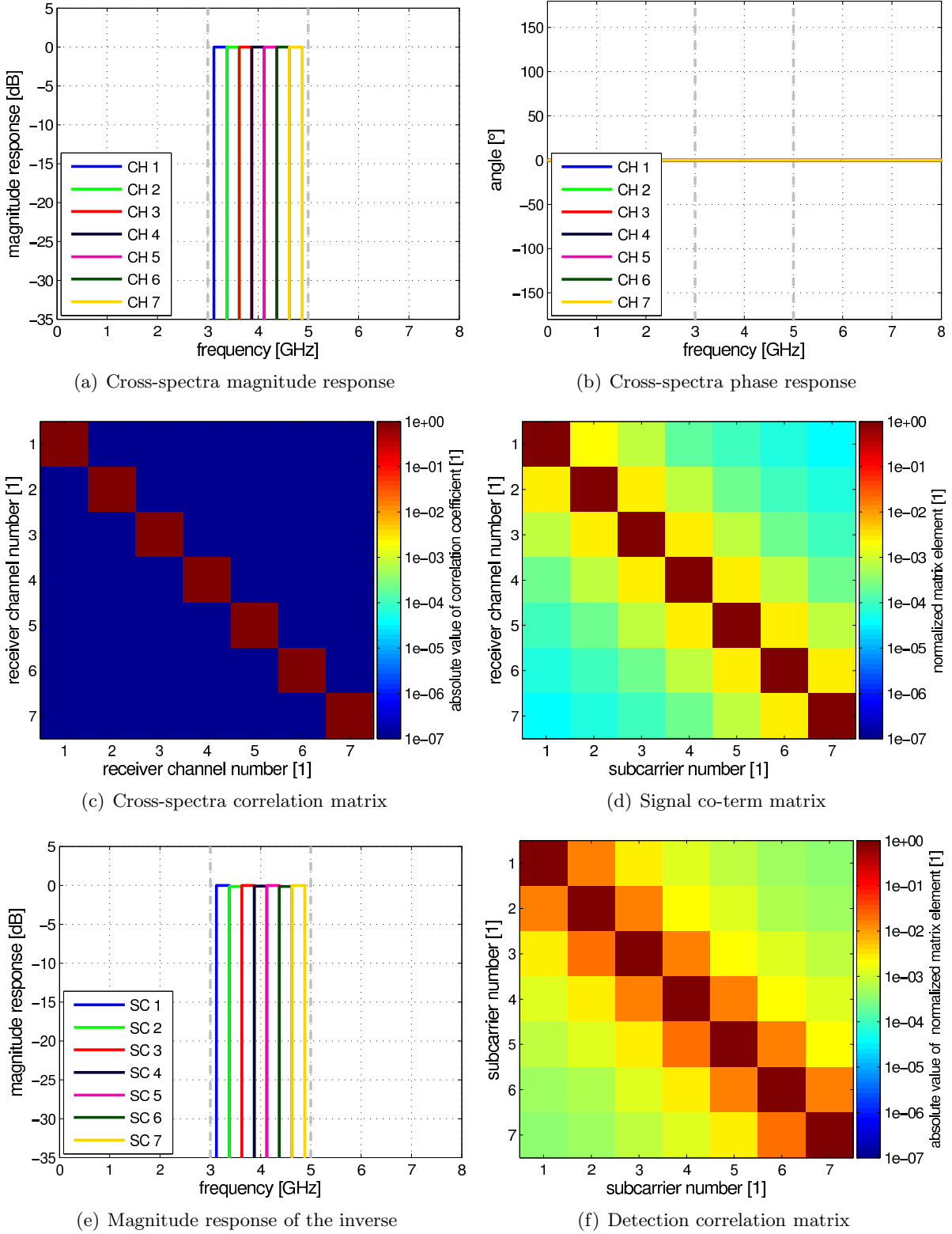
Figure 2.7: Projection filter cross-spectra, correlation matrix, signal co-term matrix $\mathbf{P}$ (cond $\{\mathbf{P}\}$ = 1.0187), and spectra of the inverse of the MC-ED projection for $M = 7$ channels.

2.6.2 Multi-Channel Matched-Filter Energy Detector

An additional example is the generic optimum noncoherent receiver which consists of projection filters matched to the transmitted waveforms [65]. The projection filters are depicted in Fig. 2.9(a) and Fig. 2.9(b) and given as

$$X_m(j\omega) = |\Phi_m(j\omega)|^2.$$ (2.59)

Each projection filter is chosen that its cross-spectra resembles the PSD of a given subcarrier, hence again only K front-end channels are needed. Each receiver channel, depicted in Fig. 2.8, computes the correlation between the PSD of the received signal with templates of the PSD of the transmitted subcarriers. Therefore, this receiver architecture shows similarities to the ideal matched filter receiver [66] in frequency domain. The big difference to the ideal matched filter receiver is, that the received noise vector $\boldsymbol{\nu}$ consists of signal-by-noise, noise-by-signal, and noise-by-noise terms instead of simple AWGN noise samples.
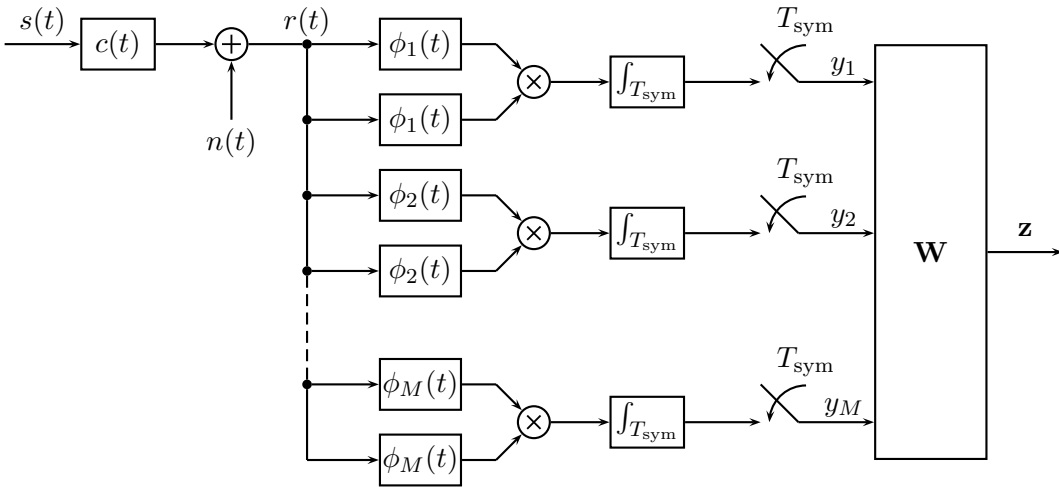
Figure 2.8: Signal flow diagram of the Multi-Channel Matched Filter Receiver.

In Fig. 2.9(c), the correlation matrix of the projection filter cross-spectra is shown. It can be seen that the projection filter cross-spectra are almost orthogonal to each other. However, the maximal cross-correlation coefficient is $1.62 \cdot 10^{-3}$. In Fig. 2.9(d) the co-term matrix $\mathbf{P}$ is depicted. Like for the MC-ED, $\mathbf{P}$ is not exactly orthogonal and has a the condition number of $\text{cond}\{\mathbf{P}\} = 1.0175$ due to the overlapping subcarrier spectra.

In Fig. 2.9(e), the spectra of the inverse $\{\mathbf{w}_k^T \mathbf{X}^H\}$ are shown. It can be seen that the spectra resembles the spectrum of the respective subcarriers. In Fig. 2.9(f) the detection correlation matrix $\mathbf{W}\mathbf{X}^H\boldsymbol{\Psi}$ for the MC-MFED is shown. A maximal non-main diagonal element has a value of $1.20 \cdot 10^{-2}$.

(a) Cross-spectra magnitude response

(b) Cross-spectra phase response

(c) Cross-spectra correlation matrix

(d) Signal co-term matrix

(e) Magnitude response of the inverse

(f) Detection correlation matrix
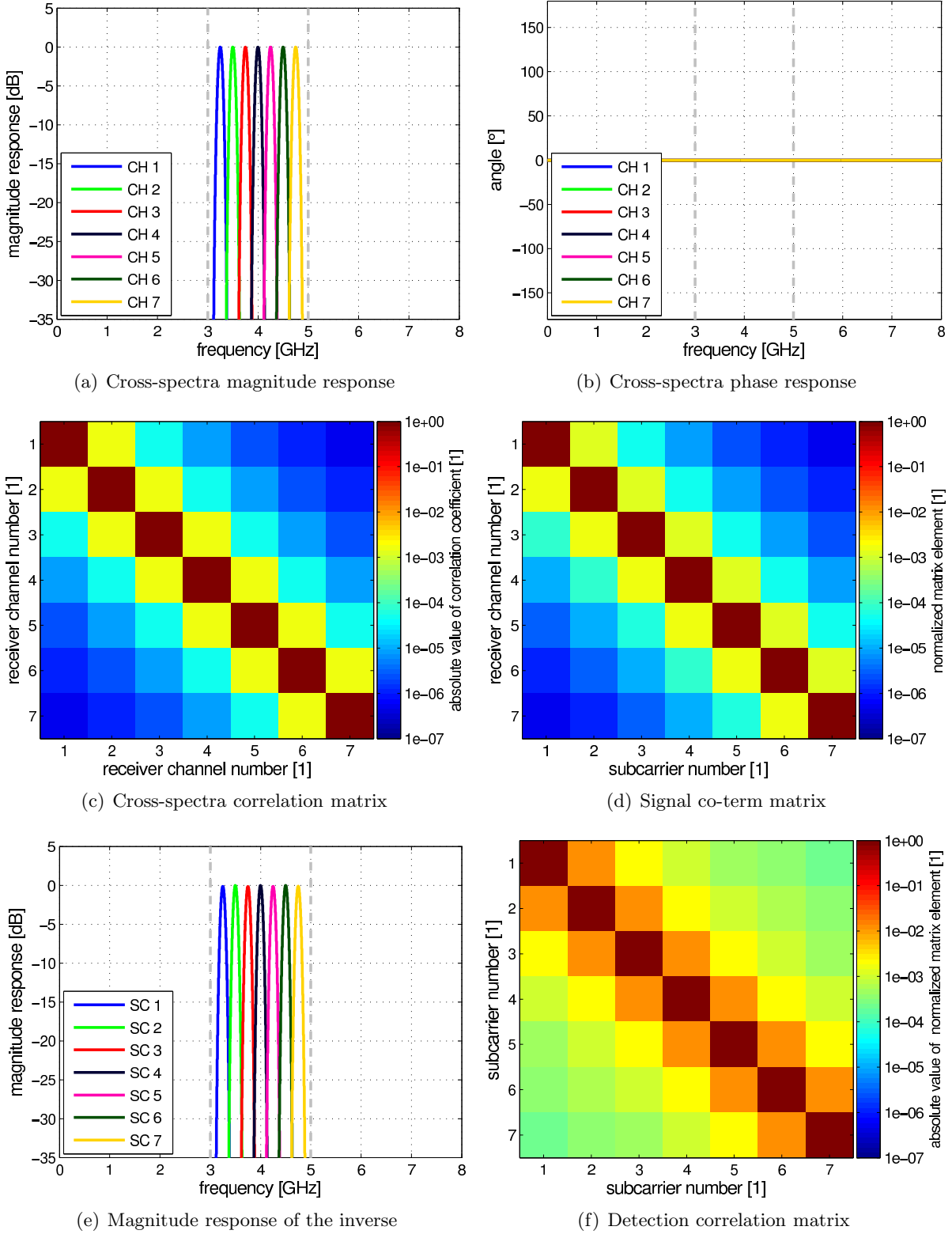
Figure 2.9: Projection filter cross-spetrca, correlation matrices, signal co-term matrix $\mathbf{P}$ (cond $\{\mathbf{P}\}$ = 1.0175), and spectra of the inverse of the MC-MFED for $M = 7$ channels.

2.6.3 Multi-Channel Autocorrelation Receivers

A completely different receiver concept is the multi-channel autocorrelation receiver (MC-AcR) [55]. This receiver was also chosen to act as hardware example (see Chapter 5). The receiver architecture and the projection filters are depicted in Fig. 2.10, Fig. 2.11(a), and Fig. 2.11(b), respectively. The cross-spectra of the MC-AcR are given as

$$X_m(j\omega) = e^{-j\tau_m\omega}, \tag{2.60}$$

which defines filters to perform different delays $\{\tau_m\}$ to compute M samples of the short-time estimate of the autocorrelation function of the received signal $r(t)$. This has the advantage that the receiver can operate in any defined UWB band without changes to the receiver hardware. This is not true for MC-ED and MC-MFED due to the fact, that the exact subcarrier frequencies and bands are fixed a-priori. For illustration the delays of the MC-AcR are chosen to be $\tau_1 = 0.25$ ns, $\tau_2 = 0.75$ ns, $\tau_3 = 1.25$ ns, $\tau_4 = 1.75$ ns, $\tau_5 = \tau_1 - \Delta\tau$, $\tau_6 = \tau_2 - \Delta\tau$, $\tau_7 = \tau_3 - \Delta\tau$, and $\tau_8 = \tau_4 - \Delta\tau$, with $\Delta\tau = \frac{2\pi}{4\omega_c} = 62.5$ ps. The first four delays are used to compute the autocorrelation of the the in-phase (I) components and the last four delays compute the autocorrelation of the quadrature-phase (Q) components of the received signal. The spacing between delays of the in-phase and quadratur-phase components is given as 0.5 ns $\approx \frac{1}{KB_p}$.
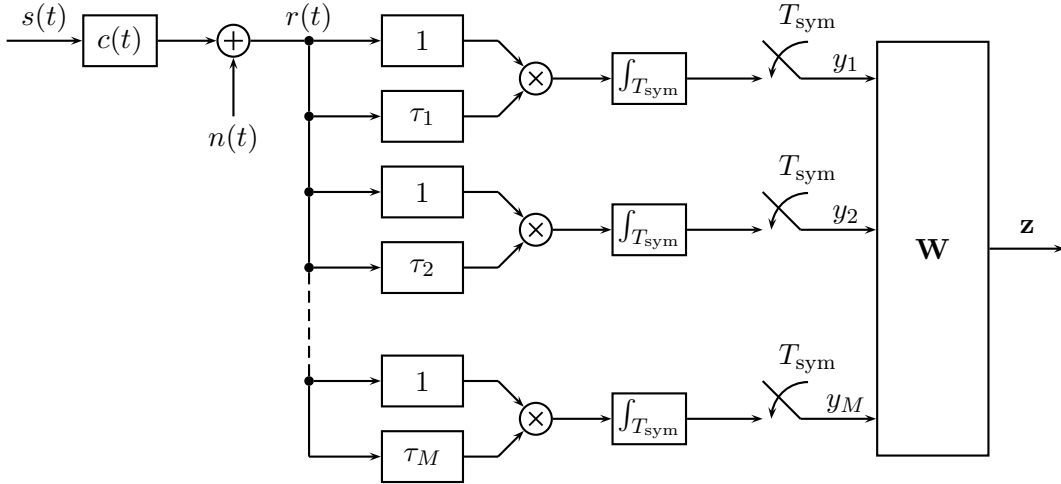
Figure 2.10: Signal flow diagram of the Multi-Channel Autocorrelation Receiver.

In Fig. 2.11(c), the correlation matrix of the projection filter cross-spectra is depicted. It can be seen that the cross-spectra are orthogonal to each other. In Fig. 2.11(d) the co-term matrix **P** is shown. The condition number of cond $\{\mathbf{P}\} = 1.1519$, which implies that **P** is a matrix with almost orthogonal columns.

In Fig. 2.11(e) the spectra of the inverse $\{\mathbf{w}_k^T\mathbf{X}^H\}$ are depicted. It can be seen that those spectra try to approximate the PSD of the subcarriers, as explained in Section 2.3. I.e., the subcarriers get separated by the passbands of the spectra of the inverse, but the passbands do overlap and many out-of-band content is let pass. These effects influence the receiver performance, as will be shown in Section 2.6.4. In Fig. 2.11(f) the detection correlation matrix $\mathbf{W}\mathbf{X}^H\mathbf{\Psi}$ for the MC-AcR is depicted. A maximal non-main diagonal element has a value of $6.60 \cdot 10^{-3}$.

(a) Cross-spectra magnitude response

(b) Cross-spectra phase response

(c) Cross-spectra correlation matrix

(d) Signal co-term matrix

(e) Magnitude response of the inverse

(f) Detection correlation matrix
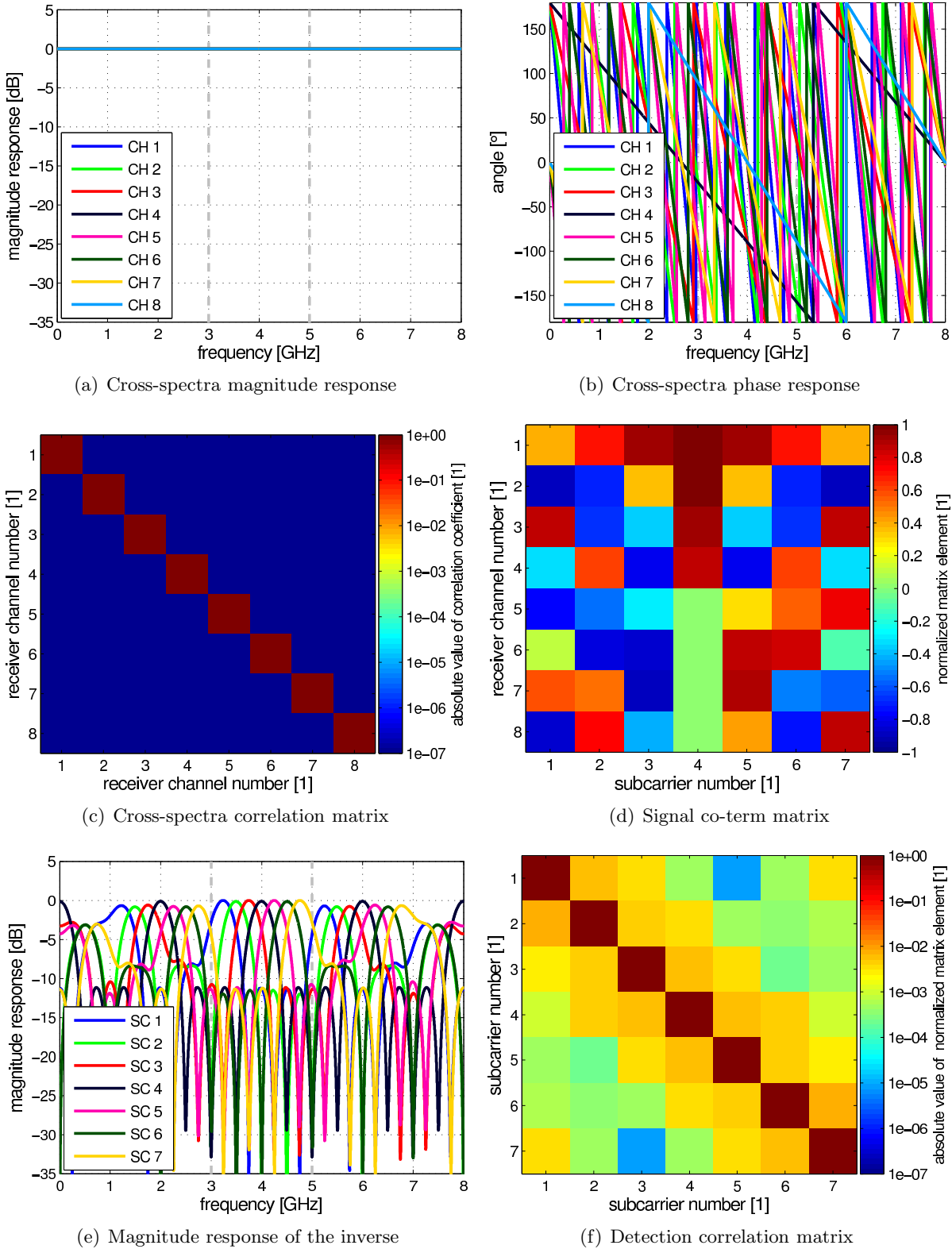
Figure 2.11: Projection filter cross-spectra, correlation matrices, signal co-term matrix $\mathbf{P}$ *(*cond$\{\mathbf{P}\}$ *= 1.1519), and spectra of the inverse of the MC-AcR for* $M = 8$ *channels.*

2.6.4 Performance Metrics of Reference Receivers

Note that all three presented receivers have in common that their co-term matrix $\mathbf{P}$ does have a condition number close to one. In Fig. 2.12 the BER, SINR, SNR, and SIR of the MC-AcR, the MC-ED, and the MC-MFED are depicted. It can be seen that the MC-MFED has the highest SIR due to the fact that the projection filters are equivalent to the orthogonal subcarrier pulses. It can also be seen that the MC-MFED has the highest SNR up to 19 dB of E_b/N_0. From $E_b/N_0 = 19$ dB the MC-ED does outperform all the other receiver architectures. This can also be seen in the BER where the MC-ED shows the best performance. This can be explained due to the fact that the MC-ED does mitigate the most noise per receiver channel due to its selective ideal rectangular bandpass filters. The MC-AcR has the worst BER performance in comparison to the other two receiver architectures. This can be explained due to the spectra of the inverse which overlaps with other subcarriers and let pass noise which is outside the respective subcarrier spectra.
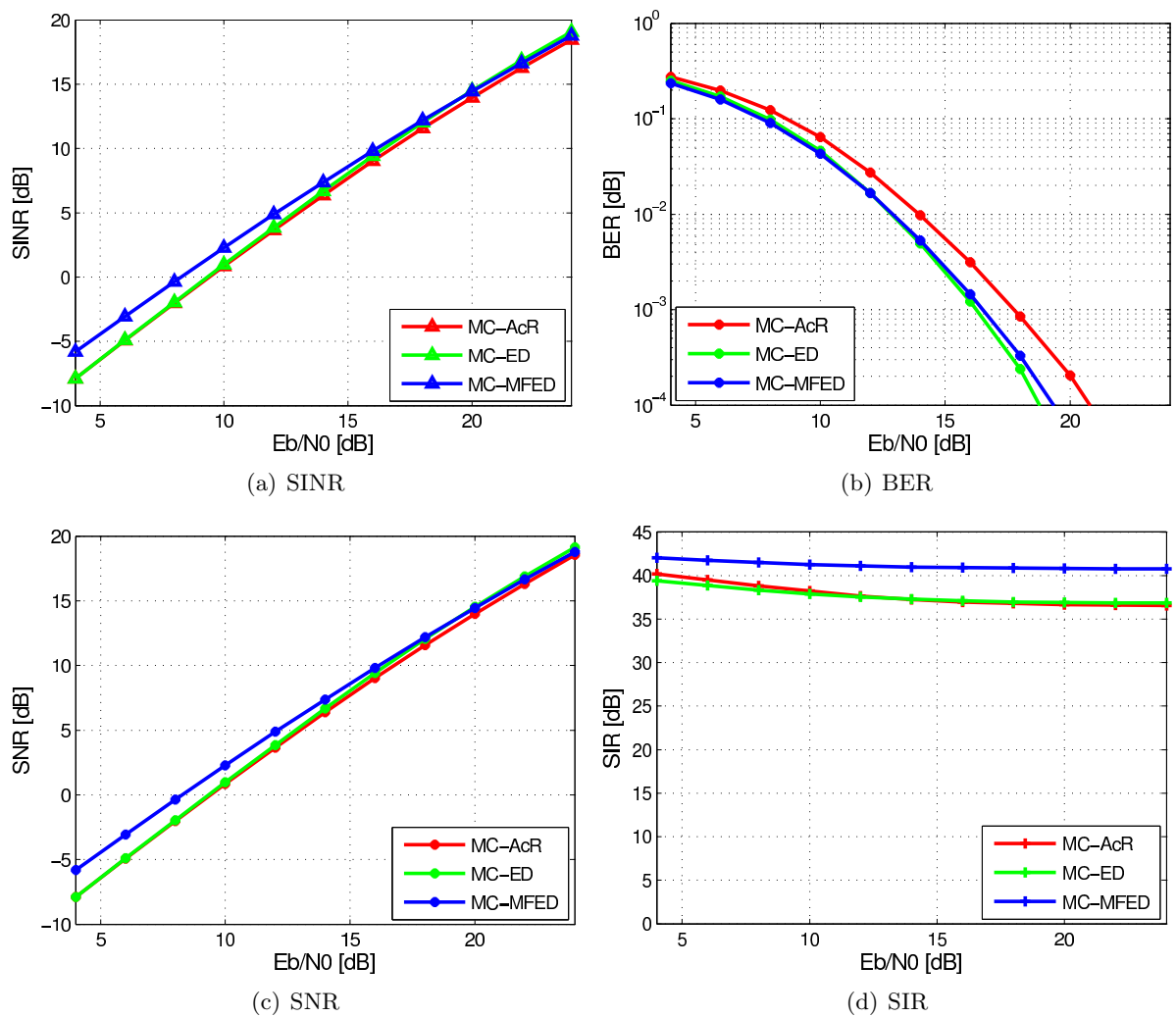
Figure 2.12: SINR, SNR, SIR, and BER of the MC-AcR, the MC-ED, and the MC-MFED.

2.7 Summary

This Chapter introduced a mathematical framework for generalized noncoherent multi-channel receivers with linear OPAM signaling. It has been shown, that the received signal $r(t)$ gets projected onto a basis defined by projection filter cross-spectra $\{X_m(j\omega) = H_m(j\omega)G_m^*(j\omega)\}$, where $H_m(j\omega)$ and $G_m(j\omega)$ represent the front-end filters of the mth receiver channel which are thus called projection filters. This means for system optimization, that it is sufficient to obtain an optimal set of cross-spectra $\{X_m(j\omega)\}$. Each $X_m(j\omega)$ may be decomposed into the combination of two separate projection filters or into the combination of one projection filter and one allpass filter. With this method even zero-phase cross-spectra are possible.

A signaling scheme for noncoherent multi-channel receivers was introduced. This signaling consists of non-overlapping subcarriers which are modulated using on-off keying or pulse position modulation.

Also some rules to obtain cross-spectra have been defined to ensure optimal receiver performance. It has been shown that linear combinations of these cross-spectra need to approximate the spectra of the transmitted subcarriers to separate the data. It also has been shown that the orthogonality of the signaling is conserved with low condition number of the co-term matrix $\mathbf{P}$.

A simulation framework with the simulation parameters has been presented. The simulation framework supports the time domain evaluation of receiver performance metrics as BER, SINR, SIR and SNR.

Finally, the MC-ED, MC-MFED, and the MC-AcR have been introduced as reference receivers. It has been shown that all three concepts have ideal projection filters. However, they show different receiver performance which can be explained by their different capability of approximating the spectra of the subcarriers.

3

Analysis of Realistic Front-End Components

The analog front-end of a noncoherent multi-channel receiver consists of several receiver channels which only differ in their projection filters. Additionally to the projection filters, each channel utilizes an analog multiplier and an integration filter. In this chapter the impact on the receiver performances of those realistic front-end components is shown and discussed.

Parts of this Section have been published as

- A. Pedross-Engel, H. Schumacher, and K. Witrisal, "Modeling and identification of ultra-wideband analog multipliers," *IEEE Transactions on Circuits and Systems I: Regular Papers,* submitted.

- A. Pedross and K. Witrisal, "Analysis of nonideal multipliers for multichannel autocorrelation UWB receivers," in *2012 IEEE International Conference on Ultra-Wideband,* Sept. 2012, pp. 140 – 144.

- A. Pedross and K. Witrisal, "Sliding window integrator approximations for multichannel autocorrelation UWB receivers," in *2012 IEEE International Symposium on Circuits and Systems,* May 2012, pp. 2537 – 2540.

3.1 Realistic Projection Filters using Meta-Heuristic Optimization

This section studies the design of optimal projection filters using global optimization algorithms with a multi-objective cost-function and the impact of the obtained filters on the receiver performance. Main filter design goals are to find filters which do increase the receiver performance as much as possible while still being easy synthesizeable in real hardware. Hence filters with low filter order are preferred and studied. For sake of simplicity only discrete-time infinite impulse response (IIR) filters are considered, due to the fact that equivalent continuous-time filters can be found easily [67, 68].

3.1.1 Cost-Function for Optimal Projection Filter Designs

Typically, filters are specified in the frequency domain. Consequently, most filter design methods employ a cost-function derived from meeting different filter specifications in frequency domain as cut-off frequency, passband and stopband attenuation. For the design of the projection filters there are no frequency domain specifications given but several design rules (cf. Section 2.3). A possible way to obtain filters which comply with those rules is the use of meta-heuristic global optimization algorithms [69]. There are several optimization algorithms available. Especially the use of population-based computation algorithms such as particle swarm optimisation [70], genetic algorithms [71–73], the seeker optimization algorithm [74], and differential evolution [75–78] is common. Irrespective of the method employed, many different objectives for the filter design process are possible [79].

A *Particle Swarm Optimization* (PSO) algorithm with multi-objective cost-functions was chosen to find optimal projection filters. Subsequently a *Hill Climbing* (HC) algorithm was used to refine the solution found by the PSO. The used parameters are listed in Tab. 3.1 and Tab. 3.2. A detailed description of both algorithms is given in Appendix C.

The Multi-Objective Cost-Function

The multi-objective cost-function $J(\mathbf{\Phi})$ consists of a weighted sum of partial cost-functions, hence

$$J(\mathbf{\Phi}) = w_1 J_{\mathrm{cond}}(\mathbf{\Phi}) + w_2 J_{\mathrm{SINR}}(\mathbf{\Phi}) + w_3 J_{\mathrm{p}}(\mathbf{\Phi}) + w_4 J_{\mathrm{z}}(\mathbf{\Phi}) + w_5 J_{\mathrm{T}}(\mathbf{\Phi}) + w_6 J_{\mathrm{G}}(\mathbf{\Phi}),$$

$$(3.1)$$

where $\{w_i\}$ are the weights of the partial cost-functions and $\mathbf{\Phi}$ is a parameter vector which consists of the filter coefficients of all $2M$ projection filters. The PSO tries to find the best solution $\mathbf{\Phi}_0$ which results in the lowest possible cost. The cost-function and the partial cost-functions are designed to obtain costs ≥ 0 only. In the following, the partial cost-functions are discussed.

Minimal Co-Term Matrix Condition Number

The main objective of the PSO is to find those set of realistic projection filters which result in a co-term matrix $\mathbf{P}$ with lowest possible condition number. The partial cost-function $J_{\mathrm{cond}}(\mathbf{\Phi})$ is given as

$$J_{\mathrm{cond}}(\mathbf{\Phi}) = \mathrm{cond}\{\mathbf{P}(\mathbf{\Phi})\} - 1,$$

$$(3.2)$$

where $\mathbf{P}$ is a function of the discrete-time projection filters cross-spectra $\{X_m(e^{j\Omega})\}$ which are parametrized by $\mathbf{\Phi}$.

Table 3.1: PSO algorithm parameters.

Parameter Name	Parameter	Value
Number of iterations	ITERATIONS	150
Number of particle	SWARMSIZE	10^9
Number of informants per particle	INFORMANTS	6
Ratio to conserve original velocity	ALPHA	0.8
Velocity ratio to particles personal best solution	BETA	0.1
Velocity ratio to particles informants best solution	GAMMA	0.1
Velocity ratio to the overall best solution	DELTA	0
Speed gain	EPSILON	1
SINR offset	γ_{SINR}	100
Impulse response drop	γ_{T}	0.1
Weight for $J_{\mathrm{cond}}(\boldsymbol{\Phi})$	w_1	10^3
Weight for $J_{\mathrm{SINR}}(\boldsymbol{\Phi})$	w_2	10^3
Weight for $J_{\mathrm{p}}(\boldsymbol{\Phi})$	w_3	1
Weight for $J_{\mathrm{z}}(\boldsymbol{\Phi})$	w_4	1
Weight for $J_{\mathrm{T}}(\boldsymbol{\Phi})$	w_5	1
Weight for $J_{\mathrm{G}}(\boldsymbol{\Phi})$	w_6	1

Table 3.2: HC algorithm parameters.

Parameter Name	Parameter	Value
Number of iterations	ITERATIONS	5000
Number of gradient samples	SAMPLES	500
std. deviation of gradient sampling	SIGMA	0.01

Maximal SINR

This objective tries to find projection filters which maximize the SINR. As the PSO searches for a minimal cost, $J_{\mathrm{SINR}}(\boldsymbol{\Phi})$ is therefore given as

$$J_{\mathrm{SINR}}(\boldsymbol{\Phi}) = \gamma_{\mathrm{SINR}} - 10\log_{10}\mathrm{SINR}(\boldsymbol{\Phi}), \tag{3.3}$$

where $\gamma_{\mathrm{SINR}} > 0$ is an offset which prohibits negative costs. The SINR is compute as given in Appendix B.1 where the filter frequency responses are parametrized by $\boldsymbol{\Phi}$.

Ensure Filter Stability

To ensure an optimal solution with stable filters, $J_{\mathrm{p}}(\boldsymbol{\Phi})$ adds a penalty for any pole of $\left\{X_m\left(e^{j\Omega}\right)\right\}$ which is outside the unit circle. The penalty for each pole p_n is given as its distance from the unit circle, hence

$$J_{\mathrm{p}}(\boldsymbol{\Phi}) = \sum_{n=1}^{N_{\mathrm{p}}} d_{\mathrm{p}}(p_n), \tag{3.4}$$

where

$$d_{\mathrm{p}}\left(p_n\right) = \begin{cases} |p_n| - 1 & \text{, for } |p_n| > 1 \\ 0 & \text{, for } |p_n| \leq 1, \end{cases} \tag{3.5}$$

and N_{p} is the number of all poles given by $\boldsymbol{\Phi}$.

Ensure Minimum-Phase Filters

The objective of this partial cost-function is to ensure minimum-phase projection filters. This cost-function adds a penalty for any zero of $\left\{ X_m\left(e^{j\Omega}\right) \right\}$ which is outside the unit circle. The penalty for each zero z_n is given as its distance from the unit circle, hence

$$J_{\mathrm{z}}\left(\boldsymbol{\Phi}\right) = \sum_{n=1}^{N_{\mathrm{z}}} d_{\mathrm{z}}\left(z_n\right), \tag{3.6}$$

where

$$d_{\mathrm{z}}\left(p_n\right) = \begin{cases} |z_n| - 1 & \text{, for } |z_n| > 1 \\ 0 & \text{, for } |z_n| \leq 1, \end{cases} \tag{3.7}$$

and N_{z} is the number of all zeros given by $\boldsymbol{\Phi}$.

Minimum Time Dispersion

To ensure ISI free detection it is necessary that the projection filter do have as little contribution to time dispersion as possible. The objective of this cost-function is to obtain projection filter impulse responses which do contribute as little as possible to time dispersion. To measure this contribution the pulse duration until the impulse responses drop to a certain percentage γ_{T} of their maximum absolute value which exceeds $T_{\mathrm{sym}} - T_{\mathrm{p}}$ is taken. The cost-function $J_{\mathrm{T}}\left(\boldsymbol{\Phi}\right)$ is hence given as

$$J_{\mathrm{T}}\left(\boldsymbol{\Phi}\right) = \sum_{m=1}^{M} d_{\mathrm{T}}(x_m[k]) \tag{3.8}$$

where

$$d_{\mathrm{T}}(h_m[k]) = \begin{cases} \underset{\tau}{\arg\min} \left\{ \left| \dfrac{x_m[\tau]}{\max_k \left\{ x_m[k] \right\}} \right| - \gamma_{\mathrm{T}} \right\} - (T_{\mathrm{sym}} - T_{\mathrm{p}}) & \text{, for } \tau > T_{\mathrm{sym}} - T_{\mathrm{p}} \\ 0 & \text{, for } \tau \leq T_{\mathrm{sym}} - T_{\mathrm{p}}, \end{cases} \tag{3.9}$$

where $x_m[k]$ is the impulse response of $X_m\left(e^{j\Omega}\right)$. If there exists for a filter more than one solution to (3.9), the solution with the maximal delay $d_{\mathrm{T}}\left(\cdot\right)$ is taken as partial cost. Note that if we restrict the pulse width of $x_m[k] = h_m[k] * g_m[-k]$ also the pulse width of $g_m[k]$ and $h_m[k]$ are restricted.

Normalized Gain

The objective of this partial cost-function is to obtain filters with unit gain at the passbands. This cost-function adds penalties for deviation of a maximum gain of 0 dB. Therefore, $J_{\mathrm{G}}\left(\boldsymbol{\Phi}\right)$

is defined as

$$J_{\mathrm{G}}\left(\mathbf{\Phi}\right) = \sum_{m=1}^{M} \left| \max_{\Omega} \left\{ 20 \log_{10} \left| X_m(e^{j\Omega}) \right| \right\} \right|. \tag{3.10}$$

3.1.2 Analysis and System Simulation

The projection filter optimization was done for 2nd, 4th, and 6th order of projection filter cross-spectra. In Fig. 3.1 the evolution of their respective cost-functions using the PSO (from iteration 1 to iteration 300) and HC (from iteration 301 to 5300) is depicted. It can be seen that the algorithms converge and have, hence, found possible filter candidates. In Appendix D.1 for two alternative results of 2nd order projection filter cross-spectra can be found for comparison.
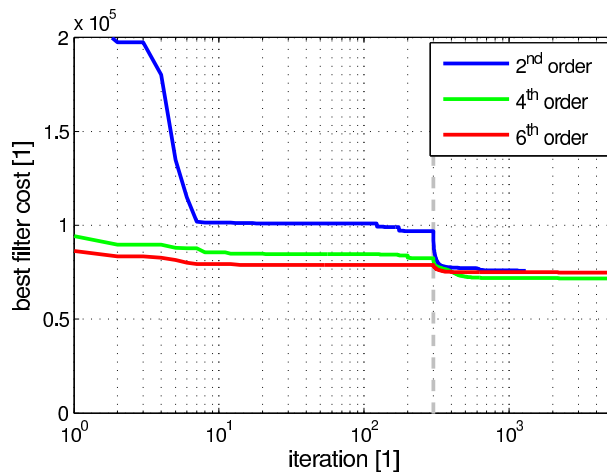
Figure 3.1: *Cost of best found filter per iteration of different order of projection filter cross-spectra for a M = 8 channel receiver.*

In Figs. 3.2 – 3.4 the projection filter cross-spectra, the cross-spectra correlation matrices, the co-term matrix $\mathbf{P}$, the spectra of the inverse $\left\{ \mathbf{w}_k^T \mathbf{X}^H \right\}$, and the detection correlation matrices of the found solutions are depicted. It can be seen that most of the filters do have their maximum within the signal bandwidth with a maximal gain of one. The correlation between the cross-spectra of the different found solutions show a maximal cross-correlation between $7.85 \cdot 10^{-1}$ and $9.24 \cdot 10^{-1}$. Therefore, the cross-spectra are not ideal orthogonal but linearly independent. The obtained filter solutions do have a low condition number of $\mathbf{P}$ between 19.35 and 25.54. It can also be seen, that the spectra of the inverse $\left\{ \mathbf{w}_k^T \mathbf{X}^H \right\}$ do function as bandpass filters for their respective subcarrier, but also let pass parts of other overlapping subcarriers. The detection correlation matrices $\mathbf{W} \mathbf{X}^H \mathbf{\Psi}$ resemble an estimate of the identity matrix $\mathbf{I}_{K \times K}$, with maximal non-main diagonal element values between $1.32 \cdot 10^{-2}$ and $2.37 \cdot 10^{-2}$.

In Fig. 3.5 the BER, SINR, SNR, and SIR of all filter sets are shown. It can be seen, that all three solutions obtain a similar BER as the MC-AcR. The SIR of the found sets are almost equivalent and are slightly worse than the MC-AcR and MC-MFED. The 2nd order projection filter cross-spectra have the best SNR performance in comparison to the other two solutions. However, they show worse SNR performance than the reference receivers caused by the overlapping bandpass filter behavior of their spectra of the inverse. The BER shows that projection filter cross-spectra of 2nd order are sufficient to obtain a BER performance similar to the MC-AcR.

(a) Cross-spectra magnitude response

(b) Cross-spectra phase response

(c) Cross-spectra correlation matrix

(d) Signal co-term matrix

(e) Magnitude response of the inverse

(f) Detection correlation matrix
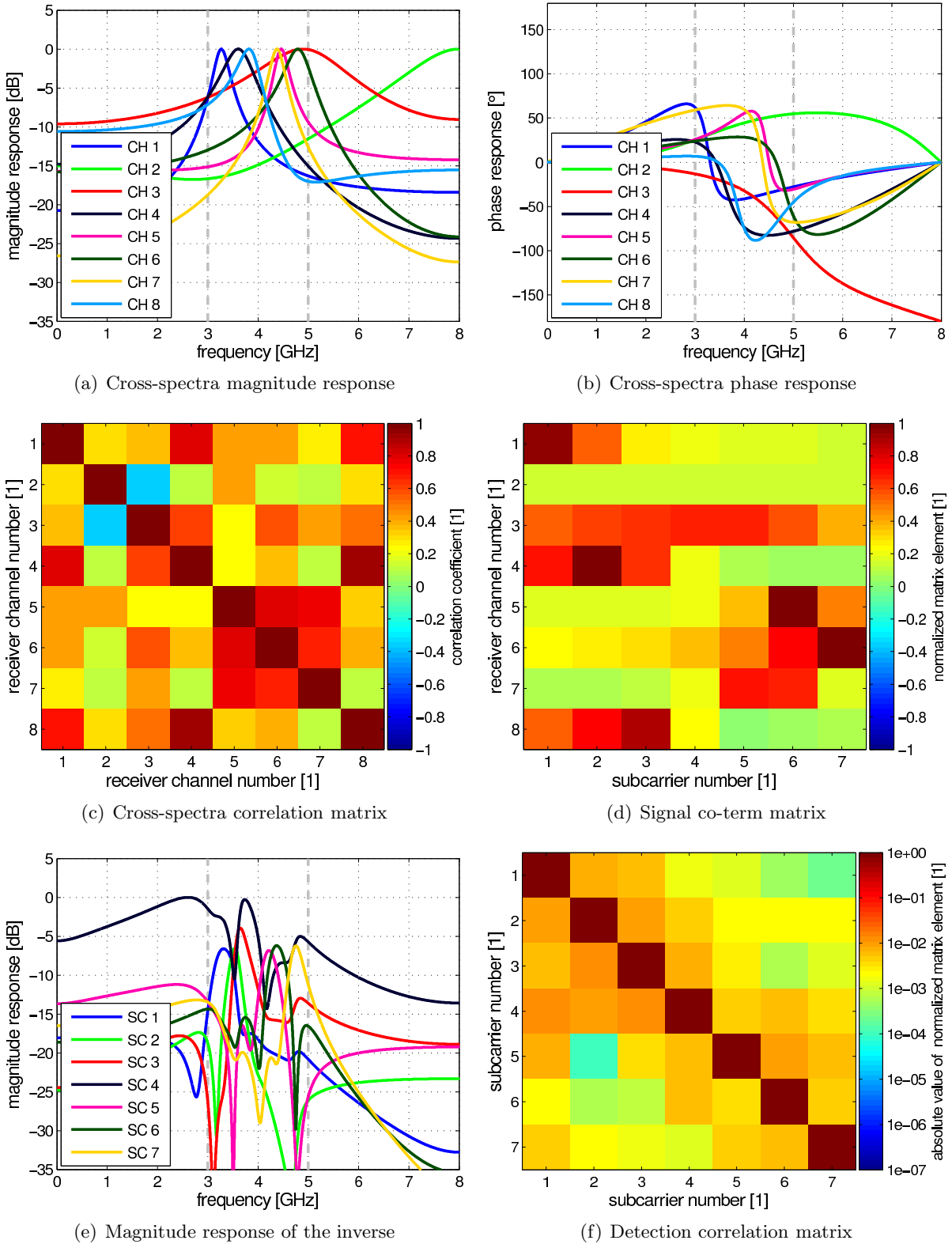
Figure 3.2: Frequency response, Correlation matrix, and signal co-term matrix $\mathbf{P}$ of a projection filter cross-spectra of 2nd order. The shown cross-spectra do have a condition number of $\mathrm{cond}\{\mathbf{P}\} = 19.48$.

(a) Cross-spectra magnitude response

(b) Cross-spectra phase response

(c) Cross-spectra correlation matrix

(d) Signal co-term matrix

(e) Magnitude response of the inverse

(f) Detection correlation matrix
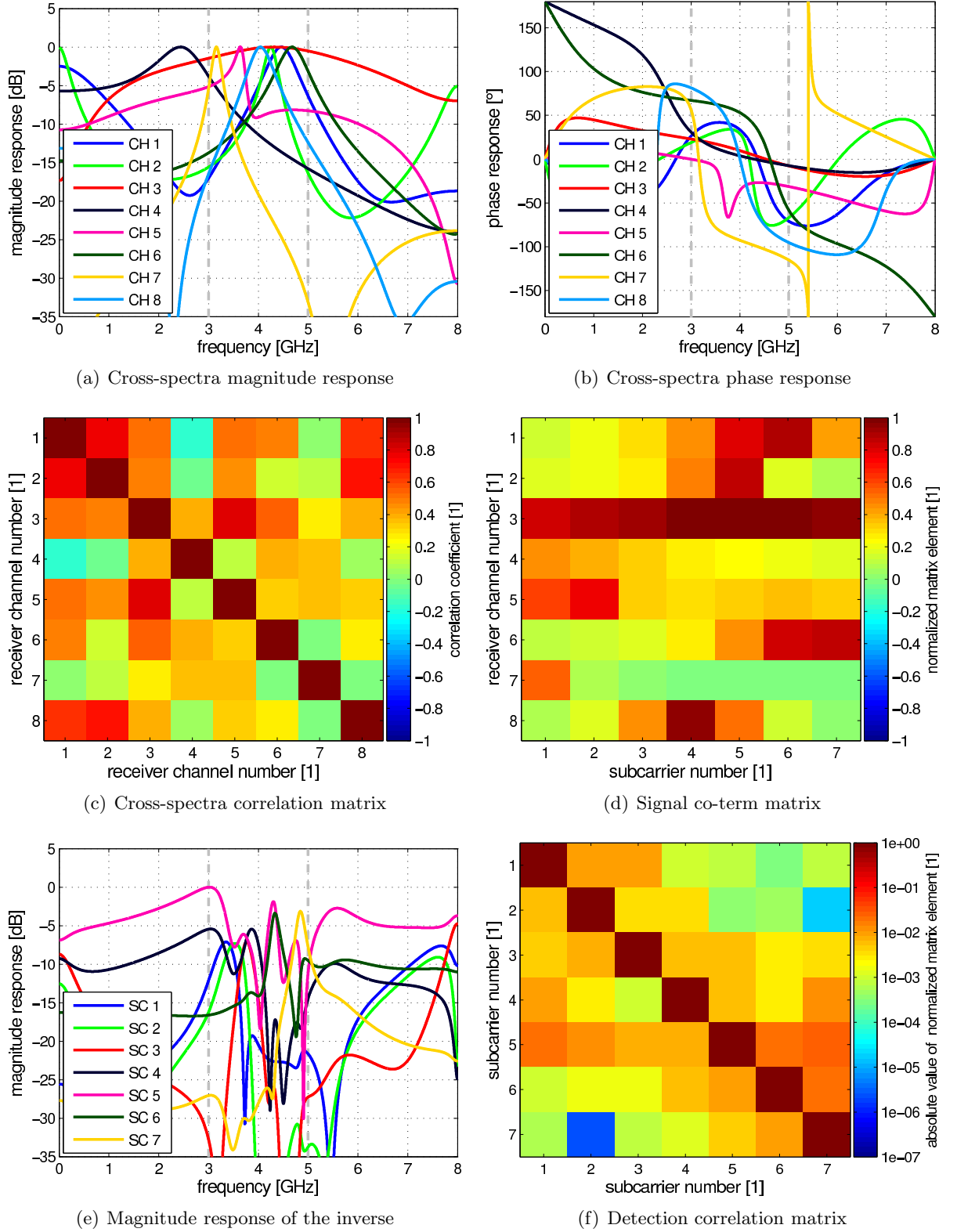
Figure 3.3: Frequency response, Correlation matrix, and signal co-term matrix **P** *of a projection filter cross-spectra of* 4th *order. The shown cross-spectra do have a condition number of* $\text{cond}\{\mathbf{P}\} = 25.53$.

(a) Cross-spectra magnitude response

(b) Cross-spectra phase response

(c) Cross-spectra correlation matrix

(d) Signal co-term matrix

(e) Magnitude response of the inverse

(f) Detection correlation matrix
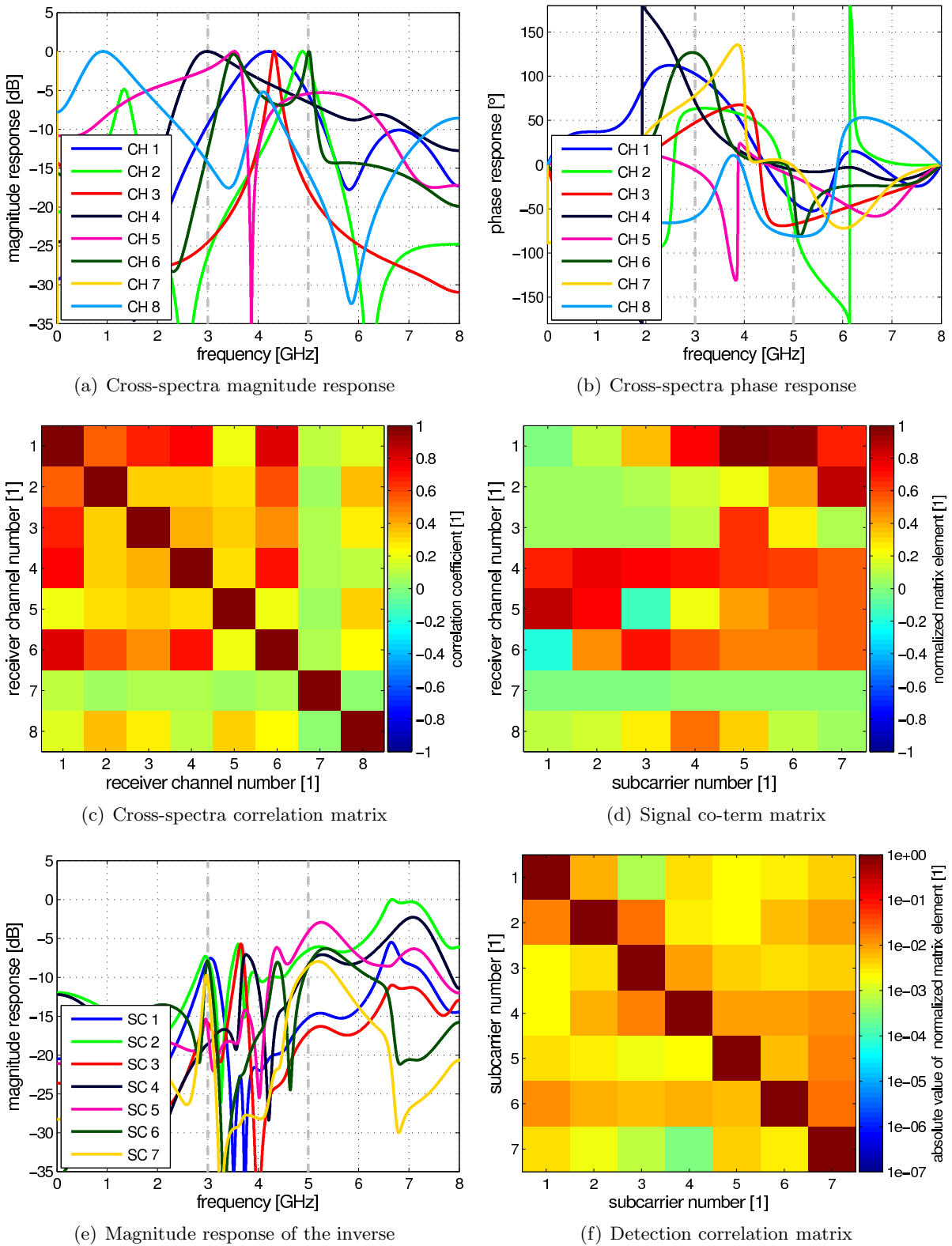
Figure 3.4: Frequency response, Correlation matrix, and signal co-term matrix $\mathbf{P}$ *of a projection filter cross-spectra of* 6th *order. The shown cross-spectra do have a condition number of* $\text{cond}\{\mathbf{P}\} = 19.35$.

(a) SINR

(b) BER

(c) SNR

(d) SIR
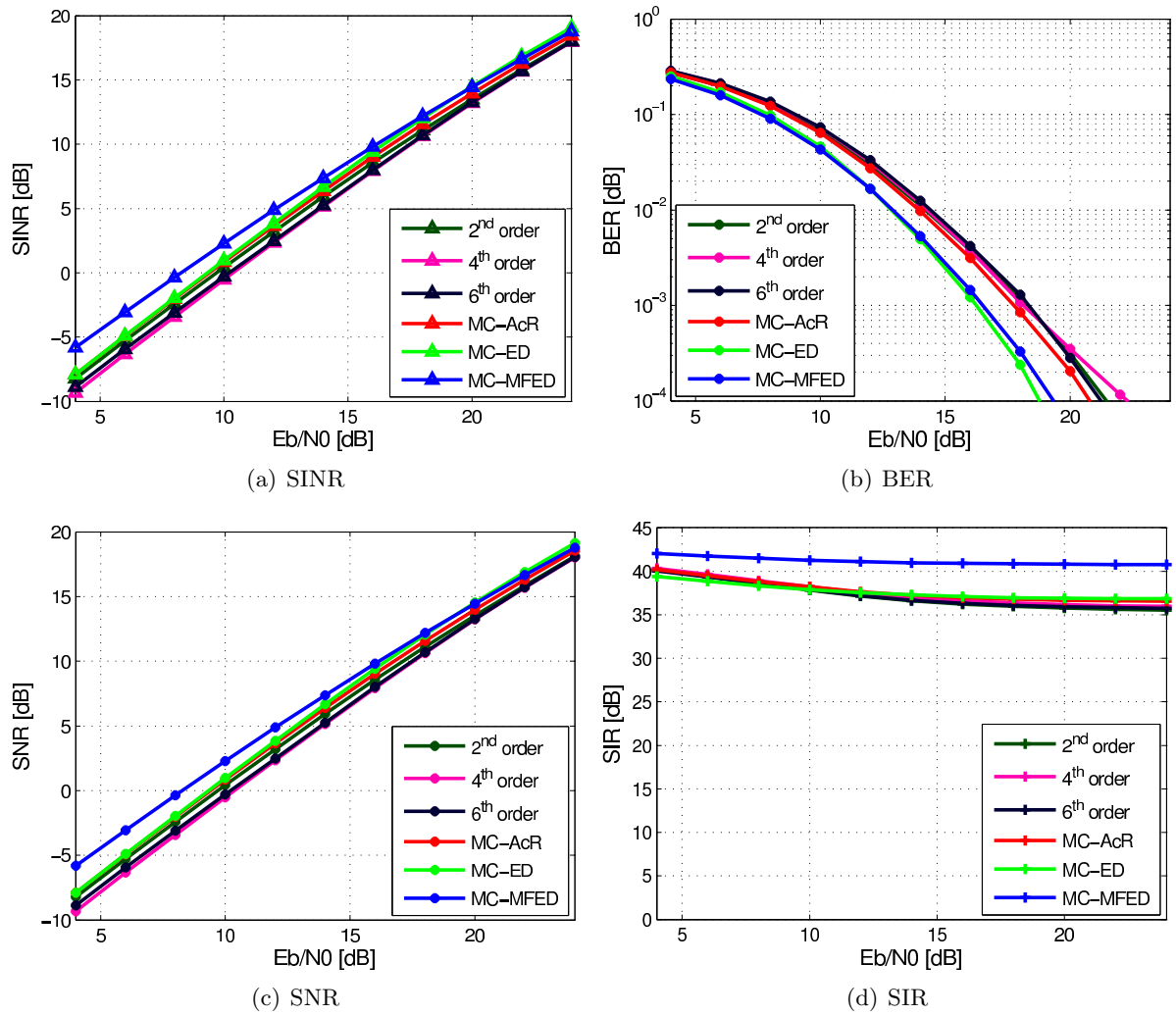
Figure 3.5: SINR, SNR, SIR, and BER of the generalized noncoherent multi-channel receivers with various orders of projection filter cross-spectra.

3.2 Analog Multipliers

The multiplication of signals is a fundamental algebraic concept that is extensively used in signal processing and communications. Its mathematical properties are well studied and understood. In fact almost all signal processing concepts utilize this basic operator, no matter if analog or digital, continuous- or discrete-time. The need for devices to perform the multiplication operation is tremendous, e.g. for digital filtering, Fourier transformation of signals, energy detection, auto- and crosscorrelation. Therefore, a lot of work has been put into studying analog and digital hardware realizations of this mathematical operation.

An important example of analog multipliers are frequency conversion mixers, which are extensively used in RF front-ends [80]. Mixers are used to change the center frequency of bandlimited signals by multiplying the input signal $x(t)$ by a single-tone signal[14], e.g.

$$z(t) = \mathcal{M}\left\{x(t), A\cos(2\pi ft + \phi)\right\}, \tag{3.11}$$

where f is the difference between the center frequencies of the input signal $x(t)$ and the desired output signal $z(t)$, A is an amplitude, ϕ is some phase offset, and $\mathcal{M}\{\cdot, \cdot\}$ represents the multiplication operator

$$\mathcal{M}\left\{x(t), y(t)\right\} = x(t) \cdot y(t). \tag{3.12}$$

Hence, such devices are commonly designed for the purpose of frequency shifting only. For analysis of this operation, the mixer can be considered as a single-input single-output (SISO) system, exploiting the fact that one mixer input signal is considered to be known, e.g. a single-tone signal $A\cos(2\pi ft + \phi)$. This assumption leads to mixer characteristics which can be obtained from single-tone and two-tone measurements of the device, e.g. conversion gains and third-order intercept-points (IP3) [80].
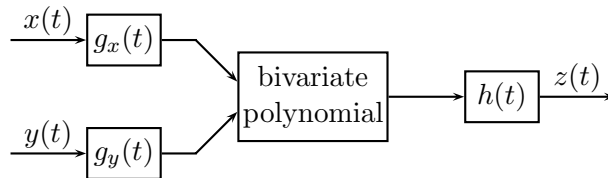
Figure 3.6: Wiener-Hammerstein system model consisting of input filters $g_x(t)$ and $g_y(t)$, an output filter $h(t)$, and a bivariate polynomial as static nonlinearity.

However, these narrowband characteristics cannot give a reasonable description of the input-output behavior of a mixer when used as a non-narrowband analog multiplier, e.g. for multiplying two UWB signals in UWB receiver systems. In particular energy detectors [81] and autocorrelation receivers [82] are noncoherent receivers [13] that are based on multipliers. Hence, multipliers play a crucial role in their performance, e.g. in mitigation of narrowband interference [54,83,84] or synchronization [85]. Multipliers are also used in alternative UWB approaches as compressed sensing [86,87] or hybrid matched filter correlation receivers [43] for which their influence on the receiver performance needs to be analyzed. In [88], for example, it was shown that analog multipliers create undesired signal content, which have an impact on the system performance of a noncoherent UWB receiver [55]. These undesired signal components cause self-interference due to nonlinearities of higher order, which results in a degradation of the

---

[14] The authors want to note, that in real mixer applications $x(t)$ gets "switched" by the signal of a local oscillator, so the input signal gets rather multiplied with a rectangular function $y(t) = A\text{sign}\left(\cos(2\pi ft + \phi)\right)$ instead of a single-tone. But for illustration of the concept of frequency shifting, we prefer to consider the ideal case of multiplication of $x(t)$ with a single sinusoidal signal.

signal-to-interference-and-noise ratio of the test statistic and hence in a degradation of the bit-error rate. These effects can only be modeled using UWB models.

In general, Volterra system models [89, 90] are often used to model nonlinear RF devices [91]. An example is shown in [92], where a Volterra system model with a periodic kernel is proposed. Such a kernel is suitable to model the frequency-conversion behavior of a mixer. It was shown that the proposed model can reconstruct metrics like transconductance or third-order intermodulation (IM3). The big drawback of Volterra systems is that they may consist of kernels of high dimensionality, which are hard to identify and which do not give insight into the operation of the devices per se.

Wiener-Hammerstein systems are a subclass of Volterra system models [93] which give better intuition about the device operation. In [94, 95] identification methods for Wiener-Hammerstein systems [90] are proposed, with the drawback that they cover SISO systems only. On the other hand, [96] shows an approach to identify multiple-input multiple-output (MIMO) Wiener and MIMO Hammerstein systems, but not their concatenations: Wiener-Hammerstein or Hammerstein-Wiener systems.

In [97] a multiple-input single-output (MISO) Wiener-Hammerstein model and a dedicated recursive identification method is presented. This model consists of parallel SISO Wiener-Hammerstein models for each input signal, while the MISO model output is the sum of the partial SISO model outputs. Although this model gives good insight into the system behavior, it cannot model multiplicative cross terms of the input signals, which is crucial for modeling analog multipliers.

This section proposes a MISO Wiener-Hammerstein system model consisting of input and output filters and a bivariate polynomial kernel (cf. Fig. 3.6) that can model accurately ultra-wideband analog multipliers. The model is flexible and, due to its structure, it gives insight in the behavior of such devices. E.g. in [88], the influence of undesired signal content on system performance metrics was shown. Performance degradations have been explained using the proposed Wiener-Hammerstein system model. A method is proposed which facilitates easy and accurate identification of the model parameters. It is shown that the proposed model reaches the accuracy of Agilent ADS circuit simulations but with less computational effort. The model allows to study the nonideal behavior of systems caused by analog multipliers, e.g. the influence of undesired signal content.

In [88] the authors introduced another method to perform identification of the model parameters on Agilent ADS simulations. The Wiener-Hammerstein input filters were estimated using intermediate signals of the circuit-level simulation, which are normally not accessible in real hardware. In contrast, the newly proposed approach is able to identify real hardware multipliers based on measurements.

3.2.1 Signal Models of Nonideal Multipliers

To study the UWB behavior of multipliers, exemplarily a UWB mixer (see Fig. 3.7) designed by Ulm University was investigated [98, 99]. This mixer was designed to perform a multiplication operation for a UWB correlation receiver [100] that supports the full UWB frequency range from 3.1 GHz to 10.6 GHz defined by the FCC [25]. It has been manufactured using Telefunken Semiconductor's Si/SiGe2 HBT technology [101] and consists of two active single-ended-to-differential converter input stages (baluns), biasing circuitry, a four-quadrant Gilbert cell multiplier, and an output buffer stage with a lowpass filter.

Gilbert cell multipliers do have, for the bipolar case, an input-output relationship given as [98]

$$z(t) = I_{\mathrm{T}}\tanh\left(\frac{x(t)}{2V_{\mathrm{T}}}\right)\tanh\left(\frac{y(t)}{2V_{\mathrm{T}}}\right), \tag{3.13}$$

where I_{T} is the total emitter bias current, V_{T} is the thermal voltage, $x(t)$ and $y(t)$ are two input voltage signals, and $z(t)$ is an output current signal. This topology is known to approximate the ideal multiplication operation sufficiently well for low input levels, due to the approximately linear working points of the tanh-functions [102].
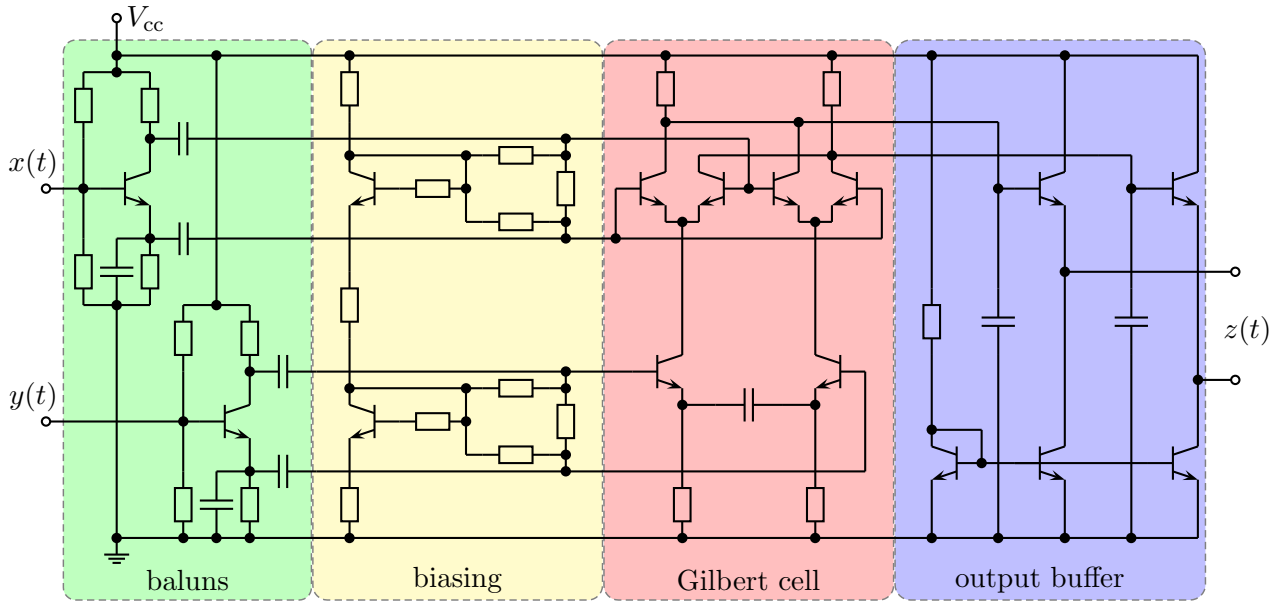
Figure 3.7: *Circuit model of the UWB mixer designed by Ulm University consisting of two active single-ended-to-differential converter input stages (baluns), biasing, a four-quadrant Gilbert cell multiplier, and an output buffer.*

Unfortunately, typical Gilbert cell mixers consist of additional circuitry as the aforementioned single-ended-to-differential converters, the output buffer stage, and some biasing circuitry. These auxiliaries introduce distortions to the output signal, which are not modeled by (3.13). Neither are parasitic effects as e.g. memory effects due to parasitic capacitors or current leakage. Therefore, a more generic approach is proposed.

A possible way is to express the tanh function using Taylor-expansion [33], which is given as

$$\tanh(x) = \sum_{n=1}^{\infty} \frac{2^{2n}\left(2^{2n}-1\right)}{(2n)!}\mathrm{B}_{2n}x^{2n-1}, \tag{3.14}$$

with B_{2n} being the $2n^{\mathrm{th}}$ Bernoulli number. Comparing (3.14) with (3.13) and having the auxiliaries in mind, it seems possible to describe the static nonlinearity of the system using a bivariate polynomial.

In addition, linear time-invariant filters need to be considered at the input and the output stages, which do not exist in an ideal multiplier. A nonideal multiplication of two independent signals $x(t)$ and $y(t)$ can hence be modeled as

$$\mathcal{M}\{x(t), y(t)\} = h(t) * \left[\sum_{u=0}^{U}\sum_{v=0}^{u} c_{u-v,v}\left(g_x(t) * x(t)\right)^{u-v}\left(g_y(t) * y(t)\right)^{v}\right], \tag{3.15}$$

which represents a Wiener-Hammerstein system with U being the maximum order of a static bivariate polynomial nonlinearity, $g_x(t)$ and $g_y(t)$ being impulse responses of linear time-invariant input filters, respectively, $h(t)$ being the impulse response of a linear time-invariant output filter, and $\{c_{u-v,v}\}$ being the coefficients of the polynomial. These coefficients can be used to derive signal metrics and to investigate the influence of output distortions on a considered application [88]. The coefficient $c_{1,1}$ represents a constant gain of the desired ideal multiplication term, $c_{0,0}$ gives the constant DC bias, and $c_{2,0}$, $c_{0,2}$ represent the gains of the squared filtered input signals. In Fig. 3.8, a multiplier model of order $U = 3$ is illustrated.
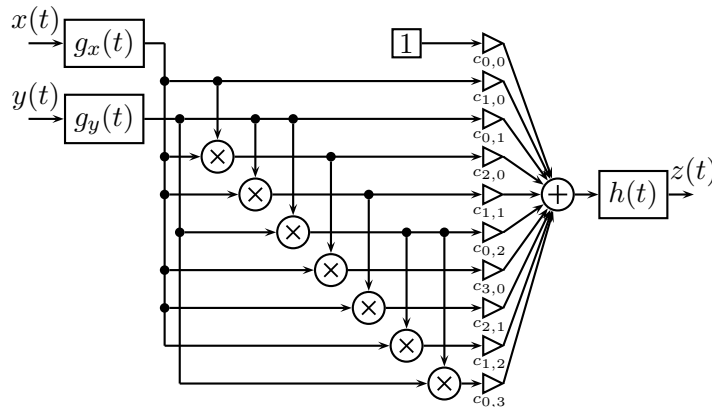
Figure 3.8: *A nonideal multiplier system $z(t) = \mathcal{M}\{x(t), y(t)\}$ of order $U = 3$ consists of two input filters and one output filter, and seven ideal multipliers and gains, which model the static bivariate nonlinearity.*

To identify the system model of the analog multiplier given in (3.15), an approach with two steps is proposed. The first step is to identify the filters $g_x(t)$, $g_y(t)$, and $h(t)$, respectively. The second step is to estimate the polynomial coefficients $\{c_{u-v,v}\}$ using these identified filters.

3.2.2 Filter Identification

A way to identify the input and output filters of a given analog multiplier is to excite the device with two different single-tones, e.g. $x(t) = A_x \cos(2\pi f_x t + \phi_x)$ and $y(t) = A_y \cos(2\pi f_y t + \phi_y)$. It is assumed that the multiplier has negligible undesired output components for small input signals, hence the signal term which is represented by $c_{1,1}$ is predominant. The output $z(t)$ of the device is thus given as

$$z(t) \approx \Re\left\{\frac{1}{2}c_{1,1}A_xA_y e^{j2\pi(f_x+f_y)t}e^{j(\phi_x+\phi_y)}G_x(f_x)G_y(f_y)H(f_x+f_y)\right\}$$
$$+\Re\left\{\frac{1}{2}c_{1,1}A_xA_y e^{j2\pi(f_x-f_y)t}e^{j(\phi_x-\phi_y)}G_x(f_x)G_y^*(f_y)H(f_x-f_y)\right\}, \tag{3.16}$$

which represents two single-tones at frequencies $|f_x+f_y|$ and $|f_x-f_y|$, respectively, where $G_x(f)$, $G_y(f)$, $H(f)$ are the frequency responses of the input and output filters, $G_y^*(f)$ represents the complex conjugate of $G_y(f)$. It can be seen that both tones exhibit complex gains which contain those frequency responses at certain frequencies. The complex amplitude of the signal with the difference frequency[15] $|f_x - f_y|$ is given as

$$\alpha(f_x, f_y) = \frac{1}{2}c_{1,1}A_xA_y e^{j(\phi_x-\phi_y)}G_x(f_x)G_y^*(f_y)H(f_x-f_y), \tag{3.17}$$

---

[15] For simplicity, the method is shown using the difference frequency $|f_x - f_y|$ only. The method can easily be expanded to support the sum frequency $|f_x + f_y|$ too.

which can be easily measured, e.g. by sampling the input and output signals and performing a discrete Fourier transform (DFT) to get the complex amplitudes of these tones.

If these measurements are done in an equidistant two-dimensional input frequency sweep, equidistant samples of the frequency responses of the filters can be obtained. N^2 measurements are taken, where $N = \frac{f_{\text{up}} - f_{\text{low}}}{\Delta f} + 1 \in \mathbb{Z}$ is the number of the frequencies within the desired input frequency range $[f_{\text{low}}, f_{\text{up}}]$ at a spacing of Δf. We define the vector

$$\boldsymbol{\sigma} = [f_{\text{low}}, f_{\text{low}} + \Delta f, f_{\text{low}} + 2\Delta f, \ldots, f_{\text{up}}]^T \tag{3.18}$$

of input frequencies[16]. The vector $\boldsymbol{\rho}$ of output frequencies is then given as

$$\boldsymbol{\rho} = [0, \Delta f, 2\Delta f, \ldots, (N-1)\Delta f]^T. \tag{3.19}$$

Magnitude Responses

The magnitude responses can be obtained by taking the absolute value and the logarithm of (3.17) to get a linear relation,

$$\log|\alpha\left(f_x, f_y\right)| = \log|\frac{1}{2}c_{1,1}| + \log|A_x A_y| + \log|G_x(f_x)| + \log|G_y(f_y)| + \log|H(|f_x - f_y|)|. \tag{3.20}$$

We formulate the linear system of equations

$$\boldsymbol{\alpha} = \mathbf{Am} + \boldsymbol{\xi} + \boldsymbol{\nu}, \tag{3.21}$$

where $\boldsymbol{\alpha}$ is the measurement vector with elements

$$[\boldsymbol{\alpha}]_{k+(l-1)N} = \log|\alpha\left([\boldsymbol{\sigma}]_k, [\boldsymbol{\sigma}]_l\right)|, \tag{3.22}$$

$k, l = 1, 2, \ldots, N$, and $\boldsymbol{\nu}$ represents any errors in the measurements or model, e.g. nonlinear terms of higher order or nonlinear memory which are not modeled, and measurement noise. The vector $\boldsymbol{\xi}$ corrects for the measured input amplitudes. Its elements are given as

$$[\boldsymbol{\xi}]_{k+(l-1)N} = \log|A_x\left([\boldsymbol{\sigma}]_k, [\boldsymbol{\sigma}]_l\right) A_y\left([\boldsymbol{\sigma}]_k, [\boldsymbol{\sigma}]_l\right)|, \tag{3.23}$$

where the possible dependency of the input signal amplitude on measurement point (k, l) is explicitly shown. The vector $\mathbf{m}$ is the concatenation of the sampled logarithmic magnitude responses given as

$$\mathbf{m} = \left[\log|\mathbf{g}_x|^T, \log|\mathbf{g}_y|^T, \log|\mathbf{h}|^T, \log|\frac{1}{2}c_{1,1}|\right]^T, \tag{3.24}$$

whose elements are $[\mathbf{g}_x]_i = G_x([\boldsymbol{\sigma}]_i)$, $[\mathbf{g}_y]_i = G_y([\boldsymbol{\sigma}]_i)$, and $[\mathbf{h}]_i = H([\boldsymbol{\rho}]_i)$, $i = 1, \ldots, N$. The matrix $\mathbf{A}$ is an indicator matrix, which is defined as

$$\mathbf{A} = [\mathbf{A}_1 \ \mathbf{A}_2 \ \mathbf{A}_3 \ \mathbf{1}_{N^2}], \tag{3.25}$$

---

[16] Note that the input frequencies can be chosen differently, e.g. variable frequency spacings or frequency regions can be covered. The output frequency vector depends on the input frequency vectors. The choice by the authors was to show a simple example.

where $\mathbf{1}_{N^2}$ is an all-ones vector with N^2 elements, and

$$[\mathbf{A}_1]_{k+(l-1)N,i} = \begin{cases} 1 & \text{, for } [\boldsymbol{\sigma}]_k = [\boldsymbol{\sigma}]_i \\ 0 & \text{, otherwise} \end{cases} \tag{3.26}$$

$$[\mathbf{A}_2]_{k+(l-1)N,i} = \begin{cases} 1 & \text{, for } [\boldsymbol{\sigma}]_l = [\boldsymbol{\sigma}]_i \\ 0 & \text{, otherwise} \end{cases} \tag{3.27}$$

$$[\mathbf{A}_3]_{k+(l-1)N,i} = \begin{cases} 1 & \text{, for } |[\boldsymbol{\sigma}]_k - [\boldsymbol{\sigma}]_l| = [\boldsymbol{\rho}]_i \neq 0 \\ 2 & \text{, for } |[\boldsymbol{\sigma}]_k - [\boldsymbol{\sigma}]_l| = 0 \\ 0 & \text{, otherwise} \end{cases} \tag{3.28}$$

where $k, l, i = 1, 2, \ldots, N$. Note that $\mathbf{A}$ needs to have a full rank, hence $N \geq 4$ needs to hold.

Using this data model, the magnitude response can be estimated in a least-squares sense using

$$\hat{\mathbf{m}} = \mathbf{A}^\dagger \left(\boldsymbol{\alpha} - \boldsymbol{\xi} \right), \tag{3.29}$$

where $\mathbf{A}^\dagger$ represents the Moore-Penrose pseudo inverse of $\mathbf{A}$. For a valid least-squares solution, the matrix $\mathbf{A}$ needs to be full rank and uncorrelated with the error $\boldsymbol{\nu}$ [103]. Measurements have shown (see Section 3.2.4), that these assumptions are fulfilled[17].

Phase Responses

The phase responses can be estimated in a similar way. The phase of the output signal $z(t)$ is given (cf. (3.17)) as

$$\begin{aligned} \angle\alpha\left(f_x, f_y\right) =\ & (\phi_x - \phi_y) \\ & + \angle G_x(f_x) - \angle G_y(f_y) + \angle H(|f_x - f_y|). \end{aligned} \tag{3.30}$$

The elements of the measured phase vector $\boldsymbol{\beta}$ are defined as

$$[\boldsymbol{\beta}]_{k+(l-1)N} = \angle\alpha([\boldsymbol{\sigma}]_k, [\boldsymbol{\sigma}]_l), \tag{3.31}$$

hence

$$\boldsymbol{\beta} = \mathbf{B}\boldsymbol{\psi} + \boldsymbol{\zeta} + \boldsymbol{\nu}, \tag{3.32}$$

where $\boldsymbol{\nu}$ represents any errors in the measurements or model which have the same causes as in (3.21). The vector $\boldsymbol{\zeta}$, with elements

$$[\boldsymbol{\zeta}]_{k+(l-1)N} = (\phi_x\left([\boldsymbol{\sigma}]_k, [\boldsymbol{\sigma}]_l\right) - \phi_y\left([\boldsymbol{\sigma}]_k, [\boldsymbol{\sigma}]_l\right)), \tag{3.33}$$

corrects for the measured input phases. The indicator matrix $\mathbf{B}$, which is full rank for $N \geq 4$, is

$$\mathbf{B} = [\mathbf{A}_1\ \mathbf{A}_2\ \mathbf{A}_3]. \tag{3.34}$$

---

[17] For the identification using measurements, the power of the error $\boldsymbol{\nu}$ was found to be -30.7 dB below the power of the dependent variable vector $\boldsymbol{\alpha} - \boldsymbol{\xi}$. For the identification using ADS, the power of $\boldsymbol{\nu}$ was found to be -28.5 dB below the power of the dependent variable vector. The corresponding correlation coefficients are 0.1452 for the identification using measurements and 0.1382 for the identification using ADS. These numbers suggest, that $\boldsymbol{\nu}$ is uncorrelated to $\mathbf{A}$.

Finally the estimate of the phase response vectors

$$\boldsymbol{\psi} = \left[\angle\mathbf{g}_x^T, -\angle\mathbf{g}_y^T, \angle\mathbf{h}^T\right]^T \tag{3.35}$$

is obtained in a least-square sense as

$$\hat{\boldsymbol{\psi}} = \mathbf{B}^\dagger \left(\boldsymbol{\beta} - \boldsymbol{\zeta}\right). \tag{3.36}$$

The matrix $\mathbf{B}$ needs to be full rank and uncorrelated with the error $\boldsymbol{\nu}$ to obtain a valid least-squares solution [103].

Equivalent IIR Filter Modeling

To model the input and output filters, the estimated magnitude and phase responses can be used to find equivalent discrete-time IIR filters, e.g. utilizing metaheuristic algorithms [69, 104, 105]. The used cost-function can be chosen, e.g. as the sum of squared differences from the given sampled target frequency responses. To avoid ambiguities due to gain exchange between the filters and the bivariate polynomial coefficients, the filters should be normalized to a passband gain of one. Effects like exchange of group delay between the input and output filters do not play a crucial role due to the fact that the identification method does identify the phase response of the input and output filters. Phase ambiguities are resolved by fitting the IIR filter models. Note that the measurement setup needs to be calibrated to ensure that any delays induced by the measurement setup are removed.

3.2.3 Polynomial Coefficients Identification

To estimate the coefficients $\{c_{u-v,v}\}$ of the bivariate polynomial kernel of the system model, the device has to be excited with signals which fit into its input frequency region and have a given amplitude distribution. The amplitude distribution can be seen as a weighting of the estimation: an amplitude interval with a higher probability mass is modeled more accurately than an amplitude interval with a lower probability mass. The amplitude distribution should hence depend on the signals of the application under consideration, just like the input frequency range[18].

Segments of length L of the sampled input signals are stored in vectors $\mathbf{x}$ and $\mathbf{y}$, respectively. These signals need to be filtered with discrete-time equivalents of the identified input filters $\hat{g}_x(t)$ and $\hat{g}_y(t)$, respectively. The filtered input signals $\hat{\mathbf{x}}$ and $\hat{\mathbf{y}}$ are thus given as

$$\hat{\mathbf{x}} = \hat{\mathbf{G}}_x\mathbf{x} \tag{3.37}$$
$$\hat{\mathbf{y}} = \hat{\mathbf{G}}_y\mathbf{y}, \tag{3.38}$$

with $\hat{\mathbf{G}}_x$ and $\hat{\mathbf{G}}_y$ being the Toeplitz matrices of the discrete-time equivalents of $\hat{g}_x(t)$ and $\hat{g}_y(t)$.

The sampled device output vector $\mathbf{z}$ is then

$$\mathbf{z} = \hat{\mathbf{X}}\mathbf{c} + \boldsymbol{\nu}, \tag{3.39}$$

where

$$\mathbf{c} = \left[c_{0,0}, c_{1,0}, c_{0,1}, c_{2,0}, c_{1,1}, c_{0,2}, \dots\right]^T \tag{3.40}$$

---

[18] It is possible to use other signals than the desired signals of the application under consideration. However, only an estimation with the desired signal amplitude distribution will lead to minimal modeling errors.

represents the vector of polynomial coefficients and the vector $\boldsymbol{\nu}$ represents the measurement noise. The Matrix and $\hat{\mathbf{X}}$ is given as

$$\hat{\mathbf{X}} = \hat{\mathbf{H}} \left[\mathbf{1}_M, \hat{\mathbf{x}}, \hat{\mathbf{y}}, \hat{\mathbf{x}}^2, (\hat{\mathbf{x}} \odot \hat{\mathbf{y}}), \hat{\mathbf{y}}^2, \dots \right] \tag{3.41}$$

where $\hat{\mathbf{H}}$ is the Toeplitz matrix of the discrete-time equivalent of $\hat{h}(t)$, $\odot$ represents the element-wise multiplication and the exponentiation represents an element-wise exponentiation of the vector elements[19]. Note that L needs to be chosen to ensure that $\hat{\mathbf{X}}$ has full rank.

The polynomial coefficient vector can finally be estimated in a least-square sense using

$$\hat{\mathbf{c}} = \hat{\mathbf{X}}^\dagger \mathbf{z}. \tag{3.42}$$

3.2.4 Model Verification

The verification of the model is performed using the aforementioned UWB mixer designed by Ulm University. The device consists of a bare mixer die which has been bonded onto a printed circuit board (PCB). The signal inputs and the output are AC coupled with capacitors of 100 pF. For comparison, the proposed identification methods are also evaluated using an Agilent ADS circuit-level model of that UWB mixer circuit.

Model Performance

A metric to evaluate the performance of the system identification is the normalized mean square error (NMSE) of the system model output $\mathbf{z}$ passed through an application-specific target filter $T(f)$ represented by its discrete-time equivalent Toeplitz matrix $\mathbf{T}$. This filter extracts the frequency range of interest. The NMSE is thus defined as

$$\text{NMSE} = \text{E} \left\{ \frac{\left(\mathbf{T}\mathbf{z} - \mathbf{T}\hat{\mathbf{X}}\hat{\mathbf{c}} \right)^T \left(\mathbf{T}\mathbf{z} - \mathbf{T}\hat{\mathbf{X}}\hat{\mathbf{c}} \right)}{\mathbf{z}^T \mathbf{T}^T \mathbf{T}\mathbf{z}} \right\}, \tag{3.43}$$

where $\text{E}\{\cdot\}$ represents the expectation operator.

The filter $T(f)$ was chosen to be a Bessel filter of order 6 with cut-off frequency of 91.9 MHz. It approximates a sliding window integrator for a noncoherent multichannel autocorrelation UWB receiver [55, 58] as described in Section 3.3.

Measurement Setup

The measurement setup is depicted in Fig. 3.9. To estimate the frequency responses, a two dimensional frequency sweep from 100 MHz to 6 GHz with a Δf of 100 MHz was performed using an Agilent E8267C signal generator and a Rohde&Schwarz ZVA24 network analyzer. The single-tones $x(t) = A_x \cos(2\pi f_x t + \phi_x)$ and $y(t) = A_y \cos(2\pi f_y t + \phi_y)$ generated by the signal generators got amplified, and after power splitting had a power of -20 dBm at the input ports of the mixer. The input and output signals were sampled at a rate of 20 GHz using an Agilent Infiniium 54855A scope. To obtain the magnitude and phase of the input tones and of the desired output tone $A_z \cos(2\pi |f_x - f_y| t + \phi_z)$, a DFT was performed[20]. The DFT has the advantage,

---

[19] We assume that the Toeplitz matrices $\hat{\mathbf{G}}_x$, $\hat{\mathbf{G}}_y$, and $\hat{\mathbf{H}}$ are designed such that transient effects at the signal boundaries are excluded.

[20] Sample rate, signal frequencies and sample lengths need to be chosen properly to avoid leakage effects of the DFT.

that it mitigates all undesired frequencies. It was observed from those measurements that such components have negligible power, which validates the assumption from Section 3.2.2 that an ideal multiplier can be assumed for the filter identification step. The signal powers of the desired output single-tones of the two-dimensional frequency sweep measurements, i.e. $|A_z(f_x, f_y)|^2$, are shown in Fig. 3.10. Each grid point represents the signal power of the output tone at a frequency of $|f_x - f_y|$, where f_x and f_y are frequencies of the input single-tones.
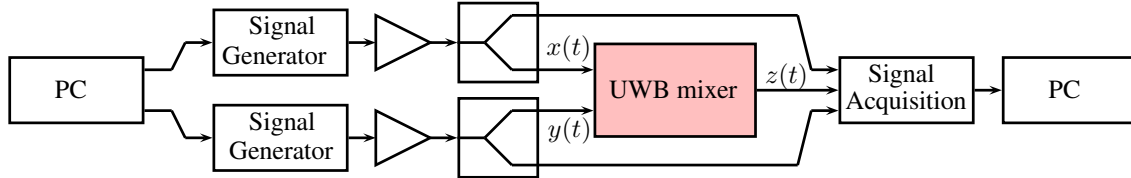
Figure 3.9: Measurement setup for mixer identification.
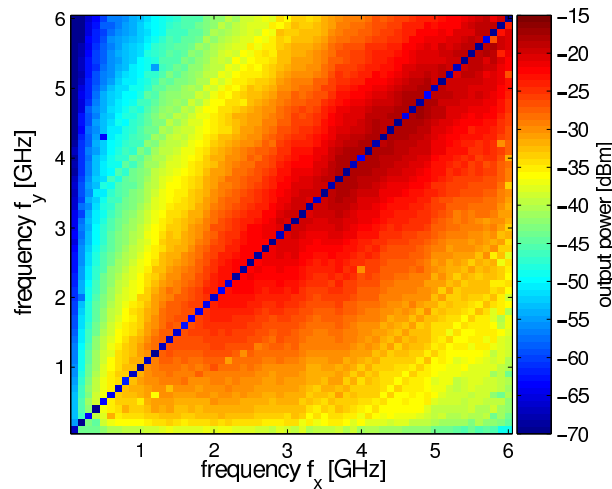
Figure 3.10: Magnitude response of two dimensional frequency sweep measurements. Each grid point represents the output power of the output single-tone at a frequency of $|f_x - f_y|$, where f_x and f_y are frequencies of the input single-tones.

To estimate the polynomial coefficients the two input ports of the device were excited with application-specific, uncorrelated signals. For this measurement, NOFDM pulses as defined in Tab. 2.1 were used. The pulses were generated using the Tektronix AWG7102 arbitrary waveform generator with a sampling rate of 10 GHz. Due to the fact that the Tektronix AWG7102 does not have a sufficient output lowpass filter to avoid an image signal of the desired one, the excitation signal shows additional frequency components from 5.125 GHz to 6.875 GHz. These image signals are accounted for in the coefficient estimation procedure. The input power to the mixer ports was −20 dBm, which is sufficient to drive the mixer at times into saturation due to a peak-to-average-power ration (PAPR) of the UWB signals of 18 dB. The input and output signals were again sampled using the Agilent Infiniium 54855A scope at a sampling rate of 20 GHz.

Model Parameter Estimation

Fig. 3.11 shows the magnitude responses of the estimated filters (cf. Section 3.2.2) obtained from the measurement. For comparison, the estimated filter magnitude responses are also shown for the ADS circuit model.
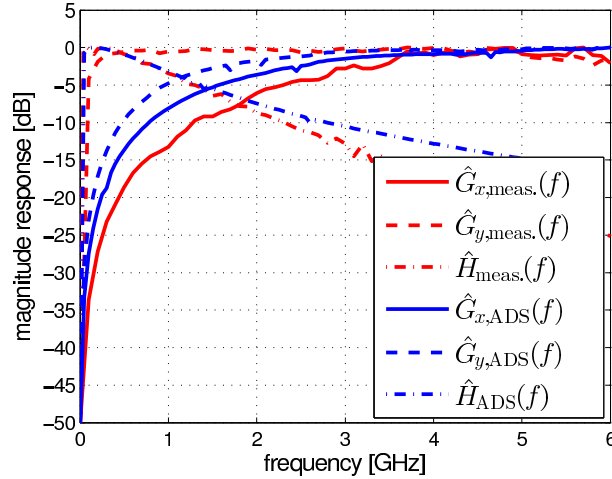
Figure 3.11: Input and output filter magnitude responses of the system model fitted to the measurement and to the ADS circuit model simulation.

It can be seen that the estimated output filters $\hat{H}_{\mathrm{meas.}}(f)$, $\hat{H}_{\mathrm{ADS}}(f)$ and the input filters $\hat{G}_{x,\mathrm{meas.}}(f)$, $\hat{G}_{x,\mathrm{ADS}}(f)$ are very similar to one another. They differ in the region of interest (from DC to 2 GHz for $\hat{H}_{\mathrm{meas.}}(f)$ and $\hat{H}_{\mathrm{ADS}}(f)$ and from 3.125 GHz to 4.875 GHz for $\hat{G}_{x,\mathrm{ADS}}(f)$ and $\hat{G}_{x,\mathrm{meas.}}(f)$) up to 1.3 dB and 1.6 dB, respectively. The input filters $\hat{G}_{y,\mathrm{meas.}}(f)$ and $\hat{G}_{y,\mathrm{ADS}}(f)$ do differ up to 18.9 dB on the shown frequency range, but 0.6 dB in the region of interest. The differences between the ADS system model and the measurement system model might be caused by parasitic effects that are not modeled by the ADS circuit-model, but which certainly exist in the hardware mixer.

To model the input and output filters, the magnitude responses of the estimated filters (cf. Section 3.2.2) were used to find equivalent discrete-time minimum-phase IIR filters, utilizing a differential evolution (DE) algorithm [79] which is in detail described in Appendix C.2. The used multi-objective cost-function is given as

$$J(\boldsymbol{\Phi}) = w_1 J_{\mathrm{mag}}(\boldsymbol{\Phi}) + w_2 J_{\mathrm{p}}(\boldsymbol{\Phi}) + w_3 J_{\mathrm{z}}(\boldsymbol{\Phi}), \tag{3.44}$$

where

$$J_{\mathrm{mag}}(\boldsymbol{\Phi}) = \sum_{f=f_{\mathrm{low}}}^{f_{\mathrm{up}}} \left(|X(f)| - \left| \hat{X}\left(e^{j\frac{2\pi}{R_s}f}, \boldsymbol{\Phi}\right) \right| \right)^2 \tag{3.45}$$

represents sum of squared differences of the solution $\hat{X}\left(e^{j\frac{2\pi}{R_s}f}, \boldsymbol{\Phi}\right)$ filter from the given sampled target magnitude response $|X(f)|$, and $J_{\mathrm{p}}(\boldsymbol{\Phi})$ and $J_{\mathrm{z}}(\boldsymbol{\Phi})$ ensure for stable and minimum-phase filters (see Section 3.1.1). The parameters of the DE algorithm are listed in Tab. 3.3. The filter order of $G_x(f)$, $G_y(f)$, and $H(f)$ were set to two.

The obtained filters were taken to identify the polynomial coefficients. The order of the bivariate polynomial was chosen to minimize the NMSE. For the given application it was found to be six. In Fig. 3.12, the estimated polynomial coefficients $\{c_{u-v,v}\}$ are depicted for the measurement system model and the ADS system model. It can be seen that both sets of coefficients are similar, however, some coefficients differ. The maximal difference is 52.9 dB for $c_{0,0}$, but at very low magnitude. The average difference is 6.6 dB. Also these differences between the ADS system model and the measurement system model might be caused by parasitic effects.

The time and frequency domain representations of the output signal are shown in Figs. 3.13 – 3.14(b). The model output signal is compared with the measured output signal, the ADS

Table 3.3: *DE algorithm parameters.*

Parameter Name	Parameter	Value
Number of iterations	GENERATIONS	100
Number of particle	POPULATION	1000
Mutation rate	ALPHA	0.75
Weight for $J_{\mathrm{mag}}\left(\boldsymbol{\Phi}\right)$	w_1	10
Weight for $J_{\mathrm{p}}\left(\boldsymbol{\Phi}\right)$	w_2	1
Weight for $J_{\mathrm{z}}\left(\boldsymbol{\Phi}\right)$	w_3	1
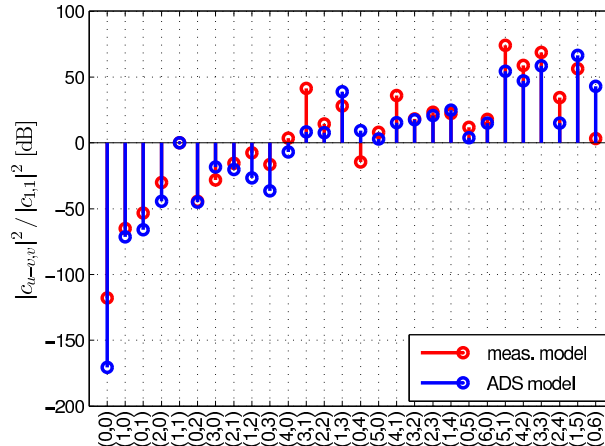
Figure 3.12: *Polynomial coefficients $\{c_{u-v,v}\}$ of the system models fitted to the measurement and to the ADS simulation, respectively. The coefficients are normalized to the desired signal coefficient $c_{1,1}$. The pair (a,b) represents the respective polynomial coefficient $c_{a,b}$.*

simulation output, and the system model output matched to the ADS simulation.

In the time domain, it can be seen that the output waveforms are similar. In the frequency domain it can be seen that all signals have a similar power-spectral-density (PSD) in the range from DC up to about 3 GHz. In Fig. 3.14(a) and Fig. 3.14(b) also the PSDs of the model errors are depicted. The power of errors is -30.5 dBm and -38.5 dBm for the the measurement-fitted model and the ADS-simulation-fitted model, respectively. (For comparison, the output power of the measurement and the ADS simulation is -24.3 dBm and -26.0 dBm, respectively.) For frequencies higher than 3 GHz, the PSDs deviate but are rather small compared to the lower frequency region. The strong attenuation of the measured output signal at frequencies higher than 6 GHz is due to the strong lowpass filter of the scope. The signal content within the frequency band from 3.125 GHz to 6.875 GHz in the measured output signal resembles the signal which is fed into the mixer and may hence be crosstalk from the inputs, e.g. it may be induced by the PCB or may be current leakage through the mixer. This crosstalk is not modeled in the proposed multiplier model and can thus not be identified and reconstructed using that particular model. However, the crosstalk and current leakage might be identified separately after subtracting the measurement-fitted model output from the sampled measurement output. Alternatively, the model could be extended to support nonlinear memory as in [93], thus representing a Volterra system model instead of a Wiener-Hammerstein system model.

The NMSE of the measurement-fitted model compared to the measurement is -11.5 dB, the NMSE of the ADS simulation compared to the measurement is -5.1 dB, and the NMSE of the ADS-simulation-fitted model compared to the ADS simulation output is -21.1 dB. These values are obtained using a training set of 750 pulses to estimate the polynomial coefficients and a validation set of 750 pulses to perform the NMSE computation. The noise level of the
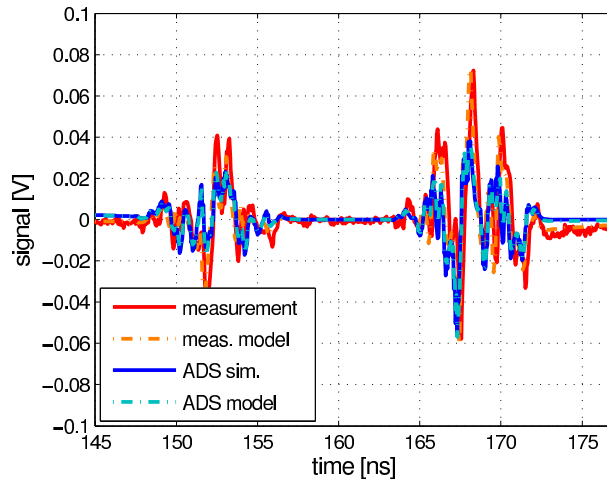
Figure 3.13: Time domain output signals of the nonideal multiplier system model in comparison to the measurement, the output signal of the ADS circuit model, and the system model fitted onto the ADS circuit model.

(a) Measurement-fitted system model.

(b) ADS-simulation-fitted system model.
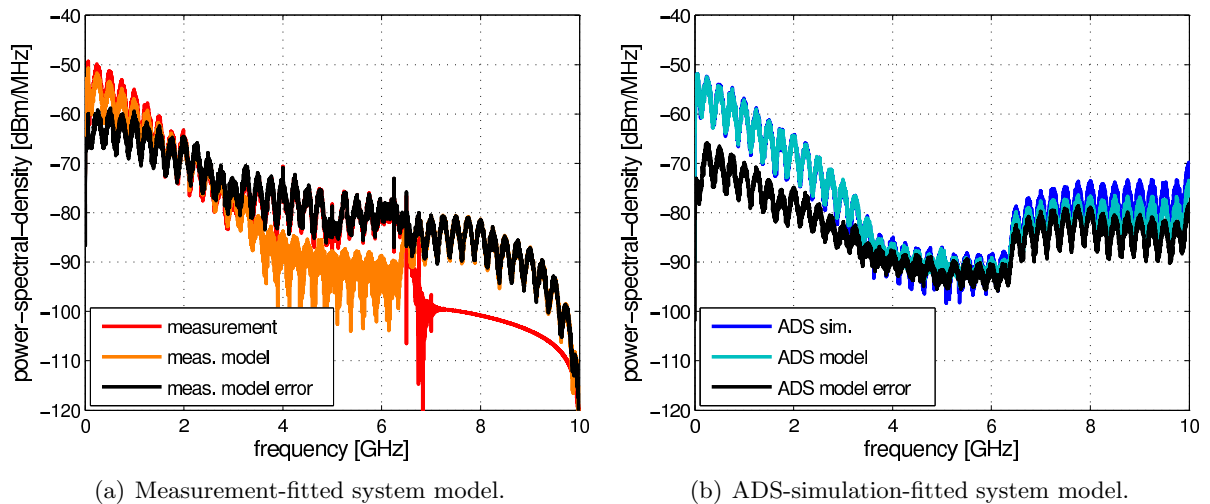
Figure 3.14: Frequency domain output signals in comparison to the ADS circuit model and the model error.

measurement is about -47.6 dBm, hence 17.1 dB less than the measurement-fitted model error. These values confirm that the fit of the proposed system model works very well. They show that the proposed system model is more accurate than the ADS circuit model simulation for the given application, due to the fact that the ADS circuit model does not model parasitic effects. Nonlinear memory effects, which are not considered in the system model, might cause the increased NMSE of the measurement-fitted model with respect to the ADS-fitted one.

In Fig. 3.15, the output power of the individual nonlinear signal parts is depicted. This representation gives intuition about the structure of the output signal and which terms are dominant or which can be neglected for further analysis. It can be seen that the desired signal with $c_{1,1}$ has the highest power of about -24 dBm. Also the signal parts of fourth order with coefficients $c_{3,1}$ and $c_{1,3}$ show significant powers. It also can be seen, although the coefficients seem to be very similar for the ADS model and the measurement model, that the power of some dominant nonlinear signal parts differ more than 30 dB. The average difference is 5.6 dB.
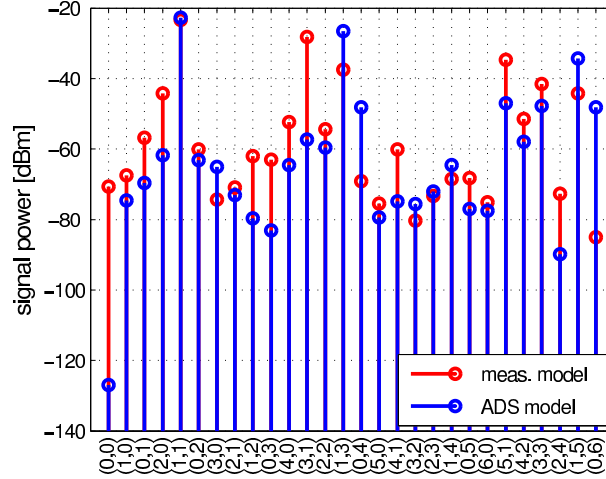
Figure 3.15: Power of the nonlinear signal with the respective coefficients $\{c_{u-v,v}\}$ of the system model fitted to the measurement and the system model fitted to the ADS simulation. The pair (a,b) represents its respective nonlinear coefficient $c_{a,b}$.

3.2.5 Analysis and System Simulations

Narrowband characteristics are not a suitable metric for evaluating broadband multipliers as they do not explain the nonlinear behavior of broadband signals in a sufficient way. Due to the nonlinear behavior of the nonideal multiplier, interference terms may be mapped into the baseband, which is the desired output signal band of noncoherent multi-channel receiver channels. Indeed, every even-order nonlinear term does map into the baseband and is therefore considered as interference term.

Substituting the ideal multiplication operator with the nonideal multiplier operator $\mathcal{M}\{\cdot,\cdot\}$, the mth receiver output can be rewritten[21] as

$$y_m = \int_{\lambda=0}^{T_{\text{sym}}} \mathcal{M}_m \{h_m(t) * r(t), g_m(t) * r(t)\} \, dt \tag{3.46}$$

$$= \sum_{u=0}^{U} \sum_{v=0}^{u} c_{u-v,v} \sum_{\kappa_1+\cdots+\kappa_K=u-v} \sum_{\iota_1+\cdots+\iota_K=v} \binom{u-v}{\kappa_1,\cdots,\kappa_K}\binom{v}{\iota_1,\cdots,\iota_K}$$

$$\times \int_{\lambda=0}^{T_{\text{sym}}} \left\{ h(t) * \Bigg[\right.$$

$$\prod_{k=1}^{K} d_k^{\kappa_k+\iota_k} \left(g_x(t) * h_m(t) * c(t) * \phi_k(t)\right)^{\kappa_k} \left(g_y(t) * g_m(t) * c(t) * \phi_k(t)\right)^{\iota_k}$$

$$\left. \Bigg] \right\} dt + \boldsymbol{\nu}. \tag{3.47}$$

Using vector notation we can rewrite the equation as

$$\mathbf{y} = \mathbf{P}\left(\mathbf{d} \odot \mathbf{d}\right) + \mathbf{Q}\left(\mathbf{d}\tilde{\otimes}\mathbf{d}\right) + \sum_{u=0}^{U} \sum_{\substack{v=0 \\ u-v\neq 1 \wedge v\neq 1}}^{u} \mathbf{M}_{u-v,v} \bigotimes_u \{\mathbf{d}\} + \boldsymbol{\nu}_m, \tag{3.48}$$

where $\mathbf{M}_{u-v,v}$ is the interference matrix corresponding to the effects of the $c_{u-v,v}$ component,

---

[21] A detailed derivation is given in Appendix B.5.

and $\bigotimes_N \{\cdot\}$ defines a manifold Kronecker product of order N, e.g.

$$\bigotimes_3 \{\mathbf{x}\} = \mathbf{x} \otimes \mathbf{x} \otimes \mathbf{x}. \tag{3.49}$$

An adequate metric to study the influence of the nonideal multiplier induced distortion is the signal to interference ratio ($\text{SIR}_{u-v,v}$) of any nonlinear term of the decision variable $\mathbf{z}$ which is defined as

$$\text{SIR}_{u-v,v} = \frac{\mathrm{E}\left\{\mathbf{d}^T\mathbf{P}^T\mathbf{W}^T\mathbf{W}\mathbf{P}^T\mathbf{d}\right\}}{\mathrm{E}\left\{\bigotimes_u\{\mathbf{d}^T\}\mathbf{M}^T_{u-v,v}\mathbf{W}^T\mathbf{W}\mathbf{M}_{u-v,v}\bigotimes_d\{\mathbf{d}\}\right\}}, \tag{3.50}$$

where the expectation operator is evaluated with respect to the symbol vector $\mathbf{d}$.

To investigate the $\text{SIR}_{u-v,v}$ for the different nonlinearity terms, a NOFDM signaling is used with an input signal $\mathrm{E_b/N_0}$ of 18 dB.

In Fig. 3.16, the SIR of various polynomial coefficients for the ADS-simulation-fitted model is depicted. It can be seen that those even-order terms which do show a significant contribution to the multiplier output signal (cf. Fig. 3.15) do disturb the signal most. Odd-order terms are mitigated very well due to the lowpass behavior of the multiplier. It also can be seen that the MC-AcR is more sensitive to the undesired multiplier terms than the MC-ED or MC-MFED, specially when considering $c_{0,4}$, $c_{1,5}$, and $c_{5,1}$.

In Fig. 3.17, the SINR for the ADS-simulation-fitted model is illustrated for different input power levels. It can be seen that for increasing input powers the SINR starts getting worse, which is due to the increased nonlinear effects which result in a decreased SIR. The BER strongly degrades with increasing input power levels due to decreasing SINR. It can be seen that, in comparison to the ideal multiplier case, the BER for the MC-AcR with higher input power values ($P_0 \geq -20$ dBm) does show a significant error floor, which are not visible for the BER of MC-ED and MC-MFED. The later are more robust to undesired nonlinear signal content, due to the fact that they compute the energy of the received signal pulses but, in contrast to the MC-AcR, do not require any additional linear post-processing to obtain spectra of the inverse to separate the received subcarriers.

A summary of SINR, SIR and BER results are listed in Appendix D.2.

(a) MC-AcR

(b) MC-ED

(c) MC-MFED
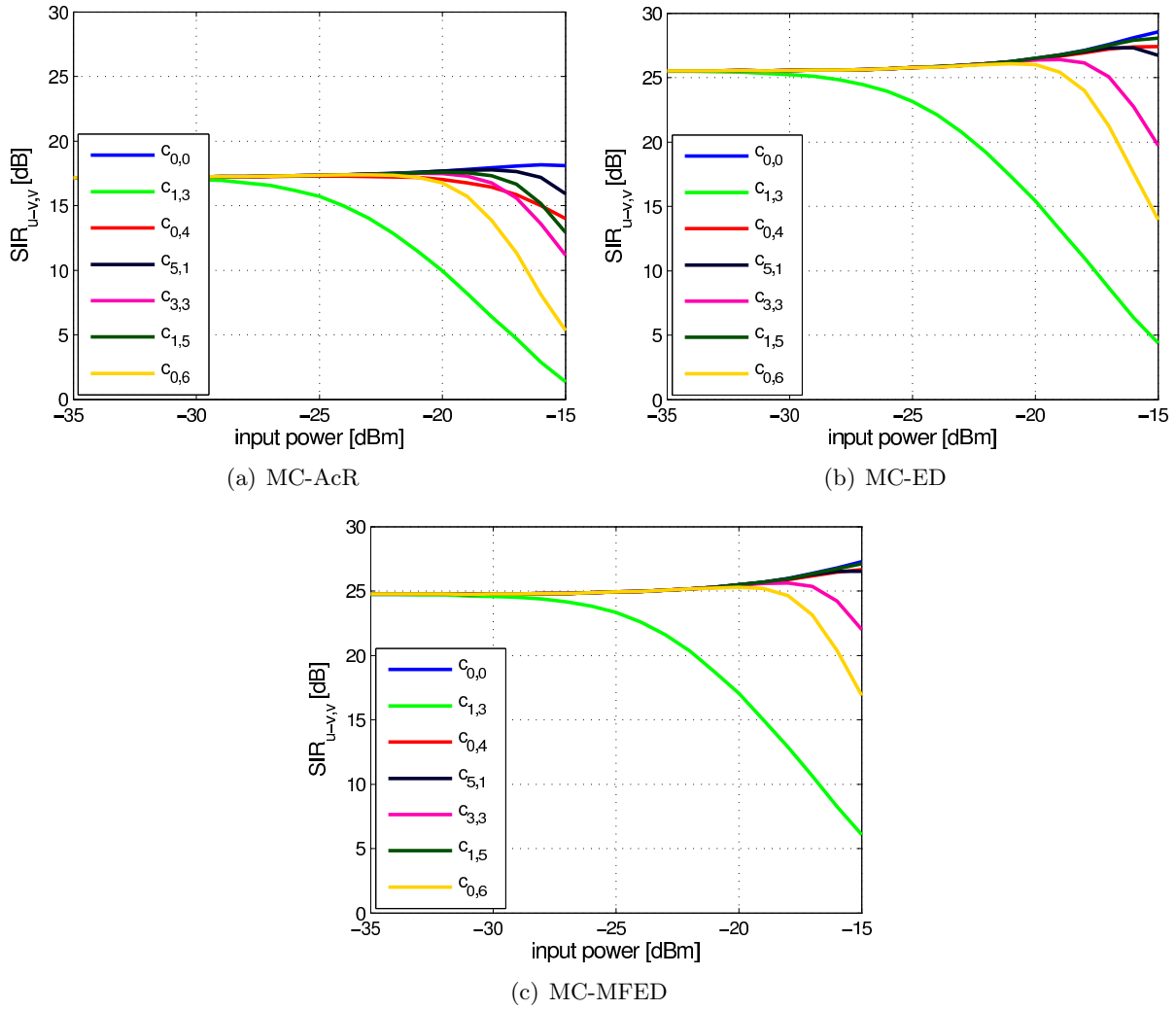
Figure 3.16: $\text{SIR}_{u-v,v}$ *for various nonlinear terms of different noncoherent multi-channel receivers.*
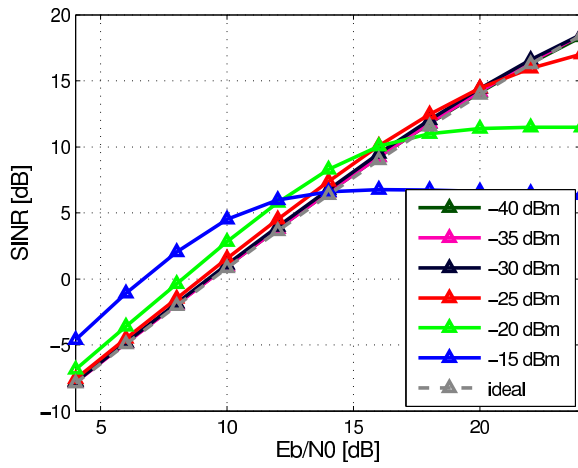
(a) SINR of MC-AcR with nonideal multipliers.
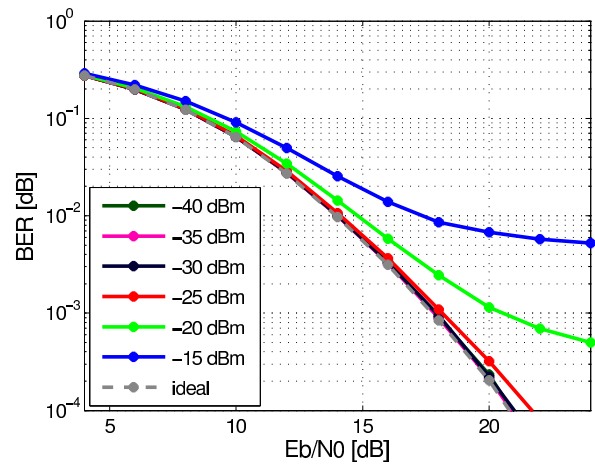
(b) BER of MC-AcR with nonideal multipliers.
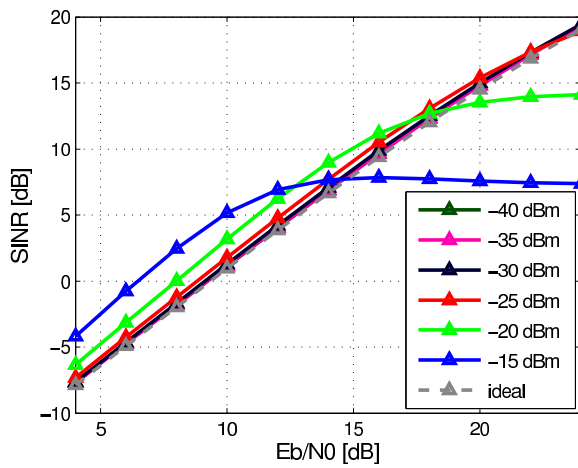
(c) SINR of MC-ED with nonideal multipliers.
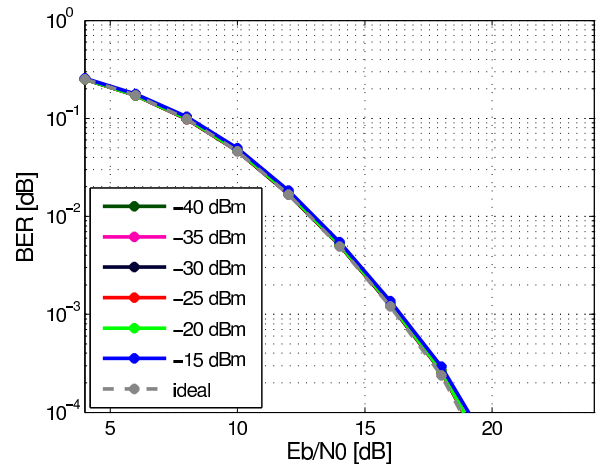
(d) BER of MC-ED with nonideal multipliers.
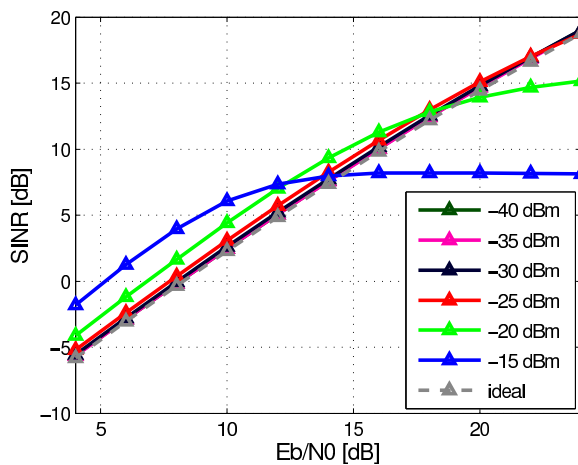
(e) SINR of MC-MFED with nonideal multipliers.
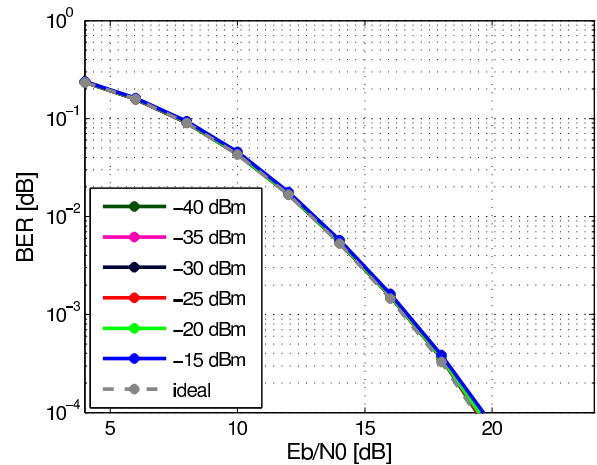
(f) BER of MC-MFED with nonideal multipliers.

Figure 3.17: SINR and BER of various multiplier input power levels of different noncoherent multi-channel receiver architectures.

3.3 Mixed-Signal Sliding Window Integrators

This section studies a realistic implementation of UWB sliding window integration devices. These devices do play an essential role in suppressing cross-products between subcarriers that arise in the nonlinear frontend. The proposed integration system consists of passive filter structures combined with conventional ADCs. This yields a solution that can potentially be realized using standard building blocks and it may save power compared with an active design as in [106] and gives a trade-off between digital sampling rate and analog filter complexity. It is also shown that the optimized filter outperforms the reference system using an ideal sliding window integrator because it is able to mitigate more system noise.

3.3.1 Approximation of Sliding Window Integrators

In (2.3) it can be seen that the system has to perform an integration over the symbol period T_{sym}. This operator can be described as a filter with the impulse response

$$h_T(t) = \sigma(t) - \sigma(t - T), \tag{3.51}$$

where T is the integration window, and $\sigma(t)$ is the Heaviside unit step function. The frequency response of the filter is given as

$$H_T(j\omega) = T e^{-j\frac{T}{2}\omega}\mathrm{sinc}\left(\frac{T}{2\pi}\omega\right), \tag{3.52}$$

where $\mathrm{sinc}(x) = \frac{\sin(\pi x)}{\pi x}$. Unfortunately, this ideal filter cannot be realized in real hardware. Therefore approximations of this ideal integration filter are needed.

A feasible approximation of the analog sliding window integrator can be obtained by using a lowpass Bessel filter and several notch-filters. The Bessel filter is used to get the dropping magnitude frequency response while maintaining a constant group-delay up to an upper frequency. The notch-filters are used to get the zeros in the frequency response. For broadband signals this could lead to analog filters of very high order, due to the need of many notch filters. A mixed analog / digital implementation can relax this issue, as described below.

The impulse response (3.51) can be rewritten as

$$h_T(t) = (\sigma(t) - \sigma(t - T_s)) * \sum_{k=0}^{N_T-1} \delta(t - kT_s), \tag{3.53}$$

where $T_s = \frac{T}{N_T}$, $N_T \in \mathbb{N}$. The sliding window integrator is hence split up into an integrator with a shorter window of length $\frac{T}{N_T}$ and a filter consisting of equally spaced Dirac impulses: a comb filter which can be described by a digital FIR filter easily, where T_s is the discrete-time sampling period. The comb filter has the discrete-time frequency response

$$D\left(e^{j\theta}\right) = \sum_{k=0}^{N_T-1} e^{-j\theta k}, \tag{3.54}$$

where θ is the normalized angular frequency, $\theta = \omega T_s$.

The frequency response of the new analog sliding window integrator $A(j\omega)$ is given as

$$A(j\omega) = T_s e^{-j\frac{T_s}{2}\omega}\mathrm{sinc}\left(\frac{T_s}{2\pi}\omega\right), \tag{3.55}$$
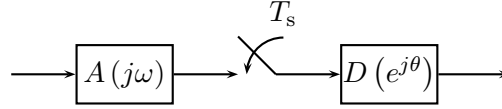
Figure 3.18: Signal flow graph of the mixed-signal sliding window integrator.

which resembles (3.52) but with reduced integration interval T_s. The frequency-spacing of the zeros increases when decreasing the integration interval, therefore the need of analog notch-filters *within the signal bandwidth* is relaxed. The digital filter introduces additional zeros at frequencies $\omega = k2\pi/(N_T T_s)$, $k \in \{\mathbb{Z} \mid (k \mod N_T) \neq 0\}$. In other words, the order of the analog filter is minimized by making the length of the sampling time T_s as small as possible. The accumulation of these partial integrations can be done by the digital comb filter without much effort. This gives a trade-off between analog filter complexity and digital sampling rate.

An additional design goal for the filter approximation is a high SINR to ensure minimal miss-detection of the receiver.

Bessel-Notch Approximation

The filter parameters, which are the upper frequency (F_g) of constant group-delay of the Bessel filter and the quality factors (Q_1, Q_2) of the notch-filters, can be found numerically for a given N_T applying the optimization

$$\boldsymbol{\theta}_I = \arg\min_{\boldsymbol{\theta}} \frac{\int |H_T(f) - A(f, \boldsymbol{\theta})D(f)G(f, \boldsymbol{\theta})|^2 \, df}{\int |H_T(f)|^2 \, df}, \tag{3.56}$$

where $\boldsymbol{\theta}_I = \{F_g, Q_1, Q_2, \tau_g\}$ is the parameter vector and $G(f, \boldsymbol{\theta}) = e^{j2\pi f \tau_g}$ is a correction term for a constant group-delay difference between the ideal filter $H_T(f)$ and the approximation filter $A(f, \boldsymbol{\theta})D(f)$. The found filter parameters for $N_T = 2$ are listed in Tab. 3.4 for various filter orders. The impulse response, magnitude response, and the group delay of an example filter with filter order of eight can be seen in Figs. 3.19 – 3.21.

Table 3.4: *Analog filter parameters (F_g, Q_1, and Q_2) of the two different filter approximations for various filter orders N.*

N	Bessel-Notch Approx.			Bessel-Only Approx.
	F_g [MHz]	Q_1	Q_2	F_g [MHz]
1				39.9
2				60.9
3				72.3
4				80.2
5	82.3	1.0	2.2	86.5
6	157.8	0.7	2.4	91.9
7	236.9	0.6	1.9	96.8
8	254.5	0.6	1.9	101.4
9	277.4	0.6	1.8	105.8
10	293.3	0.6	1.8	110.1

Bessel-Only Approximation

Other filter approximations can be made too. A possibility is to reduce the combination of a lowpass filter and notch filters to a single Bessel type lowpass filter. Its upper frequency of constant group-delay F_g can be found for given N_T applying

$$F_g = \arg\min_{F_g} \frac{\int ||H_T(f)| - |A(f, F_g)D(f)||^2 \, df}{\int |H_T(f)|^2 \, df}, \tag{3.57}$$

which is a simplification of (3.56) due to lower degree of freedom. The found filter parameters are listed in Tab. 3.4 for various filter orders with $N_T = 2$. The impulse response, the magnitude response, and the group delay of an example filter with filter order of eight can be seen in Figs. 3.19 – 3.21. Surprisingly these approximations can lead to a better performance than the ideal sliding window integrator.

(a) Bessel-Notch approximation   (b) Bessel-Only approximation
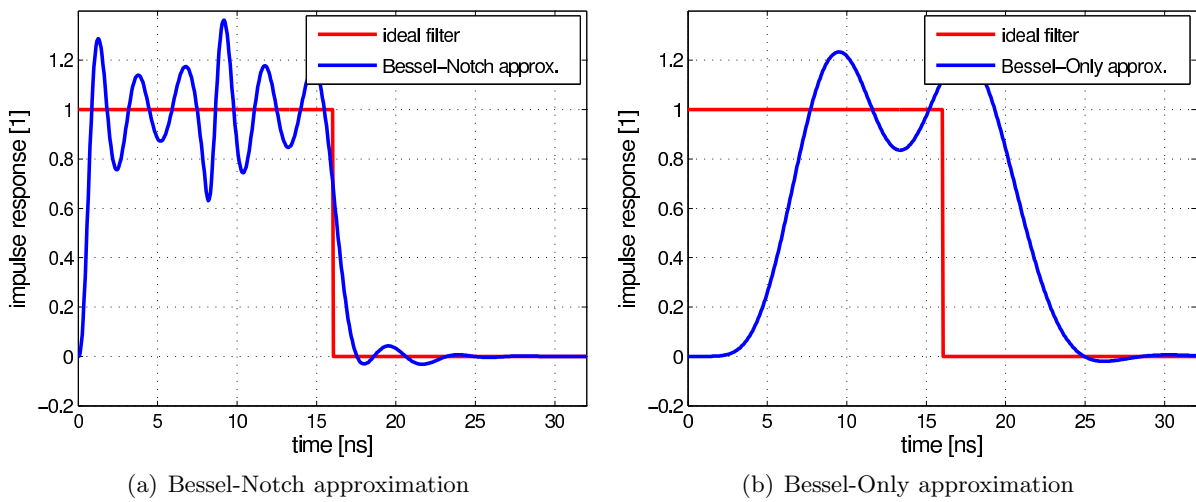
Figure 3.19: Impulse response of the Bessel-Notch approximation and Bessel-Only approximation sliding window integrator with 8th filter order.

(a) Bessel-Notch approximation   (b) Bessel-Only approximation
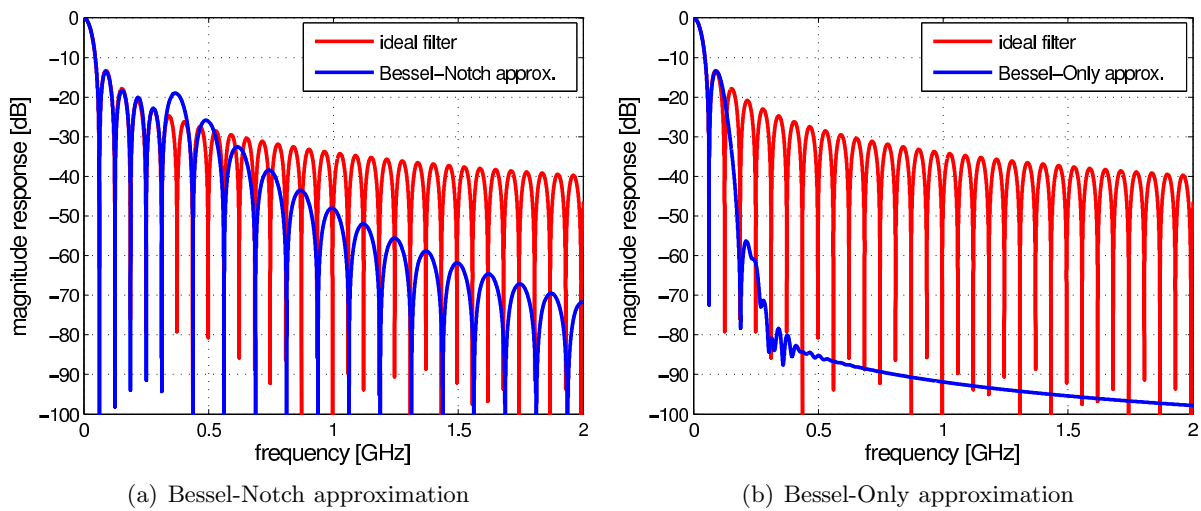
Figure 3.20: Magnitude response of the Bessel-Notch approximation and Bessel-Only approximation sliding window integrator with 8th filter order.

(a) Bessel-Notch approximation

(b) Bessel-Only approximation
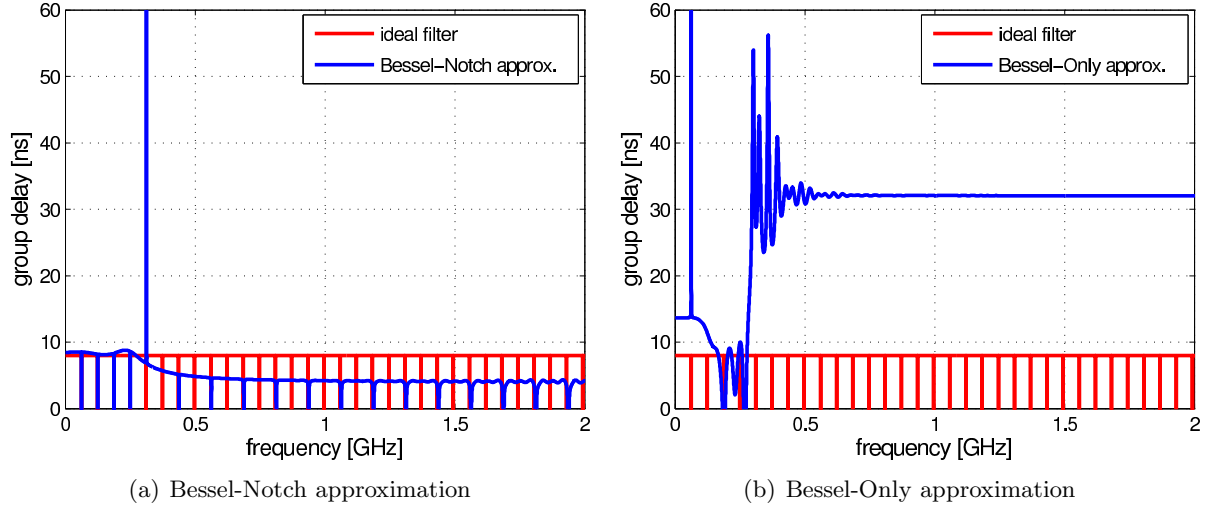
Figure 3.21: Group delays of the Bessel-Notch approximation and Bessel-Only approximation sliding window integrator with 8th filter order.

3.3.2 Analysis and System Simulations

To minimize erroneous detection of $\mathbf{d}$ (cf. Section 2.1), interference and noise have to be reduced. Because $\mathbf{d}$ is reconstructed by the linear transformation $\mathbf{W}$ of the receiver channel outputs $\mathbf{y}$, and M will be chosen only slightly greater than or equal to K for complexity reason, it is necessary to mitigate signal cross-terms and noise at the level of the receiver channel outputs $\{y_m\}$. These signal terms can be minimized by applying a lowpass filter.

When recalling (2.3) and assuming NOFDM as signaling scheme, the mth receiver front-end channel output y_m is given as

$$y_m = \int_{\lambda=0}^{T_{\text{sym}}} \left[\left(h_m(t) * c(t) * \Re \left\{ \sum_{k=1}^{K} d_k \varphi(t) e^{+j\left(k-\frac{K+1}{2}\right)\omega_{\text{sc}}t} e^{+j\omega_{\text{c}}t} \right\} \right) \right.$$
$$\left. \times \left(g_m(t) * c(t) * \Re \left\{ \sum_{l=1}^{K} d_l \varphi(t) e^{+j\left(l-\frac{K+1}{2}\right)\omega_{\text{sc}}t} e^{+j\omega_{\text{c}}t} \right\} \right) \right] dt + \nu_m. \tag{3.58}$$

Due to the lowpass behavior of the sliding window integration filter, the mth receiver channel output can be simplified to

$$y_m = \frac{1}{2} \sum_{k=1}^{K} \sum_{l=1}^{K} d_k d_l \int_{\lambda=0}^{T_{\text{sym}}} \Re \left\{ \tilde{\varphi}_{k,h_m} \tilde{\varphi}_{l,g_m}^* e^{+j(k-l)\omega_{\text{sc}}t} \right\} dt + \nu_m, \tag{3.59}$$

where

$$\tilde{\varphi}_{k,h_m} = \varphi(t) * \Re \left\{ (c(t) * h_m(t)) \, e^{-j\left(k-\frac{K+1}{2}\right)\omega_{\text{sc}}t} e^{+j\omega_{\text{c}}t} \right\} \tag{3.60}$$

and

$$\tilde{\varphi}_{l,g_m} = \varphi(t) * \Re \left\{ (c(t) * g_m(t)) \, e^{-j\left(l-\frac{K+1}{2}\right)\omega_{\text{sc}}t} e^{+j\omega_{\text{c}}t} \right\} \tag{3.61}$$

are the different subcarrier pulse shapes altered by their respective channel frequency band and their respective projection filters.

It can be seen from (3.59) that the signal co-terms terms (where $l = k$) map to baseband pulses.

A different behavior can be seen for the signal cross-terms (with $l \neq k$), where the baseband pulses are transformed to different frequencies $(k-l)\omega_{sc}$. In Fig. 3.22, the co- and cross-terms of a $K = 7$ subcarrier NOFDM signaling scheme are depicted in the frequency domain when using allpass projection filters[22] before integration. These cross-terms are undesired. Due to the fact that they are transformed to higher frequencies, they can be mitigated to a certain extent by the lowpass Bessel filter.
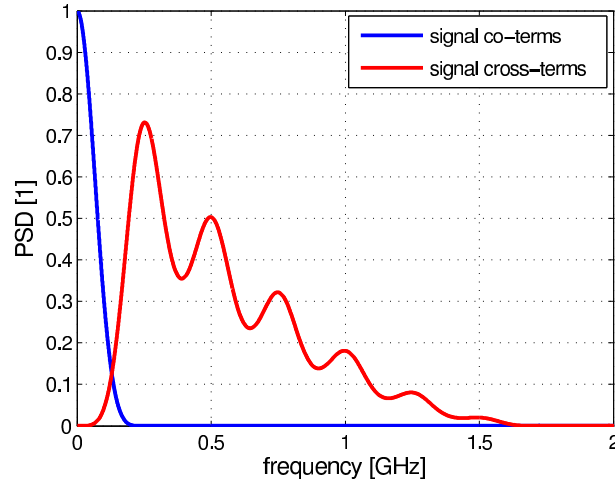
Figure 3.22: *Power spectrum density of the signal co- and cross-terms of an NOFDM transmission scheme after the multiplication in a ProjR channel for $K = 7$ subcarrier NOFDM signaling scheme.*

To investigate the performance of the various sliding window integrator approximations SINR and BER can be considered. The SINR and BER are depicted in Figs. 3.23 – 3.24. For comparison SNR and SIR can be found in Appendix D.3. It can be seen that the MC-ED and the MC-MFED are much more robust to nonidealities of the filters than MC-AcR. It can also be seen that an ideal sliding window integrator has the best SINR performance. This is obvious when considering its good SIR performance due the fact that the cross-terms should vanish completely for the ideal case. The SINR of the Bessel-Only approximation does show that offset of the slope differs depending on the filter order which is due to a different SNR. In contrast, the offset of the SINR slopes of the Bessel-Notch approximation are similar for the different filter orders. But it can be seen that for lower filter orders the SINR goes into saturation for the Bessel-Notch approximation, which is due to a lower SIR performance. The better SIR performance of the Bessel-Only approximation can be explained due to its steeper frequency response of the second approximation filter that attenuates the high-frequency parts (i.e. the cross-terms) more heavily. Note that both approximation methods are able to outperform the ideal sliding window integrator, due to the fact that the steeper filter slope of the Bessel filter is able to mitigate more noise than the the ideal sliding window filter.

---

[22] Allpass projection filters are e.g. given by the MC-AcR.
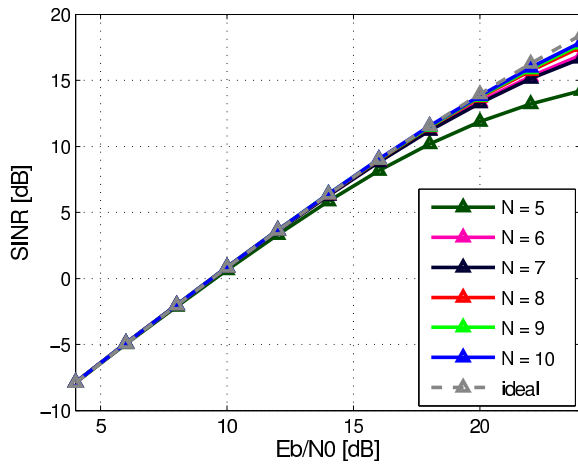
(a) SINR of MC-AcR with Bessel-Notch filter approximation.
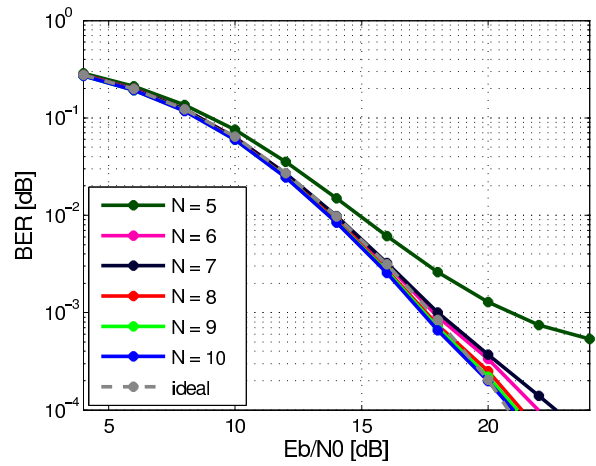
(b) BER of MC-AcR with Bessel-Notch filter approximation.
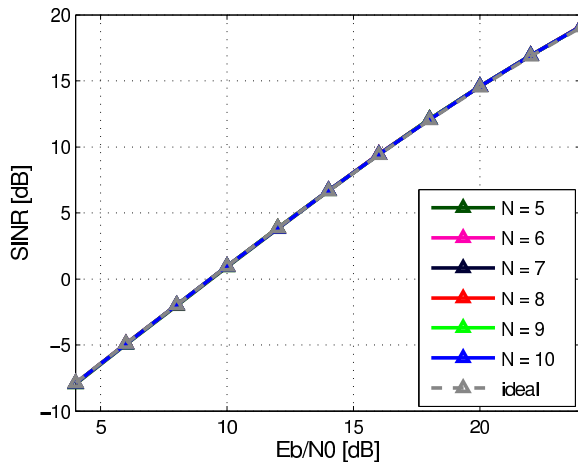
(c) SINR of MC-ED with Bessel-Notch filter approximation.
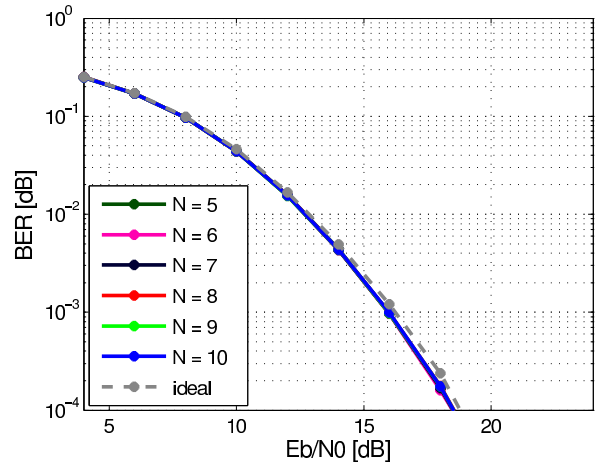
(d) BER of MC-ED with Bessel-Notch filter approximation.
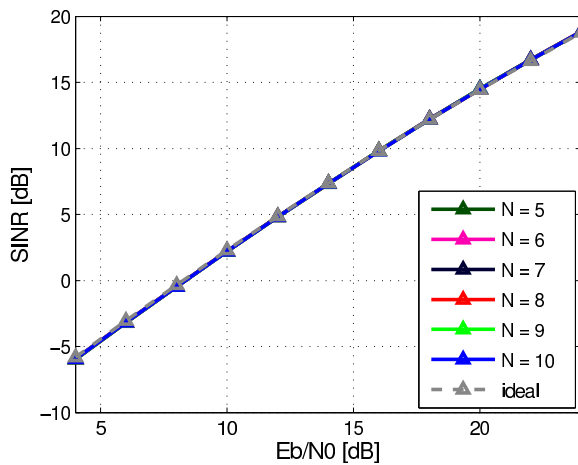
(e) SINR of MC-MFED with Bessel-Notch filter approximation.
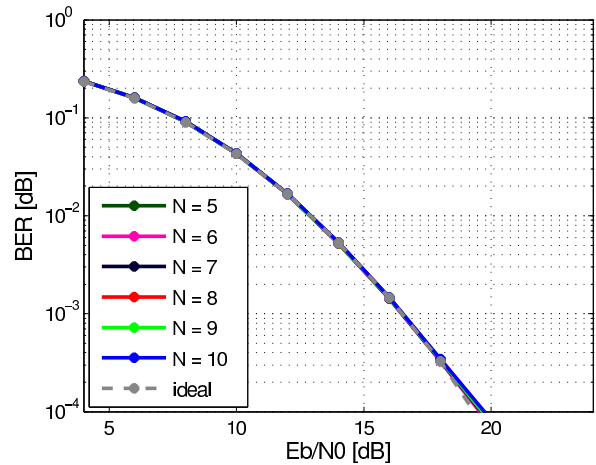
(f) BER of MC-MFED with Bessel-Notch filter approximation.

Figure 3.23: SINR and BER of various MC-ProjR architectures.
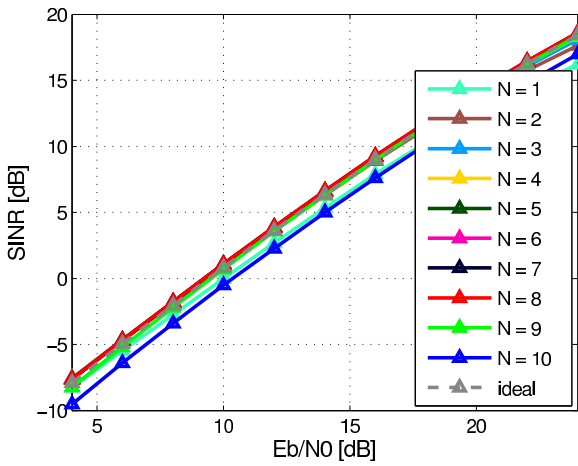
(a) SINR of MC-AcR with Bessel-Only filter approximation.
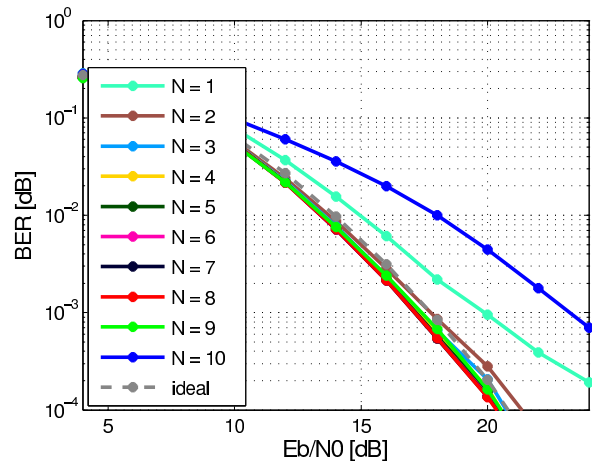
(b) BER of MC-AcR with Bessel-Only filter approximation.
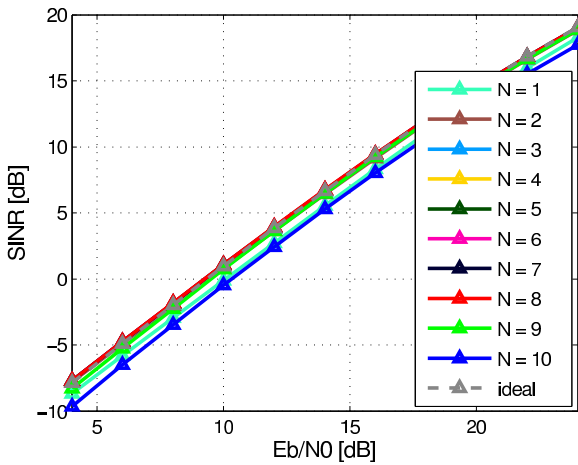
(c) SINR of MC-ED with Bessel-Only filter approximation.
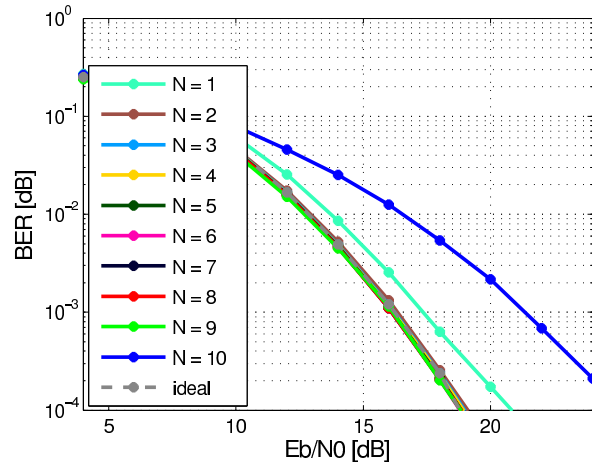
(d) BER of MC-ED with Bessel-Only filter approximation.
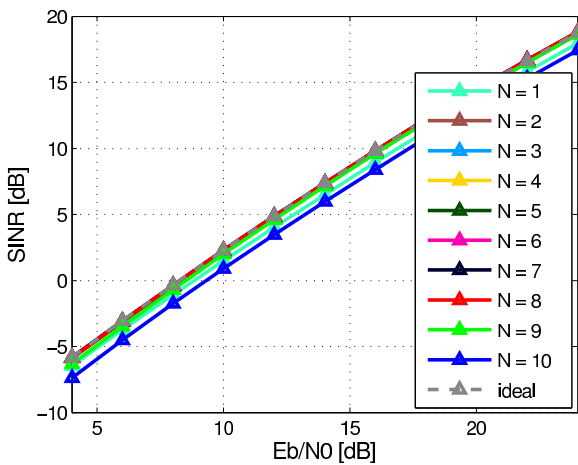
(e) SINR of MC-MFED with Bessel-Only filter approximation.
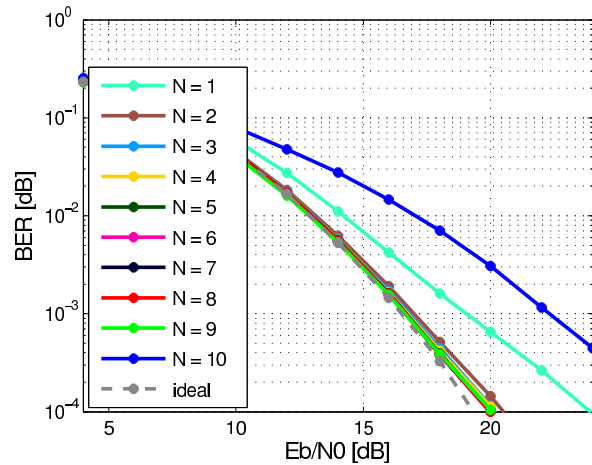
(f) BER of MC-MFED with Bessel-Only filter approximation.

Figure 3.24: SINR and BER of various MC-ProjR architectures.

3.4 Summary

In this Chapter the analysis of realistic front-end components has been presented. It has been shown that meta-heuristic optimization algorithms utilizing multi-objective cost-functions can be used to obtain projection filter cross-spectra $\left\{ X_m \left(e^{j\Omega} \right) \right\}$. It has been shown that the found filter solutions result in cond $\{\mathbf{P}\} \approx 20$ and that cross-spectra of 2nd order are sufficient to achieve similar BER than the MC-AcR reference receiver.

To analyze the influence of realistic analog multipliers a Wiener Hammerstein MISO model has been proposed. Such a model consists of linear time-invariant input and output filters and a static bivariate polynomial to model the inherent nonlinear effects. Also an identification method based on single-tone and UWB measurements has been described to obtain the model parameters from measurements and circuit-level simulations. The obtained models were verified and it has been shown that the proposed identification method does result in accurate models of an analog multiplier designed by Ulm University. Furthermore, it has been shown that undesired nonlinear terms (e.g. of fourth and sixth order), which depend on the power of the multiplier input signals, strongly influence the receiver performance. For the given UUlm UWB mixer, the mixer input power should not exceed -25 dBm. It has been shown that the MC-ED and the MC-MFED receivers are robust to those undesired effects in contrast to the MC-AcR.

Approximations of sliding window integrators have been studied. It has been shown that a mixed-signal approach gives a trade-off between analog filter complexity and digital sampling rate. In fact, approximations which utilize analog Bessel lowpass filters, with and without additional analog notch filters, are able to outperform receivers with ideal sliding window integrators in terms of BER. This is due to the steeper filter slope of the Bessel filter which can mitigate more noise in comparison to the ideal sliding window filter.

4

Enhanced Signal Detection of Nonlinear Memoryless MIMO Channels

Due to the nonideal nature of analog multiplication devices, the signal detection suffers from undesired higher-order nonlinear signal content. To conquer this problem, a nonlinear multiple-input-multiple-output (MIMO) model can be identified and post-correction methods can be applied to enhance signal detection. In [107] and [108] maximum likelihood detectors for nonlinearly distorted multi-carrier systems are proposed. These approaches use an iterative detection to correct memoryless nonlinear distortion present in transmitter amplifiers and assume AWGN after the distortions, which can not be assumed for noncoherent multi-channel receivers. In contrast, [109] proposes a polynomial MIMO model for OFDM communication systems which incorporates a linear MMSE detector and uses an iterative post-correction to mitigate the nonlinear effects despite noise characteristics. In addition [110] proposes a neural network modeling and identification approach for nonlinear MIMO channels. None of the aforementioned works do model nonlinear cross-term effects between the MIMO channels which are fundamentally present when using NOFDM signaling for noncoherent multi-channel receivers.

This chapter proposes a least-squares method to estimate the nonlinear MIMO channel including cross-term effects and to enhance signal detection.

4.1 Identification of Nonlinear Memoryless MIMO Channels

Identification of the analog receiver front-end as a whole for ISI free communication channels can be done using a respective training symbol sequence at the input of the receiver. As stated in Section 3.2.5 the system model in vector notation is given as

$$\mathbf{y} = \mathbf{M}\bar{\bar{\mathbf{d}}} + \boldsymbol{\nu}, \tag{4.1}$$

where $\bar{\bar{\mathbf{d}}} = \left[1, \mathbf{d}^H, (\mathbf{d} \otimes \mathbf{d}^*)^H, \bigotimes_3 \{\mathbf{d}\}^H, \cdots, \bigotimes_U \{\mathbf{d}\}^H\right]^H$, $\mathbf{M}$ is the nonlinear memoryless MIMO receiver model, and U is the maximum order of the nonlinearity. To identify the receiver means to estimate $\mathbf{M}$.

The estimation of $\mathbf{M}$ can be done using a least squares approach. Consider sending and receiving N different symbols, hence sending the $K \times N$ symbol matrix $\mathbf{T}$ and obtaining observation matrix

$$\mathbf{Y} = \mathbf{M}\bar{\bar{\mathbf{T}}} + \mathbf{N}, \tag{4.2}$$

where the columns $\{\bar{\bar{\mathbf{t}}}_n\}$ of $\bar{\bar{\mathbf{T}}}$ are given as $\bar{\bar{\mathbf{t}}}_n = \left[1, \mathbf{t}_n^H, (\mathbf{t}_n \otimes \mathbf{t}_n^*)^H, \bigotimes_3 \{\mathbf{t}_n\}^H, \cdots, \bigotimes_U \{\mathbf{t}_n\}^H\right]^H$, and $\mathbf{N}$ consist of all undesired terms. The vector $\mathbf{t}_n$ resembles the nth column of the symbol matrix $\mathbf{T}$. The estimated nonlinear MIMO matrix $\hat{\mathbf{M}}$ is therefore given as

$$\hat{\mathbf{M}} = \mathbf{Y}\bar{\bar{\mathbf{T}}}^\dagger. \tag{4.3}$$

Sufficient rank of $\mathbf{Y}$ and $\bar{\bar{\mathbf{T}}}$ is important, i.e. the rows of $\bar{\bar{\mathbf{T}}}$ need to be linearly independent so that $\bar{\bar{\mathbf{T}}}\bar{\bar{\mathbf{T}}}^H$ is invertible and $\bar{\bar{\mathbf{T}}}^\dagger$ exists. Simple OOK or PPM modulation where the symbols d_k are limited to $\{0, 1\}$ do not comply with this prerequisite as they cannot assure linearly independent vectors $\{\bar{\bar{\mathbf{t}}}_n\}$. Using ASK symbols (positive and negative) and a sufficient long training sequence is inevitable. To ensure proper estimation of $\hat{\mathbf{M}}$, the condition number of $\bar{\bar{\mathbf{T}}}$ needs to be as small as possible. In Fig. 4.1 the dependency of rank and condition number of the number of ASK levels for different U is shown. The length of the sequence was chosen to be 5000 symbols. It can bee seen that trainings sequences with higher number of ASK levels the condition number does decrease. An exception is $U = 1$, whereas the condition number increases. In Fig. 4.2 the dependency of rank and condition number of the length of the trainings sequence for different U is shown, where the number of ASK levels was set according to the minimum number of ASK levels listed in Tab. 4.1. It can be seen that increasing sequence lengths for a given U, the condition number does decrease. In Tab. 4.1 the minimal ASK levels and the minimal sequence length to obtain full rank are listed.

Table 4.1: *Minimum number of ASK levels and length of trainings sequence to fulfill sufficient rank and low condition number.*

U	min. ASK levels	min. length
1	2	8
2	3	36
3	4	120
4	5	330
5	6	792
6	7	1716

(a) Rank of matrix $\bar{\bar{T}}$.

(b) Condition number of matrix $\bar{\bar{T}}$.
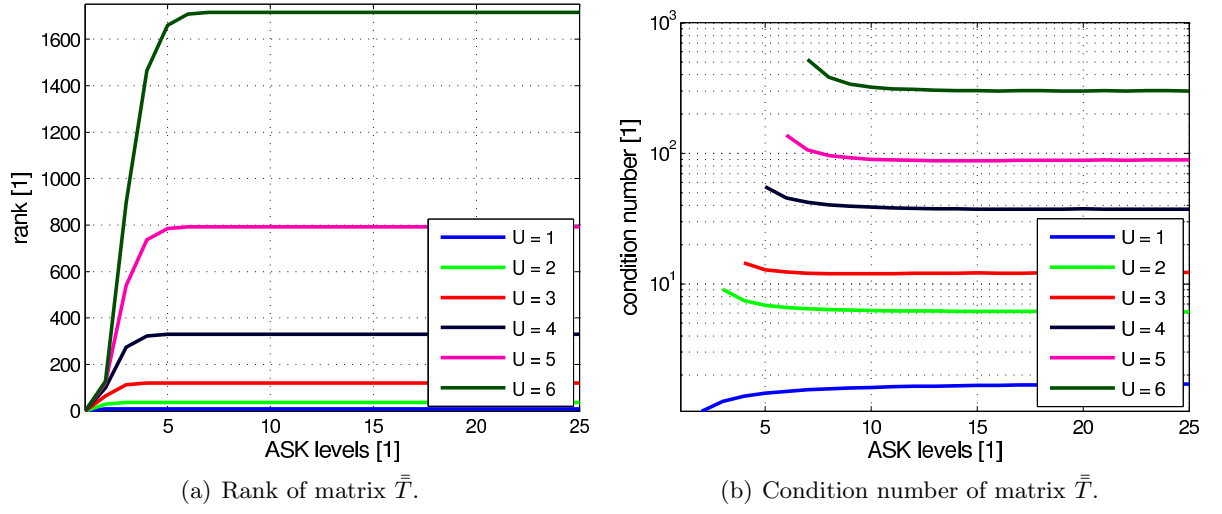
Figure 4.1: Rank and condition number of matrix $\bar{\bar{T}}$ for various ASK levels and order U of nonlinearity.

(a) Rank of matrix $\bar{\bar{T}}$.

(b) Condition number of matrix $\bar{\bar{T}}$.
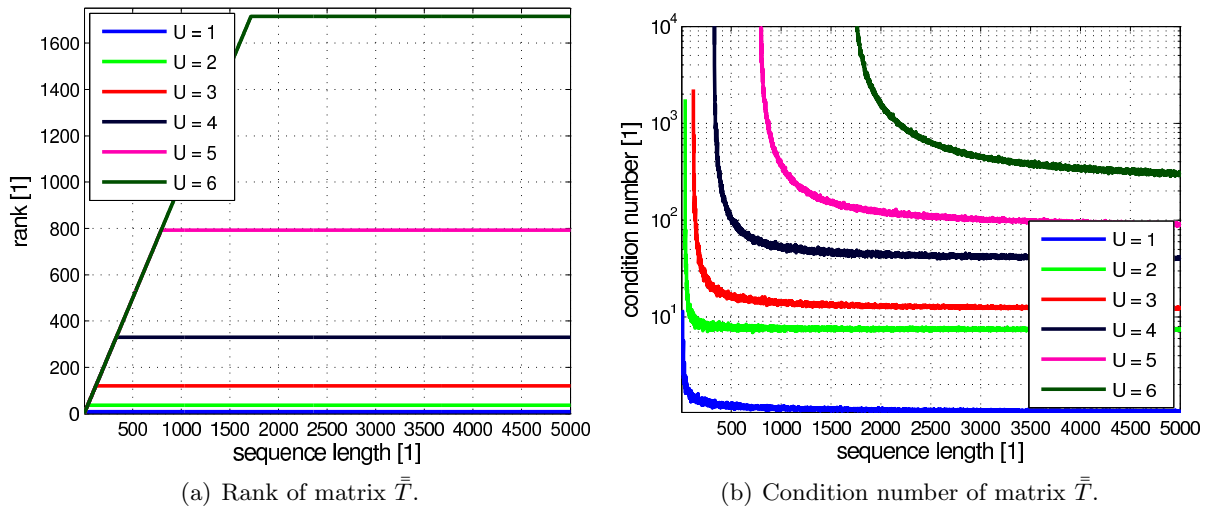
Figure 4.2: Rank and condition number of matrix $\bar{\bar{T}}$ for various sequence lengths and order U of nonlinearity.

4.2 Enhanced Signal Detection

When considering the nonlinear MIMO model identification in Section 4.1 the detection can be enhanced by estimating the nondesired and nonideal signal content. This can be done by incorporating the estimated nonlinear MIMO matrix $\hat{\mathbf{M}}$.

Consider the front-end output vector

$$\mathbf{y} = \mathbf{M}\bar{\bar{\mathbf{d}}} + \boldsymbol{\nu}. \tag{4.4}$$

Detection means to estimate $\bar{\bar{\mathbf{d}}}$ as good as possible. Signal detection can be done in the minimum-distance sense, which means to find $\mathbf{d}$ which obtains the smallest error, hence

$$\hat{\mathbf{d}} = \arg \min_{\mathbf{d}} \left\{ \left(\mathbf{y} - \hat{\mathbf{M}}\bar{\bar{\mathbf{d}}} \right)^H \left(\mathbf{y} - \hat{\mathbf{M}}\bar{\bar{\mathbf{d}}} \right) \right\} \tag{4.5}$$

$$= \arg \min_{\mathbf{d}} \left\{ \mathbf{y}^H \mathbf{y} - \bar{\bar{\mathbf{d}}}^H \hat{\mathbf{M}}^H \mathbf{y} - \mathbf{y}^H \hat{\mathbf{M}}\bar{\bar{\mathbf{d}}} + \bar{\bar{\mathbf{d}}}^H \hat{\mathbf{M}}^H \hat{\mathbf{M}}\bar{\bar{\mathbf{d}}} \right\} \tag{4.6}$$

$$= \arg \min_{\mathbf{d}} \left\{ \bar{\bar{\mathbf{d}}}^H \hat{\mathbf{M}}^H \hat{\mathbf{M}}\bar{\bar{\mathbf{d}}} - 2\bar{\bar{\mathbf{d}}}^H \hat{\mathbf{M}}^H \mathbf{y} \right\} \tag{4.7}$$

To proof the enhanced detection method, exemplarily the BER is shown for the MC-AcR with a nonideal multiplier model (see Section 3.2) in Fig. 4.3. The operating point of the multipliers were set to -15 dBm and -20 dBm, respectively. It can be seen that by using the enhanced signal detection for -20 dBm mixer input power with $U = 2$, and a trainings sequence with 3 ASK levels and a length of 4000 symbols, the BER can be minimized. To achieve a BER of 10^{-3} the enhanced signal detection method requires 2.5 dB less E_b/N_0. For lower BER the difference of required E_b/N_0 increases, e.g. for a BER of $5 \cdot 10^{-4}$ about 4.5 dB less E_b/N_0 is required. For a mixer input power of -15 dBm a model of $U = 6$ is needed. With a trainings sequence of 7 ASK levels and a length of 12000 symbols the BER can only be minimized for a $E_b/N_0 > 19$ dB.
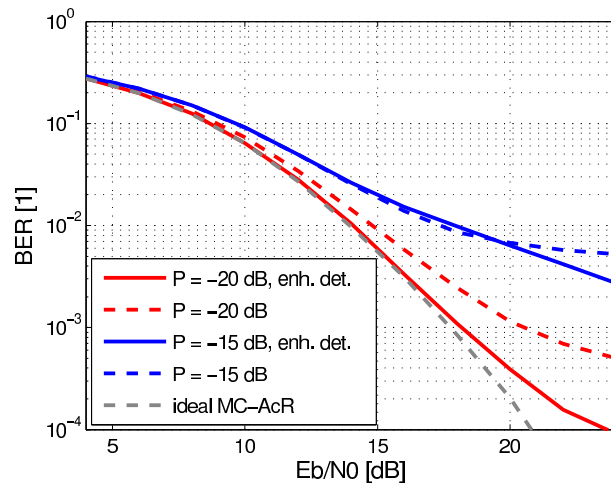
Figure 4.3: BER of the non-enhanced and enhanced detection with mixer input power of -20 dBm ($U = 2$, 3 ASK levels, 4000 symbols) and -15 dB ($U = 6$, 7 ASK levels, 12000 symbols).

4.3 Summary

In this Chapter a method to identify the nonlinear memoryless MIMO channel of noncoherent multi-channel receivers for ISI free scenarios has been proposed. The method is based on the least-squares estimation using a trainings sequence with ASK symbols. The minimum number of ASK levels and minimum sequence length was depicted.

Using the identified nonlinear memoryless MIMO channel, a minimum-distance based enhanced detection method has been proposed. It has been shown that method is able to reduce the BER of an MC-AcR with a nonideal multiplier model.

5

A Hardware Example

This chapter shows an actual hardware implementation of a noncoherent multi-channel receiver architecture: an UWB multichannel autocorrelation receiver (MC-AcR). The hardware specification, design, and validation was part of the *NOFDM - Noncoherent Orthogonal Frequency Division Multiplexing* project funded by the Autrian Research Promotion Agency (FFG) under grant 825899. Project partners were, next to *Signal Processing and Speech Communication Laboratory* of the *Graz University of Technlology*, who were responsible for the project management, system engineering, signal processing, and algorithm design, *EPCOS OHG* (in the following referred to as *EPCOS*) who were responsible for the design, production, and validation of the custom-made low-temperature cofired ceramics (LTCC) filter, *XERXES Electronics GmbH* (in the following referred to as *XERXES*) who were responsible for the design, production, assembly, and validation of the printed circuit boards (PCB), and *xFace e.U.* (in the following refered to as *xFace*) who were responsible for the digital design and validation of a field-programmable gate-array (FPGA) used for data acquisition and streaming of the captured data.

5.1 Multichannel Autocorrelation Receiver Hardware Architecture

An overview of the realized MC-AcR architecture is shown in Fig. 5.1. The target signaling was an NOFDM signaling scheme as specified in Tab. 2.1. The receiver was hence specified to consist of eight autocorrelation channels: four channels compute a short time estimate of the received *in-phase* (I) signal for four different delay lags $\{\tau_1 = 0.5 \text{ ns}, \tau_2 = 1.0 \text{ ns}, \tau_3 = 1.5 \text{ ns}, \tau_4 = 2.0 \text{ ns}\}$, and four channels compute a short time estimate of the received *quadrature-phase* (Q) signal of the same delay lags $\{\tau_1, \tau_2, \tau_3, \tau_4\}$. The I- and Q-signals are generated using delay lines with $\tau_I = 0.45 \text{ ns}$ and $\tau_Q = \tau_I + \frac{1}{4f_c} = 0.5125 \text{ ns}$ delay[23], respectively. The receiver front-end output signals are sampled with double the symbol rate with a resolution of 14 bit. The actual hardware consists of an *RF board* and a *DSP board*.

1. **RF board**: After signal reception with the UWB antenna, the received signal is filtered by a band-selection filter (BP) and amplified with a low-noise amplifier. These two devices were not part of the hardware design process. The amplified signal is then split into two signals using a resistive power splitter. Each signal branch can be attenuated (*PE43602* in Fig. 5.1) and gets amplified (*HMC311SC70*) individually to change the operating point of the receiver. The delay lags, the I-signal, and the Q-signal are produced by filtering the amplified received signal with UWB delay filters (*EPCOS NOFDM LTCC*). The multiplication of the I-signals or Q-signals with delayed versions of themselves is done by UWB multiplication devices (*UUlm UWB Mixer*). After multiplication, the resulting signals are amplified (*AD4950*) and filtered using a Bessel lowpass filters of 5th order with cut-off frequency of 86.5 MHz. Cables with SMB connectors are used to connect the RF board with the DSP board. The connector to the antenna is an SMA connector. Following is the list of the used RF board components which play a role in the signal path:

   - Peregrin Semiconductor *PE43602* [111]: digital RF attenuator, frequency range from 9 kHz up to 5 GHz, attenuation range from 0 dB to 31.5 dB in 0.5 dB steps, insertion loss of 2.2 dB.

   - Hittite *HMC311SC70* [112]: amplifier with a gain of 15 dB, frequency range from 0 Hz up to 8 GHz, noise figure is 5 dB.

   - *EPCOS NOFDM LTCC*: delay lag filters, frequency range from 3 GHz up to 5 GHz, loss between -9 dB and -25 dB.

   - *UUlm UWB Mixer* [98]: UWB multiplier, input frequency range from 3 GHz up to 11 GHz for both input ports, first-order output lowpass filter with cut-off frequency of 900 MHz, adds additional output noise of -68 dBm.

   - Analog Devices *AD4950* [113]: buffer amplifier with a gain of 4.8 dB, frequency range from 0 Hz up to 750 MHz, output voltage noise density of $9.2 \text{ nV}/\sqrt{\text{Hz}}$ (hence a noise figure of 26 dB).

   - *Bessel 5th*: 5th order Bessel lowpass filter, cut-off frequency of 86.5 MHz.

2. **DSP board**: The input of the DSP board is a buffer stage (*ADA4938*). After the buffer, the signals are converted into digital domain using an analog-to-digital converter (ADC; *AD9640*). The sampling rate is 125 MHz with an amplitude resolution of 14 bit. The sampled signals are fed to an FPGA (*XC6SLX150*) which is responsible for data acquisition and streaming of the captured data to a host PC. A Gigabit Ethernet transceiver (PHY; *VSC8641*) is responsible for the data handling on of the Ethernet interface. The host PC functions as data sink and handles the digital signal processing algorithms as equalization

---

[23] Actually planned target delays were $\tau_I = 0$ ps and $\tau_Q = 62.5$ ps which unfortunately could not be met during the LTCC design process. For all channels an additional delay was added due to the power splitters.
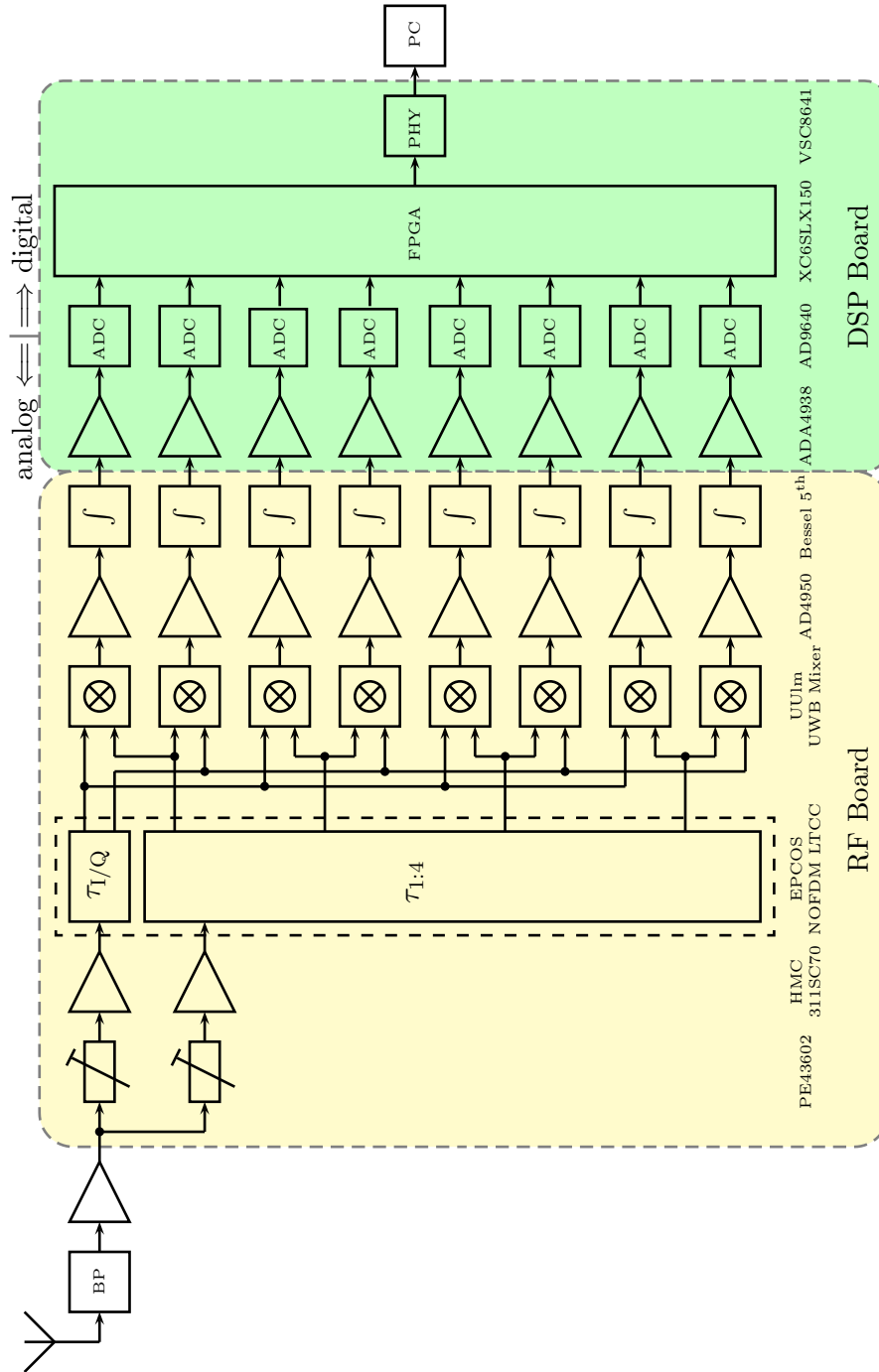
Figure 5.1: Signal flow graph of the NOFDM MC-AcR hardware architecture.

and signal detection. Following is the list of the used DSP board components which play a role in the signal path:

- Analog Devices *ADA4938* [114]: low-distortion amplifiers used as buffers with gain of 0 dB, frequency range from 0 Hz up to 1 GHz, noise figure of 26 dB.

- Analog Devices *AD9650* [115]: ADC, resolution of 14 bits (effective number of bits is 11.6 bits), sampling rate of 125 Msamples/s, frequency range from 0 Hz up to 650 MHz.

- Xilinx *XC6SLX150* [116]: FPGA, clock frequency of 150 MHz.

- Vitesse *VSC8641* [117]: Gigabit Ethernet transceiver.

Both, RF and DSP board (see Fig. 5.2), were designed, produced, and tested by *XERXES*.
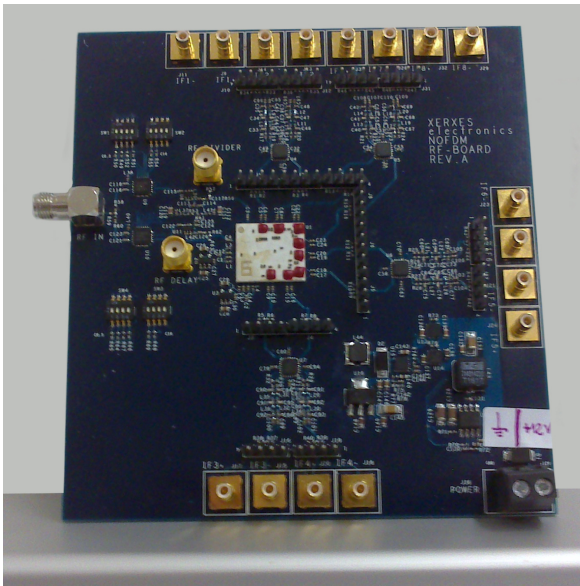
(a) RF-board

(b) DSP-board

Figure 5.2: Photographs of the RF- and DSP-board of the NOFDM MC-AcR.

5.2 Power and Noise Budget

In Tab. 5.1 the power-and noise-budget of the NOFDM receiver is shown. The maximal transmit output power was set to be −9 dBm according to the FCC regulations for UWB communications [25]. The channel loss was assumed to be between 40 dB and 60 dB, which represents a distance between transmitter and receiver between 5 cm and 50 cm, respectively, according to the Friis transmission equation [118]. For the used bandwidth of 2 GHz the noise power at the receiver antenna is given as −80.97 dBm [119]. After band selection filtering, a cascade of low-noise amplifiers and tunable attenuators give the possibility to set the operation point of the multipliers, hence the power of the multiplier input signals. The operation point of the multipliers is the most critical specification of the receiver hardware. If the multiplier input signals are chosen too low, the noise added by the multipliers would minimize the system SINR. If the multiplier input signals are chosen too high, e.g. higher than −20 dBm, the multiplier introduce much undesired signal content to their output signal (cf. Section 3.2.5).

Device		TX	Channel	Band Pass Filter	Low Noise Amp.	Power Splitter	Atten.	Amp.	Delay Line Filter	Multiplier	Amp.	Filter	Buffer	ADC
Device							PE43602	HMC 311SC70	EPCOS NOFDM LTCC	UULm UWB Mixer	AD4950	5th order Bessel	AD4938	
Gain [dB]	min.		-60				-31.5		-25					
	typ.		-50	-1	50	-3	-16	15		20	4.77	-3	0	
	max.		-40				0		-9					
Noise Figure [dB]	typ.		0	1	5	3	16	5	15	1.6	26	3	26	
Bandwidth [GHz]	typ.		2	2	2	2	2	2	2	0.9	0.75	0.1	0.1	
Signal Power [dBm]	min.		-69	-70	-20	-23			-39	-46	-41.23	-44.23	-44.23	-44.23
	typ.	-9	-59	-60	-10	-13	-29	-14						
	max.		-49	-50	0	-3			-23	-28	-23.23	-26.23	-26.23	-26.23
Noise Power Density [dBm/Hz]	min.								-147.98	-153.04	-142.04	-145.04	-143.26	-143.26
	typ.		-173.98	-173.98	-118.98	-121.98	-137.98	-122.98						
	max.								-131.98	-136.94	-131.84	-134.84	-134.63	-134.63
Noise Power [dBm]	min.								-54.97	-61.35	-52.67	-64.42	-62.84	-62.84
	typ.		-80.97	-80.97	-25.97	-28.97	-44.97	-29.97						
	max.								-38.97	-44.40	-40.26	-52.01	-51.90	-51.90

Table 5.1: Power- and noise-budget of the NOFDM MC-AcR.

The hardware design was chosen to allow tuning of the two multiplier input signals independently from each other, to be able to set different operating points for their input signal powers. The eight multipliers have different input powers due the different attenuation of the LTCC filters. The output SINR of the analog-front-end channels is given between 18.8 dB and 25.67 dB. An optional 15 dB amplification of the signals before the ADCs would be beneficial to ensure a full swing of the ADCs but were neglected due to the fact, that the 14 bit of the ADCs enable the reveicer to handle a high dynamic range.

5.3 LTCC Delay Filters

The delay line filters were designed and produced by *EPCOS* as one integrated system using low-temperature cofired ceramics (LTCC) technology. The LTCC technology is capable of providing highly integrated passive components as e.g. filters, power couplers, resonators with low resistive and dielectric loss, good thermal conductivity, and high working temperature [120]. LTCCs consist of many layers of ceramics used as insulators and silver used as conductor. Using these layers it is possible to build lumped 3D elements as inductors or capacitors. Other components as resistors or active devices can be mounted on top of the LTCC device using soldering, wire bonding or using controlled collapse chip connection[24]. So called *thermal vias* can be used to enhance heat transportation for mounted active components [121].
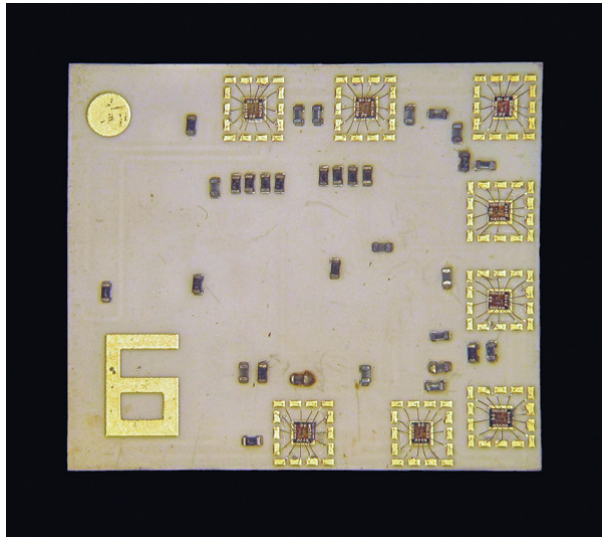
Figure 5.3: Photograph of the realized MC-AcR LTCC module with eight mounted UUlm UWB mixers.

The different delay line filters of the LTCC have a bandwidth of 2 GHz and due to the power splitters do attenuate the signal between 10 dB and 25 dB (see Fig. 5.4). The LTCC design was split into two parts. The first part consists of the delay filters with delays of $\{\tau_1, \tau_2, \tau_3, \tau_4\}$ (see Fig. 5.5(a)). The second part consists of delay filters with four delays of τ_I and four delays of τ_Q (see Fig. 5.5(b)). The LTCC was designed to serve as substrate where the eight UUlm mixer dies are bonded onto, to form a system-in-package (SiP). In Fig. 5.3 a photograph of an actual LTCC module is depicted. Note the eight mixer dies and their wire bonding. In Fig. 5.6(a) the correlation matrix of the LTCC filter cross-spectra is depicted. It can be seen that the channels CH7 and CH8 are very similar to each other, but also CH1 and CH2 do have a high correlation coefficient. This might explain the 2 dB E_b/N_0 loss of the BER shown in Fig. 5.7 compared to

---

[24] The controlled collapse chip connection is also known under the name *flip chip*.

the BER of an ideal MC-AcR. This result was obtained by system simulations using frequency response simulations of the LTCC by *EPCOS*.

(a) LTCC part 1   (b) LTCC part 2
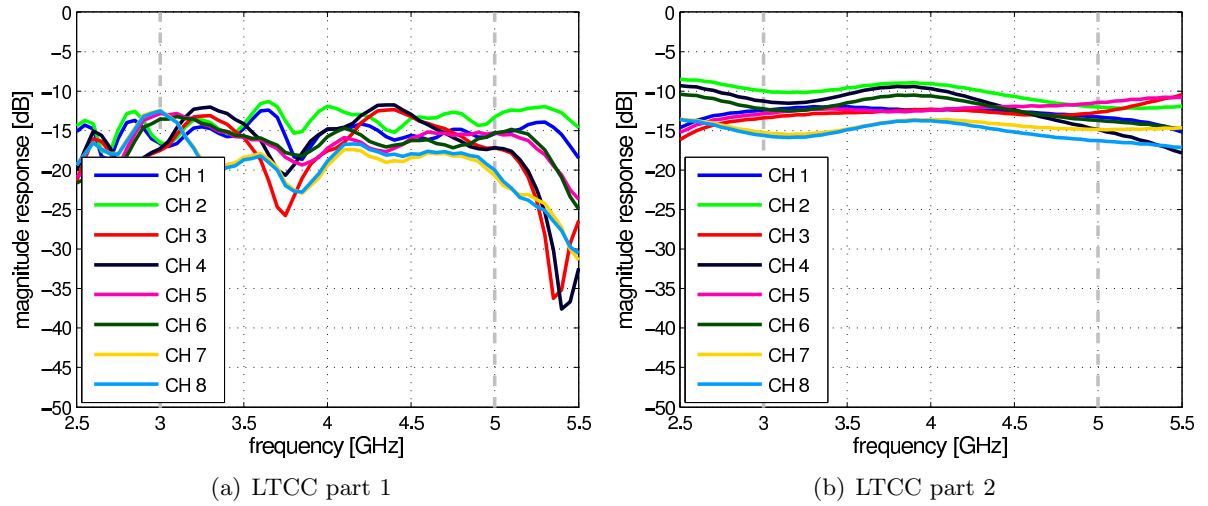
Figure 5.4: Magnitude response of the LTCC delay line filters.

(a) LTCC part 1   (b) LTCC part 2
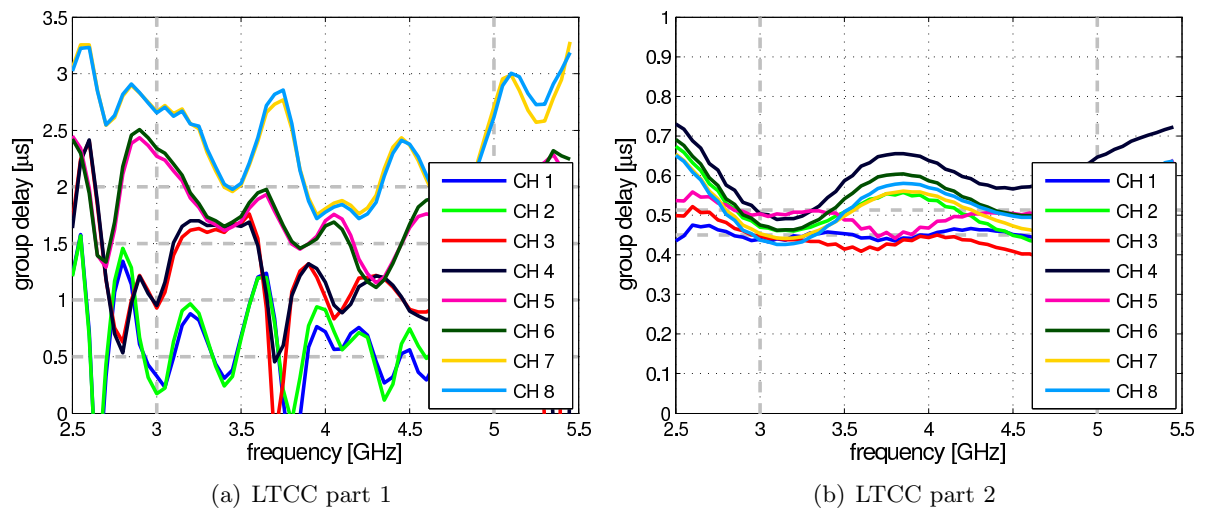
Figure 5.5: Group delay of the LTCC filters.

(a) Cross-spectra correlation matrix

(b) Signal co-term matrix
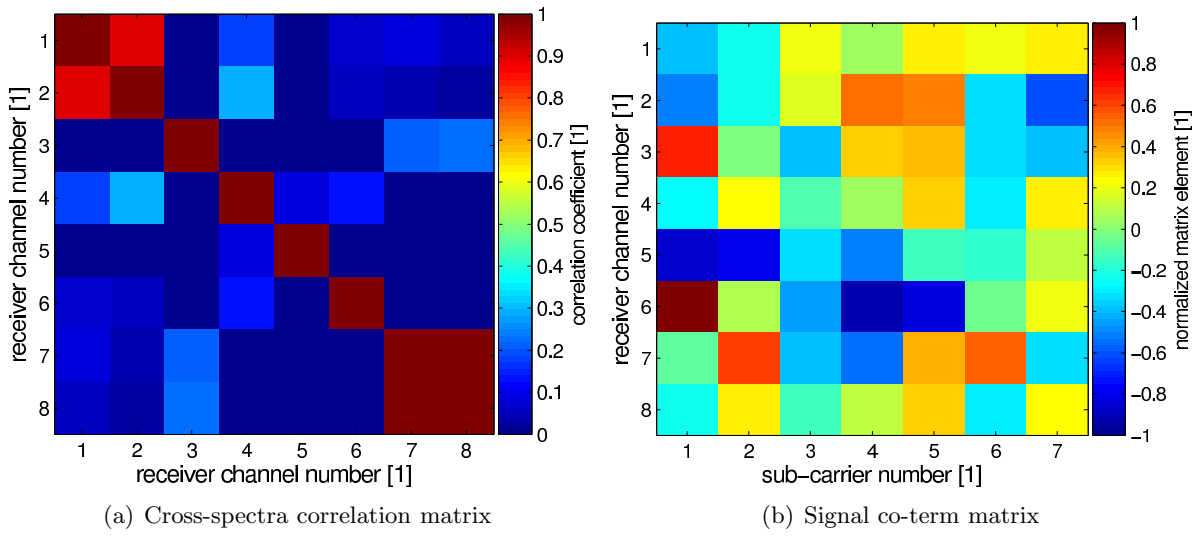
Figure 5.6: Correlation matrices of the LTCC filter cross-spectra and signal co-term matrix $\mathbf{P}$ (cond $\{\mathbf{P}\}$ = 13.86) for $M = 8$ channels.

(a) SINR

(b) BER
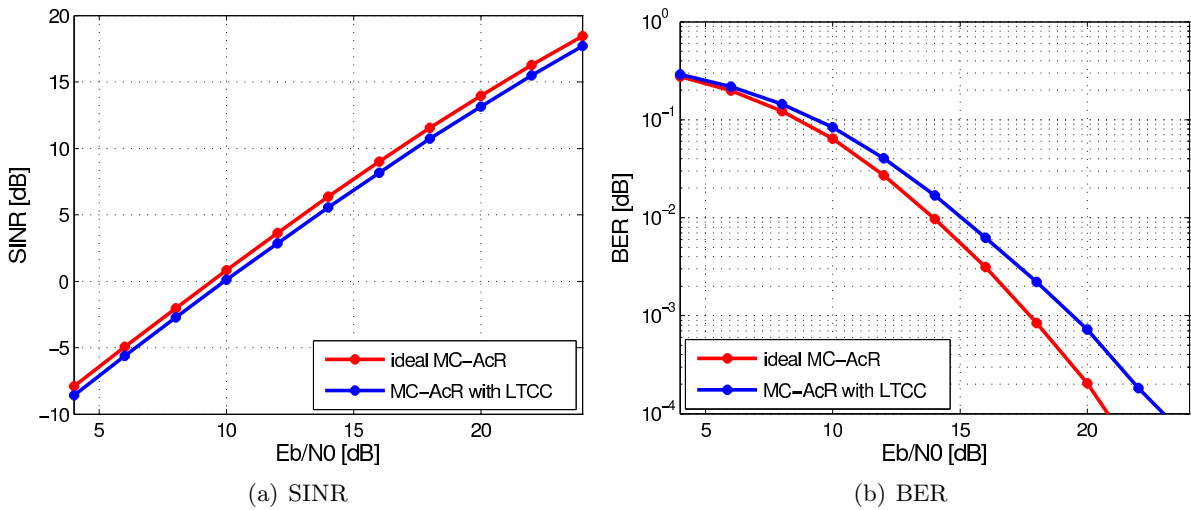
Figure 5.7: SINR and BER of the MC-AcR with LTCC filters.

5.4 UWB Multiplication Devices

The UWB multiplication devices were designed by Ulm University [98, 99]. They were designed to perform a multiplication operation for a UWB correlation receiver [100] that supports the full UWB frequency range from 3.1 GHz to 10.6 GHz defined by the FCC [25]. It has been manufactured using Telefunken Semiconductor's Si/SiGe2 heterojunction bipolar transistor (Si/Ge2 HBT) technology [101]. As seen in its schematic Fig. 3.7, it consists of two active single-ended-to-differential converter input stages (baluns), biasing circuitry, a four-quadrant Gilbert cell multiplier, and an output buffer stage with a lowpass filter. In Fig. 5.8 a micrograph of an actual mixer die is shown. In the realized MC-AcR design, the mixer dies are wire bonded onto the LTCC module to form a SiP. Detailed description on the operation of the device is given in Section 3.2 and [98].
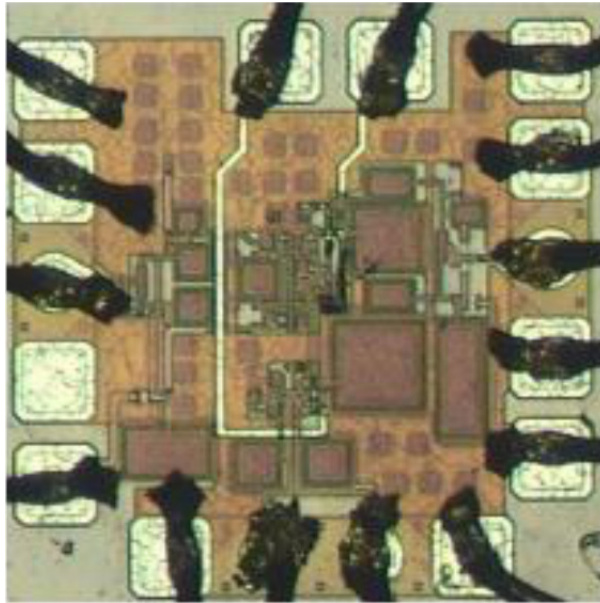
Figure 5.8: Micrograph of the UWB mixer die designed by Ulm University. (Picture taken from [99].)

5.5 Mixed-Signal Integrators

The sliding window integration operation is done using a mixed-signal approach discussed in Section 3.3 and [122]. The operator consists of a 5th order Bessel lowpass filter with a cut-off frequency of 86.5 MHz in analog-domain and two-tap comb filter in digital-domain. The impulse response and frequency response of the concatenated mixed-signal sliding window filter are shown in Fig. 5.9.

(a) Impulse response.

(b) Frequency response
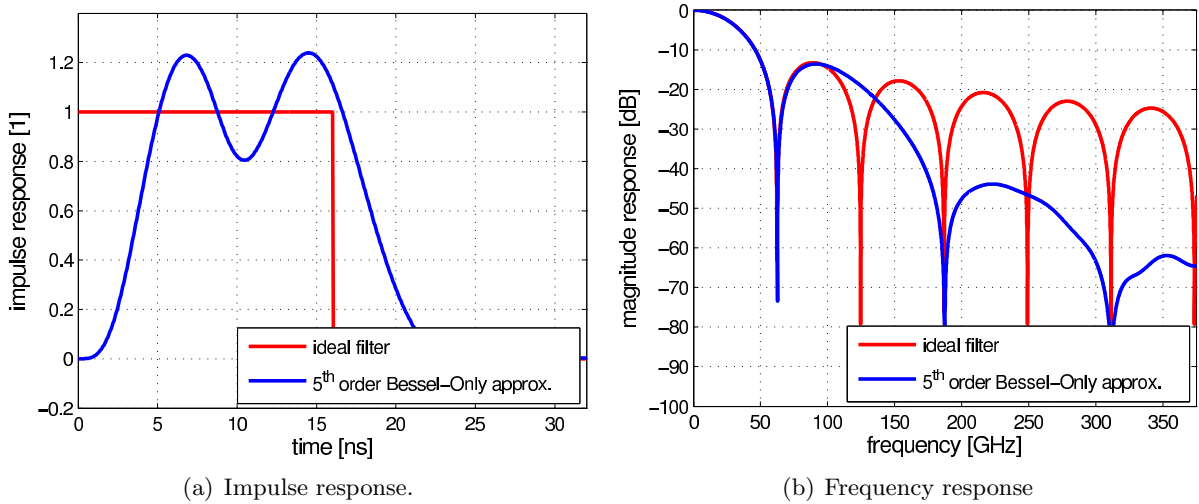
Figure 5.9: The mixed-signal impulse and magnitude response of the sliding window integration filter.

5.6 Digital Processing

After analog processing in the RF front-end, the processed signals are sampled using a 14 bit ADC and a sampling rate of 125 MHz, which is the double symbol rate $1/T_{\text{sym}}$. The digital design on the FPGA, which was designed by *xFace*, is able to perform a raw-data packet streaming of the ADC data output to a host PC using gigabit ethernet. The FPGA handles all the network protocols as address resolution protocol (ARP) and transmission control protocol of the internet protocol suite (TCP/IP).

A raw-data packet consists of 16384 samples of 9 synchronous streams with a resolution of 14 bit each which are stored in a buffer during signal capturing. The first eight streams represent the ADC outputs of the eight receiver channels. The last stream is used for triggering and synchronization.

The digital back-end of the receiver can be operated in two ways to capture data:

1. **Simple request**: the host requests the actual data streams of the receiver. After the request the receiver starts to capture the ADC raw-data. When the packet length of 16384 samples is reached, the receiver transmits the data to the host. The last stream in the data packet is nonrelevant and filled with zeros.

2. **Triggered request**: the host requests a data stream of the receiver which is triggered by the signal source. The signal source has, additionally to the data signal, to generate a trigger signal which is connected with the *CLKIN1* port of the receiver DSP-board. The receiver starts capturing the data, when a trigger event was detected. After capturing of 16384 samples, the raw-data packet is sent to the host. The last stream in the data packet shows now a one for all the samples which were captured after the trigger event.

To perform data capturing, *xFace* supports a Python [123] API which handles capturing requests to the receiver, data reception, formatting, and saving the received data on the PCs hard-disk.

5.7 System Validation

In Fig. 5.10 BER measurements are shown, where the input signal powers of the multipliers are varied. The UWB signal was generated by a Tektronix AWG7102 waveform generator with a sampling rate of 10 Gsamples/s. The input power P_1 is the signal power of the input signal fed to first part of the LTCC which is responsible for the delays $\{\tau_1, \tau_2, \tau_3, \tau_4\}$ (cf. Fig. 5.1) whereas the input power P_2 is the signal power of the input signal fed to the second part of the LTCC which is responsible for the delays τ_I and τ_Q. It can be seen that the minimal BER is given about 2.8 % at $P_1 = -2$ dBm and $P_2 = 0$ dBm. These measurements proof the general functionality of such an MC-AcR concept, but the operating point of the multipliers has a big impact on the receiver performance. It needs to be noted, that the data sampling of the receiver was not synchronized to the start of the symbol periods generated by the signal generator which caused the BER deviations that can be observed in the figure. Due to a broken RF board, planed synchronized measurements using the trigger capabilities of the DSP board could unfortunately not be carried out. Those measurements should have given a more detailed insight about the receiver operational point.
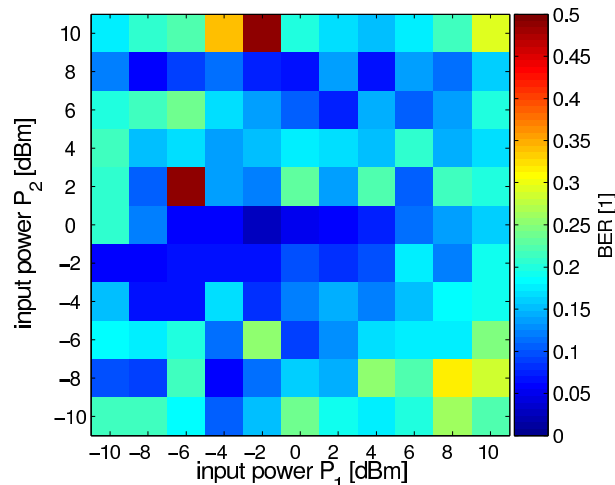
Figure 5.10: Measured BER for various LTCC input powers.

5.8 Summary

In this Chapter a hardware example of an MC-AcR has been presented. The receiver architecture, the used components, and the power and noise budgets have been discussed. The core receiver technology consists of LTCC delay lines, Si/SiGe2 HBT UWB mixers, and 5th-order analog Bessel lowpass integration filters. The frequency response of the LTCC delay line filters varied from the specifications. Nevertheless, simulations have obtained a BER only 2 dB worse than an ideal MC-AcR. Also a BER measurement has been presented, where the LTCC input signal power has been varied. The measurements of the hardware receiver have obtained a minimum BER of 2.8 %. This shows that the investigated receiver works, in principle. However, it also shows that the undesired impact of the analog multipliers plays a crucial role. The receiver performance strongly depends on the operating point of those multipliers.

6

Thesis Summary and Conclusions

To conclude this thesis, this Chapter gives a brief summary and draws some general conclusions.

6.1 Thesis Summary

Chaper 1: Introduction

- The need of noncoherent multi-channel receivers has been motivated.

- A historical summary of the evolution of the first experiments with spark-gap transmitters to noncoherent multi-channel receivers has been drawn.

- The ultra-wideband channel has been shortly discussed.

- An overview of noncoherent ultra-wideband receiver as energy detectors and autocorrelation receivers has been given. Additionally, current works on noncoherent multi-channel receivers have been discussed.

- The research question of this thesis has been stated.

Chaper 2: The Generalized Noncoherent Multi-Channel Receiver

- This thesis studies the class of noncoherent multi-channel receivers. To do so, a generalized mathematical framework has been formulated, which includes multi-channel energy detectors and multi-channel autocorrelation receivers.

- A noncoherent multi-carrier signaling, called NOFDM, has been introduced. This signaling scheme consists of subcarriers which insignificantly overlap and are modulated using on-off keying or pulse position modulation.

- Rules have been stated to obtain front-end filter to ensure optimal noncoherent multi-channel receiver performance.

- Zero-forcing and minimum-mean-square error linear detection have been described for on-off keying and binary pulse position modulated multi-carrier signals.

- Performance metrics, as bit-error rate, signal-to-interference-and-noise ration, signal-to-interference ration, and signal-to-noise ration have been introduced. To evaluate those metrics, a simulation framework has been discussed.

- Reference receivers have been defined, namely the multi-channel energy detector, the multi-channel matched-filter energy detector, and the multi-channel autocorrelation receiver. Their system performance has been discussed.

Chaper 3: Analysis of Realistic Front-End Components

- The design of optimal front-end filters using meta-heuristic optimization algorithms has been studied. A possible multi-objective cost-function was proposed. Filter solutions found by those algorithms have been discussed and their performance has been compared.

- A MIMO Wiener-Hammerstein system has been introduced, to model realistic nonideal multiplication devices. Such a model consists of linear time-invariant input and output filters and a static bivariate polynomial to model the inherent nonlinear behavior of such devices. An identification method for the model parameters has been shown using single-tone and UWB measurements and least-squares estimators. Using the obtained models, the impact of those realistic analog multipliers on the system performance has been discussed.

- A mixed-signal sliding window integrator has been proposed which consist of an analog lowpass Bessel filter and a digital comb filter. The impact of these integrators on the system performance has been shown.

Chaper 4: Enhanced Signal Detection of Nonlinear Memoryless MIMO Channels

- A postcorrection method has been proposed for noncoherent multi-channel receivers to mitigate undesired nonlinear effects for ISI free scenarios.

Chaper 5: A Hardware Example

- The architecture and hardware components of a multi-channel autocorrelation receiver have been discussed.

- The power and the noise budgets have been presented.

- The characteristics of the LTCC delay line filter have been shown. Its influence on the system performance has been discussed.

- The UWB mixer designed by Ulm University, the used mixed-signal integration filter, and the digital back-end have been discussed.

- Finally, bit-error rate measurements have been presented to validate the system performance.

6.2 Discussion of Research Hypothesis

This thesis analyzed if noncoherent multi-channel UWB communication systems are a potential low-complexity low-power alternative to coherent MB-OFDM UWB for high data rate applications. Due to the noncoherent detection, no power hungry and complex carrier and phase estimations are needed at the receiver. The multi-channel signaling drastically increases the data rate, while maintaining low-complexity receiver systems known from conventional single-channel UWB receivers as ED and AcR.

The introduced noncoherent multi-carrier signaling, called NOFDM, consists of subcarriers which insignificantly overlap and are modulated using OOK or PPM. It has proven to be suitable for noncoherent multi-channel receivers.

The generalized mathematical framework introduced in this thesis shows that all noncoherent multi-channel receivers belong to the same class. Next to receivers with ideal projection filters, such as multi-channel energy detectors, multi-channel matched-filter energy detectors, and multi-channel autocorrelation receivers, there exist many receiver types with various different projection filters. Second-order projection filter cross-spectra have proven to be sufficient to obtain a BER performance similar to the multi-channel autocorrelation reference receiver.

The most crucial components within the receiver signal processing chain are the analog multipliers. These devices may introduce many undesired signal terms if the operating point is not chosen wisely. The presented MISO Wiener-Hammerstein model gives insight about these undesired signal terms and offers the possibility to identify an optimal operating point. The obtained model parameters are also useful to compare different multiplier devices with each other, while as conventional single-tone and dual-tone mixer metrics cannot give any meaningful characteristics for mixers used as multiplication devices.

The proposed UWB mixed-signal sliding window integrators are able to improve the receiver performance by mitigating system noise and signal cross-terms using standard system blocks as analog Bessel filters and analog-to-digital converters. The inherent trade-off between analog filter order and digital sampling rate is an advantage which might also be useful in other applications.

The insight which is obtained by the MISO Wiener-Hammerstein multiplier model is a possible way forward towards equalizing undesired nonlinear signal components of noncoherent multi-channel receivers. The proposed nonlinear MIMO estimation and enhanced detection approach has shown gain.

The presented multi-channel autocorrelation hardware receiver is a proof that it is possible to design and manufacture generalized noncoherent multi-channel receivers with today's technologies. Problems caused by the analog multipliers, e.g. insertion loss, operating point, and power consumption, might be solvable for receivers completely designed in (Bi)CMOS. Due to the relaxed complexity of second-order projection filters, an integration in (Bi)CMOS appears to be possible.

A
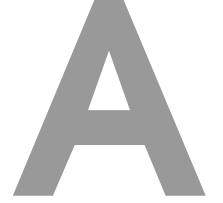
Description of UWB Channel Parameters

The multipath channel can be described, using a tapped delay line model, as

$$c(t, \tau) = \sum_{n=0}^{N-1} \alpha_n(t) \delta(\tau - \tau_n(t)),$$

where N is the number of paths a signal propagates, $\alpha_n(t)$ is the complex gain of the nth ray, $\delta(\cdot)$ is the Dirac delta function [33], and τ_n is the time the signal needs to propagate via the nth path. In general the channel $c(t, \tau)$ is time-variant, given that receivers, transmitters, or reflectors may move. For the time-variant channel $c(t, \tau)$, t is the time parameter whereas τ is the delay parameter. The received signal $r(t)$ is therefore given as

$$r(t) = \int_{\tau=-\infty}^{+\infty} s(t - \tau) c(t, \tau) d\tau + n(t),$$

where $s(t)$ is the sent signal, and $n(t)$ is noise.

The multipath channel can be modeled as stochastic processes and can be statistical described. An important figure is the power delay profile (PDP) of the channel, which is defined for wide-sense stationary uncorrelated scattering (WSSUS) channels as [32]

$$P_c(\tau) = \lim_{T \to \infty} \frac{1}{2T} \int_{-T}^{+T} |c(t, \tau)|^2 \, dt. \tag{A.1}$$

The PDP shows how much power arrives on average at the receiver with a certain delay τ. In [64] a possible simple channel model is described which will be used in this work. It defines an exemplary PDP which is given as

$$P_c(\tau) = \begin{cases} \frac{K_{\text{LOS}}}{K_{\text{LOS}}+1} \delta(\tau) & \text{, for } \tau = 0 \\ \frac{1}{K_{\text{LOS}}+1} \frac{1}{\tau_{\text{RMS}}} e^{-\frac{1}{\tau_{\text{RMS}}} \tau} & \text{, for } \tau > 0, \end{cases}$$

where we assume that the first ray is the dominant line-of-sight (LOS) ray and arrives at $\tau = 0$. All other rays with $\tau_n > 0$ are the non-line-of-sight (NLOS) rays. The parameter K_{LOS} is the Ricean K-factor which gives the ratio between the LOS power and the power of the NLOS rays. The parameter τ_{RMS} is the so called RMS delay spread [32]. The parameters of the channel

model can be obtained from stochastic processes. For independent realizations the parameters are defined as follows:

The ray amplitudes are given as

$$\alpha_n = \begin{cases} \sqrt{\frac{K_{\text{LOS}}}{K_{\text{LOS}}+1}} e^{j\gamma_n} & \text{, for } n = 0 \\ \beta_n e^{j\gamma} & \text{, for } n > 0, \end{cases}$$

where β_n shows Nakagami-m distributed statistics [124] with given probability distribution function (PDF) of

$$p(\beta_n) = \frac{2m^m}{\Gamma(m)\,\Omega^m} \beta^{2m-1} e^{-\frac{m}{\Omega}\beta^2}, \tag{A.2}$$

where $\Gamma(\cdot)$ is Euler's Gamma function [33], and

$$\Omega_n = \frac{1}{\tau_{\text{RMS}}} \frac{1}{K+1} \frac{1}{\lambda} e^{-\frac{\tau}{\tau_{\text{RMS}}}}.$$

The phase γ_n is uniformly distributed within $\gamma_n \in [0, 2\pi)$.

The delays $\{\tau_n\}$ are modeled similar to the Saleh-Valenzuela delay model [125], so that the difference between two delays $\Delta\tau = \tau_n - \tau_{n-1}$ is distributed with a PDF of

$$p(\Delta\tau) = \lambda e^{-\lambda\Delta\tau},$$

for $\Delta\tau > 0$ and where λ is the ray arrival rate.

(a) Absolute value of the channel impulse response.

(b) Magnitude response.
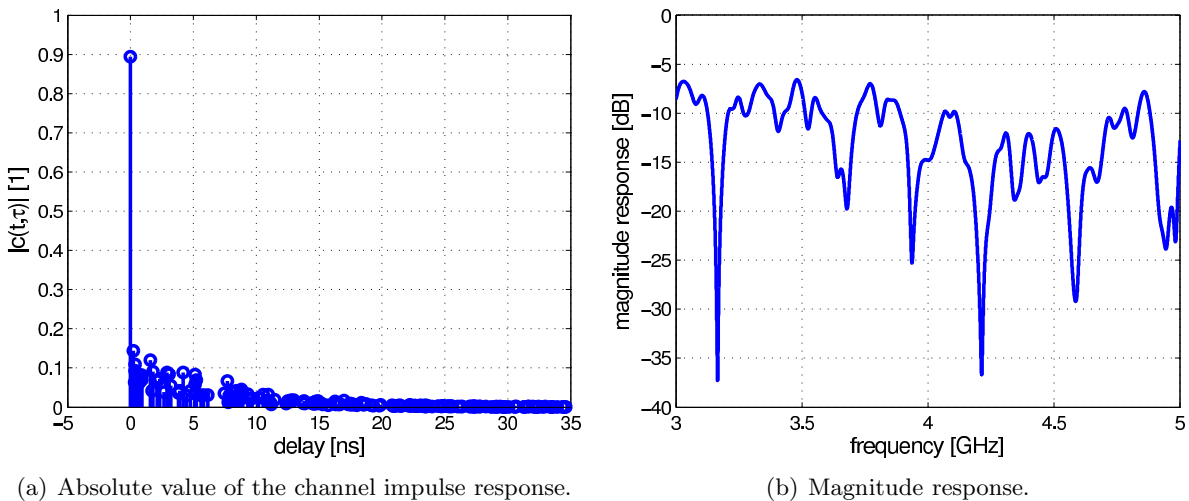
Figure A.1: Example of a time-variant multipath channel at given time t.

In Fig. A.1 a sample function of a time-variant multipath channel is shown. The channel parameters are given in Tab. 2.2. In Fig. A.1(a) the impulse response is shown. The dominant LOS ray can be easily seen. The NLOS rays have amplitudes which decay in an exponential fashion for increasing delay τ, corresponding to the exponential PDP. In Fig. 1.1(b) the magnitude response is shown. Clearly visible are the deep fading-dips which would cause narrowband and wideband communication systems which operate at those fading frequencies to experience degraded performance. Due to the ultra-wide bandwidth of UWB signals, they would still have signal components outside the fading-dips and are, hence, robust against fading in contrast to those narrowband and wideband communication signals.

B

Proofs

B.1 SINR

For ISI free condition we can consider a single symbol period T_{sym} only without loss of generality. By expanding this symbol period periodically, the sent signal $s(t)$ can be represented as the Fourier series

$$s(t) = \sum_{i=-\infty}^{+\infty} s_i e^{j\omega_0 it},$$

where $\omega_0 = \frac{2\pi}{T_{\text{sym}}}$. The Fourier coefficients s_i are given as

$$s_i = \frac{1}{T_{\text{sym}}} \int_{t=0}^{T_{\text{sym}}} s(t) e^{-j\omega_0 it} dt.$$

The received signal $r(t)$ is (as in (2.2)) given as

$$r(t) = c(t) * s(t) + n(t),$$

where $c(t)$ is the transmission channel and $n(t)$ is a band-limited Gaussian noise process with a flat power density spectrum. Using Fourier series expansion the noise process $n(t)$ can be represented in the integration interval T_{sym} as

$$n(t) = \sum_{i=-\infty}^{+\infty} n_i e^{j\omega_0 it}$$

with its Fourier coefficients

$$n_i = \frac{1}{T_{\text{sym}}} \int_{t=0}^{T_{\text{sym}}} n(t) e^{-j\omega_0 it}.$$

Hence, the Fourier coefficients r_i of the received signal

$$r(t) = \sum_{i=-\infty}^{+\infty} r_i e^{j\omega_0 it}$$

is given as

$$
\begin{aligned}
r_i &= \frac{1}{T_{\text{sym}}} \int_{t=0}^{T_{\text{sym}}} \left(c(t) * s(t) + n(t) \right) e^{-j\omega_0 it} dt \\
&= \frac{1}{T_{\text{sym}}} \int_{t=0}^{T_{\text{sym}}} \left(\int_{\tau=-\infty}^{+\infty} c(t-\tau) s(\tau) d\tau + n(t) \right) e^{-j\omega_0 it} dt \\
&= \frac{1}{T_{\text{sym}}} \int_{t=0}^{T_{\text{sym}}} \left(\int_{\tau=-\infty}^{+\infty} c(t-\tau) s(\tau) d\tau \right) e^{-j\omega_0 it} dt + \frac{1}{T_{\text{sym}}} \int_{t=0}^{T_{\text{sym}}} n(t) e^{-j\omega_0 it} dt \\
&= \frac{1}{T_{\text{sym}}} \int_{t=0}^{T_{\text{sym}}} \left(\int_{\tau=-\infty}^{+\infty} c(t-\tau) \sum_{k=-\infty}^{+\infty} s_k e^{j\omega_0 k\tau} d\tau \right) e^{-j\omega_0 it} dt + n_i \\
&= \frac{1}{T_{\text{sym}}} \int_{t=0}^{T_{\text{sym}}} \left(\sum_{k=-\infty}^{+\infty} s_k \int_{\tau=-\infty}^{+\infty} c(t-\tau) e^{j\omega_0 k\tau} d\tau \right) e^{-j\omega_0 it} dt + n_i \\
\\
&= \frac{1}{T_{\text{sym}}} \int_{t=0}^{T_{\text{sym}}} \left(\sum_{k=-\infty}^{+\infty} s_k \int_{\tau=-\infty}^{+\infty} c(\tau+t) e^{-j\omega_0 k\tau} d\tau \right) e^{-j\omega_0 it} dt + n_i \\
&= \frac{1}{T_{\text{sym}}} \int_{t=0}^{T_{\text{sym}}} \left(\sum_{k=-\infty}^{+\infty} C(j\omega_0 k) s_k e^{j\omega_0 kt} \right) e^{-j\omega_0 it} dt + n_i \\
&= \frac{1}{T_{\text{sym}}} \sum_{k=-\infty}^{+\infty} C(j\omega_0 k) s_k \int_{t=0}^{T_{\text{sym}}} e^{j\omega_0 kt} e^{-j\omega_0 it} dt + n_i \\
&= \frac{1}{T_{\text{sym}}} \sum_{k=-\infty}^{+\infty} C(j\omega_0 k) s_k \int_{t=0}^{T_{\text{sym}}} e^{j\omega_0 (k-i)t} dt + n_i.
\end{aligned}
$$

The integral

$$
\begin{aligned}
\int_{t=0}^{T_{\text{sym}}} e^{j\omega_0 (k-i)t} dt &= \int_{t=0}^{T_{\text{sym}}} \cos\left(\omega_0(k-i)t\right) + j\sin\left(\omega_0(k-i)t\right) dt \\
&= \left[\frac{\sin\left(\omega_0(k-i)t\right)}{\omega_0(k-i)} - j\frac{\cos\left(\omega_0(k-i)t\right)}{\omega_0(k-i)} \right]_{t=0}^{T_{\text{sym}}} \\
&= \frac{\sin\left(\omega_0(k-i)T_{\text{sym}}\right)}{\omega_0(k-i)} - j\frac{\cos\left(\omega_0(k-i)T_{\text{sym}}\right)}{\omega_0(k-i)} + j\frac{1}{\omega_0(k-i)} \\
&= \frac{\sin\left(2\pi(k-i)\right)}{\omega_0(k-i)} - j\frac{\cos\left(2\pi(k-i)\right)}{\omega_0(k-i)} + j\frac{1}{\omega_0(k-i)}
\end{aligned}
$$

simplifies, using L'Hôpital's rule, to

$$\int_{t=0}^{T_{\text{sym}}} e^{j\omega_0 (k-i)t} dt = T_{\text{sym}} \delta_{k-i},$$

where δ_i is the Kronecker delta. Using this equality the Fourier coefficients of $r(t)$ can be

rewritten to

$$r_i = \sum_{k=-\infty}^{+\infty} C(j\omega_0 k) s_k \delta_{k-i} + n_i$$
$$= C(j\omega_0 i) s_i + n_i.$$

With the $c_i = C(j\omega_0 i)$ the Fourier coefficients of $r(t)$ are finally given as

$$r_i = c_i s_i + n_i.$$

The mth receiver channel output y_m is hence given as

$$y_m = \int_{t=0}^{T_{\text{sym}}} (h_m(t) * r(t)) (g_m(t) * r(t)) \, dt$$
$$= \int_{t=0}^{T_{\text{sym}}} \left(h_m(t) * \sum_{k=-\infty}^{+\infty} r_k e^{j\omega_0 kt} \right) \left(g_m(t) * \sum_{l=-\infty}^{+\infty} r_l e^{j\omega_0 lt} \right) dt$$
$$= \int_{t=0}^{T_{\text{sym}}} \left(\sum_{k=-\infty}^{+\infty} H_m(j\omega_0 k) r_k e^{j\omega_0 kt} \right) \left(\sum_{l=-\infty}^{+\infty} G_m(j\omega_0 l) r_l e^{j\omega_0 lt} \right) dt$$

$$= \int_{t=0}^{T_{\text{sym}}} \left(\sum_{k=-\infty}^{+\infty} h_{m,k} r_k e^{j\omega_0 kt} \right) \left(\sum_{l=-\infty}^{+\infty} g_{m,l} r_l e^{j\omega_0 lt} \right) dt$$
$$= \sum_{k=-\infty}^{+\infty} \sum_{l=-\infty}^{+\infty} h_{m,k} g_{m,l} r_k r_l \int_{t=0}^{T_{\text{sym}}} e^{j\omega_0 kt} e^{j\omega_0 lt} dt$$
$$= \sum_{k=-\infty}^{+\infty} \sum_{l=-\infty}^{+\infty} h_{m,k} g_{m,l} r_k r_l T_{\text{sym}} \delta_{k+l}$$
$$= T_{\text{sym}} \sum_{k=-\infty}^{+\infty} h_{m,k} g_{m,-k} r_k r_{-k},$$

where $h_{m,k} = H_m(j\omega_0 k)$ and $g_{m,l} = G_m(j\omega_0 l)$. Further simplification gives

$$y_m = T_{\text{sym}} \sum_{i=-\infty}^{+\infty} h_{m,i} g_{m,i}^* r_i r_i^*$$
$$= T_{\text{sym}} \sum_{i=-\infty}^{+\infty} h_{m,i} g_{m,ik}^* (c_i s_i + n_i) (c_i^* s_i^* + n_i^*)$$
$$= T_{\text{sym}} \sum_{i=-\infty}^{+\infty} h_{m,i} g_{m,i}^* \left(c_i \sum_{k=1}^{K} d_k \varphi_{k,i} + n_i \right) \left(c_i^* \sum_{l=1}^{K} d_l^* \varphi_{l,i}^* + n_i^* \right)$$

for real valued $h_m(t)$ and $g_m(t)$.

Expansion of the mth receiver output y_m gives

$$
y_m = T_{\text{sym}} \underbrace{\sum_{i=-\infty}^{+\infty} h_{m,i} g_{m,i}^* c_i c_i^* \sum_{k=1}^{K} d_k d_k^* \varphi_{k,i} \varphi_{k,i}^*}_{\text{signal co-terms}}
$$

$$
+ T_{\text{sym}} \underbrace{\sum_{i=-\infty}^{+\infty} h_{m,i} g_{m,i}^* c_i c_i^* \sum_{k=1}^{K} \sum_{\substack{l=1 \\ l \neq k}}^{K} d_k d_l^* \varphi_{k,i} \varphi_{l,i}^*}_{\text{signal cross-terms}}
$$

$$
+ T_{\text{sym}} \underbrace{\sum_{i=-\infty}^{+\infty} h_{m,i} g_{m,i}^* c_i \left(\sum_{k=1}^{K} d_k \varphi_{k,i} \right) n_i^*}_{\text{signal-by-noise terms}}
$$

$$
+ T_{\text{sym}} \underbrace{\sum_{i=-\infty}^{+\infty} h_{m,i} g_{m,i}^* c_i^* n_i \left(\sum_{l=1}^{K} d_l^* \varphi_{l,i}^* \right)}_{\text{noise-by-signal terms}}
$$

$$
+ T_{\text{sym}} \underbrace{\sum_{i=-\infty}^{+\infty} h_{m,i} g_{m,i}^* n_i n_i^*}_{\text{noise-by-noise terms}}
$$

where the signal co-, cross-, signal-by-noise, noise-by-signal, and noise-by-noise terms are explicitly shown.

In matrix representation, the mth receiver output can be written as

$$
\begin{aligned}
y_m = \ & T_{\text{sym}} \mathbf{g}_m^H \mathbf{H}_m \mathbf{C}^H \mathbf{C} \mathbf{\Psi} \left(\mathbf{d} \odot \mathbf{d}^* \right) \\
& + T_{\text{sym}} \mathbf{g}_m^H \mathbf{H}_m \mathbf{C}^H \mathbf{C} \tilde{\mathbf{\Psi}} \left(\mathbf{d} \tilde{\otimes} \mathbf{d}^* \right) \\
& + T_{\text{sym}} \mathbf{g}_m^H \mathbf{H}_m \mathbf{C} \mathbf{N}^H \mathbf{\Phi} \mathbf{d} \\
& + T_{\text{sym}} \mathbf{g}_m^H \mathbf{H}_m \mathbf{C}^H \mathbf{N} \mathbf{\Phi}^* \mathbf{d}^* \\
& + T_{\text{sym}} \mathbf{g}_m^H \mathbf{H}_m \mathbf{n}',
\end{aligned}
$$

where the elements of the vectors $\mathbf{g}_m$ and $\mathbf{n}'$ are given as $[\mathbf{g}_m]_i = g_{m,i}$ and $[\mathbf{n}']_i = n_i n_i^*$. The matrices $\mathbf{H}_m$, $\mathbf{C}$, and $\mathbf{N}$, are diagonal matrices with $[\mathbf{H}_m]_{i,i} = h_{m,i}$, $[\mathbf{C}]_{i,i} = c_i$, and $[\mathbf{N}]_{i,i} = n_i$. The elements of the matrices $\mathbf{\Phi}$, $\mathbf{\Psi}$, and $\tilde{\mathbf{\Psi}}$ are given as $[\mathbf{\Phi}]_{i,k} = \varphi_{k,i}$, $[\mathbf{\Psi}]_{i,k} = \varphi_{k,i} \varphi_{k,i}^*$, and the columns of $\tilde{\mathbf{\Psi}}$ consist of $\boldsymbol{\varphi}_k \odot \boldsymbol{\varphi}_l^*$ for $k = 1, \ldots, K$, $l = 1, \ldots, K$, but $l \neq k$. The elements of the vector $\boldsymbol{\varphi}_k$ are given as $[\boldsymbol{\varphi}_k]_i = \varphi_{k,i}$.

Note that the projection filter cross-spectra $\left\{ \mathbf{x}_m^H = \mathbf{g}_m^H \mathbf{H}_m \right\}$ do play a crucial role in the processing of all signal, noise, and cross terms. If defining a projection filter cross-spectra matrix $\mathbf{X}$ with $[\mathbf{X}]_{i,m} = g_{m,i} h_{m,i}^*$, the receiver output vector $\mathbf{y}$ can be represented as

$$
\begin{aligned}
\mathbf{y} = \ & T_{\text{sym}} \mathbf{X}^H \mathbf{C}^H \mathbf{C} \mathbf{\Psi} \left(\mathbf{d} \odot \mathbf{d}^* \right) && \} =: \boldsymbol{\alpha} \\
& + T_{\text{sym}} \mathbf{X}^H \mathbf{C}^H \mathbf{C} \tilde{\mathbf{\Psi}} \left(\mathbf{d} \tilde{\otimes} \mathbf{d}^* \right) && \} =: \boldsymbol{\beta} \\
& + T_{\text{sym}} \mathbf{X}^H \mathbf{C} \mathbf{N}^H \mathbf{\Phi} \mathbf{d} && \left. \vphantom{\begin{array}{c} \\ \\ \\ \end{array}} \right\} \\
& + T_{\text{sym}} \mathbf{X}^H \mathbf{C}^H \mathbf{N} \mathbf{\Phi}^* \mathbf{d}^* && =: \boldsymbol{\nu} \\
& + T_{\text{sym}} \mathbf{X}^H \mathbf{n}',
\end{aligned}
$$

hence,

$$\mathbf{y} = \boldsymbol{\alpha} + \boldsymbol{\beta} + \boldsymbol{\nu}.$$

The decision variable vector $\mathbf{z}$ is therefore given as

$$\begin{aligned}
\mathbf{z} = {} & (\mathbf{d} \odot \mathbf{d}^*) \\
& + T_{\mathbf{sym}} \mathbf{W} \mathbf{X}^H \mathbf{C}^H \mathbf{C} \tilde{\boldsymbol{\Psi}} \left(\mathbf{d} \tilde{\otimes} \mathbf{d}^* \right) \\
& + T_{\mathrm{sym}} \mathbf{W} \mathbf{X}^H \mathbf{C} \mathbf{N}^H \boldsymbol{\Phi} \mathbf{d} \\
& + T_{\mathrm{sym}} \mathbf{W} \mathbf{X}^H \mathbf{C}^H \mathbf{N} \boldsymbol{\Phi}^* \mathbf{d}^* \\
& + T_{\mathrm{sym}} \mathbf{W} \mathbf{X}^H \mathbf{n}',
\end{aligned}$$

where $\mathbf{W}$ is the inverse of $\mathbf{X}^H \mathbf{C}^H \mathbf{C} \boldsymbol{\Psi}$.

B.1.1 SINR for an Arbitrary Signaling

The SINR of the decision vector can be defined as

$$\begin{aligned}
\mathrm{SINR} &= \frac{\mathrm{E} \left\{ \boldsymbol{\alpha}^H \mathbf{W}^H \mathbf{W} \boldsymbol{\alpha} \right\}}{\mathrm{E} \left\{ \boldsymbol{\beta}^H \mathbf{W}^H \mathbf{W} \boldsymbol{\beta} \right\} + \mathrm{E} \left\{ \boldsymbol{\nu}^H \mathbf{W}^H \mathbf{W} \boldsymbol{\beta} \right\} + \mathrm{E} \left\{ \boldsymbol{\beta}^H \mathbf{W}^H \mathbf{W} \boldsymbol{\nu} \right\} + \mathrm{E} \left\{ \boldsymbol{\nu}^H \mathbf{W}^H \mathbf{W} \boldsymbol{\nu} \right\}} \\
&= \frac{\mathrm{tr} \left\{ \mathbf{W} \mathrm{E} \left\{ \boldsymbol{\alpha} \boldsymbol{\alpha}^H \right\} \mathbf{W}^H \right\}}{\mathrm{tr} \left\{ \mathbf{W} \left(\mathrm{E} \left\{ \boldsymbol{\beta} \boldsymbol{\beta}^H \right\} + \mathrm{E} \left\{ \boldsymbol{\nu} \boldsymbol{\beta}^H \right\} + \mathrm{E} \left\{ \boldsymbol{\beta} \boldsymbol{\nu}^H \right\} + \mathrm{E} \left\{ \boldsymbol{\nu} \boldsymbol{\nu}^H \right\} \right) \mathbf{W}^H \right\}}.
\end{aligned}$$

The co-term covariance matrix $\mathrm{E} \left\{ \boldsymbol{\alpha} \boldsymbol{\alpha}^H \right\}$ is given as

$$\begin{aligned}
\mathrm{E} \left\{ \boldsymbol{\alpha} \boldsymbol{\alpha}^H \right\} &= T_{\mathrm{sym}}^2 \mathrm{E} \left\{ \mathbf{X}^H \mathbf{C}^H \mathbf{C} \boldsymbol{\Psi} \left(\mathbf{d} \odot \mathbf{d}^* \right) \left(\mathbf{d} \odot \mathbf{d}^* \right)^H \boldsymbol{\Psi}^H \mathbf{C}^H \mathbf{C} \mathbf{X} \right\} \\
&= T_{\mathrm{sym}}^2 \mathbf{X}^H \mathbf{C}^H \mathbf{C} \boldsymbol{\Psi} \mathrm{E} \left\{ \left(\mathbf{d} \odot \mathbf{d}^* \right) \left(\mathbf{d} \odot \mathbf{d}^* \right)^H \right\} \boldsymbol{\Psi}^H \mathbf{C}^H \mathbf{C} \mathbf{X} \\
&= T_{\mathrm{sym}}^2 \mathbf{X}^H \mathbf{C}^H \mathbf{C} \boldsymbol{\Psi} \mathbf{R}_{\mathbf{d} \odot \mathbf{d}^*} \boldsymbol{\Psi}^H \mathbf{C}^H \mathbf{C} \mathbf{X},
\end{aligned}$$

where

$$\left[\mathbf{R}_{\mathbf{d} \odot \mathbf{d}^*} \right]_{k,l} = \mathrm{E} \left\{ d_k d_k^* d_l d_l^* \right\}.$$

Using the equality

$$\mathbf{X}^H \mathbf{C}^H \mathbf{C} \tilde{\boldsymbol{\Psi}} \left(\mathbf{d} \tilde{\otimes} \mathbf{d}^* \right) = \mathbf{X}^H \mathbf{C}^H \mathbf{C} \tilde{\tilde{\boldsymbol{\Psi}}} \left(\mathbf{d} \otimes \mathbf{d}^* \right) - \mathbf{X}^H \mathbf{C}^H \mathbf{C} \boldsymbol{\Psi} \left(\mathbf{d} \odot \mathbf{d}^* \right),$$

where $\left[\tilde{\tilde{\boldsymbol{\Psi}}} \right]_{i,k+K(l-1)} = \varphi_{k,i} \varphi_{l,i}^*$ with $k = 1, \dots, K$, $l = 1, \dots, K$, the cross-term covariance matrix $\mathrm{E} \left\{ \boldsymbol{\beta} \boldsymbol{\beta}^H \right\}$ is given as

$$\begin{aligned}
\mathrm{E} \left\{ \boldsymbol{\beta} \boldsymbol{\beta}^H \right\} = {} & T_{\mathrm{sym}}^2 \mathrm{E} \Bigg\{ \left(\mathbf{X}^H \mathbf{C}^H \mathbf{C} \tilde{\tilde{\boldsymbol{\Psi}}} \left(\mathbf{d} \otimes \mathbf{d}^* \right) - \mathbf{X}^H \mathbf{C}^H \mathbf{C} \boldsymbol{\Psi} \left(\mathbf{d} \odot \mathbf{d}^* \right) \right) \\
& \times \left(\mathbf{X}^H \mathbf{C}^H \mathbf{C} \tilde{\tilde{\boldsymbol{\Psi}}} \left(\mathbf{d} \otimes \mathbf{d}^* \right) - \mathbf{X}^H \mathbf{C}^H \mathbf{C} \boldsymbol{\Psi} \left(\mathbf{d} \odot \mathbf{d}^* \right) \right)^H \Bigg\}
\end{aligned}$$

$$\mathrm{E}\left\{\boldsymbol{\beta}\boldsymbol{\beta}^{H}\right\} = T_{\mathrm{sym}}^{2}\mathrm{E}\left\{\left(\mathbf{X}^{H}\mathbf{C}^{H}\mathbf{C}\tilde{\tilde{\boldsymbol{\Psi}}}\left(\mathbf{d}\otimes\mathbf{d}^{*}\right) - \mathbf{X}^{H}\mathbf{C}^{H}\mathbf{C}\boldsymbol{\Psi}\left(\mathbf{d}\odot\mathbf{d}^{*}\right)\right)\right.$$
$$\left.\times\left(\left(\mathbf{d}\otimes\mathbf{d}^{*}\right)^{H}\tilde{\tilde{\boldsymbol{\Psi}}}^{H}\mathbf{C}^{H}\mathbf{C}\mathbf{X} - \left(\mathbf{d}\odot\mathbf{d}^{*}\right)^{H}\boldsymbol{\Psi}^{H}\mathbf{C}^{H}\mathbf{C}\mathbf{X}\right)\right\}$$
$$= T_{\mathrm{sym}}^{2}\mathbf{X}^{H}\mathbf{C}^{H}\mathbf{C}\tilde{\tilde{\boldsymbol{\Psi}}}\mathrm{E}\left\{\left(\mathbf{d}\otimes\mathbf{d}^{*}\right)\left(\mathbf{d}\otimes\mathbf{d}^{*}\right)^{H}\right\}\tilde{\tilde{\boldsymbol{\Psi}}}^{H}\mathbf{C}^{H}\mathbf{C}\mathbf{X}$$
$$- T_{\mathrm{sym}}^{2}\mathbf{X}^{H}\mathbf{C}^{H}\mathbf{C}\tilde{\tilde{\boldsymbol{\Psi}}}\mathrm{E}\left\{\left(\mathbf{d}\otimes\mathbf{d}^{*}\right)\left(\mathbf{d}\odot\mathbf{d}^{*}\right)^{H}\right\}\boldsymbol{\Psi}^{H}\mathbf{C}^{H}\mathbf{C}\mathbf{X}$$
$$- T_{\mathrm{sym}}^{2}\mathbf{X}^{H}\mathbf{C}^{H}\mathbf{C}\boldsymbol{\Psi}\mathrm{E}\left\{\left(\mathbf{d}\odot\mathbf{d}^{*}\right)\left(\mathbf{d}\otimes\mathbf{d}^{*}\right)^{H}\right\}\tilde{\tilde{\boldsymbol{\Psi}}}^{H}\mathbf{C}^{H}\mathbf{C}\mathbf{X}$$
$$+ T_{\mathrm{sym}}^{2}\mathbf{X}^{H}\mathbf{C}^{H}\mathbf{C}\boldsymbol{\Psi}\mathrm{E}\left\{\left(\mathbf{d}\odot\mathbf{d}^{*}\right)\left(\mathbf{d}\odot\mathbf{d}^{*}\right)^{H}\right\}\boldsymbol{\Psi}^{H}\mathbf{C}^{H}\mathbf{C}\mathbf{X}$$
$$= T_{\mathrm{sym}}^{2}\mathbf{X}^{H}\mathbf{C}^{H}\mathbf{C}\tilde{\tilde{\boldsymbol{\Psi}}}\mathbf{R}_{\mathbf{d}\otimes\mathbf{d}^{*}}\tilde{\tilde{\boldsymbol{\Psi}}}^{H}\mathbf{C}^{H}\mathbf{C}\mathbf{X}$$
$$- T_{\mathrm{sym}}^{2}\mathbf{X}^{H}\mathbf{C}^{H}\mathbf{C}\tilde{\tilde{\boldsymbol{\Psi}}}\tilde{\mathbf{R}}_{\mathbf{d}\otimes\mathbf{d}^{*}}\boldsymbol{\Psi}^{H}\mathbf{C}^{H}\mathbf{C}\mathbf{X}$$
$$- T_{\mathrm{sym}}^{2}\mathbf{X}^{H}\mathbf{C}^{H}\mathbf{C}\boldsymbol{\Psi}\tilde{\mathbf{R}}_{\mathbf{d}\otimes\mathbf{d}^{*}}^{H}\tilde{\tilde{\boldsymbol{\Psi}}}^{H}\mathbf{C}^{H}\mathbf{C}\mathbf{X}$$
$$+ T_{\mathrm{sym}}^{2}\mathbf{X}^{H}\mathbf{C}^{H}\mathbf{C}\boldsymbol{\Psi}\mathbf{R}_{\mathbf{d}\odot\mathbf{d}^{*}}\boldsymbol{\Psi}^{H}\mathbf{C}^{H}\mathbf{C}\mathbf{X},$$

where

$$\left[\mathbf{R}_{\mathbf{d}\otimes\mathbf{d}^{*}}\right]_{k+K(l-1),u+K(v-1)} = \mathrm{E}\left\{d_{k}d_{l}^{*}d_{u}d_{v}^{*}\right\}$$

and

$$\left[\tilde{\mathbf{R}}_{\mathbf{d}\otimes\mathbf{d}^{*}}\right]_{k+K(l-1),u} = \mathrm{E}\left\{d_{k}d_{l}^{*}d_{u}d_{u}^{*}\right\}$$

with $u = 1,\ldots,K$, $v = 1,\ldots,K$.

The correlation matrix $\mathrm{E}\left\{\boldsymbol{\nu}\boldsymbol{\beta}^{H}\right\}$ is given as

$$\mathrm{E}\left\{\boldsymbol{\nu}\boldsymbol{\beta}^{H}\right\} = T_{\mathrm{sym}}^{2}\mathrm{E}\left\{\left(\mathbf{X}^{H}\mathbf{C}\mathbf{N}^{H}\boldsymbol{\Phi}\mathbf{d} + \mathbf{X}^{H}\mathbf{C}^{H}\mathbf{N}\boldsymbol{\Phi}^{*}\mathbf{d}^{*} + \mathbf{X}^{H}\mathbf{n}'\right)\right.$$
$$\left.\times\left(\mathbf{X}^{H}\mathbf{C}^{H}\mathbf{C}\tilde{\tilde{\boldsymbol{\Psi}}}\left(\mathbf{d}\otimes\mathbf{d}^{*}\right) - \mathbf{X}^{H}\mathbf{C}^{H}\mathbf{C}\boldsymbol{\Psi}\left(\mathbf{d}\odot\mathbf{d}^{*}\right)\right)^{H}\right\}$$
$$= T_{\mathrm{sym}}^{2}\mathrm{E}\left\{\left(\mathbf{X}^{H}\mathbf{C}\mathbf{N}^{H}\boldsymbol{\Phi}\mathbf{d} + \mathbf{X}^{H}\mathbf{C}^{H}\mathbf{N}\boldsymbol{\Phi}^{*}\mathbf{d}^{*} + \mathbf{X}^{H}\mathbf{n}'\right)\right.$$
$$\left.\times\left(\left(\mathbf{d}\otimes\mathbf{d}^{*}\right)^{H}\tilde{\tilde{\boldsymbol{\Psi}}}^{H}\mathbf{C}^{H}\mathbf{C}\mathbf{X} - \left(\mathbf{d}\odot\mathbf{d}^{*}\right)^{H}\boldsymbol{\Psi}^{H}\mathbf{C}^{H}\mathbf{C}\mathbf{X}\right)\right\}$$
$$= T_{\mathrm{sym}}^{2}\mathbf{X}^{H}\mathbf{C}\mathrm{E}\left\{\mathbf{N}^{H}\right\}\boldsymbol{\Phi}\mathrm{E}\left\{\mathbf{d}\left(\mathbf{d}\otimes\mathbf{d}^{*}\right)^{H}\right\}\tilde{\tilde{\boldsymbol{\Psi}}}^{H}\mathbf{C}^{H}\mathbf{C}\mathbf{X}$$
$$+ T_{\mathrm{sym}}^{2}\mathbf{X}^{H}\mathbf{C}^{H}\mathrm{E}\left\{\mathbf{N}\right\}\boldsymbol{\Phi}^{*}\mathrm{E}\left\{\mathbf{d}^{*}\left(\mathbf{d}\otimes\mathbf{d}^{*}\right)^{H}\right\}\tilde{\tilde{\boldsymbol{\Psi}}}^{H}\mathbf{C}^{H}\mathbf{C}\mathbf{X}$$
$$+ T_{\mathrm{sym}}^{2}\mathbf{X}^{H}\mathrm{E}\left\{\mathbf{n}'\right\}\mathrm{E}\left\{\left(\mathbf{d}\otimes\mathbf{d}^{*}\right)^{H}\right\}\tilde{\tilde{\boldsymbol{\Psi}}}^{H}\mathbf{C}^{H}\mathbf{C}\mathbf{X}$$
$$- T_{\mathrm{sym}}^{2}\mathbf{X}^{H}\mathbf{C}\mathrm{E}\left\{\mathbf{N}^{H}\right\}\boldsymbol{\Phi}\mathrm{E}\left\{\mathbf{d}\left(\mathbf{d}\odot\mathbf{d}^{*}\right)^{H}\right\}\boldsymbol{\Psi}^{H}\mathbf{C}^{H}\mathbf{C}\mathbf{X}$$
$$- T_{\mathrm{sym}}^{2}\mathbf{X}^{H}\mathbf{C}^{H}\mathrm{E}\left\{\mathbf{N}\right\}\boldsymbol{\Phi}^{*}\mathrm{E}\left\{\mathbf{d}^{*}\left(\mathbf{d}\odot\mathbf{d}^{*}\right)^{H}\right\}\boldsymbol{\Psi}^{H}\mathbf{C}^{H}\mathbf{C}\mathbf{X}$$
$$- T_{\mathrm{sym}}^{2}\mathbf{X}^{H}\mathrm{E}\left\{\mathbf{n}'\right\}\mathrm{E}\left\{\left(\mathbf{d}\odot\mathbf{d}*\right)^{H}\right\}\boldsymbol{\Psi}^{H}\mathbf{C}^{H}\mathbf{C}\mathbf{X}$$

Due to $\mathrm{E}\{n_i\} = 0$ and $\mathrm{E}\{n_i^* n_i\} = \frac{\sigma_n^2}{T_{\mathrm{sym}}}$, the covariance matrix $\mathrm{E}\{\boldsymbol{\nu}\boldsymbol{\beta}\}$ simplifies to

$$
\begin{aligned}
\mathrm{E}\{\boldsymbol{\nu}\boldsymbol{\beta}^H\} &= T_{\mathrm{sym}}^2 \mathbf{X}^H \mathrm{E}\{\mathbf{n}'\} \mathrm{E}\left\{(\mathbf{d}\otimes\mathbf{d}^*)^H\right\} \tilde{\tilde{\boldsymbol{\Psi}}}^H \mathbf{C}^H \mathbf{C}\mathbf{X} \\
&\quad - T_{\mathrm{sym}}^2 \mathbf{X}^H \mathrm{E}\{\mathbf{n}'\} \mathrm{E}\left\{(\mathbf{d}\odot\mathbf{d}^*)^H\right\} \boldsymbol{\Psi}^H \mathbf{C}^H \mathbf{C}\mathbf{X} \\
&= T_{\mathrm{sym}} \sigma_n^2 \bar{\mathbf{x}}^* \mathbf{r}_{\mathbf{d}\otimes\mathbf{d}^*}^H \tilde{\tilde{\boldsymbol{\Psi}}}^H \mathbf{C}^H \mathbf{C}\mathbf{X} \\
&\quad - T_{\mathrm{sym}} \sigma_n^2 \bar{\mathbf{x}}^* \mathbf{r}_{\mathbf{d}\odot\mathbf{d}^*}^H \boldsymbol{\Psi}^H \mathbf{C}^H \mathbf{C}\mathbf{X}
\end{aligned}
$$

with

$$
[\bar{\mathbf{x}}]_m = \sum_{i=-\infty}^{+\infty} g_{m,i} h_{m,i}^*,
$$

$$
[\mathbf{r}_{\mathbf{d}\otimes\mathbf{d}^*}]_{k+K(l-1)} = \mathrm{E}\{d_k d_l^*\},
$$

and

$$
[\mathbf{r}_{\mathbf{d}\odot\mathbf{d}^*}]_k = \mathrm{E}\{d_k d_k^*\}.
$$

The correlation matrix $\mathrm{E}\{\boldsymbol{\beta}\boldsymbol{\nu}^H\}$ is similarly given as

$$
\begin{aligned}
\mathrm{E}\{\boldsymbol{\beta}\boldsymbol{\nu}^H\} &= \mathrm{E}\{\boldsymbol{\nu}\boldsymbol{\beta}^H\}^H \\
&= T_{\mathrm{sym}} \sigma_n^2 \mathbf{X}^H \mathbf{C}^H \mathbf{C}\tilde{\tilde{\boldsymbol{\Psi}}} \mathbf{r}_{\mathbf{d}\otimes\mathbf{d}^*} \bar{\mathbf{x}}^T \\
&\quad - T_{\mathrm{sym}} \sigma_n^2 \mathbf{X}^H \mathbf{C}^H \mathbf{C}\boldsymbol{\Psi} \mathbf{r}_{\mathbf{d}\odot\mathbf{d}^*} \bar{\mathbf{x}}^T.
\end{aligned}
$$

The covariance matrix $\mathrm{E}\{\boldsymbol{\nu}\boldsymbol{\nu}^H\}$ is given as

$$
\begin{aligned}
\mathrm{E}\{\boldsymbol{\nu}\boldsymbol{\nu}^H\} &= T_{\mathrm{sym}}^2 \mathrm{E}\Big\{ \big(\mathbf{X}^H \mathbf{C}\mathbf{N}^H \boldsymbol{\Phi}\mathbf{d} + \mathbf{X}^H \mathbf{C}^H \mathbf{N}\boldsymbol{\Phi}^* \mathbf{d}^* + \mathbf{X}^H \mathbf{n}'\big) \\
&\qquad\qquad \times \big(\mathbf{X}^H \mathbf{C}\mathbf{N}^H \boldsymbol{\Phi}\mathbf{d} + \mathbf{X}^H \mathbf{C}^H \mathbf{N}\boldsymbol{\Phi}^* \mathbf{d}^* + \mathbf{X}^H \mathbf{n}'\big)^H \Big\} \\
&= T_{\mathrm{sym}}^2 \mathrm{E}\Big\{ \big(\mathbf{X}^H \mathbf{C}\mathbf{N}^H \boldsymbol{\Phi}\mathbf{d} + \mathbf{X}^H \mathbf{C}^H \mathbf{N}\boldsymbol{\Phi}^* \mathbf{d}^* + \mathbf{X}^H \mathbf{n}'\big) \\
&\qquad\qquad \times \big(\mathbf{d}^H \boldsymbol{\Phi}^H \mathbf{N}\mathbf{C}^H \mathbf{X} + \mathbf{d}^T \boldsymbol{\Phi}^T \mathbf{N}^H \mathbf{C}\mathbf{X} + \mathbf{n}'^H \mathbf{X}\big) \Big\} \\
&= T_{\mathrm{sym}}^2 \mathbf{X}^H \mathbf{C}\mathrm{E}\{\mathbf{N}^H \boldsymbol{\Phi}\mathbf{d}\mathbf{d}^H \boldsymbol{\Phi}^H \mathbf{N}\} \mathbf{C}^H \mathbf{X} \\
&\quad + T_{\mathrm{sym}}^2 \mathbf{X}^H \mathbf{C}\mathrm{E}\{\mathbf{N}^H \boldsymbol{\Phi}\mathbf{d}\mathbf{d}^T \boldsymbol{\Phi}^T \mathbf{N}^H\} \mathbf{C}\mathbf{X} \\
&\quad + T_{\mathrm{sym}}^2 \mathbf{X}^H \mathbf{C}\mathrm{E}\{\mathbf{N}^H \boldsymbol{\Phi}\mathbf{d}\mathbf{n}'^H\} \mathbf{X} \\
&\quad + T_{\mathrm{sym}}^2 \mathbf{X}^H \mathbf{C}^H \mathrm{E}\{\mathbf{N}\boldsymbol{\Phi}^* \mathbf{d}^* \mathbf{d}^H \boldsymbol{\Phi}^H \mathbf{N}\} \mathbf{C}^H \mathbf{X} \\
&\quad + T_{\mathrm{sym}}^2 \mathbf{X}^H \mathbf{C}^H \mathrm{E}\{\mathbf{N}\boldsymbol{\Phi}^* \mathbf{d}^* \mathbf{d}^T \boldsymbol{\Phi}^T \mathbf{N}^H\} \mathbf{C}\mathbf{X} \\
&\quad + T_{\mathrm{sym}}^2 \mathbf{X}^H \mathbf{C}^H \mathrm{E}\{\mathbf{N}\boldsymbol{\Phi}^* \mathbf{d}^* \mathbf{n}'^H\} \mathbf{X} \\
&\quad + T_{\mathrm{sym}}^2 \mathbf{X}^H \mathrm{E}\{\mathbf{n}'\mathbf{d}^H \boldsymbol{\Phi}^H \mathbf{N}\} \mathbf{C}^H \mathbf{X} \\
&\quad + T_{\mathrm{sym}}^2 \mathbf{X}^H \mathrm{E}\{\mathbf{n}'\mathbf{d}^T \boldsymbol{\Phi}^T \mathbf{N}^H\} \mathbf{C}\mathbf{X} \\
&\quad + T_{\mathrm{sym}}^2 \mathbf{X}^H \mathrm{E}\{\mathbf{n}'\mathbf{n}'^H\} \mathbf{X}.
\end{aligned}
$$

We know and with $\mathrm{E}\{n_i n_j\} = \mathrm{E}\left\{n_i^* n_j^*\right\} = 0$ for $i,j \in \mathbb{Z}$ and for complex zero-mean n_i, n_j. Further we known from the Isserlis' theorem [126] that for Gaussian random variables $\mathrm{E}\{n_i n_j n_k\} =$

0 holds, hence

$$
\begin{aligned}
\mathrm{E}\left\{\boldsymbol{\nu}\boldsymbol{\nu}^H\right\} = {} & T_{\mathrm{sym}}^2 \mathbf{X}^H \mathbf{C}\mathrm{E}\left\{\mathbf{N}^H\boldsymbol{\Phi}\mathbf{d}\mathbf{d}^H\boldsymbol{\Phi}^H\mathbf{N}\right\}\mathbf{C}^H\mathbf{X} \\
& + T_{\mathrm{sym}}^2 \mathbf{X}^H\mathbf{C}^H\mathrm{E}\left\{\mathbf{N}\boldsymbol{\Phi}^*\mathbf{d}^*\mathbf{d}^T\boldsymbol{\Phi}^T\mathbf{N}^H\right\}\mathbf{C}\mathbf{X} \\
& + T_{\mathrm{sym}}^2\mathbf{X}^H\mathrm{E}\left\{\mathbf{n}'\mathbf{n}'^H\right\}\mathbf{X} \\
= {} & 2T_{\mathrm{sym}}\sigma_n^2\mathbf{X}^H\mathbf{C}\mathbf{S}\mathbf{C}^H\mathbf{X} \\
& + \sigma_n^4\left(\bar{\mathbf{x}}^*\bar{\mathbf{x}}^T + \mathbf{X}^H\mathbf{X}\right),
\end{aligned}
$$

where

$$
[\mathbf{S}]_{i,i} = \sum_{k=1}^K \sum_{l=1}^K \mathrm{E}\left\{d_k d_l^*\right\}\varphi_{k,i}\varphi_{l,i}^*.
$$

∎

B.1.2 SINR for an Ideal NOFDM Signaling

For a single decision variable z_m we get

$$
\begin{aligned}
z_k = {} & T_{\mathrm{sym}}\mathbf{w}_k^T\mathbf{X}^H\mathbf{C}^H\mathbf{C}\boldsymbol{\Psi}\left(\mathbf{d}\odot\mathbf{d}^*\right) \\
& + T_{\mathrm{sym}}\mathbf{w}_k^T\mathbf{X}^H\mathbf{C}^H\mathbf{C}\tilde{\boldsymbol{\Psi}}\left(\mathbf{d}\tilde{\otimes}\mathbf{d}^*\right) \\
& + T_{\mathrm{sym}}\mathbf{w}_k^T\mathbf{X}^H\mathbf{C}\mathbf{N}^H\boldsymbol{\Phi}\mathbf{d} \\
& + T_{\mathrm{sym}}\mathbf{w}_k^T\mathbf{X}^H\mathbf{C}^H\mathbf{N}\boldsymbol{\Phi}^*\mathbf{d}^* \\
& + T_{\mathrm{sym}}\mathbf{w}_k^T\mathbf{X}^H\mathbf{n}',
\end{aligned}
$$

where $\mathbf{w}_k^T$ is the kth row of $\mathbf{W}$. When we consider ideal NOFDM, that is the subcarriers are not overlapping and, hence, are mutually orthogonal, we know that $\tilde{\boldsymbol{\Psi}} = \mathbf{0}$. Hence, the SINR of ideal NOFDM is represented by its SNR.

When we consider ideal NOFDM, that is that the subcarriers are not overlapping and, hence, are ideal mutually orthogonal, and when we consider that $T_{\mathrm{sym}}\mathbf{W}\mathbf{X}^H\mathbf{C}^H\mathbf{C}\boldsymbol{\Psi} = \mathbf{I}_{K\times K}$, so that $\mathbf{W}$ is the pseudo inverse of $T_{\mathrm{sym}}\mathbf{X}^H\mathbf{C}^H\mathbf{C}\boldsymbol{\Psi}$, we know that $\tilde{\boldsymbol{\Psi}} = \mathbf{0}$ and that

$$
\hat{\boldsymbol{\psi}}_k' = T_{\mathrm{sym}}\mathbf{w}_k^T\mathbf{X}^H \approx \frac{\boldsymbol{\psi}_k'^H}{\boldsymbol{\psi}_k'^H\boldsymbol{\psi}_k'}, \tag{B.1}
$$

where $\boldsymbol{\psi}_k'$ is the kth column of $\boldsymbol{\Psi}' = \mathbf{C}^H\mathbf{C}\boldsymbol{\Psi}$. Therefore, we can simplify the previous equation to

$$
z_k = \hat{\boldsymbol{\psi}}_k'^H\boldsymbol{\Psi}'\left(\mathbf{d}\odot\mathbf{d}^*\right) + \hat{\boldsymbol{\psi}}_k'^H\mathbf{N}^H\boldsymbol{\Phi}'\mathbf{d} + \hat{\boldsymbol{\psi}}_k'^H\mathbf{N}\boldsymbol{\Phi}'^*\mathbf{d}^* + \hat{\boldsymbol{\psi}}_k'^H\mathbf{n}',
$$

where $\boldsymbol{\Phi}' = \mathbf{C}\boldsymbol{\Phi}$. With $\hat{\boldsymbol{\psi}}_k'^H\boldsymbol{\Psi}'\left(\mathbf{d}\odot\mathbf{d}^*\right) = |d_k|^2$ we obtain

$$
z_k = \underbrace{|d_k|^2}_{=:\alpha_k} + \underbrace{\hat{\boldsymbol{\psi}}_k'^H\mathbf{N}^H\boldsymbol{\Phi}'\mathbf{d} + \hat{\boldsymbol{\psi}}_k'^H\mathbf{N}\boldsymbol{\Phi}'^*\mathbf{d}^* + \hat{\boldsymbol{\psi}}_k'^H\mathbf{n}'}_{=:\nu_k},
$$

where we can see that the signal-by-noise, noise-by-signal, and noise-by-noise terms are projected onto the detection space spanned by $\left\{\hat{\boldsymbol{\psi}}_k'\right\}$.

Note that for an ideal NOFDM signal where the subcarriers are ideally separated in frequency

domain, $\frac{\boldsymbol{\psi}_k'^H}{||\boldsymbol{\psi}_k'||^2}\boldsymbol{\Phi}'\mathbf{d} = \frac{\boldsymbol{\psi}_k'^H}{||\boldsymbol{\psi}_k'||^2}d_k\boldsymbol{\varphi}_k'$, where $\boldsymbol{\varphi}_k'$ is the kth column of $\boldsymbol{\Phi}'$, we obtain

$$z_k \approx |d_k|^2 + d_k \frac{\boldsymbol{\psi}_k'^H}{\boldsymbol{\psi}_k'^H\boldsymbol{\psi}_k'}\mathbf{N}^H\boldsymbol{\varphi}_k' + d_k^* \frac{\boldsymbol{\psi}_k'^H}{\boldsymbol{\psi}_k'^H\boldsymbol{\psi}_k'}\mathbf{N}\boldsymbol{\varphi}_k'^* + \frac{\boldsymbol{\psi}_k'^H}{\boldsymbol{\psi}_k'^H\boldsymbol{\psi}_k'}\mathbf{n}',$$

where $\boldsymbol{\varphi}_k'$ is the kth column of $\boldsymbol{\Phi}'$. It needs to be noted that in this ideal case the signal-by-noise and noise-by-signal terms are only dependent on the transmitted data symbol d_k, but not on the transmitted data of the other subcarriers.

The SNR of the decision vector $\mathbf{z}$ for an ideal NOFDM signalling is given as

$$\text{SNR} = \frac{\sum_{k=1}^K \text{E}\left\{|d_k|^4\right\}}{\sum_{k=1}^K \text{E}\left\{\nu_k\nu_k^*\right\}}$$

where the expectation operator $\text{E}\left\{\cdot\right\}$ is taken in respect to the noise $\{n_i\}$.

Mean

For optimization and analysis of detectors, we need to derive noise statistics. The conditioned mean $\text{E}\left\{\nu_k|\mathbf{d}\right\}$ is given as

$$\text{E}\left\{\nu_k|\mathbf{d}\right\} = \text{E}\left\{\hat{\boldsymbol{\psi}}_k'^H\mathbf{N}^H\boldsymbol{\Phi}'\mathbf{d} + \hat{\boldsymbol{\psi}}_k'^H\mathbf{N}\boldsymbol{\Phi}'^*\mathbf{d}^* + \hat{\boldsymbol{\psi}}_k'^H\mathbf{n}'\right\}.$$

With $\text{E}\left\{n_i\right\} = 0$ the equation simplifies to

$$\begin{aligned}\text{E}\left\{\nu_k|\mathbf{d}\right\} &= \text{E}\left\{\hat{\boldsymbol{\psi}}_k'^H\mathbf{n}'\right\} \\ &= \frac{\sigma_n^2}{T_{\text{sym}}}\sum_{i=-\infty}^{+\infty}\hat{\psi}_{k,i}'^*.\end{aligned}$$

With $\hat{\boldsymbol{\psi}}_k' \approx \frac{\boldsymbol{\psi}_k'^H}{\boldsymbol{\psi}_k'^H\boldsymbol{\psi}_k'}$ and ideal NOFDM signaling we can approximate $\text{E}\left\{\nu_k|\mathbf{d}\right\}$ as in the previous equation and, finally, obtain

$$\text{E}\left\{\nu_k|\mathbf{d}\right\} = \frac{\sigma_n^2}{T_{\text{sym}}}\frac{||\varphi_{k,i}'||^2}{||\psi_{k,i}'||^2}.$$

$\blacksquare$

Correlation

The conditioned correlation $\text{E}\left\{\nu_k\nu_l^*|\mathbf{d}\right\}$ is given

$$\begin{aligned}\text{E}\left\{\nu_k\nu_l^*|\mathbf{d}\right\} = \text{E}\Big\{&\left(\hat{\boldsymbol{\psi}}_k'^H\mathbf{N}^H\boldsymbol{\Phi}'\mathbf{d} + \hat{\boldsymbol{\psi}}_k'^H\mathbf{N}\boldsymbol{\Phi}'^*\mathbf{d}^* + \hat{\boldsymbol{\psi}}_k'^H\mathbf{n}'\right) \\ &\times \left(\hat{\boldsymbol{\psi}}_l'^H\mathbf{N}^H\boldsymbol{\Phi}'\mathbf{d} + \hat{\boldsymbol{\psi}}_l'^H\mathbf{N}\boldsymbol{\Phi}'^*\mathbf{d}^* + \hat{\boldsymbol{\psi}}_l'^H\mathbf{n}'\right)^H\Big\}.\end{aligned}$$

When expanding the terms, we obtain

$$
\begin{aligned}
\mathrm{E}\left\{\nu_k\nu_l^*|\mathbf{d}\right\} = \,& \mathrm{E}\left\{\hat{\boldsymbol{\psi}}_k'^H\mathbf{N}^H\boldsymbol{\Phi}'\mathbf{d}\mathbf{d}^H\boldsymbol{\Phi}'^H\mathbf{N}\hat{\boldsymbol{\psi}}_l'\right\} \\
&+ \mathrm{E}\left\{\hat{\boldsymbol{\psi}}_k'^H\mathbf{N}^H\boldsymbol{\Phi}'\mathbf{d}\mathbf{d}^T\boldsymbol{\Phi}'^T\mathbf{N}^H\hat{\boldsymbol{\psi}}_l'\right\} \\
&+ \mathrm{E}\left\{\hat{\boldsymbol{\psi}}_k'^H\mathbf{N}^H\boldsymbol{\Phi}'\mathbf{d}\mathbf{n}'^H\hat{\boldsymbol{\psi}}_l'\right\} \\
&+ \mathrm{E}\left\{\hat{\boldsymbol{\psi}}_k'^H\mathbf{N}\boldsymbol{\Phi}'^*\mathbf{d}^*\mathbf{d}^H\boldsymbol{\Phi}'^H\mathbf{N}\hat{\boldsymbol{\psi}}_l'\right\} \\
&+ \mathrm{E}\left\{\hat{\boldsymbol{\psi}}_k'^H\mathbf{N}\boldsymbol{\Phi}'^*\mathbf{d}^*\mathbf{d}^T\boldsymbol{\Phi}'^T\mathbf{N}^H\hat{\boldsymbol{\psi}}_l'\right\} \\
&+ \mathrm{E}\left\{\hat{\boldsymbol{\psi}}_k'^H\mathbf{N}\boldsymbol{\Phi}'^*\mathbf{d}^*\mathbf{n}'^H\hat{\boldsymbol{\psi}}_l'\right\} \\
&+ \mathrm{E}\left\{\hat{\boldsymbol{\psi}}_k'^H\mathbf{n}'\mathbf{d}^H\boldsymbol{\Phi}'^H\mathbf{N}\hat{\boldsymbol{\psi}}_l'\right\} \\
&+ \mathrm{E}\left\{\hat{\boldsymbol{\psi}}_k'^H\mathbf{n}'\mathbf{d}^T\boldsymbol{\Phi}'^T\mathbf{N}^H\hat{\boldsymbol{\psi}}_l'\right\} \\
&+ \mathrm{E}\left\{\hat{\boldsymbol{\psi}}_k'^H\mathbf{n}'\mathbf{n}'^H\hat{\boldsymbol{\psi}}_l'\right\}.
\end{aligned}
$$

With $\mathrm{E}\left\{n_in_j\right\} = \mathrm{E}\left\{n_i^*n_j^*\right\} = 0$ for $i,j \in \mathbb{Z}$ and for complex zero-mean n_i, n_j and $\mathrm{E}\left\{n_in_jn_k\right\} = 0$ for Gaussian random variables we get

$$
\begin{aligned}
\mathrm{E}\left\{\nu_k\nu_l^*|\mathbf{d}\right\} = \,& \mathrm{E}\left\{\hat{\boldsymbol{\psi}}_k'^H\mathbf{N}^H\boldsymbol{\Phi}'\mathbf{d}\mathbf{d}^H\boldsymbol{\Phi}'^H\mathbf{N}\hat{\boldsymbol{\psi}}_l'\right\} \\
&+ \mathrm{E}\left\{\hat{\boldsymbol{\psi}}_k'^H\mathbf{N}\boldsymbol{\Phi}'^*\mathbf{d}^*\mathbf{d}^T\boldsymbol{\Phi}'^T\mathbf{N}^H\hat{\boldsymbol{\psi}}_l'\right\} \\
&+ \mathrm{E}\left\{\hat{\boldsymbol{\psi}}_k'^H\mathbf{n}'\mathbf{n}'^H\hat{\boldsymbol{\psi}}_l'\right\}.
\end{aligned}
$$

When rewriting the equation in index notation, we obtain

$$
\begin{aligned}
\mathrm{E}\left\{\nu_k\nu_l^*|\mathbf{d}\right\} = \,& \sum_{j=-\infty}^{+\infty}\hat{\psi}_{l,j}'\sum_{i=-\infty}^{+\infty}\hat{\psi}_{k,i}'^*\sum_{p=1}^{K}d_p\varphi_{p,i}'\sum_{q=1}^{K}d_q^*\varphi_{q,j}'^*\mathrm{E}\left\{n_i^*n_j\right\} \\
&+ \sum_{j=-\infty}^{+\infty}\hat{\psi}_{l,j}'\sum_{i=-\infty}^{+\infty}\hat{\psi}_{k,i}'^*\sum_{p=1}^{K}d_p^*\varphi_{p,i}'^*\sum_{q=1}^{K}d_q\varphi_{q,j}'\mathrm{E}\left\{n_in_j^*\right\} \\
&+ \sum_{i=-\infty}^{+\infty}\hat{\psi}_{k,i}'^*\sum_{j=-\infty}^{+\infty}\hat{\psi}_{l,j}'\mathrm{E}\left\{n_in_i^*n_jn_j^*\right\} \\
=\,& \frac{\sigma_n^2}{T_{\mathrm{sym}}}\sum_{p=1}^{K}\sum_{q=1}^{K}d_pd_q^*\sum_{i=-\infty}^{+\infty}\hat{\psi}_{l,i}'\hat{\psi}_{k,i}'^*\varphi_{p,i}'\varphi_{q,i}'^* \\
&+ \frac{\sigma_n^2}{T_{\mathrm{sym}}}\sum_{p=1}^{K}\sum_{q=1}^{K}d_p^*d_q\sum_{i=-\infty}^{+\infty}\hat{\psi}_{l,i}'\hat{\psi}_{k,i}'^*\varphi_{p,i}'^*\varphi_{q,i}' \\
&+ \frac{\sigma_n^4}{T_{\mathrm{sym}}^2}\sum_{i=-\infty}^{+\infty}\hat{\psi}_{k,i}'^*\sum_{j=-\infty}^{+\infty}\hat{\psi}_{l,j}'\left(1+\delta_{i-j}\right).
\end{aligned}
$$

For non-overlapping subcarriers, so that $\varphi_{p,i}^*\varphi_{q,i} = 0$ for $p \neq q$, we can rewrite the previous equation to

$$
\begin{aligned}
\mathrm{E}\left\{\nu_k\nu_l^*|\mathbf{d}\right\} = {} & \frac{\sigma_n^2}{T_{\text{sym}}}\sum_{p=1}^{K}|d_p|^2\sum_{i=-\infty}^{+\infty}\hat{\psi}_{l,i}'\hat{\psi}_{k,i}'^*|\varphi_{p,i}'|^2 \\
& + \frac{\sigma_n^2}{T_{\text{sym}}}\sum_{p=1}^{K}|d_p|^2\sum_{i=-\infty}^{+\infty}\hat{\psi}_{l,i}'\hat{\psi}_{k,i}'^*|\varphi_{p,i}'|^2 \\
& + \frac{\sigma_n^4}{T_{\text{sym}}^2}\sum_{i=-\infty}^{+\infty}\hat{\psi}_{k,i}'^*\sum_{j=-\infty}^{+\infty}\hat{\psi}_{l,j}' + \frac{\sigma_n^4}{T_{\text{sym}}^2}\sum_{i=-\infty}^{+\infty}\hat{\psi}_{k,i}'^*\hat{\psi}_{l,i}'.
\end{aligned}
$$

For $\left\{\hat{\boldsymbol{\psi}}_k'\right\}$ being mutually orthogonal, which can be assumed due to (B.1) and $\{\boldsymbol{\psi}_k'\}$ being mutually orthogonal, the equation can be rewritten to

$$
\begin{aligned}
\mathrm{E}\left\{\nu_k\nu_l^*|\mathbf{d}\right\} = {} & 2\delta_{k-l}\frac{\sigma_n^2}{T_{\text{sym}}}\sum_{p=1}^{K}|d_p|^2\sum_{i=-\infty}^{+\infty}|\hat{\psi}_{k,i}'|^2|\varphi_{p,i}'|^2 \\
& + \frac{\sigma_n^4}{T_{\text{sym}}^2}\sum_{i=-\infty}^{+\infty}\hat{\psi}_{k,i}'^*\sum_{j=-\infty}^{+\infty}\hat{\psi}_{l,j}' + \delta_{k-l}\frac{\sigma_n^4}{T_{\text{sym}}^2}\sum_{i=-\infty}^{+\infty}|\hat{\psi}_{k,i}'|^2.
\end{aligned}
$$

If we assume that $\left(\hat{\boldsymbol{\psi}}_k' \odot \hat{\boldsymbol{\psi}}_k'^*\right)$ is orthogonal to $\left(\boldsymbol{\varphi}_p' \odot \boldsymbol{\varphi}_p'^*\right)$ for $p \neq k$, e.g. if $\hat{\boldsymbol{\psi}}_k'$ does not overlap with $\boldsymbol{\varphi}_p$ for $p \neq k$,we get

$$
\begin{aligned}
\mathrm{E}\left\{\nu_k\nu_l^*|\mathbf{d}\right\} = {} & 2\delta_{k-l}\frac{\sigma_n^2}{T_{\text{sym}}}|d_k|^2\sum_{i=-\infty}^{+\infty}|\hat{\psi}_{k,i}'|^2|\varphi_{k,i}'|^2 \\
& + \frac{\sigma_n^4}{T_{\text{sym}}^2}\sum_{i=-\infty}^{+\infty}\hat{\psi}_{k,i}'^*\sum_{i=-\infty}^{+\infty}\hat{\psi}_{l,i}' + \delta_{k-l}\frac{\sigma_n^4}{T_{\text{sym}}^2}\sum_{i=-\infty}^{+\infty}|\hat{\psi}_{k,i}'|^2.
\end{aligned}
\tag{B.2}
$$

Note that the first term in the second line resembles $\mathrm{E}\left\{\nu_k|\mathbf{d}\right\}\mathrm{E}\left\{\nu_l^*|\mathbf{d}\right\}$.

With $\hat{\boldsymbol{\psi}}_k' \approx \frac{\boldsymbol{\psi}_k'^H}{\boldsymbol{\psi}_k'^H\boldsymbol{\psi}_k'}$ and ideal NOFDM signaling we can approximate $\mathrm{E}\left\{\nu_k\nu_l^*|\mathbf{d}\right\}$ as in (B.2) and, finally, obtain

$$
\begin{aligned}
\mathrm{E}\left\{\nu_k\nu_l^*|\mathbf{d}\right\} \approx {} & 2\delta_{k-l}\frac{\sigma_n^2}{T_{\text{sym}}}|d_k|^2\frac{\sum_{i=-\infty}^{+\infty}|\varphi_{k,i}'|^6}{||\boldsymbol{\psi}_k'||^4} \\
& + \frac{\sigma_n^4}{T_{\text{sym}}^2}\frac{||\boldsymbol{\varphi}_k'||^2}{||\boldsymbol{\psi}_k'||^2}\frac{||\boldsymbol{\varphi}_l'||^2}{||\boldsymbol{\psi}_l'||^2} + \delta_{k-l}\frac{\sigma_n^4}{T_{\text{sym}}^2}\frac{1}{||\boldsymbol{\psi}_k'||^2}.
\end{aligned}
$$

∎

B.2 Condition Numbers of Quasi-Unitary Matrices

The $M \times K$ matrix $\mathbf{P}$ can be expanded into

$$\mathbf{P} = \mathbf{U}\boldsymbol{\Sigma}\mathbf{V}^{H}$$

using the singular value decomposition (SVD) [60]. The matrices $\mathbf{U}$ and $\mathbf{V}$ are unitary by definition. The matrix $\boldsymbol{\Sigma}$ is a $M \times K$ diagonal matrix with the singular values $\{\sigma_i\}$ of $\mathbf{P}$ as diagonal elements. The maximal and the minimal singular values are $\sigma_{\max}$ and $\sigma_{\min}$, respectively, For

$$\text{cond}\,\{\mathbf{P}\} = \frac{\sigma_{\max}}{\sigma_{\min}} = 1$$

to hold, all singular values $\{\sigma_i\}$ need to be equal. With this constraint $\boldsymbol{\Sigma}$ is quasi-unitary. If we multiply $\mathbf{V}^{H}$ from the right to the quasi-unitary $\boldsymbol{\Sigma}$, we can observe that $\boldsymbol{\Sigma}\mathbf{V}^{H}$ is quasi-unitary too. This is obvious when considering that by this multiplication the orthogonal columns of $\mathbf{V}^{H}$ become scaled by their respective singular value, which does not change the orthogonality due to identical singular values. If we multiply $\mathbf{U}$ from the left to $\boldsymbol{\Sigma}\mathbf{V}^{H}$ the orthogonality in the columns stays unchanged due to the unitarity of $\mathbf{U}$. This becomes clear, when considering that $\mathbf{U}$ does perform a rotation onto $\boldsymbol{\Sigma}\mathbf{V}^{H}$. Such a rotation does not change the orthogonality. Hence, $\mathbf{U}\boldsymbol{\Sigma}\mathbf{V}^{H}$ leads to an quasi-unitary matrix!

■

B.3 Real Valued Co-Term Matrices of Real Valued Projection Filters

The elements of the co-term matrix $\mathbf{P}$ are defined in (2.40) to be

$$
\begin{aligned}
[\mathbf{P}]_{m,k} &= \left\langle H_m(j\omega)G_m^*(j\omega); |C(j\omega)|^2 |\Phi_k(j\omega)|^2 \right\rangle \\
&= \int_{\omega=-\infty}^{+\infty} H_m^*(j\omega)G_m(j\omega) |C(j\omega)|^2 |\Phi_k(j\omega)|^2 \, d\omega,
\end{aligned}
\tag{B.3}
$$

where $H_m(j\omega)$ and $G_m(j\omega)$ are the frequency responses of the input projection filters of the corresponding mth receiver channel. $C(j\omega)$ and $\Phi_k(j\omega)$ are the frequency response of the communication channel and the kth basis signal, respectively.

For real-valued filter impulse responses the relationships

$$
\begin{aligned}
H_m(-j\omega) &= H_m^*(j\omega) \text{ and} \\
G_m(-j\omega) &= G_m^*(j\omega)
\end{aligned}
$$

hold [33].

Due to linearity and the aforementioned relationships, (B.3) can be rewritten as

$$
\begin{aligned}
[\mathbf{P}]_{m,k} = &\int_{\omega=-\infty}^{0} H_m(-j\omega)G_m^*(-j\omega) |C(j\omega)|^2 |\Phi_k(j\omega)|^2 \, d\omega \\
&+ \int_{\omega=0}^{+\infty} H_m^*(j\omega)G_m(j\omega) |C(j\omega)|^2 |\Phi_k(j\omega)|^2 \, d\omega.
\end{aligned}
$$

When substituting $\nu = -\omega$, swapping the boundaries of the first integral, and keeping in mind that $|C(j\omega)|^2$ and $|\Phi_k(j\omega)|^2$ are symmetric we get

$$
\begin{aligned}
[\mathbf{P}]_{m,k} = &\int_{\nu=0}^{+\infty} H_m(j\nu)G_m^*(j\nu) |C(j\nu)|^2 |\Phi_k(j\nu)|^2 \, d\nu \\
&+ \int_{\omega=0}^{+\infty} H_m^*(j\omega)G_m(j\omega) |C(j\omega)|^2 |\Phi_k(j\omega)|^2 \, d\omega
\end{aligned}
$$

Comparing the first integral with the second, it becomes obvious that their results form a complex conjugate pair. By adding those complex values the imaginary parts of the results cancel out, hence

$$
[\mathbf{P}]_{m,k} = 2 \int_{\omega=0}^{+\infty} \Re\{H_m(j\omega)G_m^*(j\omega)\} |C(j\omega)|^2 |\Phi_k(j\omega)|^2 \, d\omega.
$$

This proofs that for real valued projection filter impulse responses the inner-product defined in (2.40) results in real-valued coefficients!

∎

B.4 Orthogonality of Projection Filter Cross-Spectras

The elements of the co-term matrix $\mathbf{P}$ are defined in (2.40) to be

$$[\mathbf{P}]_{m,k} = \left\langle H_m(j\omega)G_m^*(j\omega); |C(j\omega)|^2 |\Phi_k(j\omega)|^2 \right\rangle$$
$$= \int_{\omega=-\infty}^{+\infty} H_m^*(j\omega)G_m(j\omega) |C(j\omega)|^2 |\Phi_k(j\omega)|^2 d\omega,$$

where $H_m(j\omega)$ and $G_m(j\omega)$ are the frequency responses of the input projection filters of the corresponding mth receiver channel. $C(j\omega)$ and $\Phi_k(j\omega)$ are the frequency response of the communication channel and the kth basis signal, respectively.

Using vector equivalents of the filter frequency responses and the symbol pulse shapes, $\mathbf{P}$ can be represented as the matrix multiplication of the filter cross-spectra matrix $\mathbf{X}$ and the signal basis matrix $\mathbf{\Phi}$. I.e. the co-term matrix $\mathbf{P}$ is given as

$$\mathbf{P} = \mathbf{X}^H \mathbf{\Phi}.$$

The elements of the cross-spectra matrix $\mathbf{X}$ are defined as

$$[\mathbf{X}]_{n,m} = H_m(j\omega_0 n) G_m^*(j\omega_0 n),$$

where $n = 1, \ldots, N$, N is the number of frequency bins, and ω_0 is the spacing between the frequency bins.

The elements of the signal basis matrix $\mathbf{\Phi}$ are defined as

$$[\mathbf{\Phi}]_{n,k} = |\Phi_k(j\omega_0 n)|^2,$$

where $k = 1, \ldots, K$.

It can be shown, that for $\mathbf{P}$ and $\mathbf{\Phi}$ being quasi-unitary, also $\mathbf{X}$ needs to be a quasi-unitary matrix. Using SVD we can decompose $\mathbf{X}^H$ to

$$\mathbf{X}^H = \mathbf{U}\mathbf{\Sigma}\mathbf{V}^H,$$

where the columns of $\mathbf{U}$ span the column space of $\mathbf{X}^H$, the first K columns of $\mathbf{V}$ span the row space of $\mathbf{X}^H$, the last $N - K$ columns of $\mathbf{V}$ span the nullspace of $\mathbf{X}^H$, the first M columns of $\mathbf{\Sigma}$ consist of the diagonal matrix with the singular values of $\mathbf{X}^H$ as diagonal elements, the last $N - M$ columns are zero vectors, and $N \geq M \geq K$ [60].

It is now to show, that $\mathbf{X}^H\mathbf{x}$ and $\mathbf{X}^H\mathbf{y}$ are mutually orthogonal when $\mathbf{x}$ and $\mathbf{y}$ are mutually orthogonal under some constraints on $\mathbf{X}^H$. Lets define some vectors $\mathbf{x_U}, \mathbf{x_\Sigma}, \mathbf{x_V}, \mathbf{y_U}, \mathbf{y_\Sigma}, \mathbf{y_V}$, so that

$$\mathbf{x_U} = \mathbf{U}\mathbf{x_\Sigma}$$
$$\mathbf{x_\Sigma} = \mathbf{\Sigma}\mathbf{x_V}$$
$$\mathbf{x_V} = \mathbf{V}^H\mathbf{x},$$

and for $\mathbf{y}$ correspondingly.

For $\mathbf{x_U}$ and $\mathbf{y_U}$ being mutually orthogonal, $\mathbf{x_\Sigma}$ and $\mathbf{y_\Sigma}$ need to be mutually orthogonal, due to the fact that $\mathbf{U}$ is unitary and does preserve inner-products and angles. For $\mathbf{x_V}$ and $\mathbf{y_V}$ being mutually orthogonal $\mathbf{x}$ and $\mathbf{y}$ need to be mutually orthogonal, since $\mathbf{V}$ is unitary too. Unfortunately, these two findings do not give any constrains at all.

But for $\mathbf{x_\Sigma}$ and $\mathbf{y_\Sigma}$ being mutually orthogonal, 1) the singular values of $\mathbf{X}^H$ need to be equal and 2) $\mathbf{x_V}$ and $\mathbf{y_V}$ need to be mutually orthogonal in the first M elements.

The first constraint is sufficient for $\mathbf{X}^H$ to be quasi-unitary, which proofs the given claim. An interpretation of this result is that the input filter cross-spectra need to be mutually orthogonal to each other!

The second constraint means that the vectors $\mathbf{x}$ and $\mathbf{y}$ need to be mutually orthogonal in the row space of $\mathbf{X}^H$. Additionally it tells us, that the energies of the filters need to be equal.

<div align="right">■</div>

B.5 Receiver Channel Output with Nonideal Multiplier

As in (3.15), the nonideal multiplication of two independent signals $x(t)$ and $y(t)$ can be modeled as

$$\mathcal{M}\left\{x(t), y(t)\right\} = \ h(t) * \left[\sum_{u=0}^{U}\sum_{v=0}^{u} c_{u-v,v} \left(g_x(t) * x(t)\right)^{u-v} \left(g_y(t) * y(t)\right)^{v}\right], \qquad (B.4)$$

where $g_x(t)$ and $g_y(t)$ are input filters, $h(t)$ is the output filter, and $\{c_{u-v,v}\}$ are the coefficients of the bivariate polynomial.

The mth receiver output y_m where the multiplication is modeled using (3.15) is given as

$$y_m = \int_{\lambda=0}^{T_{\text{sym}}} \mathcal{M}_m\left\{h_m(t) * r(t), g_m(t) * r(t)\right\} dt$$

$$= \int_{\lambda=0}^{T_{\text{sym}}} \left\{h(t) * \left[\sum_{u=0}^{U}\sum_{v=0}^{u} c_{u-v,v} \left(g_x(t) * h_m(t) * r(t)\right)^{u-v} \cdot \left(g_y(t) * g_m(t) * r(t)\right)^{v}\right]\right\} dt$$

$$= \sum_{u=0}^{U}\sum_{v=0}^{u} c_{u-v,v} \int_{\lambda=0}^{T_{\text{sym}}} \left\{h(t) * \left[\left(g_x(t) * h_m(t) * r(t)\right)^{u-v} \cdot \left(g_y(t) * g_m(t) * r(t)\right)^{v}\right]\right\} dt$$

$$= \sum_{u=0}^{U}\sum_{v=0}^{u} c_{u-v,v} \int_{\lambda=0}^{T_{\text{sym}}} \left\{h(t) * \left[\left(g_x(t) * h_m(t) * c(t) * s(t) + g_x(t) * h_m(t) * n(t)\right)^{u-v}\right.\right.$$

$$\times \ \left(g_y(t) * g_m(t) * c(t) * s(t) + g_y(t) * g_m(t) * n(t)\right)^{v}\Big]\Big\} dt.$$

Using the binomial theorem $(x + y)^n = \sum_{k=0}^{n}\binom{n}{k} x^{n-k}y^k$ we get

$$y_m = \sum_{u=0}^{U}\sum_{v=0}^{u} c_{u-v,v} \int_{\lambda=0}^{T_{\text{sym}}} \left\{h(t) * \left[\vphantom{\sum_{p=0}^{u-v}}\right.\right.$$

$$\sum_{p=0}^{u-v}\binom{u-v}{p} \left(g_x(t) * h_m(t) * c(t) * s(t)\right)^{u-v-p} \left(g_x(t) * h_m(t) * n(t)\right)^{p}$$

$$\times \ \sum_{q=0}^{v}\binom{v}{q} \left(g_y(t) * g_m(t) * c(t) * s(t)\right)^{v-q} \left(g_y(t) * g_m(t) * n(t)\right)^{q}\Big]\Big\} dt$$

$$= \sum_{u=0}^{U}\sum_{v=0}^{u} c_{u-v,v} \sum_{p=0}^{u-v}\sum_{q=0}^{v}\binom{u-v}{p}\binom{v}{q} \int_{\lambda=0}^{T_{\text{sym}}} \left\{h(t) * \left[\vphantom{\sum}\right.\right.$$

$$\left(g_x(t) * h_m(t) * c(t) * s(t)\right)^{u-v-p} \left(g_x(t) * h_m(t) * n(t)\right)^{p}$$

$$\times \ \left(g_y(t) * g_m(t) * c(t) * s(t)\right)^{v-q} \left(g_y(t) * g_m(t) * n(t)\right)^{q}\Big]\Big\} dt.$$

After substituting for the definition of the sent signal $s(t) = \sum_{k=1}^{K} d_k \phi_k(t)$ we obtain

$$y_m = \sum_{u=0}^{U} \sum_{v=0}^{u} c_{u-v,v} \sum_{p=0}^{u-v} \sum_{q=0}^{v} \binom{u-v}{p} \binom{v}{q} \int_{\lambda=0}^{T_{\text{sym}}} \left\{ h(t) * \left[\right. \right.$$

$$\left(g_x(t) * h_m(t) * c(t) * \sum_{k=1}^{K} d_k \phi_k(t) \right)^{u-v-p} (g_x(t) * h_m(t) * n(t))^p$$

$$\left. \times \left(g_y(t) * g_m(t) * c(t) * \sum_{l=1}^{L} d_l \phi_l(t) \right)^{v-q} (g_y(t) * g_m(t) * n(t))^q \left. \right] \right\} dt.$$

The multinomial theorem $\left(\sum_{i=1}^{I} x_i \right)^n = \sum_{\kappa_1 + \cdots + \kappa_I = n} (\kappa_1, \cdots, \kappa_I) \prod_{i=1}^{I} x_i^{\kappa_i}$ simplifies the equation to

$$y_m = \sum_{u=0}^{U} \sum_{v=0}^{u} c_{u-v,v} \sum_{p=0}^{u-v} \sum_{q=0}^{v} \binom{u-v}{p} \binom{v}{q} \int_{\lambda=0}^{T_{\text{sym}}} \left\{ h(t) * \left[\right. \right.$$

$$\sum_{\kappa_1 + \cdots + \kappa_K = u-v-p} \binom{u-v-p}{\kappa_1, \cdots, \kappa_K} \prod_{k=1}^{K} d_k^{\kappa_k} (g_x(t) * h_m(t) * c(t) * \phi_k(t))^{\kappa_k} (g_x(t) * h_m(t) * n(t))^p$$

$$\left. \times \sum_{\iota_1 + \cdots + \iota_K = v-q} \binom{v-q}{\iota_1, \cdots, \iota_K} \prod_{l=1}^{K} d_l^{\iota_l} (g_y(t) * g_m(t) * c(t) * \phi_l(t))^{\iota_l} (g_y(t) * g_m(t) * n(t))^q \left. \right] \right\} dt$$

$$= \sum_{u=0}^{U} \sum_{v=0}^{u} c_{u-v,v} \sum_{p=0}^{u-v} \sum_{q=0}^{v} \sum_{\kappa_1 + \cdots + \kappa_K = u-v-p} \sum_{\iota_1 + \cdots + \iota_K = v-q} \binom{u-v}{p} \binom{v}{q} \binom{u-v-p}{\kappa_1, \cdots, \kappa_K} \binom{v-q}{\iota_1, \cdots, \iota_K}$$

$$\times \int_{\lambda=0}^{T_{\text{sym}}} \left\{ h(t) * \left[\right. \right.$$

$$\prod_{k=1}^{K} d_k^{\kappa_k} (g_x(t) * h_m(t) * c(t) * \phi_k(t))^{\kappa_k} \prod_{l=1}^{K} d_l^{\iota_l} (g_y(t) * g_m(t) * c(t) * \phi_l(t))^{\iota_l}$$

$$\left. \times (g_x(t) * h_m(t) * n(t))^p (g_y(t) * g_m(t) * n(t))^q \left. \right] \right\} dt.$$

With the equality $\left(\prod_k x_k \right) \left(\prod_k y_k \right) = \prod_k x_k y_k$ the equation cn be rewritten to

$$y_m = \sum_{u=0}^{U} \sum_{v=0}^{u} c_{u-v,v} \sum_{p=0}^{u-v} \sum_{q=0}^{v} \sum_{\kappa_1 + \cdots + \kappa_K = u-v-p} \sum_{\iota_1 + \cdots + \iota_K = v-q} \binom{u-v}{p} \binom{v}{q} \binom{u-v-p}{\kappa_1, \cdots, \kappa_K} \binom{v-q}{\iota_1, \cdots, \iota_K}$$

$$\times \int_{\lambda=0}^{T_{\text{sym}}} \left\{ h(t) * \left[\right. \right.$$

$$\prod_{k=1}^{K} d_k^{\kappa_k + \iota_k} (g_x(t) * h_m(t) * c(t) * \phi_k(t))^{\kappa_k} (g_y(t) * g_m(t) * c(t) * \phi_k(t))^{\iota_k}$$

$$\left. \times (g_x(t) * h_m(t) * n(t))^p (g_y(t) * g_m(t) * n(t))^q \left. \right] \right\} dt.$$

Finally we obtain

$$
y_m = \sum_{u=0}^{U} \sum_{v=0}^{u} c_{u-v,v} \sum_{\kappa_1+\cdots+\kappa_K=u-v} \sum_{\iota_1+\cdots+\iota_K=v} \binom{u-v}{\kappa_1, \cdots, \kappa_K} \binom{v}{\iota_1, \cdots, \iota_K}
$$

$$
\times \int_{\lambda=0}^{T_{\text{sym}}} \Bigg\{ h(t) * \Bigg[
$$

$$
\prod_{k=1}^{K} d_k^{\kappa_k+\iota_k} \left(g_x(t) * h_m(t) * c(t) * \phi_k(t) \right)^{\kappa_k} \left(g_y(t) * g_m(t) * c(t) * \phi_k(t) \right)^{\iota_k}
$$

$$
\Bigg] \Bigg\} dt + \boldsymbol{\nu}.
$$

∎

C

Meta-Heuristic Algorithms

Meta-heuristic algorithms are tools for a strategic search for the *best* solution $\boldsymbol{\Phi}_0$ of an optimization problem. For whatever *best* stands for. In general the best solution is the solution with the minimal (or maximal[25]) cost $J(\boldsymbol{\Phi}_0)$. The cost of a solution is defined by a so called cost-function $f(\boldsymbol{\Phi})$, hence

$$J(\boldsymbol{\Phi}) = f(\boldsymbol{\Phi}).$$

A way of finding the best solution is by finding the roots of the gradient of the cost-function. In a more mathematical sense, this means to find $\boldsymbol{\Phi}_0$ for which

$$\frac{\partial f}{\partial \boldsymbol{\Phi}} \overset{!}{=} 0$$

holds. If $f(\boldsymbol{\Phi})$ is given analytically, and if $f(\boldsymbol{\Phi})$ is differentiable, a analytical expression of $\boldsymbol{\Phi}_0$ can be found. If there exist only a single solution for which $\frac{\partial f}{\partial \boldsymbol{\Phi}} \overset{!}{=} 0$ is true, the optimization problem is called *convex*, *non-convex* otherwise. If the problem is non-convex, the best solution $\boldsymbol{\Phi}_0$ is still the solution with the minimal cost compared to all the other possible solutions.

The aforementioned method for finding the best solution has the drawback, that it does not work if the analytical gradient is not known or does not exist (differentiability). Also if the problem is non-convex, there might be too many possible solutions which might make it hard to find the best one. Here, meta-heuristic algorithms come into play: they do only require the cost-function and use heuristic search strategies to find the best solution.

For efficient search, those algorithms need to be configured to make a trade off between exploration and exploitation. Exploration is the capability of the algorithm to explore the full search space and to find new possible solutions, whereas exploitation denotes to the capability of the algorithm to refine found possible solution and to converge on the best one.

In this appendix a short overview of meta-heuristic algorithms is given with a focus on three algorithms which are used in this work: the *Hill Climbing* algorithm (see Appendix C.1), the *Differential Evolution* algorithm (see Appendix C.2), and the *Particle Swarm Optimization* algorithm (see Appendix C.3). A more elaborate overview of many meta-heuristic algorithms with easy to use code samples can be found in [69].

---

[25] "minimal" and "maximal" can be seen interchangeable in optimization and only depend on how *best* is interpreted. For sake of simplicity we will stick with "minimal" cost and minimizing the cost-function.

C.1 Hill Climbing

The *Hill Climbing*[26] (HC) algorithm does only work properly for convex cost-functions, where it is ensured that he does find the global optimal solution if the algorithm is run long enough. For non-convex problems the algorithm might converge to a local optimum, depending on its initialization, tendency to explore or exploit.

Starting with a random initial starting point, it heuristically samples the cost-function in the proximity of this point. If one of the sampled points has a lower cost, this point will be set to the new starting point for the next iteration. These steps are done until the algorithm converges or a before defined maximal number of iterations is reached. This algorithm can be interpreted as a heuristic version of a gradient-decent algorithm. In Listing C.3 a MATLAB pseudo code of the used HC algorithm (*Hill Climbing with steepest gradient*) is shown.

The presented HC algorithm can be configured using some parameters: `ITERATIONS` sets the number of iterations, `SAMPLES` sets the number of samples evaluated in the proximity of the best solution found so far to sample the gradient, `PARAMETERS` sets the dimension of the parameter search space, and `SIGMA` sets the deviation of the gradient evaluation samples from the so far best found solution. The `cost_function()` defines the optimization problem and is a function which needs to be minimized by finding the optimal solution.

---

[26] The *Hill Climbing* algorithm has his name by searching for the "maximal" cost, hence metaphorically "climbing up the cost hill". Because this work focuses on minimizing the cost, the algorithm should maybe be renamed to *Crater Sliding* or *Dungeon Crawling*.

```
1    % HILL CLIMBING WITH STEEPEST GRADIENT
2
3    % Setting Algorithm Parameters:
4    % ############################################################################
5    N_iterations = ITERATIONS;                        % number of interations
6    N_samples = SAMPLES;                              % number of neighborhood sam-
7                                                      % ples
8    N_parameters = PARAMETERS;                        % dimension of parameter space
9    sigma = SIGMA;                                    % spreading of the neighbor-
10                                                     % hood samples
11
12   % Initialization:
13   % ############################################################################
14   Best = random_init(N_parameters);                % random initialization of
15                                                     % best solution
16   Best_cost = cost_function(Best);                  % set cost of initial best so-
17                                                     % lution
18   R = zeros(N_parameters,N_samples);               % initializing random neigh-
19                                                     % borhood samples
20   R_cost = Inf*ones(1,N_samples);                  % setting initial costs of
21                                                     % random neighborhood sample
22   S = Best;                                         % initialize best neighborhood
23                                                     % sample
24   S_cost = Best_cost;                               % initialize best neighborhood
25                                                     % sample cost
26
27   % Iterations:
28   % ############################################################################
29   for iter = 1:N_iterations
30
31     % Gradient Sampling:
32     % ############################################################################
33     for samp = 1:N_samples
34       R(:,samp) = Best + random_offset(mu);         % random sample in the neigh-
35                                                      % borhood of best solution
36       R_cost(samp) = cost_function(S(:,samp));      % obtaining the cost of the
37                                                      % random sample
38     end
39
40     % Searching for the Solution with Steepest Gardient:
41     % ############################################################################
42     S = Best;                                        % setting the actual best
43                                                      % neighboorhood solution
44     S_cost = Best_cost;                              % setting the cost of the ac-
45                                                      % tual best neighboorhood so-
46                                                      % lution
47     for samp = 1:N_samples
48       if R_cost(samp) < S_cost                       % comparing actual best neigh-
49                                                      % borhood solution with a
50                                                      % neighborhood solution
51         S = R(:,samp);                               % storing new best neighbor-
52                                                      % hood if better one found
53         S_cost = R_cost;                             % storing the new best neigh-
54                                                      % borhood sample cost
55       end
56     end
57
58     % Storing the Best Solution:
59     % ############################################################################
60     if S_cost < Best_cost                            % comparing overall best solu-
61                                                      % tion with best found neigh-
62                                                      % borhood solution
63       Best = S;                                      % storing new overall best so-
64                                                      % lution if one found
65       Best_cost = S_cost;                            % storing the new overall best
66                                                      % solution cost
67     end
68
69   end
```

Listing C.1: MATLAB pseudo code of the Hill Climbing algorithm with steepest gradient.

C.2 Differential Evolution

The *Differential Evolution* algorithm is a population based algorithm. Instead of remembering only a single best solution from iteration to iteration, it remembers a full set of solutions. Such a set is called population. Population based methods are summarized in the field of *Evolutionary Computation*. Population based methods use nature as model, eg. from biology, genetics, or evolution and generate or revise a new population per iteration based on the results from older ones. Well known *Evolutionary Computation* algorithms are th *Genetic Algorithm*, *Evolution Strategies*, and the *Differential Evolution* (DE) algorithm.

From each iteration (or called generation in *Evolutionary Computation*) a new population (the children) for the next iteration is generated from the actual population (the parents) using concepts as mutation, crossover, and selection. **Mutation:** A child $Q(i)$ is generated by linear combination of three randomly picked parents (A, B, and C), hence $Q(i) = A + \alpha (B - C)$, where α (commonly set between 0.5 and 1.0) is the mutation rate. The idea is, that if the parent generation is widely spread in the parameter space, the new children will also be widely spread after generation. If the parents are more condensed, the mutation to generate the children will be small. This results in an adaptive mutation where at the end of the runtime the population converges to the best solution. **Crossover:** The child $Q(i)$ is crossed over with its parent $R(i)$. This is done by copying a random number of parameters of the parent. This ensures that in each child $Q(i)$ some parameters from its parent $R(i)$ survives. **Selection:** the cost (or called fitness in *Evolutionary Computation*) of each child $Q(i)$ is compared to the cost of its parent $R(i)$. If the child has a smaller cost than its parent, the child replaces the parent for the next iteration, otherwise the parent stays in the population. This is a selection by based on the survival of the fittest.

The presented DE algorithm can be configured using some parameters: `GENERATIONS` sets the number of iterations, `POPULATION` sets the size of the population, `PARAMETERS` sets the dimension of the parameter search space, and `ALPHA` sets the mutation rate α. The `cost_function()` defines the optimization problem and is a function which needs to be minimized by finding the optimal solution.

```
 1    % DIFFERENTIAL EVOLUTION
 2
 3    % Setting Algorithm Parameters:
 4    % ##########################################################################
 5    N_generations = GENERATIONS;                      % number of generations (iter-
 6                                                      % ations)
 7    N_popsize = POPULATION;                           % size of population
 8    N_parameters = PARAMETERS;                        % dimension of parameter space
 9    alpha = ALPHA;                                    % mutation rate
10
11    % Initialization:
12    % ##########################################################################
13    Best = random_init(N_parameters);                % random initialization of
14                                                      % best solution
15    Best_fitness = cost_function(Best);              % obtaining the cost of best
16                                                      % solution
17    R = random_init(N_parameters,N_population);      % random initialization of pa-
18                                                      % rent generation
19    R_fitness = Inf*ones(1,N_population);            % setting initial fitness of
20                                                      % parent generation
21    Q = zeros(N_parameters,N_population);            % initializing the children
22                                                      % generation
23    Q_fitness = Inf*ones(1,N_population);            % setting initial fitness of
24                                                      % childern generation
25
26    % Iteration over Generations:
27    % ##########################################################################
28    for gen = 1:N_generations
29
30      % Children obtained by Mutation of Parents:
31      % ##########################################################################
32      for pop = 1:N_popsize
33        a_idx = random_index(pop);                    % random index which is not
34                                                      % pop, but between 1 and
35                                                      % N_popsize
36        A = R(:,a_ide);                               % storing parent A
37        b_idx = random_index([pop,a_idx]);            % random index which is not
38                                                      % pop or a_idx, but between 1
39                                                      % and N_popsize
40        B = R(:,b_ide);                               % storing parent B
41        c_idx = random_index([pop,a_idx,b_idx]);      % random index which is not
42                                                      % pop or a_idx or b_idx
43        C = R(:,c_ide);                               % storing parent C, but be-
44                                                      % tween 1 and N_popsize
45        Q(:,pop) = A + alpha*(B - C);                 % mutation to get new chil-
46                                                      % dren
47      end
48
49      % Crossover of Children with their Parents:
50      % ##########################################################################
51      for pop = 1:N_popsize
52        swap_idx = random_swap_indices;               % list of random length with
53                                                      % random swap indices;
54                                                      % maximal N_parameters - 1 el-
55                                                      % ements in list
56        Q(swap_idx,pop) = R(swap_idx,pop);            % crossover between child and
57                                                      % parent
58        Q_fitness(i) = Inf;                           % setting fitness of child
59      end
60
61      % Obtaining Fitness of Children:
62      % ##########################################################################
63      for pop = 1:N_popsize
64        Q_fitness(pop) = cost_function(Q(:,pop));     % obtaining fitness of child-
65                                                      % ren generation
66      end
67
68      % Selection (Survival of the Fittest):
69      % ##########################################################################
70      for pop = 1:N_popsize
71        if Q_fitness(pop) < R_fitness(pop)            % comparing the fitness of ac-
```

```
72                                                % tual generation with its pa-
73                                                % rent
74           R(:,pop) = Q(:,pop);                 % if parent is fitter, it
75                                                % stays in population
76           R_fitness(pop) = Q_fitness(pop);     % storing the fitness of old
77                                                % parent
78       end
79     end
80
81     % Storing Best Solution:
82     % ##################################################################
83     for pop = 1:N_popsize
84       if R_fitness(pop) < Best_fitness          % comparing the fitness of
85                                                % best solution with new pa-
86                                                % rents
87         Best = R(:,pop);                        % storing best solution if new
88                                                % one is found
89         Best_fitness = R_fitness(pop);          % storing the best fitness
90       end
91     end
92
93   end
```

Listing C.2: MATLAB pseudo code of the Differential Evolution algorithm.

C.3 Particle Swarm Optimization

The *Particle Swarm Optimization* (PSO) algorithm does also belong to the field of *Evolutionary Computation*. But in contrast to the in this work discussed DE (see Appendix C.2) is this algorithm not modeled after evolution but after the behavior of animals swarms, like swarms of birds and fishes. It does also not resample the population to produce a new population for the next iteration. There is also no selection process involved. The PSO algorithm does maintain a single swarm of particles which are moved in the parameter space from iteration to iteration. The movement of the swarm is towards the best solutions found so far.

A particle of a swarm consists of a location $R(i)$ and a velocity $R_v(i)$ in the parameter space which both are initialized at the beginning. The swarm remembers the best solution $S(i)$ each particle has found so far, the best solution $I(i)$ so far found by random informants of each particle (commonly a small number of informants is used, also $R(i)$ is an informant), and the best solution A any particle has found so far. The particle position for the next iteration is given as $R(i) = R(i) + \epsilon R_v(i)$, with $R_v(i) = \alpha R_v(i) + \beta \left(S(i) - R(i) \right) + \gamma \left(I(i) - R(i) \right) + \delta \left(A - R(i) \right)$. The parameter α controls how much of original velocity is retained, β controls how much of the personal best of each particle in mixed in, γ controls how much of the informants best is mixed in, δ controls how much of the overall best is mixed in (commonly set to 0), and ϵ controls the gain of the speed of the particles (commonly set to 1).

The presented PSO algorithm can be configured using some parameters: `ITERATIONS` sets the number of iterations, `SWARMSIZE` sets the number of particles in the swarm, `PARAMETERS` sets the dimension of the parameter search space, `INFORMANTS` sets the number of informants of each particle, and `ALPHA`, `BETA`, `GAMMA`, `DELTA`, and `EPSILON` sets α, β, γ, δ, and ϵ. The `cost_function()` defines the optimization problem and is a function which needs to be minimized by finding the optimal solution.

```
1    % PARTICLE SWARM OPTIMIZATION
2
3    % Setting Algorithm Parameters:
4    % ##########################################################################
5    N_iterations = ITERATIONS;                   % number of iterations
6    N_swarmsize = SWARMSIZE;                      % number of particles in the
7                                                  % swarm
8    N_parameters = PARAMETERS;                    % dimension of parameter space
9    N_informants = INFORMANTS;                    % number of informants per
10                                                 % particle
11   alpha = ALPHA;                               % ratio of retained original
12                                                 % velocity
13   beta =  BETA;                                % attraction parameter to the
14                                                 % best solution found by sin-
15                                                 % gle particle
16   gamma = GAMMA;                               % attraction parameter to the
17                                                 % best solution found by in-
18                                                 % formant particles
19   delta = DELTA;                              % attraction parameter to the
20                                                 % best solution found by all
21                                                 %  particles
22   epsilon = EPSILON;                          % movement speed parameter of
23                                                 % whole swarm
24
25   % Initialization:
26   % ##########################################################################
27   Best = random_init(N_parameters);           % random initialization of
28                                                 % best solution
29   Best_cost = cost_function(Best);            % obtaining cost of best solu-
30                                                 % tion
31   R = random_init(N_parameters,N_swarmsize);  % random initialization of
32                                                 % swarm
33   Rv = R - random_init(N_parameters,N_swarmsize); % random initialization of ve-
34                                                 % locity of particles
35   R_cost = Inf*ones(1,N_swarmsize);           % initialization of cost of
36                                                 % particles
37   S = random_init(N_parameters,N_swarmsize);  % random initialization of
38                                                 % best solution found by sin-
39                                                 % gle particle
40   S_cost = Inf*ones(1,N_swarmsize);           % initialization of cost of
41                                                 % best solution found by sin-
42                                                 % gle particle
43   A = randnom_init(N_parameters);             % random initialization of
44                                                 % best solution found by all
45                                                 % particels
46   A_cost = Inf;                               % initialization of cost of
47                                                 % best solution found by all
48                                                 % particels
49   I = random_init(N_parameters,N_swarmsize);  % random initialization of
50                                                 % best solution of informants
51   I_cost = Inf*ones(1,N_swarmsize);           % initialization of cost of
52                                                 % informants
53
54   % Iterations:
55   % ##########################################################################
56   for iter = 1:N_iterations
57
58     % Obtaining Cost of Swarm:
59     % ##########################################################################
60     for swm = 1:N_swarmsize
61       R_cost(swm) = cost_function(R(:,swm));   % obtaining costs of swarm
62                                                 % particles
63     end
64
65     % Storing Very Best Solution:
66     % ##########################################################################
67     for swm = 1:N_swarmsize
68       if R_cost(swm) < Best_cost                % comparing cost of swarm par-
69                                                 % ticles with cost of best so-
70                                                 % lution
71         Best = R(:,swm);                        % storing new best solution if
```

```matlab
72                                                    % found
73              Best_cost = R_cost(swm);              % storing cost of best solu-
74                                                    % tion
75          end
76      end
77
78      % Storing Best Solution of each Single Particel:
79      % ########################################################################
80      for swm = 1:N_swarmsize
81        if R_cost(swm) < S_cost(swm)                % comparing cost of particle
82                                                    % with the cost of the
83                                                    % best solution ever found by
84                                                    % itself
85          S(:,swm) = R(:,swm);                      % storing new best solution if
86                                                    % found
87          S_cost(swm) = R_cost(swm);                % storing cost of best solut-
88                                                    % ion
89        end
90      end
91
92      % Storing Best Solution of All Particles:
93      % ########################################################################
94      for swm = 1:N_swarmsize
95        if R_cost(swm) < A_cost                     % comparing cost of swarm par-
96                                                    % ticles with cost of best so-
97                                                    % lution ever found by swarm
98          A = R(:,swm);                             % storing new best solution if
99                                                    % found
100         A_cost = R_cost(swm);                     % storing cost of best solu-
101                                                   % tion
102       end
103     end
104
105     % Retrieving Best Solution of Informant Particles:
106     % ########################################################################
107     for swm = 1:N_swarmsize
108       idx = random_index(N_informants);          % generating indices to each
109                                                   % praticle's random informants
110       I(:,swm) = R(:,swm);                        % initially set best informant
111                                                   % to be the particle
112       I_cost(swm) = R_cost(swm);                  % initially set best informant
113                                                   % cost
114       for infts = 1:N_informants
115         if S_cost(idx(infts)) < I_cost(swm)       % search for best informant of
116                                                   % the particle
117           I(:,swm) = S(:,idx(infts));             % storing new best informant
118                                                   % solution if found
119           I_cost(swm) = S_cost(idx(infts));       % storing cost of best infor-
120                                                   % mant solution
121         end
122       end
123     end
124
125     % Swarm Movement:
126     % ########################################################################
127     for swm = 1:N_swarmsize
128       b = beta*rand(1)*(S(:,swm)-R(:,swm));       % randomly partial velocity to
129                                                   % the best solution ever found
130                                                   % by the particle
131       c = gamma*rand(1)*(I(:,swm)-R(:,swm));      % randomly partial velocity to
132                                                   % the best solution ever found
133                                                   % by the particle's informants
134       d = delta*rand(1)*(A - R(:,swm));           % randomly partial velocity to
135                                                   % the best solutions ever
136                                                   % found by all particles
137       Rv(:,swm) = alpha*Rv(:,swm) + b + c + d;    % new velocity of particle
138     end
139     R = R + epsilon*Rv;                           % new location of swarm par-
140                                                   % ticles
141   end
```

Listing C.3: MATLAB pseudo code of the Particle Swarm Optimization algorithm.

D

Collection of Simulation Results

D.1 Alternative Second Order Projection Filter Cross-Spectra
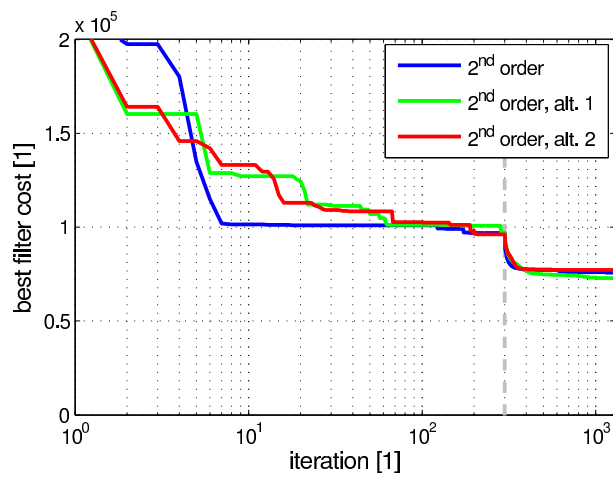
Figure D.1: Cost of best found filter per iteration of three 2nd order projection filter cross-spectra for a $M = 8$ channel receiver.

(a) Cross-spectra magnitude response

(b) Cross-spectra phase response

(c) Cross-spectra correlation matrix

(d) Signal co-term matrix

(e) Magnitude response of the inverse

(f) Detection correlation matrix
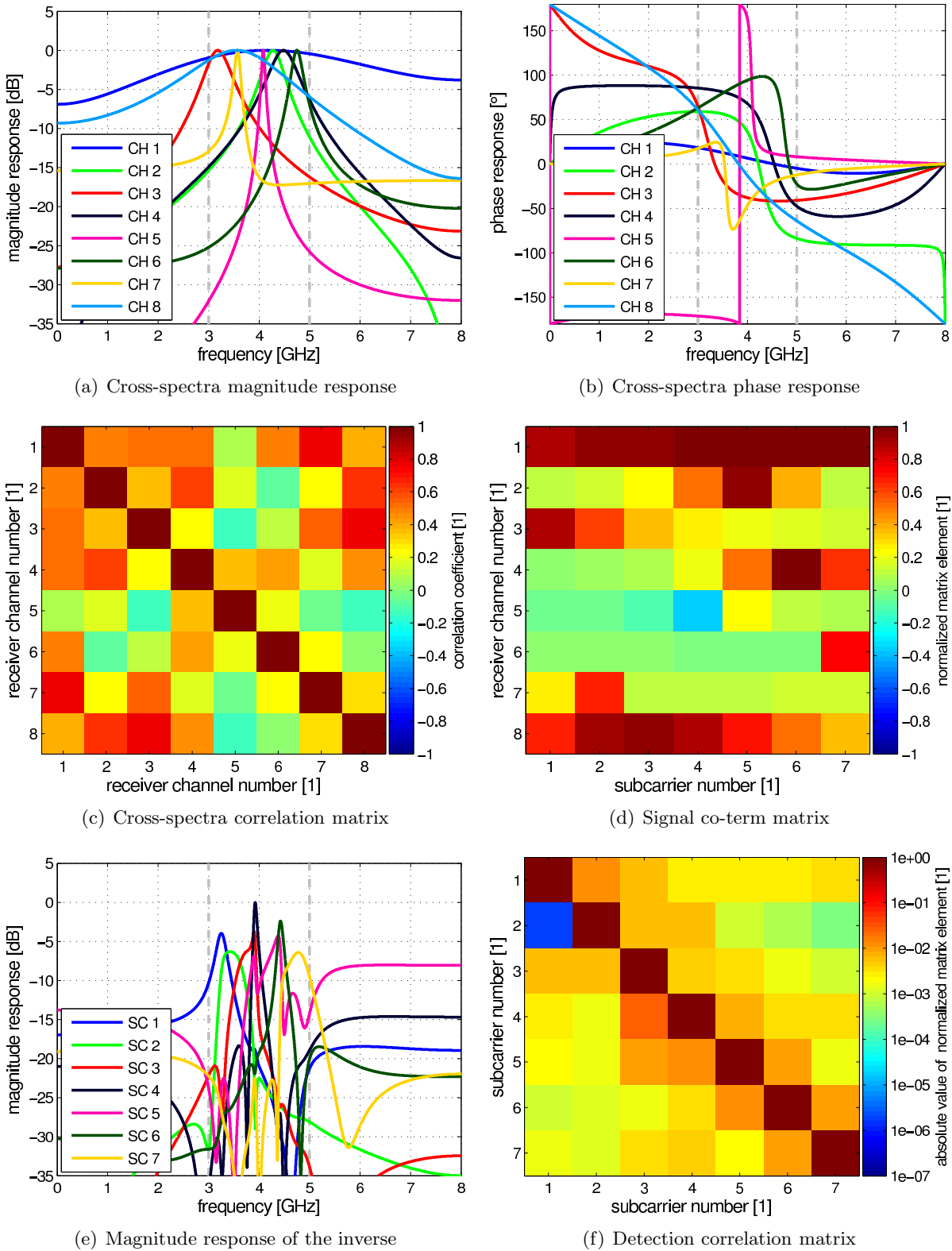
Figure D.2: Frequency response, Correlation matrix, and signal co-term matrix $\mathbf{P}$ of an alternative (alt. 1) projection filter cross-spectra of 2nd order. The shown cross-spectra do have a condition number of $\mathrm{cond}\{\mathbf{P}\} = 16.78$.
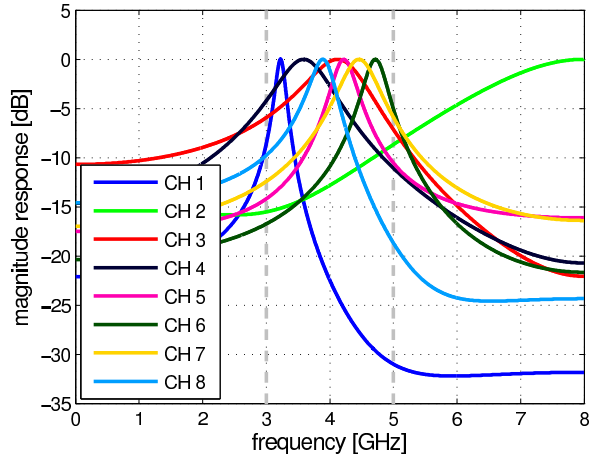
(a) Cross-spectra magnitude response
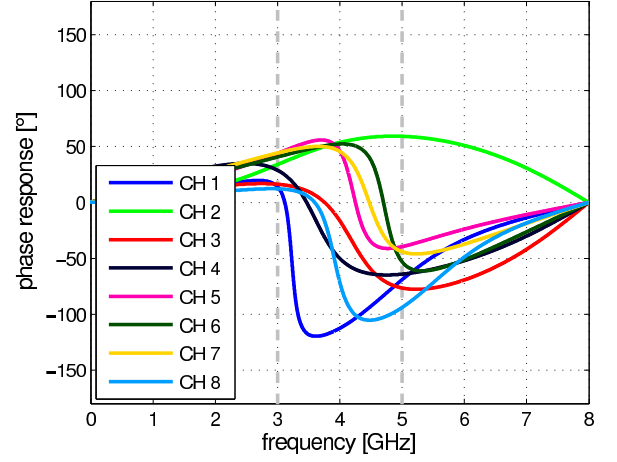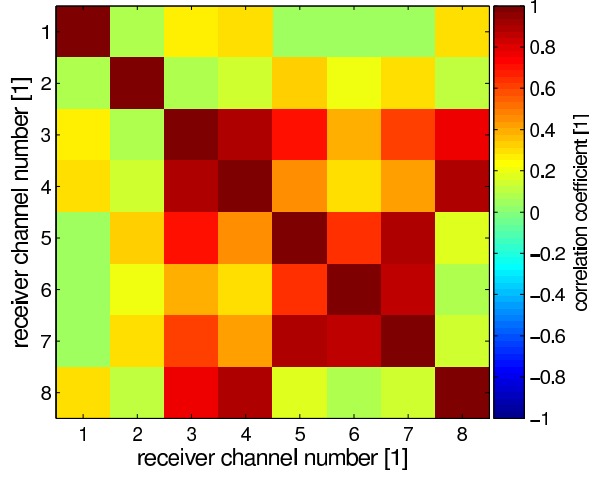
(b) Cross-spectra phase response

(c) Cross-spectra correlation matrix
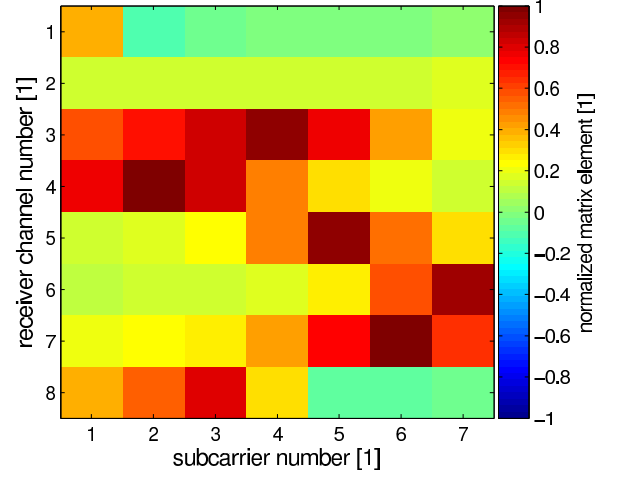
(d) Signal co-term matrix
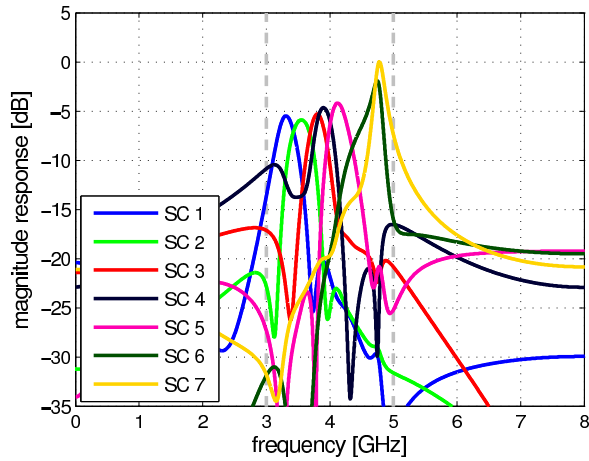
(e) Magnitude response of the inverse
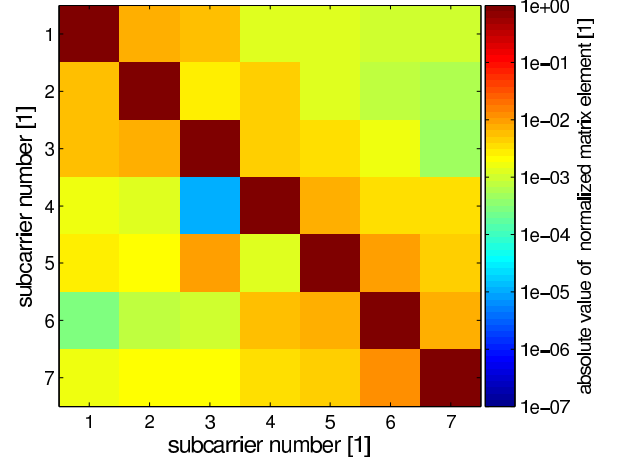
(f) Detection correlation matrix

Figure D.3: Frequency response, Correlation matrix, and signal co-term matrix $\mathbf{P}$ of an alternative (alt. 2) projection filter cross-spectra of 2nd order. The shown cross-spectra do have a condition number of cond$\{\mathbf{P}\} = 20.83$.

(a) SINR

(b) BER

(c) SNR

(d) SIR
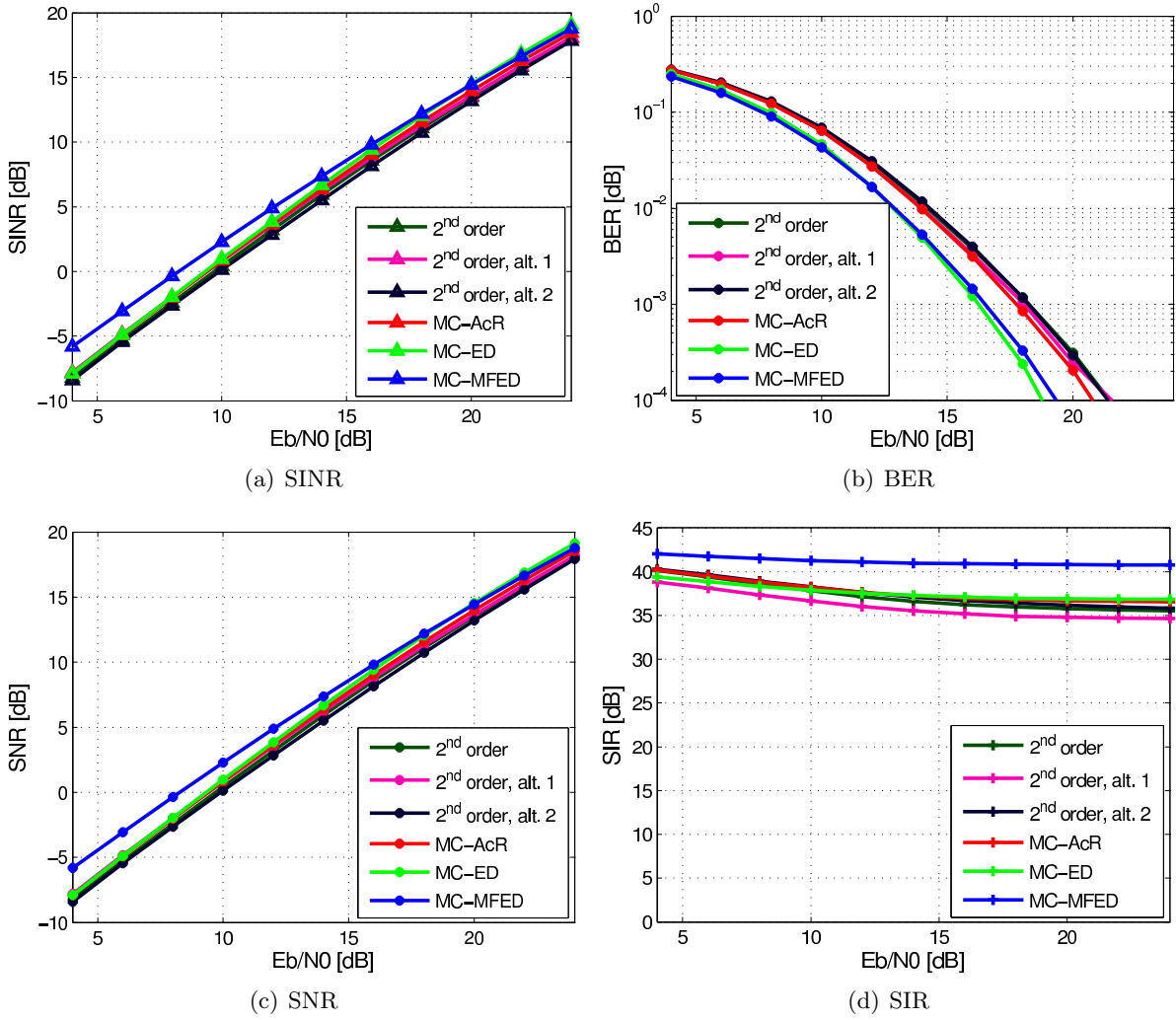
Figure D.4: SINR, SNR, SIR, and BER of the generalized noncoherent multi-channel receivers with various 2nd order projection filter cross-spectra.

D.2 SINR, SNR, SIR, and BER of various Multiplication Device Input Powers

(a) SINR

(b) BER

(c) SNR

(d) SIR
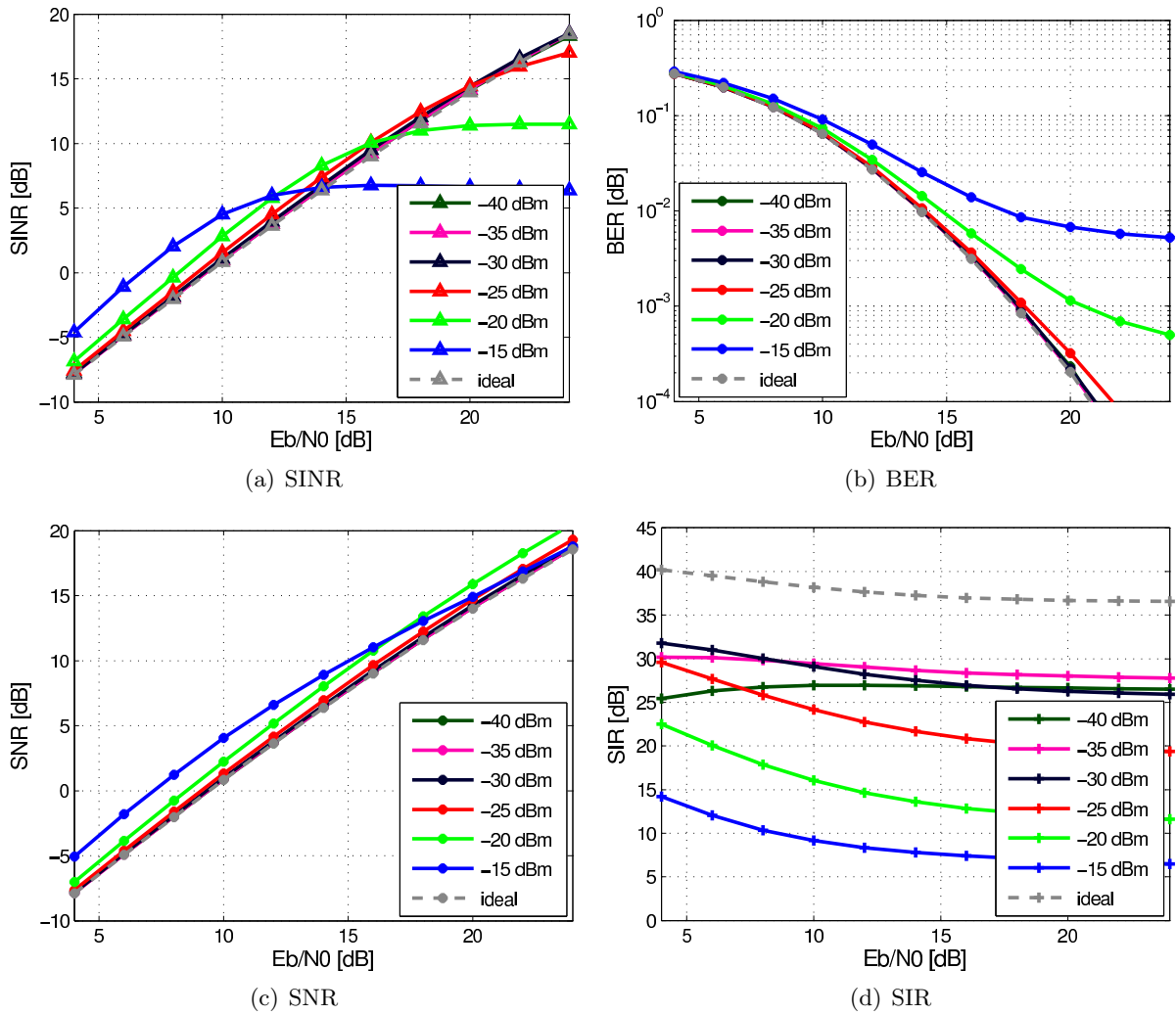
Figure D.5: SINR, SNR, SIR, and BER of the MC-AcR simulation-fitted multiplier model.

(a) SINR

(b) BER

(c) SNR

(d) SIR
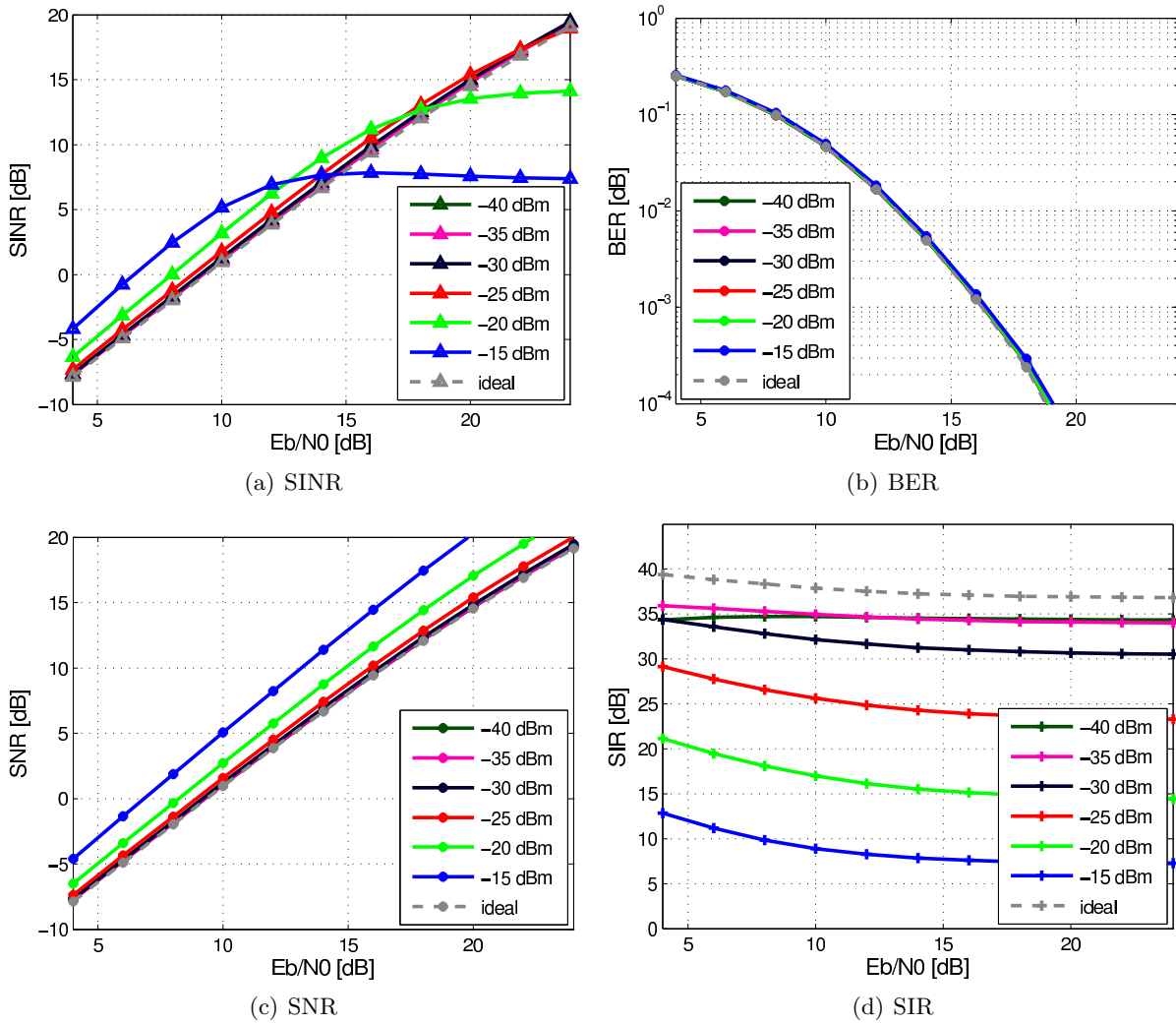
Figure D.6: SINR, SNR, SIR, and BER of the MC-ED simulation-fitted multiplier model.

(a) SINR

(b) BER

(c) SNR

(d) SIR
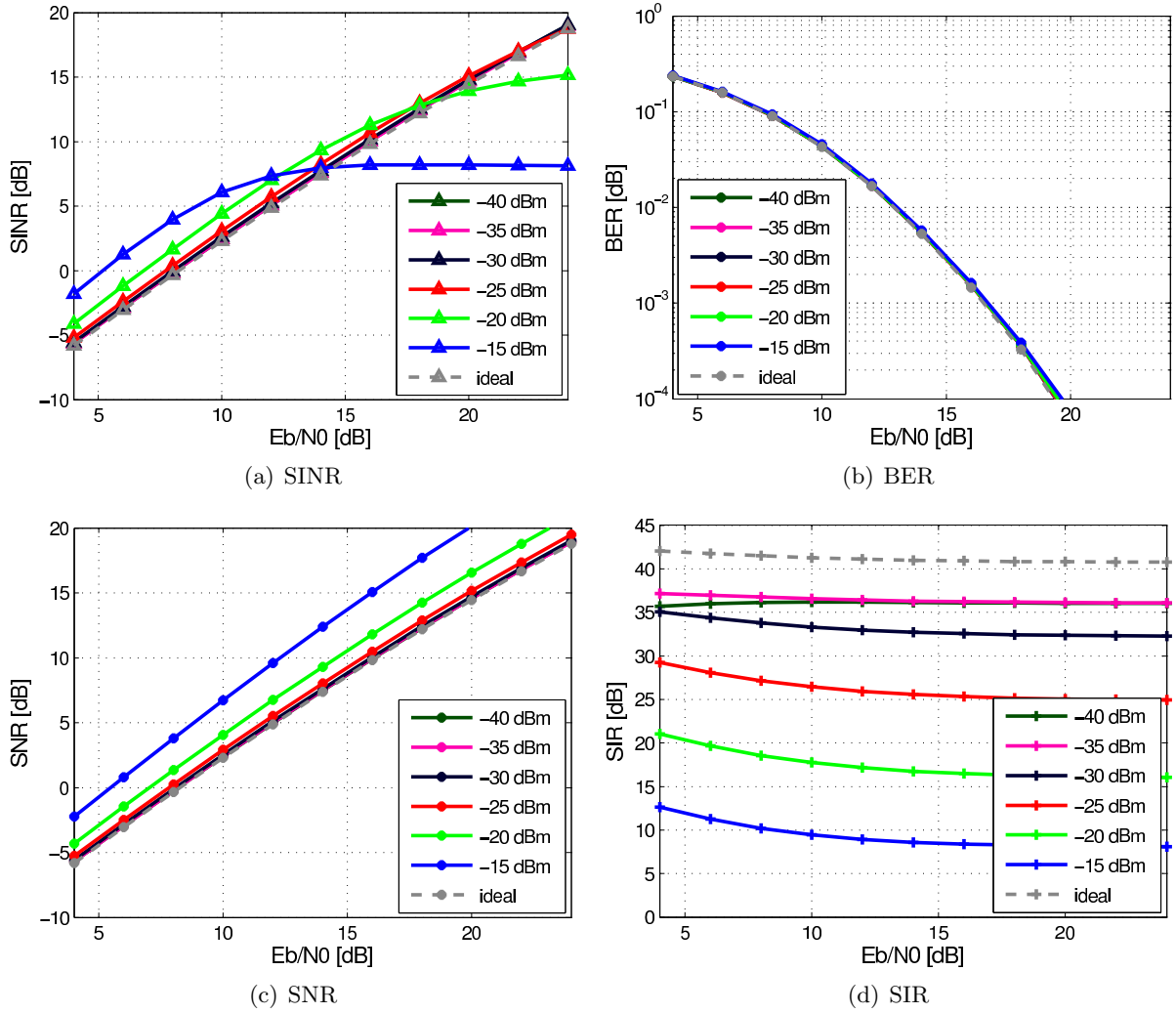
Figure D.7: SINR, SNR, SIR, and BER of the MC-MFED simulation-fitted multiplier model.

D.3 SINR, SNR, SIR, and BER of Sliding Window Approximation Filters

(a) SINR

(b) BER

(c) SNR

(d) SIR
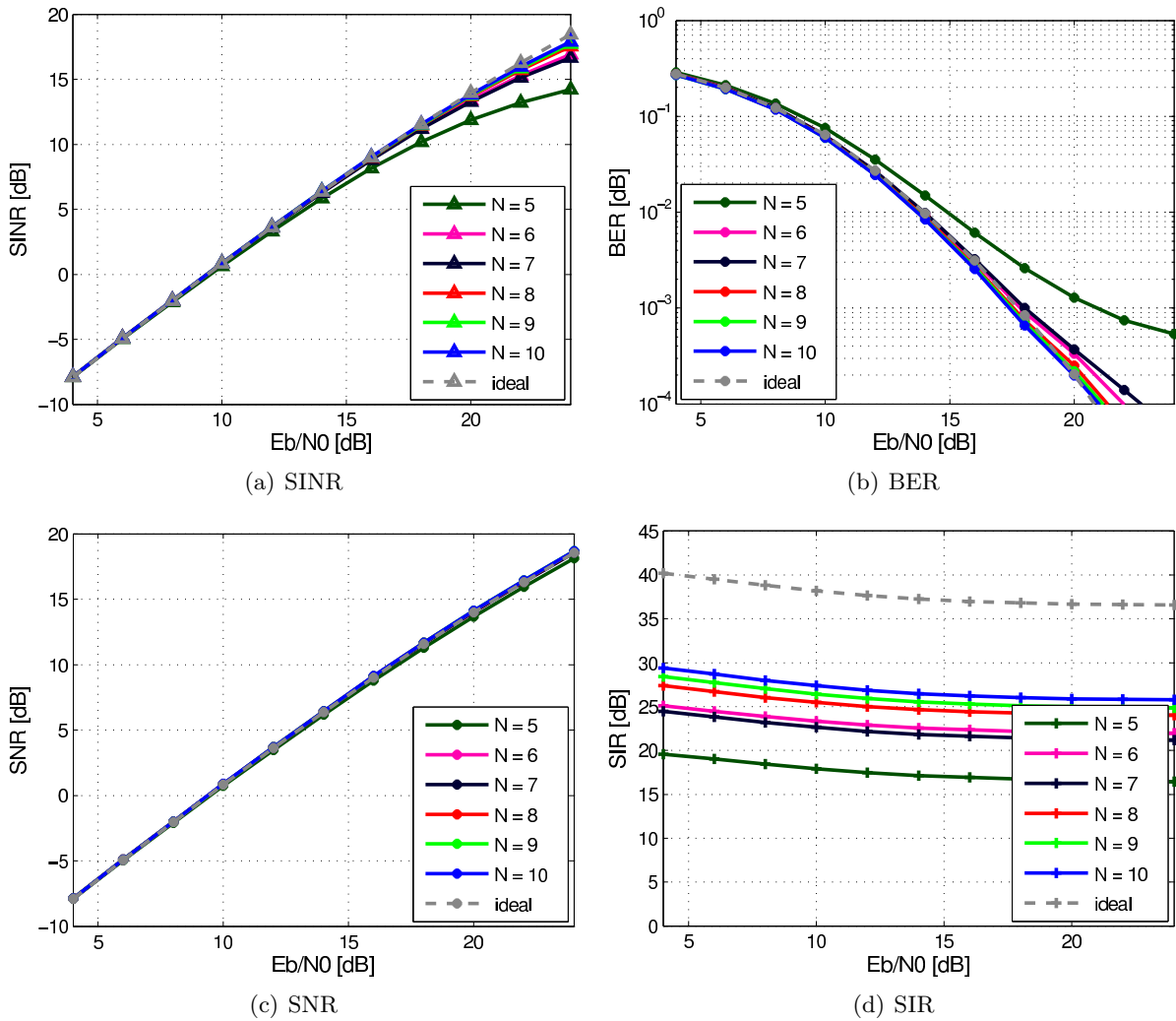
Figure D.8: SINR, SNR, SIR, and BER of the MC-AcR with various filter orders N of Bessel-Notch filter approximations.

(a) SINR

(b) BER

(c) SNR

(d) SIR
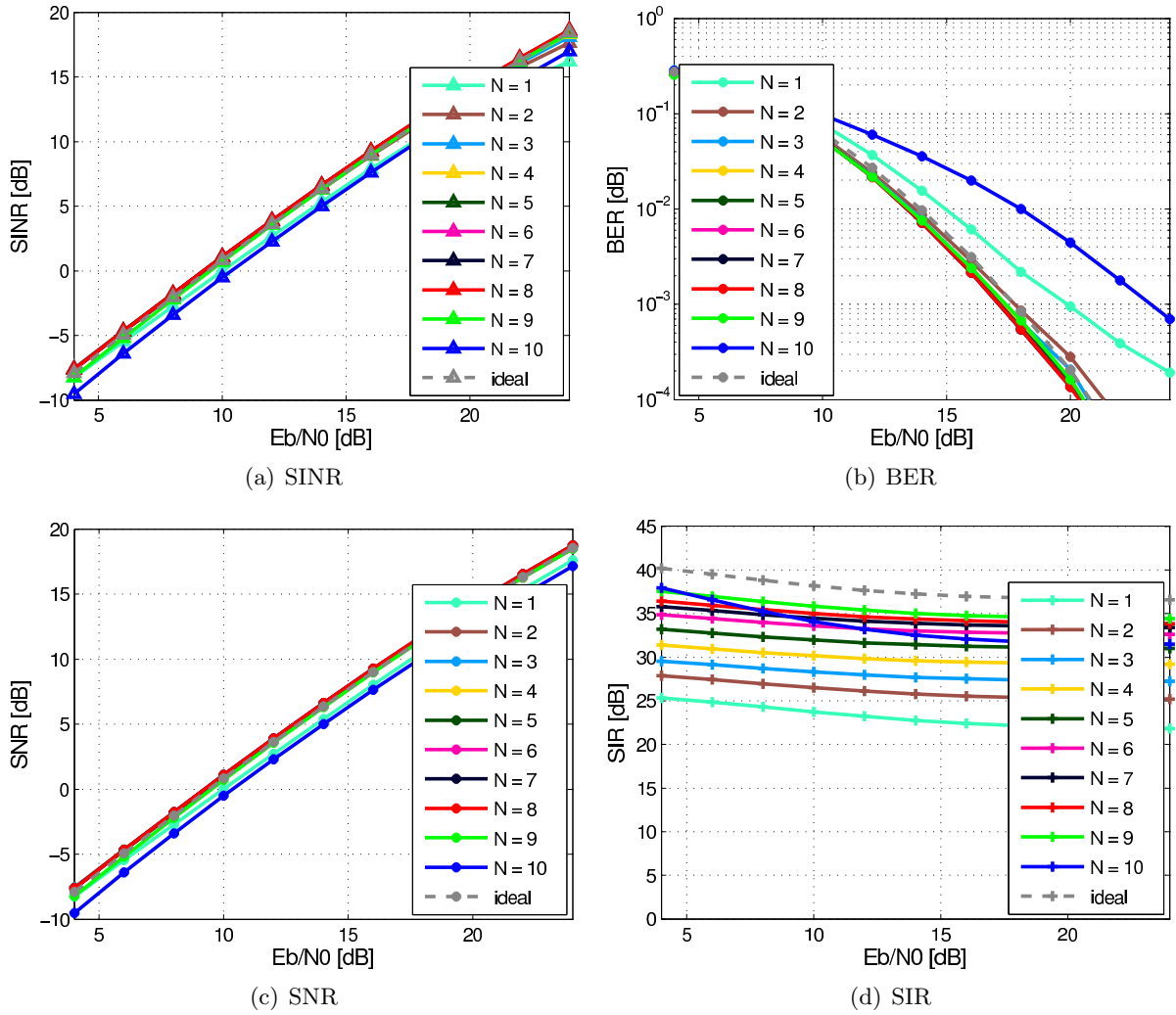
Figure D.9: SINR, SNR, SIR, and BER of the MC-AcR with various filter orders N of Bessel-Only filter approximations.

(a) SINR

(b) BER

(c) SNR

(d) SIR
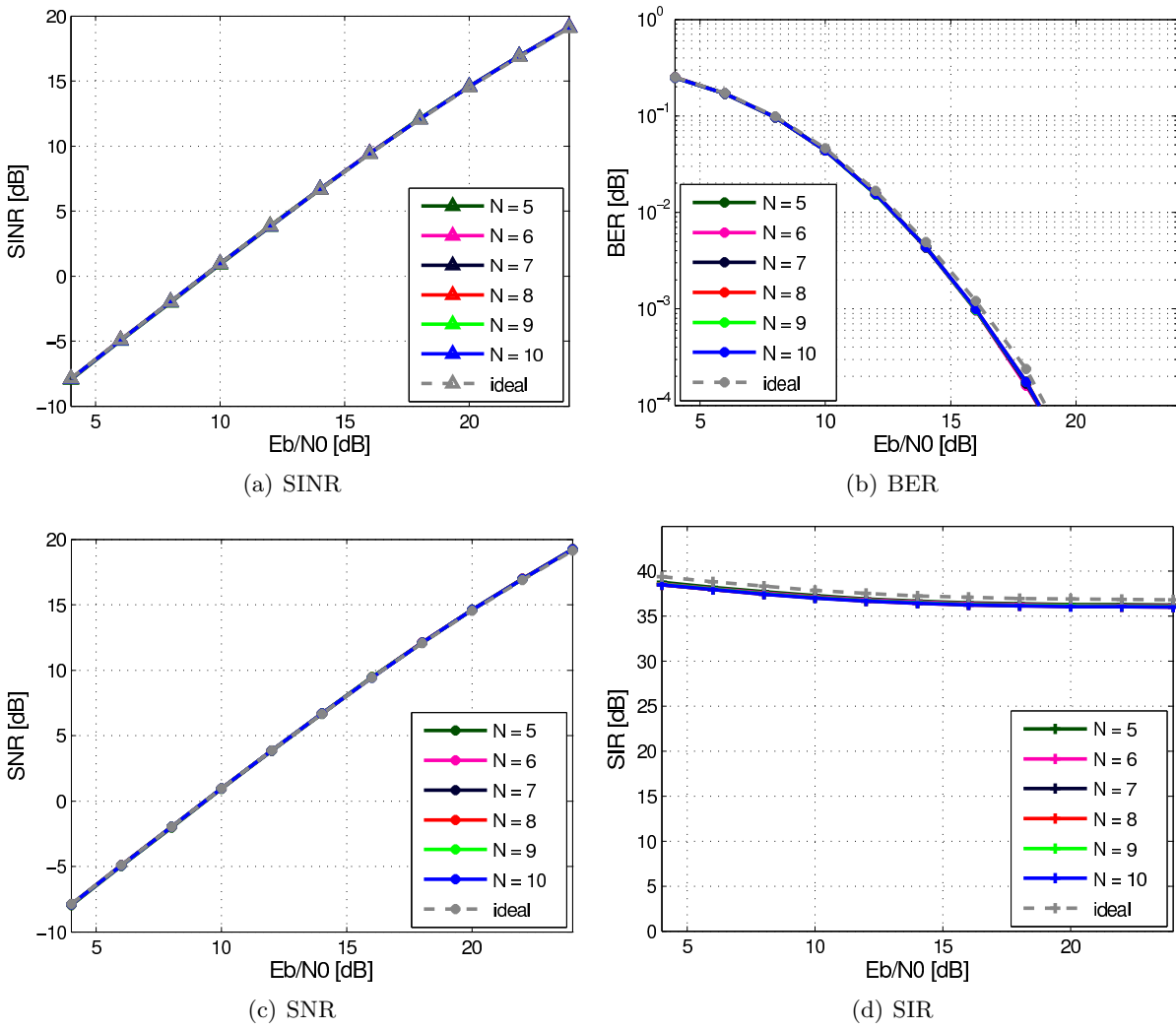
Figure D.10: SINR, SNR, SIR, and BER of the MC-ED with various filter orders N of Bessel-Notch filter approximations.

(a) SINR

(b) BER

(c) SNR

(d) SIR
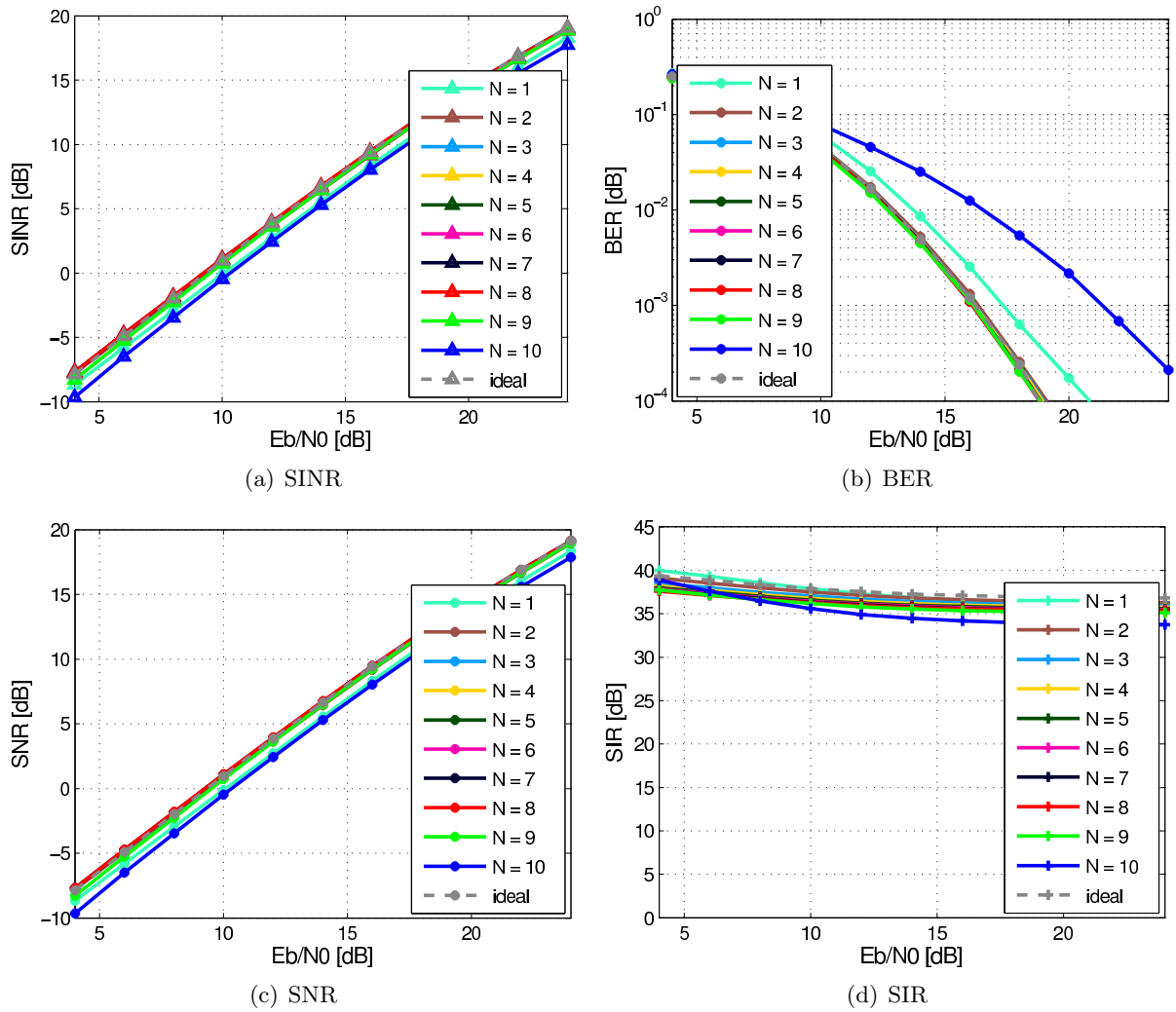
Figure D.11: SINR, SNR, SIR, and BER of the MC-ED with various filter orders N of Bessel-Only filter approximations.

(a) SINR

(b) BER

(c) SNR

(d) SIR
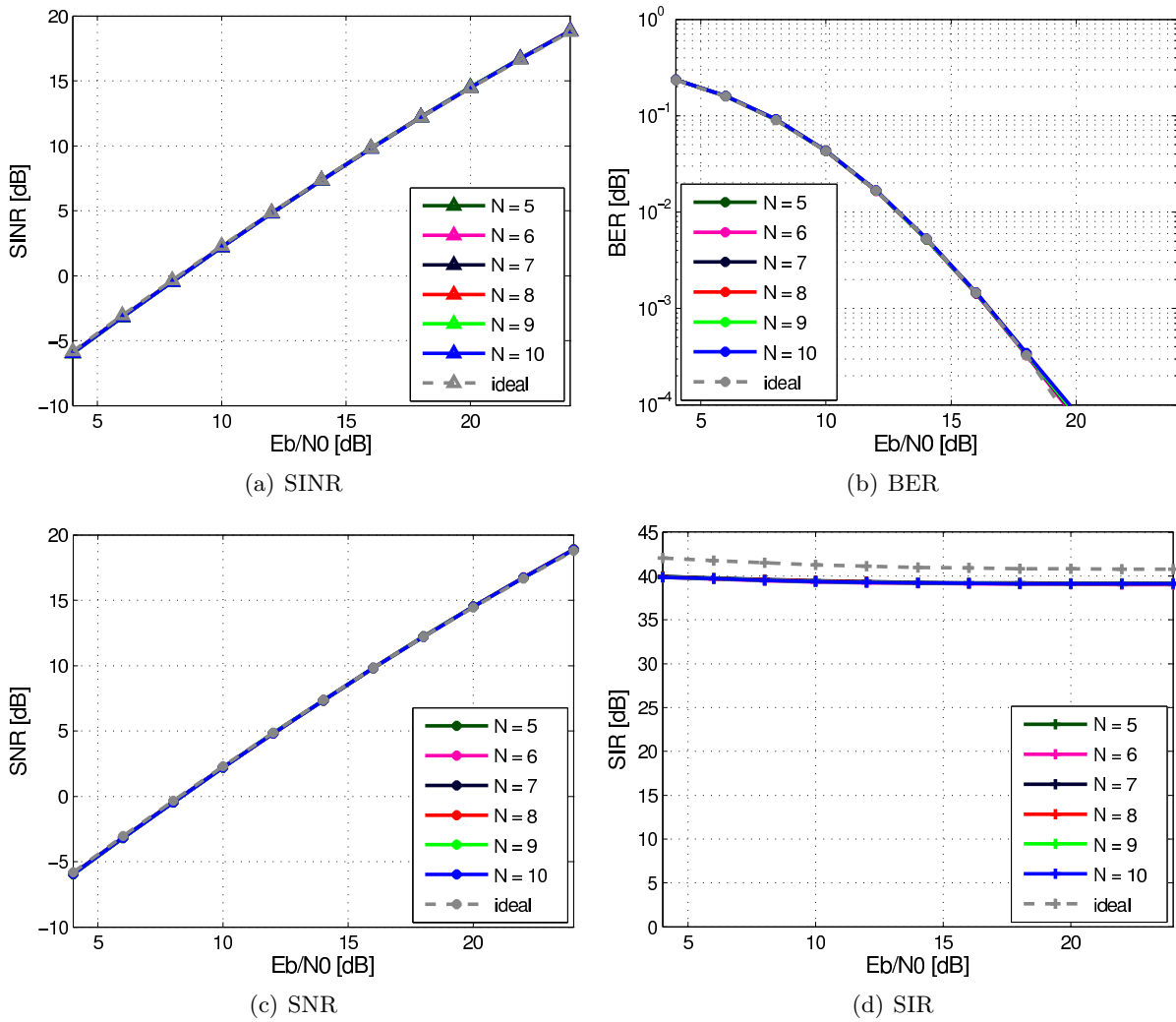
Figure D.12: SINR, SNR, SIR, and BER of the MC-ED with various filter orders N of Bessel-Notch filter approximations.

(a) SINR

(b) BER

(c) SNR

(d) SIR
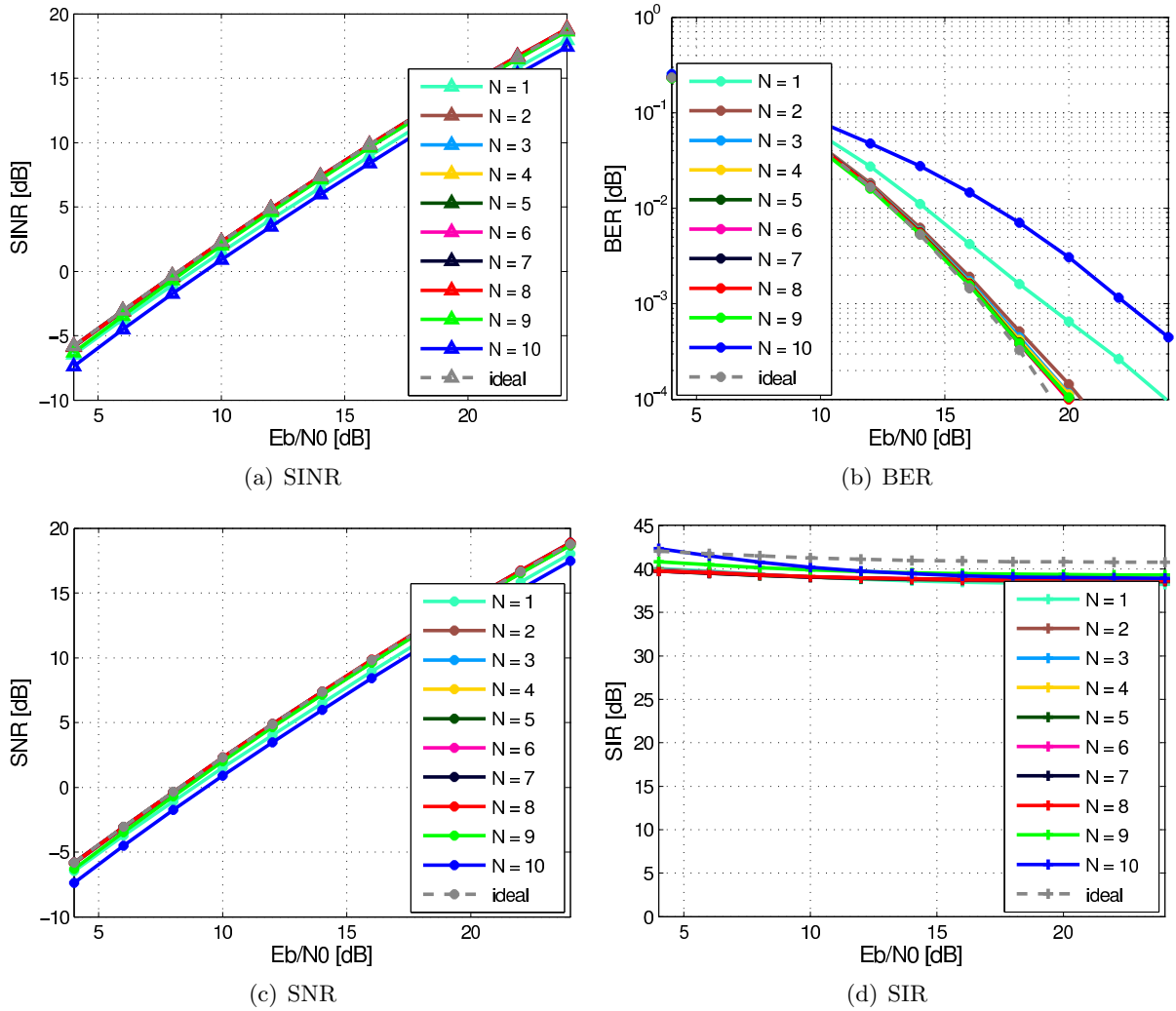
Figure D.13: SINR, SNR, SIR, and BER of the MC-ED with various filter orders N of Bessel-Only filter approximations.

E

Timetable of High Data Rate Ultra-Wideband Communications

1864 James Clerk Maxwell: publishes "dynamical theory of the electromagnetic field" where he introduced general equations of the electromagnetic field: the well known Maxwell's equations [127].

1879 David Edward Hughes: first attempts (trial and error) producing wireless signal using a spark generator which could be detected by a telephone receiver [14].

1886 Heinrich Hertz: prove of of existence of electromagnetic waves [128].

1891 Nikola Tesla: starts research on high frequency [129].

1895 Guglielmo Marconi: first transmission of wireless signals over long distance [18].

1896 Guglielmo Marconi: first radio patent [17].

1897 Nikola Tesla: first US radio patents [15, 16].

1898 Nikola Tesla: first remote radio control (radio controlled boat) [130].

1901 Guglielmo Marconi: first transatlantic transmission [131].

1904 Otto Nußbaumer: first broadcast of music ("Dachsteinlied", at Graz University of Technology) [20].

1906 Reginald Fessenden: first amplitude modulated audio broadcast using an alternator-transmitter [20].

1907 Guglielmo Marconi: first transatlantic radio service [131].

1912 The White Star liner R.M.S. Titanic collides with an iceberg and sinks during its maiden voyage. A Marconi spark-gap wireless telegraphs saved 705 lives [19].

1933 Edwin Howard Armstrong: patent on FM radio [132].

1947 John Bardeen, Walter Brattain, and William Shockley: invention of the transistor [133].

1948 Claude Elwood Shannon: foundation of modern digital communication and its theory [134].

1971 Gerald F. Ross: first modern UWB patent [22].

1987 foundation of GSM by four members of the European Economic Community (a predecessor of the European Union) [135].

1990 Charles Fowler et al.: first public Ultra-wideband technology for radar [23].

1997 Robert A. Scholtz and Moe Z. Win: first works on modern UWB impulse radio [24].

2002 FCC defines rules regarding UWB transmission systems [25].

2004 Stéphane Paquelet, Louis-Marie Aubertl, and Bernard Uguen: introduction of noncoherent UWB signals for high data rate communications [46].

2006 first IEEE standard which specifies low data rate UWB communications (IEEE 802.15.4a) [26].

2006 first IEEE standard which specifies high data rate UWB communications (IEEE 802.15.3a) was withdrawn [27].

2007 parts of the withdrawn IEEE 802.15.3a got adopted by ISO/IEC as ISO/IEC 26907 and ISO/IEC 26908 [28, 29].

F

Bibliography

[1] SINTEF. (2013, May) Big Data, for better or worse: 90% of world's data generated over last two years. ScienceDaily. (accessed April 17, 2014). [Online]. Available: www.sciencedaily.com/releases/2013/05/130522085217.htm

[2] G. Brumfiel, "Down the petabyte highway," *Nature*, vol. 469, pp. 282 – 283, Jannuary 2011.

[3] J. Kim, J.-C. Liu, P. Swarnam, and T. Urbanik, "The areawide real-time traffic control (ARTC) system: a new traffic control concept," *IEEE Transactions on Vehicular Technology*, vol. 42, no. 2, pp. 212 – 224, May 1993.

[4] M. Li, H. Cheng, and Y. Wang, "Novel airborne real-time survey system," *IEEE Transactions on Instrumentation and Measurement*, vol. 56, no. 6, pp. 2404 – 2410, Dec 2007.

[5] S. Chandana and H. Leung, "A system of systems approach to disaster management," *IEEE Communications Magazine*, vol. 48, no. 3, pp. 138 – 145, March 2010.

[6] A. Jalote-Parmar and P. Badke-Schaub, "Critical factors influencing intra-operative surgical decision-making," in *IEEE International Conference on Systems, Man and Cybernetics*, Oct 2008, pp. 1091–1096.

[7] "LTE; evolved universal terrestrial radio access (E-UTRA); physical channels and modulation (3GPP TS 36.211 version 8.7.0 release 8)," *ETSI TS 136 211 V8.7.0 (2009-06)*, 2009.

[8] "IEEE standard for local and metropolitan area networks part 16: Air interface for fixed and mobile broadband wireless access systems amendment 2: Physical and medium access control layers for combined fixed and mobile operation in licensed bands and corrigendum 1," *IEEE Std 802.16e-2005 and IEEE Std 802.16-2004/Cor 1-2005 (Amendment and Corrigendum to IEEE Std 802.16-2004)*, pp. 1 – 822, 2006.

[9] "IEEE standard for telecommunications and information exchange between systems - LAN/MAN - specific requirements - part 15: Wireless medium access control (MAC) and physical layer (PHY) specifications for wireless personal area networks (WPANs)," *IEEE Std 802.15.1-2002*, pp. 1 – 473, June 2002.

[10] "IEEE standard for information technology– local and metropolitan area networks– specific requirements– part 15.4: Wireless medium access control (MAC) and physical layer (PHY) specifications for low rate wireless personal area networks (WPANs)," *IEEE Std 802.15.4-2006 (Revision of IEEE Std 802.15.4-2003)*, pp. 1 – 320, Sept 2006.

[11] "ANT message protocol and usage," Dynastream Innovations Inc., 2013.

[12] "nRF24AP2 product specification v1.2," Nordic Semiconductor, 2010, single-chip ANT ultra-low power wireless network solution.

[13] K. Witrisal, G. Leus, G. Janssen, M. Pausini, F. Troesch, T. Zasowski, and J. Romme, "Noncoherent ultra-wideband systems," *IEEE Signal Processing Magazine*, vol. 26, no. 4, pp. 48 – 66, July 2009.

[14] D. E. Hughes, "Prof. D. E. Hughe's research in wireless telegraphy," *The Electrician*, vol. May 5, pp. 40 – 41, 1899.

[15] N. Tesla, "System of transmission of electrical energy," U.S. Patent 645,576, March 20, 1900.

[16] ——, "Apparatus for transmission of electrical energy," U.S. Patent 649,621, May 15, 1900.

[17] G. Marconi, "Improvements in transmitting electrical impulses and signals, and in apparatus therefor," GB Patent 12,039, July 2, 1897.

[18] U. S. Supreme Court, "Marconi Wireless T. Co. of America v. U.S." June 1943.

[19] "Wireless equipment of the Titanic," *The Marconigraph*, May 1912.

[20] R. L. Hilliard and M. C. Keith, *The Broadcast Century and Beyond: A Biography of American Broadcasting*, 5th ed. Focal Press, 2010.

[21] F. Nekoogar, *Ultra-Wideband Communications: Fundamentals and Applications.* Prentice Hall, 2005.

[22] G. F. Ross, "Transmission and reception system for generating and receiving base-band pulse duration pulse signals without distortion for short base-band communication system," U.S. Patent 3,728,632, April 17, 1973.

[23] C. Fowler, J. Entzminger, and J. Corum, "Assessment of ultra-wideband (UWB) technology," *IEEE Aerospace and Electronic Systems Magazine*, vol. 5, no. 11, pp. 45 – 49, 1990.

[24] M. Win and R. Scholtz, "Impulse radio: how it works," *IEEE Communications Letters*, vol. 2, no. 2, pp. 36 – 38, 1998.

[25] Federal Communications Commission (FCC), "Revision of part 15 of the commission's rules regarding ultra-wideband transmission systems," Federal Communications Commission (FCC), Tech. Rep., 2002, first Report and Order, ET Docket 98-153, FCC 02-48; Adopted: February 2002; Released: April 2002.

[26] "IEEE standard for information technology - telecommunications and information exchange between systems - local and metropolitan area networks - specific requirement part 15.4: Wireless medium access control (MAC) and physical layer (PHY) specifications for low-rate wireless personal area networks (WPANs)," *IEEE Std 802.15.4a-2007 (Amendment to IEEE Std 802.15.4-2006)*, pp. 1 – 203, 2007.

[27] K.-L. Du and S. M. N. S., *Wireless Communication Systems: From RF Subsystems to 4G Enabling Technologies.* Cambridge University Press, 2010.

[28] "Information technology - telecommunications and information exchange between systems - high-rate ultra-wideband PHY and MAC standard," *ISO/IEC 26907:2009*, 2009.

[29] "Information technology - telecommunications and information exchange between systems - MAC-PHY interface for ISO/IEC 26907," *ISO/IEC 26908:2009*, 2009.

[30] USB Implementers Forum, Inc., "Wireless universal serial bus specification 1.1," 2010.

[31] R. Merritt. (2009, October) Bluetooth group drops ultrawideband, eyes 60 GHz. EE Times. (accessed April 18, 2014). [Online]. Available: http://www.eetimes.com/document.asp?doc_id=1172117&page_number=1

[32] A. F. Molisch, *Wireless Communications*, 2nd ed. John Wiley & Sons Ltd., 2011.

[33] M. Abramowitz and I. A. Stegun, *Handbook of Mathematical Functions with Formulas, Graphs, and Mathematical Tables.* Dover Publications Inc., 1964.

[34] Y. Alemseged and K. Witrisal, "Modeling and mitigation of narrowband interference for transmitted-reference uwb systems," *IEEE Journal of Selected Topics in Signal Processing*, vol. 1, no. 3, pp. 456 – 469, Oct 2007.

[35] C. Snow, L. Lampe, and R. Schober, "Impact of WiMAX interference on MB-OFDM UWB systems: analysis and mitigation," *IEEE Transactions on Communications*, vol. 57, no. 9, pp. 2818 – 2827, September 2009.

[36] K. Witrisal, G. Leus, M. Pausini, and C. Krall, "Equivalent system model and equalization of differential impulse radio UWB systems," *IEEE Journal on Selected Areas in Communications*, vol. 23, no. 9, pp. 1851 – 1862, Sept 2005.

[37] M. Pausini, G. Janssen, and K. Witrisal, "Performance enhancement of differential UWB autocorrelation receivers under ISI," *IEEE Journal on Selected Areas in Communications*, vol. 24, no. 4, pp. 815 – 821, April 2006.

[38] M. Win and R. Scholtz, "Ultra-wide bandwidth time-hopping spread-spectrum impulse radio for wireless multiple-access communications," *IEEE Transactions on Communications*, vol. 48, no. 4, pp. 679 – 689, Apr 2000.

[39] M. Z. Win and R. A. Scholtz, "On the robustness of ultra-wide bandwidth signals in dense multipath environments," *IEEE Communications Letters*, vol. 2, no. 2, pp. 51 – 53, Feb 1998.

[40] A. Adalan, M. Fischer, T. Gigl, K. Witrisal, A. Scholtz, and C. Mecklenbrauker, "Ultra-wideband radio pulse shaping filter design for IEEE 802.15.4a transmitter," in *IEEE Wireless Communications and Networking Conference (WCNC 2009)*, April 2009, pp. 1 – 6.

[41] D. Dahlhaus, "Post detection integration for ultra-wideband systems with binary orthogonal signaling," in *2005 IEEE International Conference on Ultra-Wideband (ICU 2005)*, Sept. 2005, pp. 136 – 141.

[42] L. Yang and G. Giannakis, "Ultra-wideband communications: an idea whose time has come," *IEEE Signal Processing Magazine*, vol. 21, no. 6, pp. 26 – 54, Nov 2004.

[43] F. Tufvesson, S. Gezici, and A. Molisch, "Ultra-wideband communications using hybrid matched filter correlation receivers," *IEEE Transactions on Wireless Communications*, vol. 5, no. 11, pp. 3119–3129, 2006.

[44] C. Rushforth, "Transmitted-reference techniques for random or unknown channels," *IEEE Transactions on Information Theory*, vol. 10, no. 1, pp. 39 – 42, Jan 1964.

[45] T. Zasowski, F. Troesch, and A. Wittneben, "Partial channel state information and inter-symbol interference in low complexity UWB PPM detection," in *2006 IEEE International Conference on Ultra-Wideband*, Sept. 2006, pp. 369 – 374.

[46] S. Paquelet, L.-M. Aubert, and B. Uguen, "An impulse radio asynchronous transceiver for high data rates," in *2004 International Workshop on Ultra Wideband Systems, Joint with Conference on Ultrawideband Systems and Technologies*, May 2004, pp. 1 – 5.

[47] M. Mroué, S. Haese, G. El-Zein, S. Mallégol, and S. Paquelet, "A non-coherent multi-band IR-UWB HDR transceiver based on energy detection," in *2010 17th IEEE International Conference on Electronics, Circuits, and Systems*, Dec. 2010, pp. 898 – 901.

[48] S. Mallegol, J.-P. Coupez, C. Person, T. Lespagnol, S. Paquelet, and A. Bisiaux, "Microwave (de) multiplexer for ultra-wideband (UWB) non-coherent high data rates transceiver," in *36th European Microwave Conference*, Sept. 2006, pp. 1825 – 1828.

[49] H.-U. Dehner, M. Linde, R. Moorfeld, H. Jakel, D. Burgkhardt, F. Jondral, and A. Finger, "A low complex and efficient coexistence approach for non-coherent multiband impulse radio UWB," in *Sarnoff Symposium, 2009. SARNOFF '09. IEEE*, 2009, pp. 1 – 5.

[50] A. Lecointre, D. Dragomirescu, and R. Plana, "Methodology to design advanced MR-IR-UWB communication system," *Electronics Letters*, vol. 44, no. 24, pp. 1412 – 1413, November 2008.

[51] M. Mroue, S. Paquelet, G. El Zein, and S. Haese, "Channel capacity evaluation of a non-coherent ir-uwb system for hdr wpan applications," in *2011 18th International Conference on Telecommunications*, May 2011, pp. 539 – 543.

[52] H. Dehner, D. Figielek, H. Jekel, M. Braun, F. Jondral, and K. Witrisal, "High data rate coexistence-based channel coding for noncoherent multiband impulse radio UWB," in *2012 IEEE International Conference on Ultra-Wideband (ICUWB)*, Sept 2012, pp. 120 – 124.

[53] H. Dehner, Y. Koch, H. Jakel, D. Burgkhardt, F. Jondral, R. Moorfeld, and A. Finger, "Narrow-band interference robustness for energy detection in OOK/PPM," in *2010 IEEE International Conference on Communications*, May 2010, pp. 1 – 5.

[54] H.-U. Dehner, H. Jakel, D. Burgkhardt, and F. Jondral, "The Teager-Kaiser energy operator in presence of multiple narrowband interference," *IEEE Communications Letters*, vol. 14, no. 8, pp. 716 – 718, 2010.

[55] K. Witrisal, "Noncoherent autocorrelation detection of orthogonal multicarrier UWB signals," in *2008 IEEE International Conference on Ultra-Wideband*, vol. 2, Sept. 2008, pp. 161 – 164.

[56] J. R. Barry, E. A. Lee, and D. G. Messerschmitt, *Digital Communication*. Springer Science+Business Media Inc., 2004.

[57] S. M. Kay, *Fundamentals of Statistical Signal Processing: Estimation Theory*. Prentice Hall PTR, 1993.

[58] P. Meissner and K. Witrisal, "Analysis of a noncoherent UWB receiver for multichannel signals," in *2010 IEEE 71st Vehicular Technology Conference (VTC 2010-Spring)*, May 2010, pp. 1 – 5.

[59] P. Meissner, "Multichannel ultra-wideband systems with noncoherent autocorrelation detection," Master's thesis, Graz University of Technology, April 2009.

[60] G. Strang, *Linear Algebra and its Applications*. Harcourt Brace & Company, 1988.

[61] R. A. Horn and C. R. Johnson, *Matrix Analysis*, 2nd ed. Cambridge University Press, 2012.

[62] G. H. Golub, *Matrix Computations*, 4th ed. Johns Hopkins University Press, 2012.

[63] W. Ford and W. R. Topp, *Introduction to Computing Using C++ and Object Technology*. Prentice Hall, 1998.

[64] K. Witrisal and M. Pausini, "Statistical analysis of UWB channel correlation functions," *IEEE Transactions on Vehicular Technology*, vol. 57, no. 3, pp. 1359 – 1373, May 2008.

[65] M. K. Simon and M.-S. Alouini, *Digital Communication over Fading Channels*, 2nd ed. Wiley-IEEE Press, 2004.

[66] J. G. Proakis and M. Salehi, *Digital Communications*, 5th ed. McGraw - Hill, 2008.

[67] L. Wanhammar, *Analog Filters using MATLAB*. Springer, 2009.

[68] A. V. Oppenheim and R. W. Schafer, *Discrete-Time Signal Processing*. Pearson Education Limited, 2013.

[69] S. Luke, *Essentials of Metaheuristics*, 2nd ed. Lulu, 2013, available for free at http://cs.gmu.edu/∼sean/book/metaheuristics/.

[70] S. A. Hashemi and B. Nowrouzian, "A novel finite-wordlength particle swarm optimization technique for FRM IIR digital filters," in *IEEE International Symposium on Circuits and Systems*, May 2011, pp. 2745 – 2748.

[71] M. Haseyama and D. Matsuura, "A filter coefficient quantization method with genetic algorithm, including simulated annealing," *IEEE Signal Processing Letters*, vol. 13, no. 4, pp. 189 – 192, April 2006.

[72] Y. Yang and X. Yu, "Cooperative coevolutionary genetic algorithm for digital iir filter design," *IEEE Transactions on Industrial Electronics*, vol. 54, no. 3, pp. 1311 – 1318, June 2007.

[73] M. Nilsson, M. Dahl, and I. Claesson, "Digital filter design of iir filters using real valued genetic algorithm," in *Proceedings of the 2nd WSEAS International Conference on Electronics, Control and Signal Processing*. World Scientific and Engineering Academy and Society (WSEAS), Dec. 2003.

[74] C. Dai, W. Chen, and Y. Zhu, "Seeker optimization algorithm for digital iir filter design," *Transactions on Industrial Electronics*, vol. 57, no. 5, pp. 1710 – 1718, May 2010.

[75] R. Storn and K. Price, "Differential evolution - a simple and efficient heuristic for global optimization over continuous spaces," *Journal of Global Optimization*, vol. 11, no. 4, pp. 314 – 359, 1997.

[76] N. Karaboga, "Digital IIR filter design using differential evolution algorithm," *EURASIP Journal on Advances in Signal Processing*, vol. 7, pp. 1269 – 1276, 2005.

[77] B. Luitel and G. Venayagamoorthy, "Differential evolution particle swarm optimization for digital filter design," in *IEEE Congress on Evolutionary Computation*, June 2008, pp. 3954 – 3961.

[78] K.-S. Tang, K.-F. Man, S. Kwong, and Z.-F. Liu, "Design and optimization of IIR filter structure using hierarchical genetic algorithms," *IEEE Transactions on Industrial Electronics*, vol. 45, no. 3, pp. 481 – 487, Jun 1998.

[79] A. Melzer, A. Pedross, and M. Mücke, "Holistic biquadratic IIR filter design for communication systems using differential evolution," *Journal of Electrical and Computer Engineering, Special Issue on Hardware Implementation of Digital Signal Processing Algorithms*, vol. 2013, March 2013.

[80] B. Razavi, *RF Microelectronics.* Pearson Education, 2012.

[81] A. Gerosa, S. Soldà, A. Bevilacqua, D. Vogrig, and A. Neviani, "An energy-detector for noncoherent impulse-radio UWB receivers," *IEEE Transactions on Circuits and Systems I: Regular Papers*, vol. 56, no. 5, pp. 1030 – 1040, 2009.

[82] L. Stoica, A. Rabbachin, and I. Oppermann, "Impulse radio based non-coherent UWB transceiver architectures - an example," in *IEEE International Conference on Ultra-Wideband*, 2006, pp. 483 – 488.

[83] A. Rabbachin, T. Quek, P. Pinto, I. Oppermann, and M. Win, "Non-coherent UWB communication in the presence of multiple narrowband interferers," *IEEE Transactions on Wireless Communications*, vol. 9, no. 11, pp. 3365 – 3379, 2010.

[84] T. Q. Quek, M. Z. Win, and D. Dardari, "Unified analysis of UWB transmitted-reference schemes in the presence of narrowband interference," *IEEE Transactions on Wireless Communications*, vol. 6, no. 6, pp. 2126 – 2139, 2007.

[85] L. Zwirello, C. Heine, X. Li, and T. Zwick, "An UWB correlation receiver for performance assessment of synchronization algorithms," in *IEEE International Conference on Ultra-Wideband*, Sept. 2011, pp. 210 – 214.

[86] L. Lampe and K. Witrisal, "Challenges and recent advances in IR-UWB system design," in *IEEE International Symposium on Circuits and Systems*, May 2010, pp. 3288 – 3291.

[87] A. Oka and L. Lampe, "A compressed sensing receiver for bursty communication with UWB impulse radio," in *IEEE International Conference on Ultra-Wideband*, Sept. 2009, pp. 279 – 284.

[88] A. Pedross and K. Witrisal, "Analysis of nonideal multipliers for multichannel autocorrelation UWB receivers," in *2012 IEEE International Conference on Ultra-Wideband*, Sept. 2012, pp. 140 – 144.

[89] M. Schetzen, *The Volterra & Wiener Theories of Nonlinear Systems.* Krieger Publishing Company, 2006.

[90] V. J. Mathews and G. L. Sicuranza, *Polynomial Signal Processing.* John Wiley & Sons, Inc., 2000.

[91] P. Li and L. Pileggi, "Efficient per-nonlinearity distortion analysis for analog and RF circuits," *IEEE Transactions on Computer-Aided Design of Integrated Circuits and Systems*, vol. 22, pp. 1297 – 1309, 2003.

[92] G. Theodoratos, A. Vasilopoulos, G. Vitzilaios, and Y. Papananos, "Calculating distortion in active CMOS mixers using Volterra series," in *2006 IEEE International Symposium on Circuits and Systems*, 2006.

[93] D. Morgan, Z. Ma, J. Kim, M. Zierdt, and J. Pastalan, "A generalized memory polynomial model for digital predistortion of RF power amplifiers," *IEEE Transactions on Signal Processing*, vol. 54, no. 10, pp. 3852 – 3860, 2006.

[94] S. Billings and S. Y. Fakhouri, "Identification of a class of nonlinear systems using correlation analysis," *Proceedings of the Institution of Electrical Engineers*, vol. 125, no. 7, pp. 691 – 697, 1978.

[95] J. Paduart, L. Lauwers, R. Pintelon, and J. Schoukens, "Identification of a Wiener–Hammerstein system using the polynomial nonlinear state space approach," *Control Engineering Practice*, vol. 20, no. 11, pp. 1133 – 1139, 2012. [Online]. Available: http://www.sciencedirect.com/science/article/pii/S0967066112001281

[96] F. Ikhouane and F. Giri, "A unified approach for the identification of SISO/MIMO Wiener and Hammerstein systems," in *16th IFAC Symposium on System Identification*, July 2012, pp. 2 – 6.

[97] M. Boutayeb and M. Darouach, "Recursive identification method for MISO Wiener-Hammerstein model," *IEEE Transactions on Automatic Control*, vol. 40, no. 2, pp. 287 – 291, 1995.

[98] J. Dederer, *Si/SiGe HBT ICs for Impulse Ultra-Wideband (I-UWB) Communications and Sensing.* Cuvillier Verlag, 2009.

[99] J. Dederer, B. Schleicher, F. De Andrade Tabarani Santos, A. Trasser, and H. Schumacher, "FCC compliant 3.1 - 10.6 GHz UWB pulse radar system using correlation detection," in *2007 IEEE/MTT-S International Microwave Symposium*, June 2007, pp. 1471 – 1474.

[100] J. Dederer, B. Schleicher, A. Trasser, T. Feger, and H. Schumacher, "A fully monolithic 3.1 - 10.6 GHz UWB Si/SiGe HBT Impulse-UWB correlation receiver," in *2008 IEEE International Conference on Ultra-Wideband*, vol. 1, Sept. 2008, pp. 33 – 36.

[101] A. Schüppen, J. Berntgen, P. Maier, M. Tortschanoff, W. Kraus, and M. Averweg, "An 80 GHz SiGe production technology," *III-Vs Review*, vol. 14, no. 6, pp. 42 – 46, 2001. [Online]. Available: http://www.sciencedirect.com/science/article/pii/S0961129001805305

[102] B. Gilbert, "A precise four-quadrant multiplier with subnanosecond response," *IEEE Journal of Solid-State Circuits*, vol. 3, no. 4, pp. 365 – 373, Dec. 1968.

[103] F. Hayashi, *Econometrics.* Princeton Univ Press, 2000.

[104] R. Pintelon and J. Schoukens, *System Identification: A Frequency Domain Approach.* IEEE Press, 2001.

[105] L. Ljung, *System Identification: Theory for the User*, 2nd ed. Prentice Hall, 1999.

[106] L. Stoica, A. Rabbachin, H. Repo, T. Tiuraniemi, and I. Oppermann, "An ultrawideband system architecture for tag based wireless sensor networks," *IEEE Transactions on Vehicular Technology*, vol. 54, no. 5, pp. 1632 – 1645, sept. 2005.

[107] J. Tellado, L. Hoo, and J. Cioffi, "Maximum likelihood detection of nonlinearly distorted multicarrier symbols by iterative decoding," in *Global Telecommunications Conference*, vol. 5, 1999, pp. 2493 – 2498.

[108] P. Drotár, J. Gazda, P. Galajda, D. Kocur, and P. Pavelka, "Receiver technique for iterative estimation and cancellation of nonlinear distortion in MIMO SFBC-OFDM systems," *IEEE Transactions on Consumer Electronics*, vol. 56, no. 2, pp. 471 – 475, May 2010.

[109] M. Cherif Dakhli, R. Zayani, and R. Bouallegue, "A theoretical characterization and compensation of nonlinear distortion effects and performance analysis using polynomial model in MIMO OFDM systems under rayleigh fading channel," in *IEEE Symposium on Computers and Communications*, July 2013, pp. 583 – 587.

[110] M. Ibnkahla, "Neural network modeling and identification of nonlinear MIMO channels," in *International Symposium on Signal Processing and Its Applications*, Feb. 2007, pp. 1 – 4.

[111] "PE43602 product specification," Peregrine Semiconductor Corporation, San Diego, CA, USA, 2009, 50 Ω RF digital attenuator, 6-bit, 31.5 dB, 9 kHz - 5.0 GHz.

[112] "HMC311SC70 / HMC311SC70E data sheet," Hittite Microwave Corporation, Chelmsford, MA, USA, 2009, InGaP HBT gain block MMIC amplifier, DC - 8 GHz.

[113] "AD4950-1/AD4950-2 data sheet," Analog Devices, Norwood, MA, USA, 2013, low power, selectable gain differential ADC driver, G = 1, 2, 3.

[114] "ADA4938-1/ADA4938-2 data sheet," Analog Devices, Norwood, MA, USA, 2009, ultralow distortion differential ADC driver.

[115] "AD9650 data sheet," Analog Devices, Norwood, MA, USA, 2011, 16-Bit, 25 Msps/65 Msps/80 Msps/105 Msps, 1.8 V dual analog-to-digital converter (ADC).

[116] "Spartan-6 family overview," Xilinx Inc., San Jose, CA, USA, 2011, product specification.

[117] "VSC8641 data sheet," Vitesse, Camarillo, CA, USA, 2009, 10/100/1000BASE-T PHY with RGMII and GMII MAC interface.

[118] H. Friis, "A note on a simple transmission formula," *Proceedings of the IRE*, vol. 34, no. 5, pp. 254 – 256, May 1946.

[119] ——, "Noise figures of radio receivers," *Proceedings of the IRE*, vol. 32, no. 7, pp. 419 – 422, July 1944.

[120] R. Kravchenko, "Development of passive LTCC components with improved characteristics for microwave front-end applications," Ph.D. dissertation, Graz University of Technology, April 2011.

[121] Y. Imanaka, *Multilayered Low Temperature Cofired Ceramics (LTCC) Technology.* Springer, 2005.

[122] A. Pedross and K. Witrisal, "Sliding window integrator approximations for multichannel autocorrelation UWB receivers," in *2012 IEEE International Symposium on Circuits and Systems*, May 2012, pp. 2537 – 2540.

[123] G. van Rossum and F. L. J. Drake, *The Python Language Reference Manual.* Network Theory Ltd., 2011.

[124] A. Goldsmith, *Wireless Communications.* Cambridge University Press, 2005.

[125] A. A. M. Saleh and R. Valenzuela, "A statistical model for indoor multipath propagation," *IEEE Journal on Selected Areas in Communications*, vol. 5, no. 2, pp. 128 – 137, February 1987.

[126] L. Isserlis, "On an formula for the product-moment coefficient of any order of a noermal frequency distribution in any number of variables," *Biometrika*, vol. 12, no. 1 - 2, pp. 134 – 139, 1918.

[127] J. C. Maxwell, "A dynamical theory of the electromagnetic field," *Philosophical Transactions of the Royal Society of London*, vol. 155, pp. 459 – 512, 1865.

[128] H. Hertz, "Über sehr schnelle elektrische schwingungen," *Annalen der Physik*, vol. 267, 1887.

[129] N. Tesla, "Experiments with alternating currents of high frequency," *The Electrical Engineer*, vol. May 18, 1891.

[130] ——, "Method of and apparatus for controlling mechanism of moving vehicle or vehicles," U.S. Patent 613,809, Nov. 8, 1898.

[131] P. Bondyopadhyay, "Guglielmo Marconi - the father of long distance radio communication - an engineer's tribute," in *25th European Microwave Conference*, vol. 2, Sept. 1995, pp. 879 – 885.

[132] E. H. Armstrong, "Radio signaling system," U.S. Patent 1,941,066, July 30, 1930.

[133] D. Lindley, "Landmarks: Birth of modern electronics," *Physical Review Focus*, vol. 23, p. 16, May 2009. [Online]. Available: http://link.aps.org/doi/10.1103/PhysRevFocus.23.16

[134] C. E. Shannon, "A mathematical theory of communication," *The Bell System Technical Journal*, vol. 27, pp. 379 – 423, 623 – 656, July, October 1948. [Online]. Available: http://cm.bell-labs.com/cm/ms/what/shannonday/shannon1948.pdf

[135] "Memorandum of understanding in the implementation of a PAN european 900 MHz digital cellular mobile telecommunication service by 1991," Sept. 1987.

G

Collection of Papers

In the following an annotated list is shown of works published by the author. This list discusses the relationship between the previous published works and this actual PhD thesis. Parts which are taken from previous works are disclosed and commented. It is also shown which works were completed jointly with third parties. Following the annotated list of publications, reprints of the respective works are attached.

- **A. Pedross and K. Witrisal, "Sliding window integrator approximations for multichannel autocorrelation UWB receivers," in** *2012 IEEE International Symposium on Circuits and Systems,* **May 2012, pp. 2537 − 2540.**
  This work focuses on integration devices, which are part of multi-channel autocorrelation receivers and are essential to suppress nonlinear cross-products between data carriers. Passive filter structures are analyzed for this purpose. It is shown that the optimized filter outperforms the reference system using an ideal sliding window integrator because it is able to mitigate more system noise. Parts of this paper are shown in Section 3.3.

- **A. Pedross and K. Witrisal, "Analysis of nonideal multipliers for multichannel autocorrelation UWB receivers," in** *2012 IEEE International Conference on Ultra-Wideband,* **Sept. 2012, pp. 140 − 144.**
  This work focuses on multiplication devices, which are a core part of multi-channel auto-correlation receivers and introduce strong interference due to nonlinear effects. To analyze the signal-to-interference ratio performance of the receiver system, a combined Wiener-Hammerstein system model of the multiplication device is introduced. It is shown that the receiver performance strongly depends on the input power of the nonideal multiplier devices. Parts of this paper are shown in Section 3.2.

- **A. Melzer, A. Pedross, and M. Mücke, "Holistic biquadratic IIR filter design for communication systems using differential evolution,"** *Journal of Electrical and Computer Engineering, Special Issue on Hardware Implementation of Digital Signal Processing Algorithms,* **vol. 2013, March 2013.**
  This work focuses on optimization of digital IIR filter implementations with regard on the chosen number format (fixed-point, floating-point; precision). This work considers IIR filter design as an integral part of communication system optimization with implicit filter specification in the time domain (via symbol/bit error rate). A holistic design flow is presented with the bit-error rate of the system as the main objective. Differential Evolution

is used for efficient sampling of the huge finite design space. The performance of a communication system is presented based on bit-true simulations. It is shown that very small number formats are acceptable for complex filters and that the choice between fixed-point and floating-point number formats is nontrivial if precision is a free parameter. This work presents the outcome of a Master thesis written by A. Melzer, now with the Institute of Signal Processing at Johannes Kepler University Linz, Austria, and supervised by the author of this PhD thesis and M. Mücke, with Sustainable Computing Research, Vienna, Austria. The results of this journal paper did not contribute to this PhD thesis. However, references of the literature studies are reused in Section 3.1.

- **A. Pedross-Engel, H. Schumacher, and K. Witrisal, "Modeling and identification of ultrawideband analog multipliers,"** *IEEE Transactions on Circuits and Systems I: Regular Papers,* **submitted.**
  This work focuses on modeling and identification of realistic RF multipliers. It proposes and validates a multiple-input single-output Wiener-Hammerstein model for ultrawideband analog multipliers. The structure of the proposed model gives insight in the distortions created and it provides the possibility to study the realistic behavior of systems involving those multipliers, e.g. the influence of undesired nonlinear signal content. A comparison of the model performance is shown with respect to measurements and Agilent ADS circuit simulations. Parts of this paper are shown in Section 3.2. Prof. Schumacher is head of the Institute of Electron Devices and Circuits at Ulm University, Germany. His institute contributed the hardware multipliers which are investigated in this paper.

Sliding Window Integrator Approximations for Multichannel Autocorrelation UWB Receivers

Andreas Pedross* and Klaus Witrisal*

*Graz University of Technology, Austria; {andreas.pedross,witrisal}@tugraz.at

Abstract—Noncoherent UWB receivers promise low power consumption and low processing complexity but their peak data rate is limited by the delay spread of the multipath radio channel. A recently proposed multichannel autocorrelation receiver (AcR) can break this rate limit because it can demodulate multicarrier signals. The hardware implementation of this receiver architecture is addressed in this paper. We focus on the integration device, which is part of the AcR and essential to suppress nonlinear cross-products between data carriers. Passive filter structures are analyzed for this purpose. It is shown that the optimized filter outperforms the reference system using an ideal sliding window integrator because it is able to mitigate more system noise.

I. Introduction

Noncoherent receivers are a possible way forward to exploit the advantages of UWB technology in low-complexity, low-power devices [1]. However, their simplicity comes at the cost of reduced robustness in presence of noise and multipath interference. For instance to achieve high data rate using an energy detection receiver, a rather hard limit is set by the excess delay of the multipath channel. Equalization schemes achieve limited gains only [2].

An alternative approach to increasing the data rate is multicarrier transmission [3], [4], where an analog frontend is used to separate the received signal into its subcarriers. The subcarriers can be sampled and processed at much lower bandwidth; typically at symbol rate. A fixed implementation of a suitable filter bank would result in a very robust high-rate receiver, but it would require highly selective frontend filters and lack any flexibility concerning the band selection. The flexibility improves with the receiver architecture described in [4], which performs an autocorrelation operation in the analog frontend (cf. Fig. 1) and leaves the bandselection to a digital backend running at moderately slow symbol rate.

This paper addresses the hardware requirements of the latter receiver. It concentrates on the integration and sampling blocks, which have an essential role in suppressing cross-products between subcarriers that arise in the nonlinear frontend. We investigate passive filter structures combined with conventional ADCs. This yields a solution that can potentially be realized using standard building blocks and it may save power compared with an active design as in [5].

The paper is organized as follows. In Section II a review of the multichannel AcR system is given for a better under-
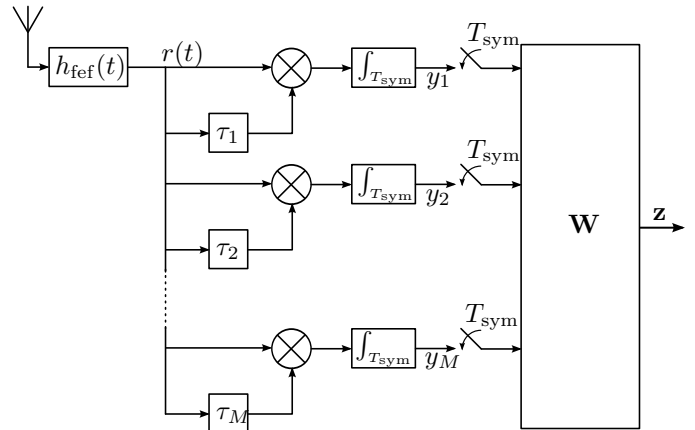
Fig. 1. The multichannel AcR architecture consists of delay filters, multiplication devices, and integration filters.

standing of the integrator design constraints. The passive filter design is addressed in Section IV. The analysis and system performance concerning the signal, noise, and self-interference is given in Section V. In Section VI bit-error-rate comparisons are shown, followed by conclusions.

II. Review of the MC-AcR

The aim of the multichannel AcR is to avoid the need for directly sampling the passband signal, which would require sampling-rates of several GSamples/s. The crucial signal processing is the computation of a short-time estimate of the autocorrelation function for the delays $\{\tau_m\}$. It is done in the analog domain, therefore the received signal only needs to be sampled at symbol-rate R_{sym}.

The system is briefly reviewed below to understand the requirements of the sliding window integrator in the multichannel AcR system.

Assuming an inter-symbol-interference (ISI) free scenario, by introduction of a sufficient long zero guard interval, our analysis can concentrate on a single transmitted symbol with period T_{sym}. The transmitted signal can be written as

$$s(t) = \Re\left\{ e^{+j\omega_{\mathrm{c}}t} \sum_{k=-\frac{K-1}{2}}^{+\frac{K-1}{2}} s_k \varphi(t) e^{+jk\omega_{\mathrm{sc}}t} \right\}, \quad (1)$$

where s_k is the $(\frac{K+1}{2}+k)$-th element of a K-dimensional symbol vector $\mathbf{s}$, $\varphi(t)$ is the sub-carrier pulse shape, ω_{sc} is the sub-carrier spacing, ω_{c} is the center frequency, j is the imaginary

unit, and $\Re\{.\}$ is the real operator. The terms $\varphi(t)e^{+jk\omega_{\mathrm{sc}}t}$, with $k \in \mathcal{K}$, $\mathcal{K} = \left\{-\frac{K-1}{2},...,+\frac{K-1}{2} \mid K \text{ is odd}\right\}$, are orthogonal basis functions which span a K-dimensional signal space.

The received signal is given as

$$r(t) = h_{\mathrm{ch}}(t) * s(t) + n(t) \tag{2}$$

$$= \Re\left\{e^{+j\omega_{\mathrm{c}}t}\sum_{k\in\mathcal{K}}s_k\tilde{\varphi}_k(t)e^{+jk\omega_{\mathrm{sc}}t}\right\} + n(t), \tag{3}$$

where $h_{\mathrm{ch}}(t)$ is the convolution of the channel impulse response (CIR) and the front-end band-selection filter $h_{\mathrm{fef}}(t)$, $\tilde{\varphi}_k(t)$ is the k-th sub-carrier pulse shape which is distorted by the channel $h_{\mathrm{ch}}(t)$, and $n(t)$ is filtered Gaussian noise.

The analog signal processing of the multichannel noncoherent autocorrelation receiver, c.f. Fig. 1, consists of a front end filter for frequency band selection and M AcR channels which perform the autocorrelation. The m-th AcR output is given as

$$y_m = \int_{\lambda=0}^{T_{\mathrm{sym}}} r(\lambda) \cdot r(\lambda - \tau_m)d\lambda \tag{4}$$

$$\approx \frac{1}{2}\sum_{k\in\mathcal{K}}s_k^2\Re\left\{\tilde{\Phi}_{kk}(\tau_m)e^{+j\omega_{\mathrm{c}}\tau_m}\right\} +$$

$$+ \frac{1}{2}\sum_{k\in\mathcal{K}}\sum_{\substack{l\in\mathcal{K}\\l\neq k}}s_k s_l\Re\left\{\tilde{\Phi}_{kl}(\tau_m)e^{+j\omega_{\mathrm{c}}\tau_m}\right\} +$$

$$+ \nu_m \tag{5}$$

$$\approx s_{\mathrm{co}}\left(\tau_m\right) + s_{\mathrm{cross}}\left(\tau_m\right) + \nu_m, \tag{6}$$

where τ_m is its delay time, $s_{\mathrm{co}}\left(\tau_m\right)$ is the signal co-terms, $s_{\mathrm{cross}}\left(\tau_m\right)$ is the the signal cross-terms, ν_m is the combination of all noise terms, and

$$\tilde{\Phi}_{kl}(\tau_m) = e^{+jl\omega_{\mathrm{sc}}\tau_m}\int_{\lambda=0}^{T_{\mathrm{sym}}}\tilde{\varphi}_k(\lambda)\tilde{\varphi}_l^*(\lambda - \tau_m)e^{+j(k-l)\omega_{\mathrm{sc}}\lambda}d\lambda \tag{7}$$

is the cross-correlation of the k-th and l-th basis function at given τ_m. Because the basis functions are assumed to be orthogonal for any delay τ_m, the cross-terms (where $l \neq k$) will vanish [4], [6]. For $l = k$ we get the autocorrelation of the k-th basis function at delay lag τ_m.

It can be seen from (7) that the autocorrelation terms ($l = k$) of the basis set map to baseband pulses plus an additional phase shift dependent on the sub-carrier frequency $l\omega_{\mathrm{sc}}$ and the AcR channel delay lag τ_m. A similar behavior can be seen for $l \neq k$, except that the baseband pulses are transformed to different frequencies $(k - l)\omega_{\mathrm{sc}}$. In Fig. 2, the co- and cross-terms, before integration, of a $K = 7$ sub-carrier UWB OFDM signaling scheme are depicted in the frequency domain.

Using vector notation we can rewrite (6) as

$$\mathbf{y} = \mathbf{H}\mathbf{s} + \mathbf{G}\left(\mathbf{s}\otimes\mathbf{s}\right) + \boldsymbol{\nu}, \tag{8}$$

where $\mathbf{H}$ is the MIMO channel matrix of the co-terms, $\mathbf{G}$ is the cross-terms interference matrix ($\otimes$ denotes the reduced Kronecker product), and $\boldsymbol{\nu}$ is the noise vector. This equation
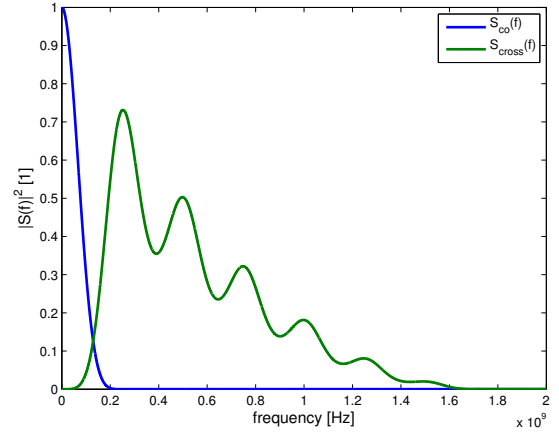
Fig. 2. Power spectrum density of the co- and cross-terms of an OFDM transmission scheme after the multiplication in an AcR channel for $K = 7$ sub-carrier UWB OFDM signaling scheme.

becomes $\mathbf{y} = \mathbf{H}\mathbf{s} + \boldsymbol{\nu}$ for orthogonal basis functions, given that the cross-terms vanish and therefore $\mathbf{G} = \mathbf{0}$.

Assuming $M \geq K$ it is possible to reconstruct $\mathbf{s}$ using the Moore-Penrose pseudoinverse or a minimum-mean-square-error (MMSE) approach [6], [7], which is denoted by a transformation matrix $\mathbf{W}$. The decision variable vector $\mathbf{z}$ (c.f. Fig. 1) is therefore defined as

$$\mathbf{z} = \mathbf{W}\mathbf{y} \tag{9}$$

$$= \mathbf{W}\mathbf{H}\mathbf{s} + \mathbf{W}\mathbf{G}\left(\mathbf{s}\otimes\mathbf{s}\right) + \mathbf{W}\boldsymbol{\nu}. \tag{10}$$

III. MOTIVATION

To minimize erroneous detection of $\mathbf{s}$, interference and noise have to be reduced. Because $\mathbf{s}$ is reconstructed by the linear transformation $\mathbf{W}$ of the AcR channel outputs $\mathbf{y}$, and M will be chosen only slightly greater than K for complexity reason, it is necessary to mitigate signal cross-terms and noise at the level of the AcR channel outputs y_m. These signal terms can be minimized by applying a low-pass filter (c.f Fig. 2).

In (7) it can be seen that the system has to perform an integration over the symbol period T_{sym}. This operator can be described as a filter with the impulse response

$$h_T(t) = \sigma(t) - \sigma(t - T), \tag{11}$$

where T is the integration window, and $\sigma(t)$ is the unit step function. The frequency response of the filter is given as

$$H_T(j\omega) = Te^{-j\frac{T}{2}\omega}\mathrm{sinc}\left(\frac{T}{2\pi}\omega\right), \tag{12}$$

where $\mathrm{sinc}(x) = \frac{\sin(\pi x)}{\pi x}$ and ω is the angular frequency. Unfortunately, this ideal filter cannot be realized in real hardware. Therefore approximations of this ideal integration filter are needed.

Design goals for the filter approximation are a high output signal-to-noise ratio ($\mathrm{SNR_z}$), which is defined as

$$\mathrm{SNR_z} = \frac{\mathrm{E}\left\{\mathbf{s}^T\mathbf{H}^T\mathbf{W}^T\mathbf{W}\mathbf{H}\mathbf{s}\right\}}{\mathrm{E}\left\{\boldsymbol{\nu}^T\mathbf{W}^T\mathbf{W}\boldsymbol{\nu}\right\}}, \tag{13}$$
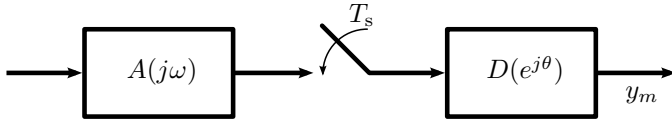
Fig. 3. Signal flow graph of the mixed-singal sliding window integrator.

and a high output signal-to-interference ratio (SIR$_\mathbf{z}$), which is defined as (c.f. (6), (10))

$$\text{SIR}_\mathbf{z} = \frac{\text{E}\left\{\mathbf{s}^T \mathbf{H}^T \mathbf{W}^T \mathbf{W} \mathbf{H} \mathbf{s}\right\}}{\text{E}\left\{(\mathbf{s} \otimes \mathbf{s})^T \mathbf{G}^T \mathbf{W}^T \mathbf{W} \mathbf{G} (\mathbf{s} \otimes \mathbf{s})\right\}}. \qquad (14)$$

IV. APPROXIMATED SLIDING WINDOW INTEGRATORS

Approximation of the sliding window integrator (12) can be obtained using a low-pass Bessel filter and several notch-filters. The Bessel filter is used to get the magnitude frequency response and a constant group-delay up to an upper frequency, while the notch-filters are used for the zeros in the frequency response. For broadband signals this could lead to analog filters of very high order, due to the need of many notch filters. A mixed analog / digital implementation can relax this issue, as described below.

A. Approximation I

The impulse response (11) is rewritten as

$$h_T(t) = (\sigma(t) - \sigma(t - T_s)) * \sum_{k=0}^{N_T - 1} \delta(t - kT_s), \qquad (15)$$

where $T_s = \frac{T}{N_T}$, $N_T \in \mathbb{N}$. The sliding window integrator is split up into an integrator with a shorter window of length $\frac{T}{N_T}$ and a filter consisting of equally spaced Dirac impulses: a comb filter which can be described by a digital FIR filter easily, where T_s is the discrete-time sampling period. The comb filter has the discrete-time frequency response

$$D\left(e^{j\theta}\right) = \sum_{k=0}^{N_T - 1} e^{-j\theta k}, \qquad (16)$$

where θ is the normalized angular frequency, $\theta = \omega T_s$.

The new sliding window integrator $A(j\omega)$ is given by (12) but with reduced integration interval T_s. The frequency-spacing of the zeros increases when decreasing the integration interval, therefore the need of analog notch-filters *within the signal bandwidth* is relaxed. The digital filter introduces additional zeros at frequencies $\omega = k2\pi/(N_T T_s)$, $k \in \{\mathbb{Z} \mid (k \mod N_T) \neq 0\}$. In other words, the order of the analog filter is minimized by making the length of the sampling time T_s as small as possible. The accumulation of these partial integrations can be done by the digital comb filter without much effort.

The filter parameters (the upper frequency (F$_g$) of constant group-delay of the Bessel filter and the quality factors (Q$_1$, Q$_2$) of the notch-filters) can be found numerically, applying

$$\boldsymbol{\theta}_\text{I} = \arg\min_{\boldsymbol{\theta}} \frac{\int |H_T(f) - A(f, \boldsymbol{\theta})D(f)G(f, \boldsymbol{\theta})|^2 \, df}{\int |H_T(f)|^2 \, df}, \quad (17)$$

where $\boldsymbol{\theta}_\text{I}$ is a parameter vector and $G(f, \boldsymbol{\theta}) = e^{j2\pi f \tau_g}$ is a correction term for a constant group-delay difference between the ideal filter $H_T(f)$ and the approximation filter $A(f, \boldsymbol{\theta})D(f)$. The magnitude responses and the impulse responses of an example filter can be seen in Fig. 4.

B. Approximation II

Other filter approximations can be made too. A possibility is to reduce the combination of a low-pass filter and notch filters to a single Bessel type low-pass filter. Its upper frequency of constant group-delay F$_g$ can be found applying

$$\text{F}_g = \arg\min_{\text{F}_g} \frac{\int ||H_T(f)| - |A(f, \text{F}_g)D(f)||^2 \, df}{\int |H_T(f)|^2 \, df}, \qquad (18)$$

which is a simplification of (17) due to lower degree of freedom. The magnitude responses and the impulse responses of an example filter are illustrated in Fig. 4. Surprisingly this approximation can lead to a better performance than the ideal sliding window integrator.

V. FILTER ANALYSIS

To investigate the performance of the various sliding window integrator approximations SNR$_\mathbf{z}$ and SIR$_\mathbf{z}$ are considered, c.f Section III. The signaling scheme is a $K = 7$ sub-carrier UWB OFDM signal, where a truncated root-raised-cosine pulse was used with signal bandwidth and sub-carrier spacing of 250 MHz, and binary pulse position modulation (BPPM). This signaling scheme is used for the rest of the paper. The input signal $\frac{\mathcal{E}_b}{N_0}$ (bit energy $\mathcal{E}_b$ over noise spectral density N_0) was set to be 18 dB.

In Table I, the SNR$_\mathbf{z}$ and SIR$_\mathbf{z}$ values and filter parameters are listed for the two different approximation techniques, c.f. Section IV, as a function of the overall analog filter order. It can be seen, that the ideal sliding window integrator has the best SIR$_\mathbf{z}$ performance, which is obvious when considering that the cross-terms should vanish completely for the ideal case. The SIR$_\mathbf{z}$ of the second approximation method is in general higher than that of the first approximation with comparable filter order. This is due to the steeper frequency response of the second approximation filter that attenuates the high-frequency parts (i.e. the cross-terms) more heavily. The SNR$_\mathbf{z}$ of the second approximation exceeds the SNR$_\mathbf{z}$ of the ideal sliding window integration filter, due to the steeper magnitude response.

VI. SYSTEM SIMULATIONS & RESULTS

In Fig. 5 a comparison of the bit-error-rate (BER) of the aforementioned approximation methods is depicted. The simulated communication system and signals are described in Sections II and V. The resulting BER shows that both approximation methods are able to achieve similar performance compared with with an ideal sliding window integrator. Due to the better SNR$_\mathbf{z}$, Approx. II shows the best BER results.
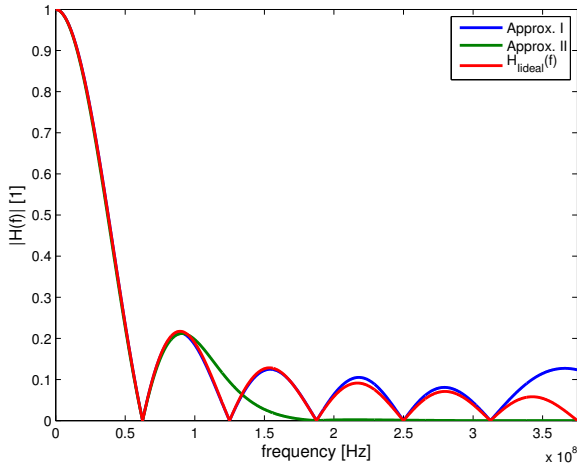
(a) Magnitude response
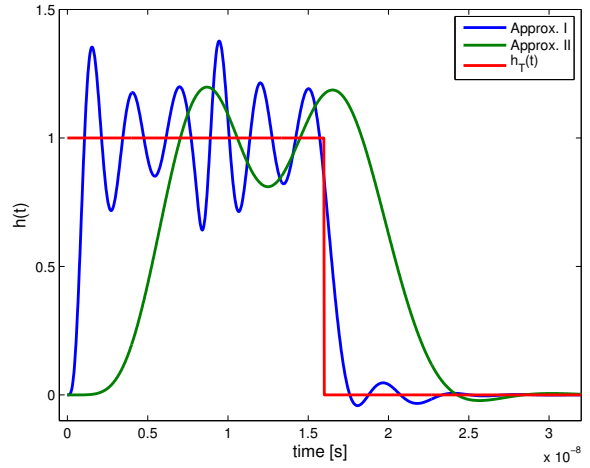
(b) Impulse response

Fig. 4.   Magnitude response and impulse response of the Approx. I and Approx. II sliding window integrator.

TABLE I
ANALOG FILTER PARAMETERS (FILTER ORDER N, F_G, Q_1, AND Q_2) AND OUTPUT SNR (SNR_z) AND OUTPUT SIR (SIR_z) OF THE TWO FILTER APPROXIMATIONS. THE IDEAL INTEGRATOR HAS AN SNR_z OF 13.4 DB AND AN SIR_z OF 49.0 DB.

N	Approx. I					Approx. II		
	F_g [MHz]	Q_1	Q_2	SNR_z [dB]	SIR_z [dB]	F_g [MHz]	SNR_z [dB]	SIR_z [dB]
1						39.9	12.6	33.2
2						60.9	13.4	28.4
3						72.3	13.5	28.3
4						80.2	13.5	29.5
5	82.3	1.0	2.2	13.0	18.9	86.5	13.5	31.2
6	157.8	0.7	2.4	13.3	24.2	91.9	13.5	33.0
7	236.9	0.6	1.9	13.3	23.3	96.8	13.5	34.2
8	254.5	0.6	1.9	13.4	26.4	101.4	13.5	35.3
9	277.4	0.6	1.8	13.4	27.6	105.8	13.4	37.8
10	293.3	0.6	1.8	13.4	28.7	110.1	12.2	37.8

Fig. 5.   BER for the given approximation setups in comparison to an ideal integrator.

VII. CONCLUSION

This work investigates approximation methods for ideal sliding window integrators. It has been shown that a simple mixed-signal system is able to perform a sliding window integration with low-complexity and rather high accuracy compared to the reference system with an ideal sliding window integrator. Additionally, it has been shown for the discued UWB OFDM scenario that the resulting mixed-signal implementation can exceed the performance of the reference system.

REFERENCES

[1] K. Witrisal, G. Leus, G. Janssen, M. Pausini, F. Troesch, T. Zasowski, and J. Romme, "Noncoherent ultra-wideband systems," *Signal Processing Magazine, IEEE*, vol. 26, no. 4, pp. 48 –66, 2009.
[2] T. Zasowski, F. Troesch, and A. Wittneben, "Partial channel state information and intersymbol interference in low complexity UWB PPM detection," Sep. 2006, pp. 369–374.
[3] S. Paquelet, L.-M. Aubert, and B. Uguen, "An impulse radio asynchronous transceiver for high data rates," in *Ultra Wideband Systems, 2004. Joint with Conference on Ultrawideband Systems and Technologies. Joint UWBST IWUWBS. 2004 International Workshop on*, may 2004, pp. 1 – 5.
[4] K. Witrisal, "Noncoherent autocorrelation detection of orthogonal multicarrier UWB signals," in *Ultra-Wideband, 2008. ICUWB 2008. IEEE International Conference on*, vol. 2, 2008, pp. 161 –164.
[5] L. Stoica, A. Rabbachin, H. Repo, T. Tiuraniemi, and I. Oppermann, "An ultrawideband system architecture for tag based wireless sensor networks," vol. 54, no. 5, pp. 1632–1645, Sep. 2005.
[6] P. Meissner and K. Witrisal, "Analysis of a noncoherent UWB receiver for multichannel signals," in *Vehicular Technology Conference, VTC2010-Spring*, IEEE, Ed., IEEE.   Taipei: IEEE, May 2010, pp. 1 – 5. [Online]. Available: http://www.ieeevtc.org/vtc2010spring
[7] J. R. Barry, E. A. Lee, and D. G. Messerschmitt, *Digital Communication*. Springer Science+Business Media Inc., 2004.

Analysis of Nonideal Multipliers for Multichannel Autocorrelation UWB Receivers

Andreas Pedross* and Klaus Witrisal*

*Graz University of Technology, Austria; {andreas.pedross,witrisal}@tugraz.at

Abstract—**Noncoherent UWB receivers promise low power consumption and low processing complexity but their peak data rate is limited by the delay spread of the multipath radio channel. A recently proposed multichannel autocorrelation receiver (AcR) can break this rate limit due to its multicarrier signal demodulation capability. In this paper, the hardware implementation of this receiver architecture is addressed. We focus on the multiplication device, which is a core part of the AcR and introduces strong interference due to nonlinear effects. To analyze the signal-to-interference ratio performance of the receiver system, a combined Wiener-Hammerstein system model of the multiplication device is introduced. It is shown that the receiver performance strongly depends on the input power of the nonideal multiplier devices.**

Index Terms—**Autocorrelation receiver, Mixers, Nonlinear distortions, Noncoherent receivers, UWB**

I. INTRODUCTION

Noncoherent receivers are a possible way forward to exploit the advantages of UWB technology in low-complexity, low-power devices [1]. However, their simplicity comes at the cost of reduced robustness in presence of noise and multipath interference. To achieve, for instance, high data rate using an energy detection receiver, a rather hard limit is set by the excess delay of the multipath channel. Equalization schemes can achieve limited gains only [2].

An alternative approach to increasing the data rate is multicarrier transmission [3], [4], where an analog frontend is used to separate the received signal into its subcarriers. The subcarriers can be sampled and processed at much lower bandwidth; typically at symbol rate. A fixed implementation of a suitable filter bank would result in a very robust high-rate receiver, but it requires highly selective frontend filters and lack any flexibility concerning the band selection. The flexibility improves with the receiver architecture described in [4], which performs an autocorrelation operation in the analog frontend (cf. Fig. 1) and leaves the bandselection to a digital backend running at moderately slow symbol rate.

For computing autocorrelation in analog hardware, a device is needed with a transfer function given as

$$z(t) = x(t) \cdot y(t), \tag{1}$$

where $x(t)$ and $y(t)$ are input signals, $z(t)$ is the output signal.

Well known multiplication devices are the so called mixers. In communication systems, mixers are used to transform
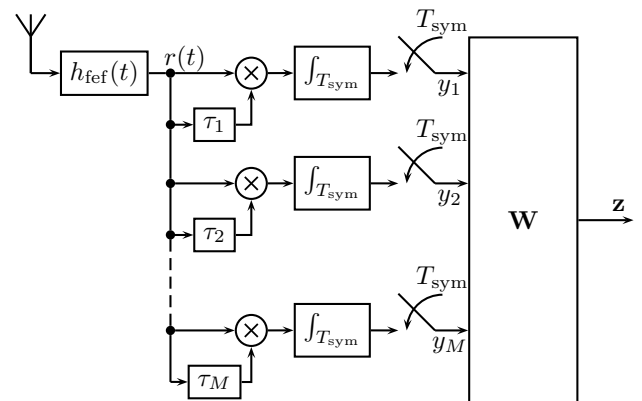
Fig. 1. The multichannel AcR architecture consists of delay filters, multiplication devices, and integration filters.

baseband signals or signals with low center frequency up to radio frequency (RF) and vice versa. They are doing this by multiplying the input signal with a single tone signal e.g. $z(t) = x(t) \cdot \cos(2\pi F t + \phi)$, where $x(t)$ is a broadband input signal, F is the difference between the center frequency of the input signal $x(t)$ and the center frequency of the output signal $z(t)$, and ϕ is some phase offset. I.e., these devices are designed only for the specific frequency transformation purpose. For analysis of this frequency transformation, the mixer can be considered as single-input-single-output (SISO) device, due to the fact that the input from the local oscillator, except for the phase offset, is considered to be known. This assumption leads to mixer characteristics which are taken from single-tone and two-tone excitation of the signal port, e.g. conversion gains and input intercept points of third order (IIP3). However, these narrowband characteristics cannot give a reasonable description of the mixer output for using it as UWB multiplication device.

This paper addresses the hardware requirements of the multichannel AcR. In a previous work, the influence on the signal-to-interference ratio of the implementation of the integrate-and-dump device using a mixed-signal approach was shown [5]. In contrast, this work concentrates on the self-interference induced by the nonideal multiplier used to compute the autocorrelation.

The paper is organized as follows. In Section II a review of the multichannel AcR system is given for a better under-

standing of the nonlinear multiplier induced self-interference. The multiplier signal model is addressed in Section III. The analysis and system performance concerning self-interference is given in Section V. In Section VI bit-error-rate comparisons are shown, followed by conclusions.

II. REVIEW OF THE MC-AcR

The aim of the multichannel AcR is to avoid the need for ADCs for sampling the passband signal, which would require sampling-rates of several GSamples/s. The crucial signal processing is the computation of a short-time estimate of the autocorrelation function for the delays $\{\tau_m\}$. It is done in the analog domain, therefore the received signal only needs to be sampled at symbol-rate $R_{\text{sym}} = \frac{1}{T_{\text{sym}}}$.

Assuming an inter-symbol-interference (ISI) free scenario by introduction of a sufficient long zero guard interval, our analysis can concentrate on a single transmitted symbol with period T_{sym}. The transmitted signal can be written as

$$s(t) = \Re\left\{ e^{+j\omega_c t} \sum_{k=-\frac{K-1}{2}}^{+\frac{K-1}{2}} s_k \varphi(t) e^{+jk\omega_{\text{sc}} t} \right\}, \quad (2)$$

where s_k is the $(k+\frac{K+1}{2})$-th element of a K-dimensional symbol vector $\mathbf{s}$, $\varphi(t)$ is the sub-carrier pulse shape, ω_{sc} is the sub-carrier spacing, ω_c is the center frequency, j is the imaginary unit, and $\Re\{.\}$ is the real operator. The terms $\varphi(t) e^{+jk\omega_{\text{sc}} t}$, with $k \in \mathcal{K}$, $\mathcal{K} = \left\{ -\frac{K-1}{2}, ..., +\frac{K-1}{2} \mid K \text{ is odd} \right\}$, are orthogonal basis functions which span a K-dimensional signal space.

The received signal is given as

$$r(t) = h_{\text{ch}}(t) * s(t) + n(t) \quad (3)$$

$$= \Re\left\{ e^{+j\omega_c t} \sum_{k\in\mathcal{K}} s_k \tilde{\varphi}_k(t) e^{+jk\omega_{\text{sc}} t} \right\} + n(t), \quad (4)$$

where $h_{\text{ch}}(t)$ is the convolution of the channel impulse response (CIR) and the front-end band-selection filter $h_{\text{fef}}(t)$, $\tilde{\varphi}_k(t)$ is the k-th sub-carrier pulse shape which is distorted by the channel $h_{\text{ch}}(t)$, and $n(t)$ is filtered Gaussian noise.

The analog signal processing of the multichannel noncoherent autocorrelation receiver, c.f. Fig. 1, consists of a front end filter for frequency band selection and M AcR channels which perform the autocorrelation. The m-th AcR output is given as

$$y_m = \int_{\lambda=0}^{T_{\text{sym}}} r(\lambda) \cdot r(\lambda - \tau_m) d\lambda \quad (5)$$

$$\approx \frac{1}{2} \sum_{k\in\mathcal{K}} s_k^2 \Re\left\{ \tilde{\Phi}_{kk}(\tau_m) e^{+j\omega_c\tau_m} \right\} +$$

$$+ \frac{1}{2} \sum_{k\in\mathcal{K}} \sum_{\substack{l\in\mathcal{K} \\ l\neq k}} s_k s_l \Re\left\{ \tilde{\Phi}_{kl}(\tau_m) e^{+j\omega_c\tau_m} \right\} +$$

$$+ \nu_m, \quad (6)$$

where τ_m is its delay time, ν_m is the combination of all noise terms, and

$$\tilde{\Phi}_{kl}(\tau_m) = e^{+jl\omega_{\text{sc}}\tau_m} \int_{\lambda=0}^{T_{\text{sym}}} \tilde{\varphi}_k(\lambda) \tilde{\varphi}_l^*(\lambda - \tau_m) e^{+j(k-l)\omega_{\text{sc}}\lambda} d\lambda \quad (7)$$

is the cross-correlation of the k-th and l-th basis function at given τ_m. Because the basis functions are assumed to be orthogonal for any delay τ_m, the cross-terms (where $l \neq k$) will vanish [4], [6]. For $l = k$ we get the autocorrelation of the k-th basis function at delay lag τ_m.

Using vector notation we can rewrite (6) as

$$\mathbf{y} = \mathbf{H}\mathbf{s} + \mathbf{G}\left(\mathbf{s}\tilde{\otimes}\mathbf{s}\right) + \boldsymbol{\nu}, \quad (8)$$

where $\mathbf{H}$ is the MIMO channel matrix of the co-terms, $\mathbf{G}$ is the cross-terms interference matrix ($\tilde{\otimes}$ denotes the reduced Kronecker product), and $\boldsymbol{\nu}$ is the noise vector. This equation becomes $\mathbf{y} = \mathbf{H}\mathbf{s} + \boldsymbol{\nu}$ for orthogonal basis functions, given that the cross-terms vanish and therefore $\mathbf{G} = \mathbf{0}$.

Assuming $M \geq K$, it is possible to reconstruct $\mathbf{s}$ using the Moore-Penrose pseudoinverse or a minimum-mean-square-error (MMSE) approach [6], [7], which is denoted by a transformation matrix $\mathbf{W}$. The decision variable vector $\mathbf{z}$ (c.f. Fig. 1) is therefore defined as

$$\mathbf{z} = \mathbf{W}\mathbf{y} \quad (9)$$

$$= \mathbf{W}\mathbf{H}\mathbf{s} + \mathbf{W}\mathbf{G}\left(\mathbf{s}\tilde{\otimes}\mathbf{s}\right) + \mathbf{W}\boldsymbol{\nu}. \quad (10)$$

III. SIGNAL MODEL OF NONIDEAL MULTIPLIERS

To study the UWB behavior of commercial multipliers, an Agilent ADS circuit-level model of a UWB mixer designed by the University of Ulm [8] was used. This mixer was designed to perform a multiplication operation for a UWB correlation receiver that supports the full UWB frequency range defined by the FCC. It is produced using TELEFUNKEN Semiconductor's SiGe2 HBT technology and consists of two active single-ended-to-differential converter input stages, an output buffer stage with lowpass filter, and a four-quadrant Gilbert cell multiplier.

Gilbert cell multipliers do have, for the bipolar case, a transfer function given as [8]

$$z(t) = I_{\text{s}}\tanh\left(\frac{x(t)}{2V_{\text{T}}}\right)\tanh\left(\frac{y(t)}{2V_{\text{T}}}\right), \quad (11)$$

where I_{s} is a total bias current driven by an ideal current source, V_{T} is the thermal voltage, $x(t)$ and $y(t)$ are two input voltage signals, and $z(t)$ is an output current signal. This topology is known to approximate the ideal multiplication operation sufficient well for very low input levels due to the approximate linear working points of the tanh functions [9]. On the other hand, the Taylor-expansion of the tanh function [10], given as

$$\tanh(\text{x}) = \sum_{n=1}^{\infty} \frac{2^{2n}\left(2^{2n}-1\right)}{(2n)!}\text{B}_{2n}x^{2n-1}, \quad (12)$$
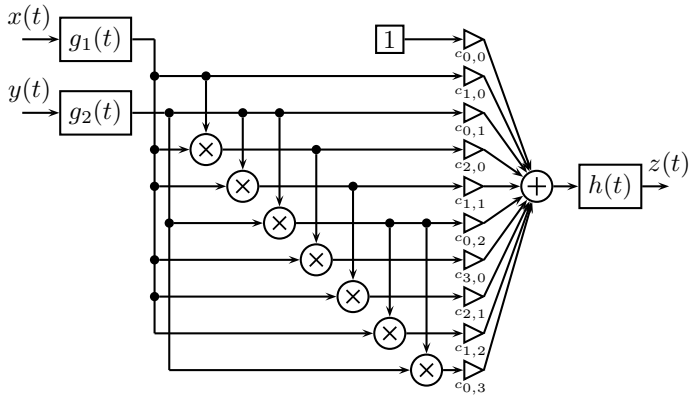
Fig. 2. A nonideal multiplier system $z(t) = \mathcal{M}\{x(t), y(t)\}$ of order $U = 3$ consists of two input and one output filters, and seven ideal multipliers and gains, which model the static bivariate nonlinearity.

with B_{2n} being the n-th Bernoulli number, shows certain effects which needs to be modeled for a detailed analysis of system self-interference due to nonlinearities. In addition to the nonlinear behavior of the Gilbert cell, the linear time-invariant filters at the input and the output stages, which do not exist in an ideal multiplier, need to be considered for real devices.

In general, such a nonideal multiplication of two independent signals $x(t)$ and $y(t)$ can be described as

$$z(t) = \mathcal{M}\{x(t), y(t)\} \tag{13}$$

with

$$\mathcal{M}\{x(t), y(t)\} = h(t)* \\ \left[\sum_{u=0}^{U}\sum_{v=0}^{u} c_{u-v,u}\left(g_1(t)*x(t)\right)^{u-v}\left(g_2(t)*y(t)\right)^v\right], \tag{14}$$

where $\mathcal{M}\{x(t), y(t)\}$ is the multiplier signal model which represents a combined Wiener-Hammerstein system [11], with U being the maximum order of the a static bivariate polynomial nonlinearity, $g_1(t)$, $g_2(t)$, and $h(t)$ being linear time-invariant filters and the coefficients $\{c_{u-v,u}\}$ being the gains of the nonlinear terms. In Fig. 2 a nonideal multiplier system of order $U = 3$ is illustrated. Using $g_1(t) = g_2(t) = h(t) = \delta(t)$ with $\delta(t)$ being Dirac impulses, and $c_{u-v,u} = \delta[u-v-1]\delta[u-1]$ with $\delta[n]$ being the Kronecker delta, the model represents a simple ideal multiplication of the input signals (c.f. (1)). In general, it has to be assumed that the filters and the gains depend on the power of the input signals $x(t)$ and $y(t)$.

Substituting the ideal multiplication operator with the nonideal multiplier operator $\mathcal{M}\{\cdot, \cdot\}$, the m-th AcR output can be rewritten as

$$y_m = \int_{\lambda=0}^{T_{\text{sym}}} \mathcal{M}\{r(\lambda), r(\lambda - \tau_m)\}\, d\lambda \tag{15}$$

$$= \sum_{u=0}^{U}\sum_{v=0}^{u}\sum_{|\alpha_k|=u-v}^{K}\sum_{|\beta_k|=v}^{K}\binom{u-v}{\alpha_1,...,\alpha_K}\binom{v}{\beta_1,...,\beta_K}\cdot$$

$$\int_{\lambda=0}^{T_{\text{sym}}} c_{u-v,v}\tilde{h}(\lambda)*\left\{\prod_{n=0}^{K} s_n^{\alpha_n+\beta_n}\right.$$

$$\cdot \Re\left\{\tilde{\varphi}_{\left(n-\frac{K+1}{2}\right),1}(\lambda)e^{+j\left(\omega_c+\left(n-\frac{K+1}{2}\right)\omega_{\text{sc}}\right)\lambda}\right\}^{\alpha_n}\cdot$$

$$\cdot \Re\left\{\tilde{\varphi}_{\left(n-\frac{K+1}{2}\right),2}(\lambda-\tau_m)e^{+j\left(\omega_c+\left(n-\frac{K+1}{2}\right)\omega_{\text{sc}}\right)(\lambda-\tau_m)}\right\}^{\beta_n}$$

$$\left.\right\}d\lambda + \nu_m, \tag{16}$$

where the multifold sum $\sum_{|\alpha_n|=A}^{K}$ is defined as

$$\sum_{|\alpha_n|=A}^{K} = \sum_{\alpha_1=0}^{K}...\sum_{\alpha_K=0}^{K}\delta\left[\alpha_1+...+\alpha_K-A\right], \tag{17}$$

with $\binom{A}{\alpha_1,...,\alpha_K}$ being the multinomial coefficient which is defined as

$$\binom{A}{\alpha_1,...,\alpha_K} = \frac{A!}{\alpha_1!...\alpha_K!}, \tag{18}$$

where $\tilde{\varphi}_{n,1}(t)$ is the received $\left(n-\frac{K+1}{2}\right)$-th sub-carrier pulse shape convolved with $g_1(t)$, and $\tilde{\varphi}_{n,2}(t)$ is the received $\left(n-\frac{K+1}{2}\right)$-th sub-carrier pulse shape convolved with $g_2(t)$. Note that the nonlinear term corresponding to the effects of the $c_{1,1}$ component denotes to the desired ideal multiplication as in (6). All other terms, e.g. corresponding to $c_{u-v,v}$ with $u-v \neq 1$ and $v \neq 1$, lead to signal interference due to the nonideal multiplication device.

Using vector notation we can rewrite (16) as

$$\mathbf{y} = \mathbf{H}\mathbf{s} + \mathbf{G}\left(\mathbf{s}\tilde{\otimes}\mathbf{s}\right) + \sum_{u=0}^{U}\sum_{\substack{v=0 \\ u-v\neq 1\wedge v\neq 1}}^{u}\mathbf{M}_{u-v,v}\bigotimes_u\{\mathbf{s}\} + \boldsymbol{\nu}, \tag{19}$$

where $\mathbf{M}_{u-v,v}$ is the interference matrix corresponding to the effects of the $c_{u-v,v}$ component, and $\bigotimes_N\{\cdot\}$ defines a manifold Kronecker product of order N, e.g.

$$\bigotimes_3\{\mathbf{x}\} = \mathbf{x}\otimes\mathbf{x}\otimes\mathbf{x}. \tag{20}$$

IV. BROADBAND MODEL IDENTIFICATION

A fitting of a given multiplier device to the signal model in (14) can be done in a two steps approach:

In the first step, an identification of the input and output filters needs to be performed. For a given circuit-level simulation model of the multiplier, intermediate signals of the filter inputs and outputs can be accessed. Using these intermediate signals and exciting the inputs with uncorrelated noise, it is possible to use a least mean square (LMS) approach for identifying the two input filters. Using the same excitation signals, the output of the multiplier is noise shaped by the output filter. From the topology of the multiplier circuit, we know that this filter is a first-order lowpass filter. To identify its cut-off frequency, the power spectral density (PSD) of the output signals is calculated and the lowpass filter is fitted to the PSD using a squared error norm.

In the second step, the coefficients $\{c_{u-v,v}\}$ of the static nonlinearity are identified using a least squares method (LS), since the signal model (14) is linear in these coefficients. The excitation signals for this identification can be chosen using
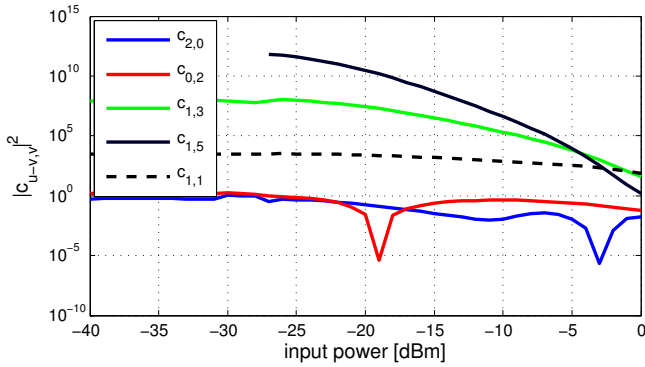
Fig. 3. Coefficients of the static nonlinearity.

Fig. 4. Time domain output signals of the nonideal multiplier model in comparison to the output signal of the circuit model of five NOFDM pulses. The input signals had a power of -20 dBm.

Fig. 5. Frequency domain output signals of the nonideal multiplier model in comparison to the output signal of the circuit model of five NOFDM pulses. The input signals had a power of -20 dBm.

the input signals of the desired multiplier application, e.g. NOFDM signals given in (4).

To investigate the behavior of the UWB mixer by the University of Ulm (c.f. Section IV), the identification was done using the previously mentioned ADS circuit model. The input filters $g_1(t)$ and $g_2(t)$ were modeled as 32 tap FIR filters. They show a highpass behavior with an input power independent cut-off frequency of approximately 3 GHz. The output filter $h(t)$ of the signal model was identified to be a first-order lowpass filter with an input power independent cut-off frequency of approximately 380 MHz. In Fig. 3, the signal model parameters $\{c_{u-v,v}\}$ of the dominant static nonlinearities (which introduce most of the interference) are listed for various input power levels at both input ports. It can be seen that the coefficients stay fairly constant up to -20 dBm where the saturation of the tanh function starts to have a stronger influence on the coefficients.

In Fig. 4 and Fig. 5 , a time domain signal and the PSD of a multiplier output of the identified signal model is illustrated in comparison to the circuit model. The mean square error (MSE$_{\text{fit}}$) of the approximation for this signal is about -18 dB.

Note that the integration operation of each AcR channel is done using a mixed-signal approach introduced in [5]. It proposes an analog seven-order Bessel lowpass filter with a frequency up to which the group delay is considered to be constant of 96.8 MHz, and a digital two tap summation filter. All MSE values in this work are evaluated after lowpass filtering the signals in consideration using the introduced integration filter.

V. INTERFERENCE ANALYSIS

Narrowband characteristics are not a suitable metric for evaluating broadband multipliers as they do not explain the nonlinear behavior of broadband signals in a sufficient way.

Due to the nonlinear behavior of the nonideal multiplier, interference terms may be mapped into the baseband, which is the desired signal band of the AcR channels. Indeed, every even-order nonlinear term does map into the baseband and is therefore considered as interference term.

An adequate metric to study the influence of the nonideal multiplier induced distortion is the signal to interference ratio
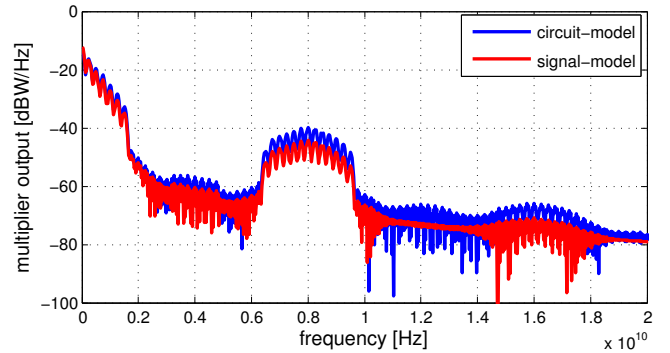
(SIR) of any nonlinear term of the decision variable $\mathbf{z}$ which is defined as

$$\text{SIR}_{u-v,v}^{\mathbf{z}} = \frac{\text{E}\left\{\mathbf{s}^T \mathbf{H}^T \mathbf{W}^T \mathbf{W} \mathbf{H}^T \mathbf{s}\right\}}{\text{E}\left\{\bigotimes_u \{\mathbf{s}^T\} \mathbf{M}_{u-v,v}^T \mathbf{W}^T \mathbf{W} \mathbf{M}_{u-v,v} \bigotimes_u \{\mathbf{s}\}\right\}},$$
(21)

where the expectation operator is evaluated with respect to the symbol vector $\mathbf{s}$.

To investigate the $\text{SIR}_{u-v,v}^{\mathbf{z}}$ for the different nonlinearity terms, a signaling scheme of a $K = 7$ sub-carrier UWB OFDM signal was used. The sub-carriers were truncated root-raised-cosine pulses with signal bandwidth and sub-carrier spacing of 250 MHz using binary pulse position modulation (BPPM). This signaling scheme is used for the rest of the paper. The input signal $\frac{\mathcal{E}_b}{N_0}$ (bit energy $\mathcal{E}_b$ over noise power spectral density N_0) was set to be 18 dB.

In Fig. 6, the SIR of various signal model coefficients is depicted. It can be seen that even-order terms do disturb the signal most. Odd-order terms are mitigated very well due to the lowpass behavior of the multiplier. Also the fitting MSE (MSE$_{\text{fit}}$), the MSE (MSE$_{\text{cm}}$) of the circuit model output and the MSE (MSE$_{\text{sm}}$) of the signal model output regarding an ideal multiplication, and the total SIR (SIR$^{\mathbf{z}}$) are depicted in Fig. 6 for comparison.
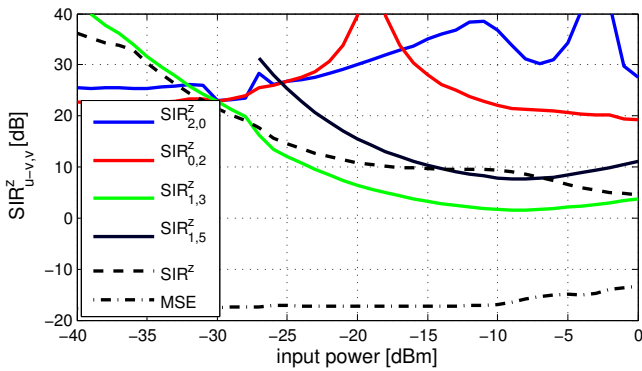
Fig. 6. Signal-to-interference ratio for various nonlinear terms.

Fig. 8. Bit-error rate for various input power levels.

Fig. 7. Signal-to-interference-and-noise ratio for various input power levels.

VI. System Simulations & Results

To evaluate the influence of the nonideal multiplier on the receiver performance two figures-of-merit are considered: the signal-to-interference-and-noise ratio of the decision variable **z**, which is defined as

$$\text{SINR}^{\mathbf{z}} = \frac{\text{E}\left\{\mathbf{s}^T\mathbf{H}^T\mathbf{W}^T\mathbf{W}\mathbf{H}\mathbf{s}\right\}}{\text{E}\left\{(\mathbf{W}\mathbf{y} - \mathbf{W}\mathbf{H}\mathbf{s})^T(\mathbf{W}\mathbf{y} - \mathbf{W}\mathbf{H}\mathbf{s})\right\}}, \quad (22)$$

and the bit-error rate (BER).

In Fig. 7, the $\text{SINR}^{\mathbf{z}}$ is illustrated for different input power levels. It can be seen that for increasing input powers the $\text{SINR}^{\mathbf{z}}$ start getting worse, which is due to the increased nonlinear effects which result in a decreased $\text{SIR}^{\mathbf{z}}$.

The BER strongly degrades with increasing input power levels due to decreasing $\text{SINR}^{\mathbf{z}}$. In Fig. 8, the BER curves are depicted for different input power levels. It can be seen that, in comparison to the ideal multiplier case, the BER for higher input power values ($P_0 \geq -20$ dBm) does show a significant error floor.

VII. Conclusion

This work proposes a signal model of nonideal multiplication devices for UWB applications. It has been shown that the identified signal model is able to reconstruct the output of a circuit model with an MSE of about -18 dB. Using the identified multiplier model the influence of the input power levels on the receiver system performance was shown. Due to nonlinear effects of the multiplier device, the SINR degrades strongly for increasing multiplier input power. However, the BER does not degrade as strongly as the SINR. The system model in (19) shows that the nonlinear terms are additive, therefore additional postprocessing might be able to enhance the SINR and BER of the receiver system.

References

[1] K. Witrisal, G. Leus, G. Janssen, M. Pausini, F. Troesch, T. Zasowski, and J. Romme, "Noncoherent ultra-wideband systems," *Signal Processing Magazine, IEEE*, vol. 26, no. 4, pp. 48–66, July 2009.

[2] T. Zasowski, F. Troesch, and A. Wittneben, "Partial channel state information and intersymbol interference in low complexity UWB PPM detection," in *Ultra-Wideband, The 2006 IEEE 2006 International Conference on*, Sept. 2006, pp. 369–374.

[3] S. Paquelet, L.-M. Aubert, and B. Uguen, "An impulse radio asynchronous transceiver for high data rates," in *Ultra Wideband Systems, 2004. Joint with Conference on Ultrawideband Systems and Technologies. Joint UWBST IWUWBS. 2004 International Workshop on*, May 2004, pp. 1–5.

[4] K. Witrisal, "Noncoherent autocorrelation detection of orthogonal multicarrier UWB signals," in *Ultra-Wideband, 2008. ICUWB 2008. IEEE International Conference on*, vol. 2, Sept. 2008, pp. 161–164.

[5] A. Pedross and K. Witrisal, "Sliding window integrator approximations for multichannel autocorrelation UWB receivers," in *2012 IEEE International Symposium on Circuits and Systems (ISCAS 2012)*. Seoul, Republic of Korea: IEEE, May 2012, pp. 2537–2540.

[6] P. Meissner and K. Witrisal, "Analysis of a noncoherent UWB receiver for multichannel signals," in *Vehicular Technology Conference (VTC 2010-Spring), 2010 IEEE 71st*, May 2010, pp. 1–5.

[7] J. R. Barry, E. A. Lee, and D. G. Messerschmitt, *Digital Communication*. Springer Science+Business Media Inc., 2004.

[8] J. Dederer, *Si/SiGe HBT ICs for Impulse Ultra -Wideband (I -UWB) Communications and Sensing*. Cuvillier Verlag, 2009.

[9] B. Gilbert, "A precise four-quadrant multiplier with subnanosecond response," *Solid-State Circuits, IEEE Journal of*, vol. 3, no. 4, pp. 365–373, Dec. 1968.

[10] E. Kreyszig, *Advanced Engineering Mathemaics*. John Wiley & Sons, Inc., 1999.

[11] V. J. Mathews and G. L. Sicuranza, *Polynomial Signal Processing*. John Wiley & Sons, Inc., 2000.

Research Article

Holistic Biquadratic IIR Filter Design for Communication Systems Using Differential Evolution

Alexander Melzer,[1,2] Andreas Pedross,[2] and Manfred Mücke[3]

[1] *Maxim Integrated GmbH, 8403 Lebring, Austria*
[2] *Graz University of Technology, Signal Processing and Speech Communication Laboratory, 8010 Graz, Austria*
[3] *Sustainable Computing Research, 1040 Vienna, Austria*

Correspondence should be addressed to Manfred Mücke; manfred.muecke@scr.or.at

Digital IIR filter implementations are important building blocks of most communication systems. The chosen number format (fixed-point, floating-point; precision) has a major impact on achievable performance and implementation cost. Typically, filter design for communication systems is based on filter specifications in the frequency domain. We consider IIR filter design as an integral part of communication system optimisation with implicit filter specification in the *time domain* (via symbol/bit error rate). We present a holistic design flow with the system's bit error rate as the main objective. We consider a discrete search space spanned by the quantised filter coefficients. *Differential Evolution* is used for efficient sampling of this huge finite design space. We present communication system performance (based on bit-true simulations) and both measured and estimated receiver IIR chip areas. The results show that very small number formats are acceptable for complex filters and that the choice between fixed-point and floating-point number formats is nontrivial if precision is a free parameter.

1. Introduction

In signal processing, filters are building blocks removing unwanted signal components (often, but not exclusively, specified in the frequency domain). Design (i.e., identification of suitable structures and coefficients) of digital filters given some specification in the frequency domain (e.g., passband ripple, cutoff frequency, stop-band frequency, or stop-band attenuation) is a well-established field [1]. In many advanced systems, however, the ultimate goal is rarely specifiable in the frequency domain but is reflected in a more complex measure. Examples include bit error rate, peak power consumption, or power trace entropy. Designing efficient systems therefore requires embedding of the filter design process in a larger system design context. Implementation of digital filters requires identification of arithmetic units to be implemented, the choice of a specific number format for each arithmetic unit, and quantisation of filter coefficients. These actions alter the filter characteristics and, if not foreseen in the design process, can have a severe impact on the system's performance.

There is a vast literature on digital filter design and optimisation of resource usage under some constraints. All design approaches we are aware of have in common that the number format's underlying error model has to be chosen in advance; that is, the designer has to take the decision if fixed-point or floating-point arithmetic is used prior to optimisation. Optimisation then identifies acceptable filter coefficients. Some systems allow for estimating minimally required precision.

We hypothesise that both the choice of the best error model (i.e., if fixed-point or floating-point arithmetic allows for the most efficient implementation) and identification of quantised filter coefficients are nontrivial and do not lend themselves to direct specification. In contrast to current practice, identification of number format and filter coefficients should be included in the communication system design process which should be seen as an integrated optimisation process. To verify our hypothesis, we developed a bit-true time domain simulation of a prototypical communication system including an IIR receiver filter. This simulation is used

for cost function evaluation in a global optimisation algorithm directly searching for quantised filter coefficients. The central requirement of a communication system is considered achieving some target bit error rate (BER) while minimising implementation costs (like chip area and power consumption). We employ Differential Evolution (DE) [2] as a direct search method to identify the most efficient implementation under varying constraints.

The scientific contributions of our work are

   (i) considering IIR filter design in the context of communication systems (i.e., BER-guided filter coefficient identification);

  (ii) providing a bit-accurate simulation framework allowing for evaluation of the objective function;

 (iii) employing DE to the previous process;

 (iv) considering the previous process without prior choice of number format (fixed- or floating-point; precision);

  (v) identification of minimum required precision as a function of system constraints;

 (vi) extending the objective function by implementation specific measures allowing for ASIC- or FPGA-specific ranking of BER-equivalent filter realisations.

The paper is structured as follows. Section 2 reviews related work. Section 3 introduces a prototypical communication system and related measures. Section 4 details the general IIR filter design process. It recapitulates the idea of formulating digital filter design as an optimisation problem. Filter realisation is assumed to be a cascade of biquadratic filter stages. Section 5 presents the DE algorithm as a means to quickly sample a huge multimodal search space. Section 6 considers the problem of filter design under the objective of optimising a communication system's performance and details the use of DE to directly search the resulting design space. Section 7 describes in detail all implementation and choices made for performing experiments. Section 8 reports results of different experiments employing DE to search directly for the most suitable IIR filter implementation minimising BER of the communication system considered. Giving an acceptable BER allows to search for the minimal acceptable precision of floating-point and fixed-point implementations. Further experiments extend the objective function by measures relevant to the filter's implementation cost. Section 9 discusses the experiment's results. Section 10 summarises the work and discusses challenges ahead. Section 11 details possible future research directions.

2. Related Work

Many authors have described strategies to derive filter coefficients for some given filter structure such that a given frequency response is matched. Usually, quantisation of coefficients is considered as a distinct and subsequent task.

Shyu and Lin [3] employ a variational approach to identify quantised coefficients by trying to match an ideal

impulse response. After initial identification of continuous coefficients, they are iteratively substituted by quantised ones while the remaining coefficients are modified to compensate for the resulting modification.

Alternatively, direct derivation of quantised filter coefficients can be done by considering filter design a search problem over a huge (yet finite) discrete space. Storn [4, 5] used differential evolution to search for realisable filter coefficients using specifications in the frequency domain. Ramos and López [6] combine a direct search method with a heuristic parametric optimization to identify optimal realisable filter coefficients of an equaliser structure for loudspeakers implemented using biquadratic filter stages.

There are several optimisation algorithms available that tackle this issue. Especially the use of population-based computation algorithms such as genetic algorithms [7–9], differential evolution [2, 9–12], particle swarm optimisation [13], and the seeker optimization algorithm [14] is common.

Irrespective of the method employed, many different objectives for guiding the filter design process are possible. Typically, filters are specified in the frequency domain. Consequently, most filter design methods employ an objective function derived from filter specifications in frequency domain (like the integral over the frequency response mismatch).

The matched filter theory readily provides optimal filter specification in frequency domain relevant under communication system constraints. The matched filter theory relies on linear system characteristics, though. This assumption is violated many times for real-world systems. Stücke et al. [15] investigate nonlinear effects in communication systems and their impact on ZigBee transceiver systems in terms of BER. To the best of our knowledge, our work is the first one employing a BER objective function in a direct search approach, basically solving the inverted problem compared to the work of Stücke et al. A related approach for optimising transmitter and receiver FIR filter specifications under BER constraints in a MIMO setting is presented by Hjorungnes et al. [16].

The DE algorithm was presented by Storn in 1995 in a technical report followed by a paper authored by Storn and Price in 1997 [2]. Design of digital filters was one of the original motivations for the development of the algorithm. In 2005, DE was presented in the IEEE Signal Processing Magazine [4]. The up-to-date references for DE are the books by Price et al. [17] and Chakraborty [18] as well as the recent survey by Das and Suganthan [19]. Compared to the original schemes suggested by Storn and Price [2], many additional variants have been conceived and methods for selecting parameters have been described. Notably, Zhu et al. [20] propose a method to adapt the (usually static) population size, while Pan [21] suggests a scheme where the DE parameters F and λ are adapted during optimisation. Zaharie [22] investigates the effect of different crossover schemes.

Pan [21] applies DE for pole-placement design, while Zhu et al. [20] apply DE for IIR coefficient identification in the context of system identification.

Most current design methods do not perform a rigour verification of the actual filter being implemented, that is, taking all quantisation effects into account.

Widrow and Kollár [23] have suggested a generic method for modeling the probability density functions of intermediate results yielded by limited-precision arithmetic and have employed it to (both arithmetic and coefficient) error analysis of IIRs. They point out, however, that the method becomes more unreliable with decreasing precision. Cox et al. [24] present bit-precise verification techniques and show cases where reasoning on the bit level is necessary. Kar [25] presents a stability criterion for digital filters considering both quantisation and overflow effects.

While many methods derive filter coefficients in double-precision floating point, this is a very costly number format to be implemented in hardware. Hardware implementation of digital filters typically resorts to low-precision fixed-point arithmetic as the respective operations are considered less expensive in terms of time-area product. Very few authors have investigated low-precision floating-point number formats for the implementation of digital filters.

To the best of our knowledge, our work is the first one considering floating-point precision a free parameter on a per-bit resolution in the IIR design process.

Our work is the first in-depth comparison between respective implementation costs of fixed-point and floating-point custom-precision IIR filter implementations.

3. System Model

This section presents the communication system which will be used throughout the rest of this paper. The communication system is a base-band transceiver concept as illustrated in Figure 1. Without loss of generality, the system is modeled in discrete-time. The signaling under consideration is a one-dimensional pulse-amplitude modulation (PAM). We assume absence of intersymbol interference (ISI). Therefore, only a single symbol period of duration N_{sym} needs to be considered. The sent signal $s[n]$ is therefore given as

$$s[n] = a * h_T[n], \tag{1}$$

where $a \in \{a_l\}$ is the transmitted symbol, $\{a_l\}$ is the set of L available complex valued symbols, $h_T[n]$ is the pulse shape, and $*$ denotes to the convolution operator.

For simplicity, the transmission channel is modeled using additive white Gaussian noise (AWGN). The received signal $r[n]$ is therefore given as

$$r[n] = s[n] + \nu[n], \tag{2}$$

where $\nu[n]$ is a white Gaussian noise process with a power spectrum density of $N_0/2$.

To remove out-of-band noise at the receiving side, a receiver filter with impulse response $h_R[n]$ is required. The receiver filter's output is given as

$$y[n] = h_R[n] * s[n] + h_R[n] * \nu[n]. \tag{3}$$

It is known that the optimal (i.e., minimising detection errors) receiver filter for AWGN channels and linear signaling
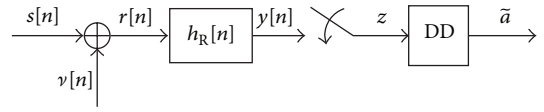
FIGURE 1: Discrete-time domain communication system model.

schemes is the matched filter [26]. Therefore, $h_R[n] = h_T^*[-n]$, where $(\cdot)^*$ denotes the complex conjugate. It should be noted that the matched filter gives a lower bound with respect to the bit error rate [26]. Any approximation of this matched filter can only perform worse. As shown later, direct search (using DE) can find a filter solution close to the theoretical matched filter BER performance.

After filtering, the signal $y[n]$ is sampled, which results into the decision variable z. The ideal sample time is at the end of the symbol period; hence, the decision variable z is given as

$$z = y[N_{sym}]$$
$$= s + \nu, \tag{4}$$

where s is the projection of the transmit pulse $h_T[n]$ onto the receiver filter $h_R[n]$ scaled by the transmitted symbol s, and thus

$$s = a \sum_{k=-\infty}^{+\infty} h_T[k] h_R[k], \tag{5}$$

and ν is a zero-mean Gaussian distributed random variable with variance $\sigma_\nu^2 = (N_0/2) \sum_{k=-\infty}^{+\infty} |h_R[k]|^2$. Note that for the case that the receiver's impulse response $h_R[n]$ does have unit energy, hence, $\sum_{k=-\infty}^{+\infty} |h_R[k]|^2 = 1$, and the variance σ_ν^2 of the random variable ν is equal to the noise power spectral density $N_0/2$ of the noise sequence $\nu[n]$ so that $\sigma_\nu^2 = N_0/2$. Note that s is given as $s \in \{a_l\}$ if $h_T[n]$ with unit energy and $h_R[n]$ represents the corresponding unit energy matched filter.

For detection, the decision device (DD) compares the decision variable z with a set of thresholds $\{\gamma_l\}$. The interval between two threshold values γ_l and γ_{l+1} defines the range of the symbol a_l. If z is in the interval of the two threshold values γ_l and γ_{l+1}, the decision device decides for $\tilde{a} = a_l$.

For a binary antipodal one-dimensional PAM, for example, binary phase-shift-keying (BPSK), the symbols a are given as $a \in \{-\sqrt{\mathcal{E}_b}, +\sqrt{\mathcal{E}_b}\}$, where $\mathcal{E}_b$ denotes the bit energy for a unit energy pulse shape. The ratio $\mathcal{E}_b/N_0$ is a well-known metric for comparing the performance of communication systems. The theoretical bit error probability P_e for the optimum matched filter receiver of a binary antipodal PAM is given as

$$P_e = Q\left\{\sqrt{\frac{2\mathcal{E}_b}{N_0}}\right\}, \tag{6}$$

where $Q\{\cdot\}$ is the Q-function. As discussed before, this theoretical bit error probability represents a lower bound to technically achievable (i.e., approximating $h_R[n]$) BERs.

4. IIR Filter Design

Infinite impulse response filters provide comparable performance at less computational/hardware requirements compared to finite impulse response (FIR) filters. The disadvantage of IIR filters is the fact that they can become unstable and that the error surface for finite-precision implementations is nonlinear and multimodal [10]. The latter renders finding an optimal set of quantised filter coefficients for implementation in finite precision arithmetic a hard problem.

Due to the relevance of digital filters in general and the resource savings possible through use of IIRs, there exists a high interest in converting continuous into quantised filter coefficients. Consequently, many different respective methods have evolved. Matching a certain frequency response specification is the major target of most of them. However, there are also interesting approaches that design the filter in the time domain. The latter is used in this work as it has several advantages for the design of digital filters used in communication systems.

Especially for IIR filters designed to meet certain filter specifications such as pass-band ripple, cutoff frequency, stop-band frequency, or stop-band attenuation, it is common to adjust poles and zeros in the z-plane as this automatically ensures stability [27]. However, for a digital implementation, coefficients still need to be calculated out of the poles/zeros and quantised. Furthermore, depending on the filter structure, scaling factors that are used to limit the numerical range for finite-wordlength architectures do not come out from such designs in the z-plane. That is why, in contrast to [27], we adjust the coefficients of the filter directly in order to avoid this issue. To verify stability of these coefficients, poles and zeros need to be computed. Verifying location of poles and zeros is a simple operation with low computational effort, though.

Designing the filter in time domain can be incorporated by trying to match, for instance, a reference impulse response. Besides the fact that the evaluation is simple, quantisation errors can be evaluated convenient in time domain. Furthermore, computations of the impulse response can be done bit-true such that the simulation corresponds exactly to the final hardware implementation.

Instead of taking the impulse response, we generate a random data sequence as reference out of the communication system model (Figure 1) and aim at to minimising the bit error rate.

4.1. Filter Structure. There exist many possible filter structures to implement a given transfer function. The cascading of second-order (or biquadratic) filter sections is beneficial as the number range is limited by the scale values in front of each section. Therewith, even quantisation errors are reduced [28] which is the main purpose of utilizing SOS direct-form II filter structures in this work (see Figure 2). Alternative filter structures include lattice wave filters [29, 30], but there is the issue that in general this filter structure needs the double amount of multipliers compared to direct-form II implementations [1].
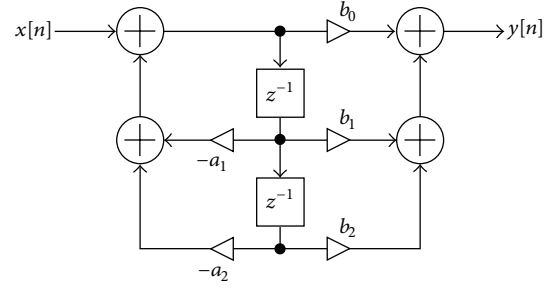
FIGURE 2: Direct-form 2 implementation of a biquadratic (or second-order) filter stage.

The transfer function of a cascaded SOS is given as

$$H(z) = \prod_{k=1}^{N_s} s_k \frac{b_{0k} + b_{1k}z^{-1} + b_{2k}z^{-2}}{1 - a_{1k}z^{-1} + a_{2k}z^{-2}}, \tag{7}$$

where N_s is the number of sections, s_k is the scale value for each SOS, and the filter coefficients are represented by b_{0k}, b_{1k}, b_{2k}, a_{1k}, and a_{2k}. Note that there is full freedom in ordering the sections itself.

Starting at the entry of an SOS, the scale value is a useful factor for limiting the numerical range of finite-precision arithmetic; thus, overflows can be suppressed in an elegant way. Furthermore, this scale value can be used to weight the SOS itself. As each SOS is a filter of order two, quantisation errors are mainly influencing one section. The impact on the overall filter transfer function is reduced as the signal is damped and the noise bandlimited by subsequent sections. Finally, the number of delay elements is decreased compared to direct-form I sections [1, 12, 28].

4.2. Filter Evaluation. The typical quality measure employed to quantify how well a filter matches the system specification is the mean squared error (MSE) between original specification and actual filter characteristic. For demonstration, we compare in the following the magnitude response of the matched filter with the one of the considered standard filter design approaches given the matched filter magnitude response as design objective.

For the transceiver system model presented in Section 3 with root-raised-cosine shaped pulses, the matched filter is a lowpass. We design three standard lowpass filter types to demonstrate the achievable match of magnitude responses. The filter types are Butterworth, Elliptic, and Chebyshev type I [1]. All filters are designed with order 6. A simulation is done exemplary for a binary antipodal PAM. The optimum BER is obtained by varying the cut-off frequency f_c between 0.05π and 0.1π in steps of 0.005π. These parameters are selected by evaluating the magnitude response of the pulse shaping filter $h_T[k]$. The reference filters are designed to match it as close as possible (Figure 11). Table 1 lists the identified best cut-off frequency f_c for each filter type together with the respective MSE compared to the matched filter's magnitude response. The Butterworth filter performs best; that is, its magnitude response is closest to the matched filter's

TABLE 1: Best cut-off frequency f_c and corresponding MSE to the matched filter's magnitude's response.

Filter type	f_c normalised frequency	MSE (dB)
Butterworth	0.07π	-10.63
Elliptic	0.075π	-8.83
Chebyshev	0.075π	-8.61
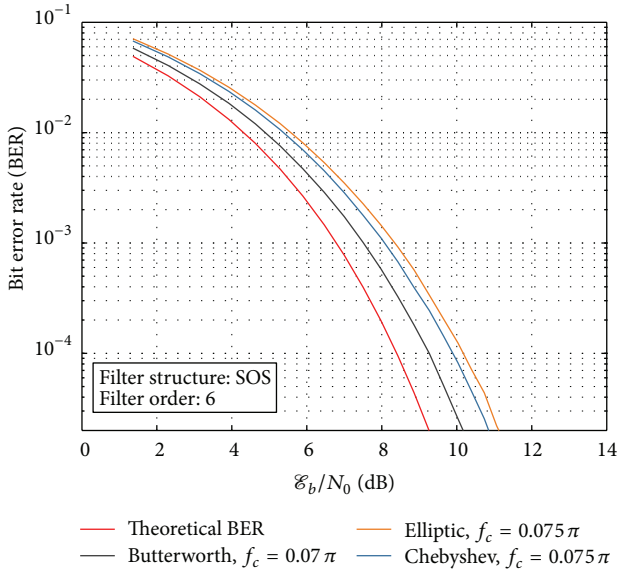
FIGURE 3: Transceiver BER for a Butterworth, elliptic, and Chebyshev filters based on the exemplary communication system model (Figure 1). All filters are designed with order 6. The simulation is done for $N_b = 10^6$ bits.

one. As illustrated in Figure 3, the theoretical BER given in (6) is not reached.

4.3. Discrete Design Space. Given some filter structure implemented using finite precision arithmetic, the set of possible filter coefficients (and therefore filter characteristics) can be enumerated. This set represents a huge, yet finite design space. Given a sixth-order IIR filter implemented as a cascade of biquadratic filter stages, every possible implementation can be described by an instance of the SOS matrix **C**, representing the filter coefficients where

$$\mathbf{C} = \begin{bmatrix} b_{01} & b_{11} & b_{21} & 1 & a_{11} & a_{21} \\ b_{02} & b_{12} & b_{22} & 1 & a_{12} & a_{22} \\ \vdots & \vdots & \vdots & \vdots & \vdots & \vdots \\ b_{0N_s} & b_{1N_s} & b_{2N_s} & 1 & a_{1N_s} & a_{2N_s} \end{bmatrix} \quad (8)$$

and the scale vector **s**

$$\mathbf{s} = \begin{bmatrix} s_1, s_2, \ldots, s_{N_s} \end{bmatrix}^{\mathrm{T}}, \quad (9)$$

where N_s is the number of biquadratic filter stages.
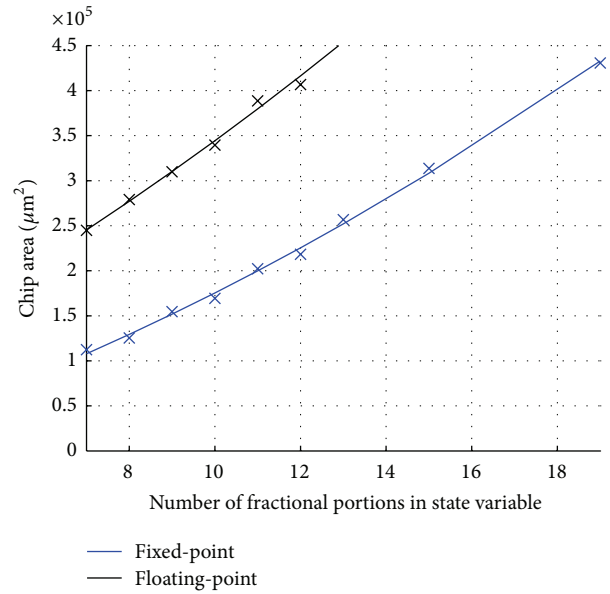
FIGURE 4: Chip area for programmable coefficients of the IIR filter with three biquadratic filter stages for fixed- and floating-point.

4.4. Arithmetic. Besides the filter architecture, the arithmetic in which the computations are performed in digital hardware is a major design decision. Especially the number of fractional bits for fixed-point and the precision for floating-point implementations is a major design decision as a tradeoff between performance and hardware costs needs to be found. This will be evaluated in detail in Section 7.4.

4.5. Implementation Cost-Chip Area. Digital filters are complex structures requiring a significant amount of chip area for implementation. We have developed a generic code describing the cascaded filter structure in both fixed- and floating-point with the precision as a parameter. There exist two versions. One integrates the coefficients directly into the design while the other one implements a register. The latter option allows for arbitrary changes of parameters through reprogramming of the registers. All multiplier paths, however, need to be fully instantiated, resulting in a much higher area requirement compared to predefined coefficients.

Synthesis results for different floating-point and fixed-point number formats are given in Table 2 and depicted in Figure 4.

4.6. Limit Cycle. An IIR filter can exhibit an unstable behavior under finite precision arithmetic for specific constant input signals. This type of instability usually results in an oscillatory periodic output called a *limit cycle* [31].

There are two types of limit cycles: (1) granular limit cycle (LSB oscillations; typically of low amplitude) and (2) overflow limit cycle (MSB oscillations; typically of large amplitude).

Criteria considering the combined effect of these two phenomena have only recently started to appear [25].

Many filter design methods aim at reducing or avoiding limit cycle effects. Our chosen filter realisation (cascaded

TABLE 2: Chip area for an IIR filter (order 6, cascade of three biquadratic filter stages) with programmable coefficients.

Fractional bits (bit)	Area fixed-point (μm^2)	Area floating-point (μm^2)
7	112370	244905
8	125379	279039
9	154582	309891
10	169388	339441
11	202143	388644
12	218251	406734
13	256645	458154
15	313606	533592
19	430632	705147

TABLE 3: Evolutionary computation nomenclature (from [32]).

Individual	A candidate solution
Child, parent	A child is the tweaked copy of its parent
Population	Set of candidate solutions
Fitness	Quality, directly related to the cost function
Selection	Picking individuals based on their fitness
Mutation	Plain tweaking of parameters based on population

biquadratic DF II filter) is known to limit the possible effects of limit cycles but does not exclude them. The current design flow does not check for possible limit cycles.

5. Differential Evolution

The Differential Evolution (DE) optimisation algorithm is proposed in [2]. Since it shows excellent performance compared to other much more complex heuristic optimisation algorithms [19], we utilize this algorithm. As described in Section 2, many variants and improvements of the original schemes have been conceived. As the task at hand is performed offline and the basic scheme does deliver good results, we have not explored further opportunities for tweaking the DE scheme. We discuss future improvements in Section 11. In the following, the DE algorithm's steps are described in detail. As evolutionary computation methods have different naming conventions, a short nomenclature is provided in Table 3.

(1) Initialization. The following constants need to be chosen. N_s is the number of biquadratic filter stages, P is the population size, and G the maximum number of generations. Furthermore, the number format (fixed- or floating-point) and the respective precision needs to be selected.

The initial population of individuals is randomly generated. One individual represents the scale vector **s** and the SOS matrix **C**. The scales are generated as

$$s_i = \mathcal{U}(0, 0.1) \quad \forall i = 1, \ldots, N_s, \quad (10)$$

where $\mathcal{U}(a, b)$ denotes the continuous uniform distribution in between a and b. The coefficient matrix is initialized as

$$C_{ij} = \mathcal{U}(-1, 1) \quad \forall i = 0, \ldots, 5, \ j = 1, \ldots, N_s. \quad (11)$$

In general, the number range of coefficients and scales of the initial population is of little importance. We found that the algorithm finds a satisfying solution with any random initialization.

(2) Scales and Coefficient Quantisation (Optional). In case of optimisation for bit-true filter coefficients (i.e., fixed- or floating-point), the scales and coefficients are quantised to their predefined number format.

(3) Compute and Evaluate the Cost Function. A system simulation is performed for all individual in the current generation (i.e., $s_{i,g}$ and $\mathbf{C}_{i,g}$ $\forall i = 1, \ldots, P$) and the BER computed at a given operating point according to (16). Depending on the objective function used, additional criteria are evaluated to arrive at the final fitness of each individual.

(4) Mutation and Selection. There are two basic schemes for mutation suggested in [2] (DE1 and DE2). DE1 performs mutation relying on a random difference vector. The difference vector is built using two randomly selected individuals (indices $i, \xi, \eta \in \{1, \ldots, P\}$ and mutually different). The scales and coefficients are tweaked according to

$$s_{i,g+1} = s_{i,g} + F \cdot \left(s_{\xi,g} - s_{\eta,g}\right) \quad \forall i = 1, \ldots, P,$$
$$\mathbf{C}_{i,g+1} = \mathbf{C}_{i,g} + F \cdot \left(\mathbf{C}_{\xi,g} - \mathbf{C}_{\eta,g}\right) \quad \forall i = 1, \ldots, P. \quad (12)$$

DE2 performs mutation as DE1 but takes the best solution in the current generation into account, too. The scales and coefficients are tweaked according to

$$s_{i,g+1} = s_{i,g} + \lambda \cdot \left(s_{\text{best},g} - s_{i,g}\right) + F \cdot \left(s_{\xi,g} - s_{\eta,g}\right),$$
$$\mathbf{C}_{i,g+1} = \mathbf{C}_{i,g} + \lambda \cdot \left(\mathbf{C}_{\text{best},g} - \mathbf{C}_{i,g}\right) + F \cdot \left(\mathbf{C}_{\xi,g} - s_{\eta,g}\right). \quad (13)$$

Choice of DE variant and parameters F and λ will be discussed in Section 7.5.

Depending on the cost function, the parents or the mutated children stay within the population or not [2, 4].

(5) Termination. The termination condition is met if the number of maximum generations (i.e., $g = G$) is reached. Otherwise, the algorithm continues with step 2.

6. Filter Design under Communication System Constraints

In this section, the optimisation of a quantised IIR filter considering the overall system model is derived. After definition of the optimisation problem, the theoretical optimum receiver and the DE optimisation algorithm are proposed. The transceiver performance is then analysed with respect to implementation costs in digital hardware.

6.1. Optimisation Problem Definition. Based on the blocks of the transceiver model described so far (Figure 1),
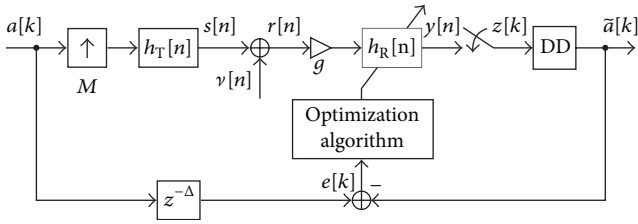
FIGURE 5: Communication system optimisation. Transmitted symbols are compared against the received ones to design the receiver filter.

the optimisation problem to minimise the bit errors of the receiver is defined and illustrated in Figure 5. The received symbols $\tilde{a}[k]$ are compared against the transmitted symbols $a[k]$ defining the error as

$$e[k] = a[k] - \tilde{a}[k - \Delta], \tag{14}$$

where Δ is a time delay introduced by the communication system.

For stable coefficient sets, we define the bit error rate as the squared error

$$\text{BER} = \frac{1}{N_b} \sum_{k=0}^{N_b - 1} e^2[k], \tag{15}$$

where N_b is the number of transmitted symbols for the training sequence. The cost function is dependent on the SOS matrix $\mathbf{C}$ representing the filter coefficients and the scale vector $\mathbf{s}$.

The specific cost functions used will be detailed in Section 7.

7. Experiment Setup

In the following, we detail the experiment setup. Results of experiments performed are reported in Section 8.

7.1. System Model Specification. Without loss of generality, the signaling scheme is chosen to be a binary antipodal PAM with $a = \{-\sqrt{\mathscr{E}_b}, +\sqrt{\mathscr{E}_b}\}$. The symbol rate R_{sym} is 125 kbit/s and the upsampling factor $M = 16$. The pulse shape of the transmitted pulses is a root-raised-cosine pulse with a roll-off factor of $\alpha = 0.5$. The symbol sequence $\{a[k]\}$ is randomly generated with equiprobal symbols, and the simulation is done for $N_b = 10^6$ bits.

The communication system's target BER is set to 10^{-3} (or better). The corresponding $\mathscr{E}_b/N_0$ ratio is 7.288 dB (see Figure 6 for an illustration).

The gain g which is introduced in Figure 5 is used to prescale the input number range of the receiver filter to ensure fair comparison between fixed- and floating-point.

7.2. Emulation of Finite Precision Hardware. In order to allow for a correct evaluation of quantisation effects, a bit-true simulation of the implementations considered is required. We provide bit-true simulation of BER calculation for both
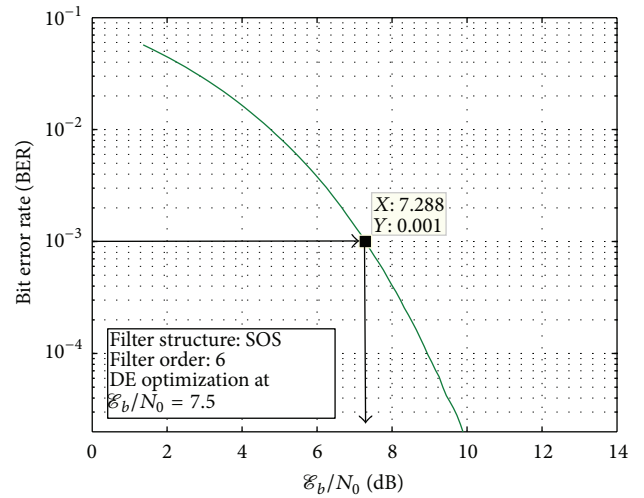
FIGURE 6: Transceiver BER for the optimum solution found by the DE algorithm. The operating point for fixed- and floating-point analysis is chosen to be at a BER of 10^{-3} resulting in an $\mathscr{E}_b/N_0$ ratio of 7.288 dB.

floating-point and fixed-point arithmetics. Both simulations allow the choice of arbitrary values for the number format's precision.

7.2.1. Fixed-Point. For fixed-point, the BER is evaluated for different $Qm \cdot n$ number formats for the state variable of the filter. This notation defines the number of integer (m) and fractional (n) bits within the representation. m is kept constant at 8 bits. Experimentally, this has been found to be sufficient to avoid overflows for all of the different solutions obtained by the DE. An overflow is indicated by a dedicated flag in the bittrue reference design. However, it might occur depending on the randomly generated noise added to the data sequence, especially when approaching a low number of fractional bits as the quantisation noise increases.

The signal range at the input of the filter is scaled to 90% of the input value range by setting $g = 0.9$ in Figure 5. This choice is significant, especially when comparing the BER to the floating-point scenario. Furthermore, it implies that for any $\mathscr{E}_b/N_0$ ratio the signal needs to be scaled accordingly by a dedicated gain control unit.

The filtering for the analysis is done based on a hardware equivalent implementation in C code and called from MATLAB using MEX [33] interface. Due to this, the filtering operation lasts a multiple of the double-precision floating-point implementation. A comparison is given in Table 4.

7.2.2. Floating-Point. For the floating-point analysis, the BER computation in Figure 12(b) is performed for different precisions while the exponent is constrained to 4 bits.

For hardware equivalent filtering, the GNU MPFR [34] library is used. It allows for floating-point operations on custom number formats (i.e., arbitrary mantissa (precision) and exponent bit widths). As the execution time is dominated by the Matlab-to-C interface, observed times are equivalent to the fixed-point implementation (see Table 4).

Table 4: Execution time analysis of a single generation of the DE1 algorithm (population size: 100).

	Matlab (double) [s]	Bit-true (fixed/float) [s]
Initialization	0.935	0.908
Filtering operation	0.603	27.25
Evaluate fitness/cost function		
Calculate BER	2.488	2.488
Check stability	0.327	0.327
Multiobjective fitness functions	—	0.123
Mutation and selection	0.284	0.284
Total time for single generation	4.637	31.380

7.3. Single-Objective Optimisation for Target Bit Error Rate.
The objective function uses the BER definition given in (16).

For stable coefficient sets, we define the cost function to equal the bit error rate

$$J_{\text{BER}}\left(\mathbf{s}, \mathbf{C}, N_b, \frac{\mathscr{E}_b}{N_0}\right) = \text{BER}. \tag{16}$$

(a) Stability. Digital filters can be specified using filter coefficients or pole/zeros. In $\mathbb{R}$, these specifications are interchangeable. Using pole/zero description has the advantage of restricting the search space to stable systems (i.e., all poles reside inside the unit circle) by design. When considering quantised coefficients, however, there is—due to quantisation—not necessarily a one-to-one mapping between pole/zero and parameters anymore. As DE is a direct search method, the native approach appears to be using quantised filter coefficients as parameters. DE might, however, consider parameter combinations resulting in unstable filters. The objective function therefore needs to exclude unstable solutions. From quantised coefficients C, poles can be computed and the stability criterion be checked. We define a condition function $J_{\text{Stable}}(\mathbf{s}, \mathbf{C})$ for the objective function $J(\mathbf{s}, \mathbf{C}, N_b, \mathscr{E}_b/N_0)$. $J_{\text{Stable}}(\mathbf{s}, \mathbf{C})$ is assigned the value 1 if the filter is stable, 0 otherwise.

For an unstable parameter set, we define

$$J_{\text{BER}}\left(\mathbf{s}, \mathbf{C}, N_b, \frac{\mathscr{E}_b}{N_0}\right) = \max\left(J\left(\mathbf{s}, \mathbf{C}, N_b, \frac{\mathscr{E}_b}{N_0}\right)\right) = 1. \tag{17}$$

7.4. Multiobjective Optimisation.
The DE optimisation algorithm proposed so far is able to find optimised coefficients with respect to the receiver performance as given by the bit error rate (BER) measure. It already generates fully quantised coefficients that can be plugged into a hardware description. However, for FPGAs/ASICs, the hardware costs, that is, area and power, are of very high relevance. In the vicinity of the optimum found by the DE, there might be several other solutions with the same BER but with less amount of hardware requirements due to different sets of coefficients. We therefore extend the existing framework to a

multiobjective optimisation approach that tries to minimise these costs at system-level design. The cost function and optimisation procedure is described later.

(b) Signal Range. In order to maximise the sensitivity of the receiver, the filters' internal signal range is evaluated. The quantisation noise is minimised if the available fractional bits of the implemented registers are used in its whole width. We define

$$J_{\text{SR}} = \begin{cases} 0, & \text{if } 2^{n-1} \leq \max\left(\text{abs}\left(\boldsymbol{\delta}\right)\right) < 2^{n+1}, \\ 1 - \dfrac{\max\left(\text{abs}\left(\boldsymbol{\delta}\right)\right)}{2^n}, & \text{if } \max\left(\text{abs}\left(\boldsymbol{\delta}\right)\right) < 2^{n-1}, \\ 1, & \text{else}, \end{cases} \tag{18}$$

where $\boldsymbol{\delta}$ is a vector of all the register values after multiplication in the biquadratic filter stages and n is the number of fractional bits. Below the acceptable value range, the cost function is linearly increasing or directly forced to one if it exceeds it.

(c) Hardware Cost. A multiplier in digital hardware is, in general, built from adders. Still, an adder is only instantiated if the corresponding bit in the multiplicand (i.e., the coefficient) is set (1). As the optimisation algorithm tweaks the coefficients, this can be reformulated as an optimisation criterion. The amount of nonzero bits can be minimised by introducing a dedicated cost function J_{HW}.

For modeling the hardware costs, a full synthesis run for each individual within the population could be investigated to obtain the final area and even power consumption for a certain stimuli. However, this is impractical since the synthesis and simulation would need enormous amount of time. Therefore, the hardware costs need to be approximated. For fixed-point, several synthesis runs with different coefficient sets were performed for the digital filter. They show that the area is maximised if half of the bits are set alternating within the coefficient number representation. It drops if more or less of half of all the bits are set. Thus, we define a function $\Gamma(x, B)$ as

$$\Gamma(x, B) = \begin{cases} B_{\text{set}}, & \text{if } B_{\text{set}} \leq \dfrac{B}{2}, \\ B - B_{\text{set}}, & \text{if } B_{\text{set}} > \dfrac{B}{2}, \end{cases} \tag{19}$$

where B is the bitwidth of x and B_{set} is the count of nonzero bits within the number representation of x. Then, the hardware costs are defined by summing all the set bits for the scales and coefficients and normalizing them, which is

$$J_{\text{HW}}(\mathbf{s}, \mathbf{C}) = \frac{\sum_{i=1}^{N_s} \Gamma\left(s_i, B_s\right)}{N_s B_s} + \frac{\sum_{i=0}^{5} \sum_{j=1}^{N_s} \Gamma\left(C_{ij}, B_c\right)}{6 N_s B_c}, \tag{20}$$

where B_s and B_c are the bitwidths of the scales and coefficients, respectively.

(d) Summation of Cost Functions. For the multiobjective optimisation, we sum the partial costs by weighting. Given that

the filter is stable, we wish to minimise the communication system's BER. For a given set of parameters resulting in a stable filter, we therefore evaluate the cost function J as

$$J\left(\mathbf{s}, \mathbf{C}, N_b, \frac{\mathcal{E}_b}{N_0}\right) = \alpha_{\text{BER}} J_{\text{BER}}\left(\mathbf{s}, \mathbf{C}, N_b, \frac{\mathcal{E}_b}{N_0}\right) + \alpha_{\text{HW}} J_{\text{HW}}\left(\mathbf{s}, \mathbf{C}\right)$$

$$+ \alpha_{\text{SR}} J_{\text{SR}}\left(\mathbf{s}, \mathbf{C}, N_b, \frac{\mathcal{E}_b}{N_0}\right), \quad (21)$$

where J_{BER}, J_{HW}, J_{CR} are the partial cost functions and α_{BER}, α_{HW}, α_{CR} are the weighting parameters, respectively. The cost function is evaluated at step 3 of the algorithm proposed in Section 5.

For an unstable parameter set, we define

$$J\left(\mathbf{s}, \mathbf{C}, N_b, \frac{\mathcal{E}_b}{N_0}\right) = \max\left(J\left(\mathbf{s}, \mathbf{C}, N_b, \frac{\mathcal{E}_b}{N_0}\right)\right). \quad (22)$$

In order to obtain the weighting parameters, we analyse the cost functions itself. J_{BER} is depending on the operation point of the optimisation, that is, defined by $\mathcal{E}_b/N_0$. J_{HW} is normalized by the total number of possible set bits and is found to be approximately 0.33 for scale and coefficient sets generated in the form of (10) and (11). In order to not influence the BER significantly, J_{HW} is chosen to be in the same number range as J_{BER}. Thus, for an expected BER of 10^{-3}, $\alpha_{\text{HW}} = 0.003$ while $\alpha_{\text{BER}} = 1$. In order to minimise the quantisation noise by fully using the fractional bits of the implemented registers, we expect J_{CR} to vanish. Hence, we set $\alpha_{\text{CR}} = 1$ as well.

Note that even with reprogrammable coefficients via registers, the DE optimised solution is able to reduce the power consumption by minimizing the number of nonzero bits of the coefficients for fixed-point. In this case, the hardware cost function is simply reformulated to

$$\Gamma(x, B) = B_{\text{set}} \quad (23)$$

as the power consumption will rise proportional with the increasing number of nonzero bits.

7.5. Choice of DE Variant. Two DE schemes were presented in Section 5. Here, we discuss identification of the variant most suitable for the design space at hand. Figure 7 shows the objective's function value over 2000 generations for 20 optimisation runs per DE variant (DE1 and DE2). DE1 provides a much more uniform behaviour and often provides better final solutions than DE2. We therefore choose DE1 as the DE variant of choice in all experiments reported in Section 8.

The control variable F in (12) and (13) was found by performing 20 simulation runs for each value between 0.1 and 0.8 with step size 0.1. Comparing the average and best fitness over generations, we found $F = 0.5$ to be the best choice delivering fast initial convergence with satisfying final solutions over multiple runs. This choice coincides with the value suggested in [2]. For λ, a value of 0.2 was found to be a reasonable choice.
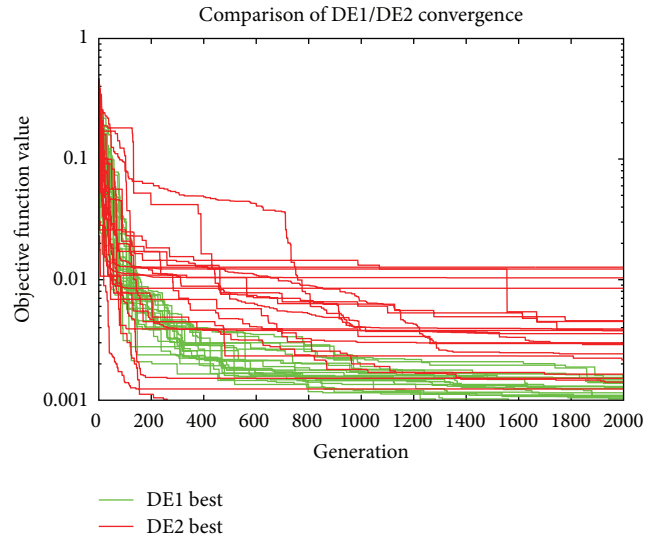
FIGURE 7: Comparison of convergence rate between DE1 and DE2 with multiobjective cost function. Twenty runs per DE variant. Population size 100.

8. Experiments

In the following, we report on experiments with a single objective (BER) and multiple objectives.

8.1. Single-Objective Optimisation for Target Bit Error Rate. In the first experiment, DE is used to search for a solution using double-precision floating point coefficients. Population size is 100 and maximum simulation run-time is set to 1000 generations (i.e., optimisation is stopped, even if results do not converge). The execution of a single generation takes 4.6 seconds on a Linux server (2x Intel Xeon CPU X5677 running at 3.47 GHz. System memory: 47 GB RAM), resulting in a maximum run time of $1000 \cdot 4.6\,\text{s} = 1\,\text{h}\,17\,\text{min}$. Refer to Table 4 for a detailed breakdown of execution times.

Figure 8(a) shows the BER of the best solution found by DE in every iteration. It shows how the final optimum BER curve is obtained iteratively. Figure 8(b) depicts the population's best and average BER as well as the average BER of the best 25% of all individuals within the population for each generation. Note that the latter converges fast, providing several potential candidate solutions close to the optimum BER.

Figure 9 shows the BER of the individual with the lowest BER in Generation 1000 and the BER curves for the standard filters (see Section 4). As can be seen, the filter coefficients identified by DE result in a superior filter (in terms of BER) compared to all considered standard filter design approaches.

To give an impression of the design space's structure, Figure 10 shows the cost function J in the a_1/a_2 plane while all other parameters are fixed at the optimum solution identified by DE.

8.1.1. Filter Magnitude Response. Because filter specification and evaluation in the frequency domain is so ubiquitous, we compare here the DE's solutions magnitude response with the

(a) BER over generations

(b) Cost function over generations
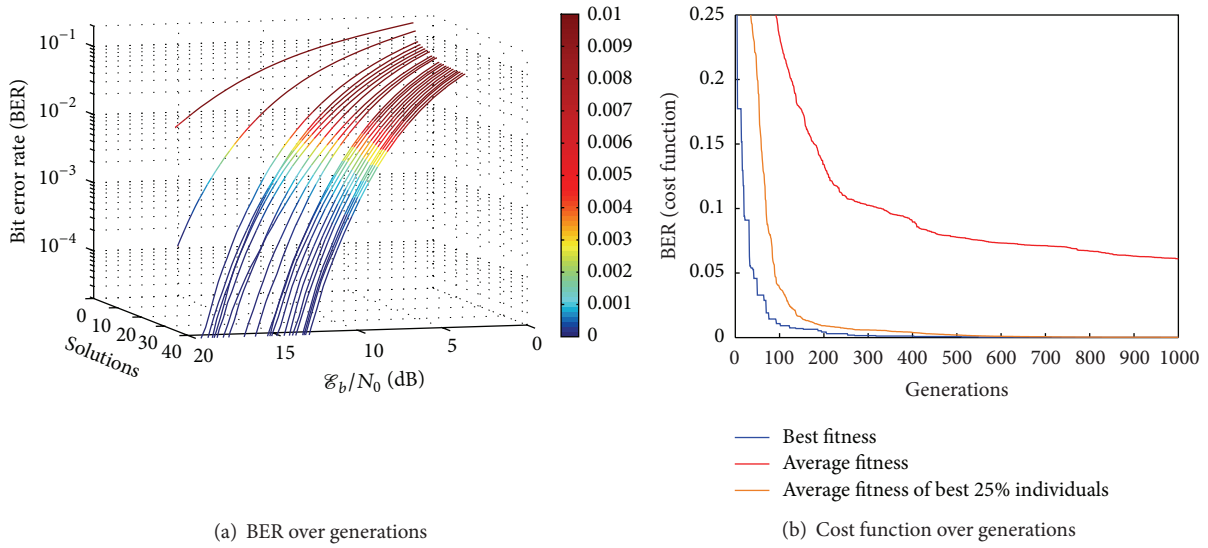
FIGURE 8: (a) BER of the best solutions found by the DE iteratively. (b) Cost function over iterations for a single optimisation run. The average cost is computed out of the whole population.
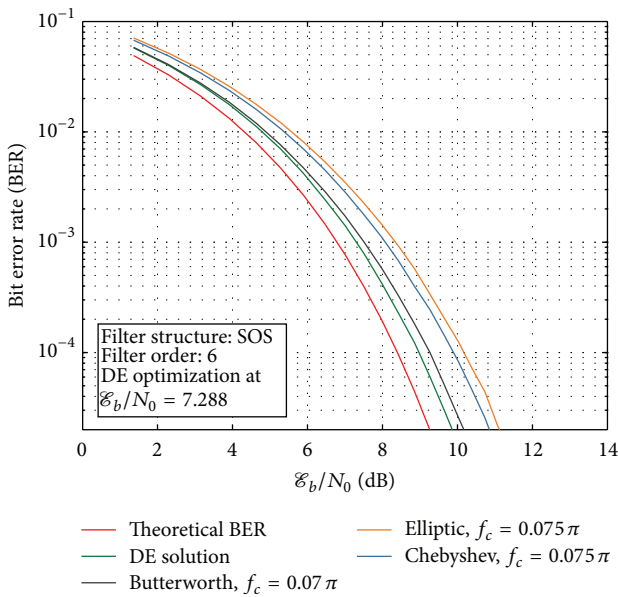
FIGURE 9: Transceiver BER for the optimum solution found by the DE algorithm at an operation point of $\mathscr{E}_b/N_0 = 7.288$. Butterworth, elliptic, and Chebyshev filters are plotted as reference. $N_b = 10^6$ bits.

FIGURE 10: Visualisation of the cost function J over a_1 and a_2.

magnitude responses of standard reference filters. Note that the design methods are completely different. The reference filters are designed with a certain cut-off frequency which defines the filters frequency response characteristics. The optimised DE filter considers the overall system in which it is embedded and iteratively identifies suitable filter coefficients relying on a time domain perspective.

Figure 11 shows the magnitude response of Butterworth, elliptic, and Chebyshev filters as detailed in Section 4.2 together with the magnitude response of the solution identified by DE. Observe that the optimal solution's gain is

significantly higher than the filter specification derived from the matched filter assumption.

8.1.2. Choice of Number Format. A communication system's performance is significantly depending on the receiving's filter number format and precision chosen. Quantifying this dependency is the goal of the following experiment.

DE was used to search for the optimal solution given a fixed-point receiver filter implementation and given a floating-point receiver implementation.

Figure 12(a) shows the BER over different fixed-point $Qm \cdot n$ formats, where m is constantly set to 8 and n is the number of fractional bits. Figure 12(b) shows the BER over different floating-point precisions, where the exponent is limited to the range of ±15. The red line shows the BER
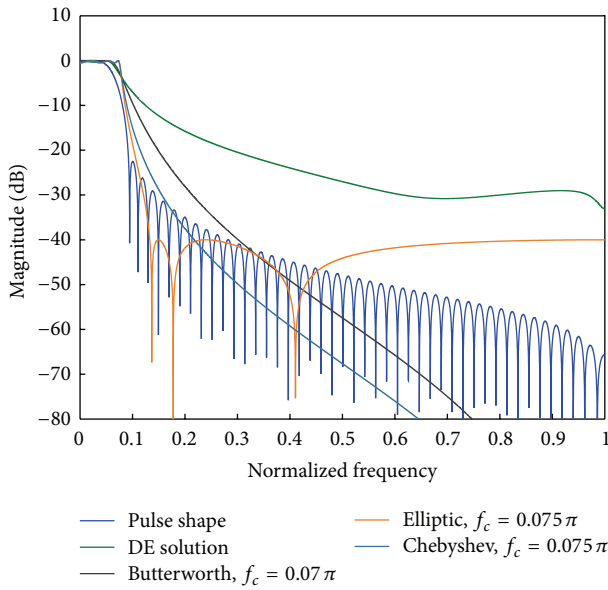
FIGURE 11: Magnitude responses of transmission, DE optimised and reference filters. DE optimised and reference filters are designed with order 6.

achieved with the software reference implementation using double-precision floating point.

8.2. Multiobjective Optimisation for Hardware Efficiency. To give an impression of the design space's structure when using a multiobjective cost function, Figure 13 shows the cost function J in the a_1/a_2 plane while all other parameters are fixed at the optimum solution identified by DE.

The required chip area found by the DE with and without multiobjective optimisation in fixed-point arithmetic is presented in Figure 14. The synthesis is performed for predefined coefficients, which means that they are constants at synthesis time. On average, around 4.4% can be saved utilizing the multiobjective optimisation with hardware costs (Table 5) while at the same time the BER from Figure 12(a) is retained. It is clear that, for the DE algorithm without dedicated cost function, the hardware costs are purely random. Thus, also the saving in area compared to the multiobjective optimisation is varying between 1% and 12%.

9. Discussion

Using the BER as optimisation objective, the DE algorithm is able to identify coefficient sets which outperform systems relying on conventional filter design methods with specification in the frequency domain (matched filter). Inspecting the resulting filter in the frequency domain reveals that the magnitude response deviates significantly from the matched filter's magnitude response. This result does not interfere with the matched filter theory. It reveals, though, that under the presence of channel noise and nonlinearities (finite-precision arithmetic), a filter optimising the overall BER can be implemented with a magnitude response significantly different than the specification of the matched filter. This
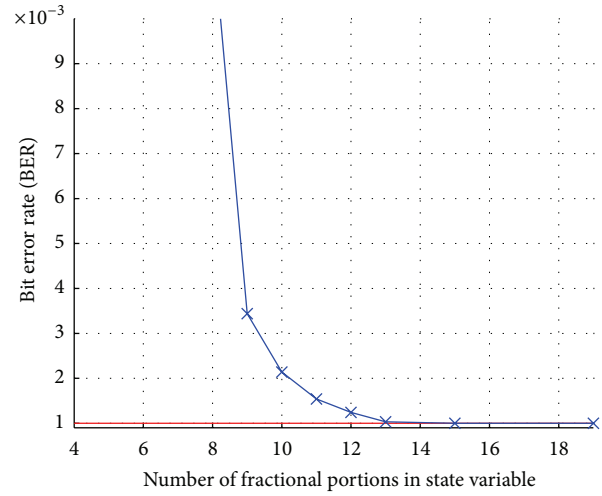
(a) BER fixed-point
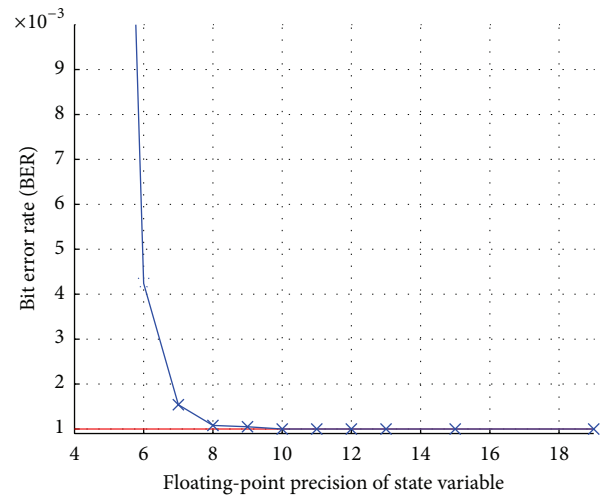
(b) BER floating-point

FIGURE 12: (a) BER over different fixed-point $Qm \cdot n$ formats, where m is constantly set to 8 and n is the number of fractional bits. (b) BER over different floating-point precisions, where the exponent is limited to the range of ±15.

is a strong argument against direct specification of filters approximating a matched filter.

Employing a direct search algorithm has the advantage that—given it works reliably on the original problem space—new search criteria (i.e., extended cost functions) can be added (almost) at will. Additional partial cost functions will not break the search algorithms efficiency (i.e., reduce the convergence rate). We have demonstrated this strategy successfully by adding hardware measures. This results in reliably cheaper implementations with identical BERs.

Using the DE algorithm with a single BER objective can result in many solutions with almost identical cost (i.e., BER)

TABLE 5: Chip area in μm^2 for predefined coefficients (constant at synthesis time) with and without multi-objective optimisation for hardware efficiency (fixed-point). The mean is computed out of the best 25% solutions within the final population. Populations size is 100.

Fractional bits (n)	Area predefined coeffs without hardware opt.		Area predefined coeffs with hardware opt.		Area savings
	Mean best 25%	Best	Mean best 25%	Best	
7	40048	37738	39009	33183	12%
8	45441	42977	44736	42688	1%
9	51879	49506	50513	47065	5%
10	58855	54360	55379	49585	9%
11	67323	62873	66895	61007	3%
12	74079	68240	73835	64848	5%
13	82066	77486	80760	75403	3%
15	99119	91118	98238	90403	1%
19	145077	136627	142296	135049	1%
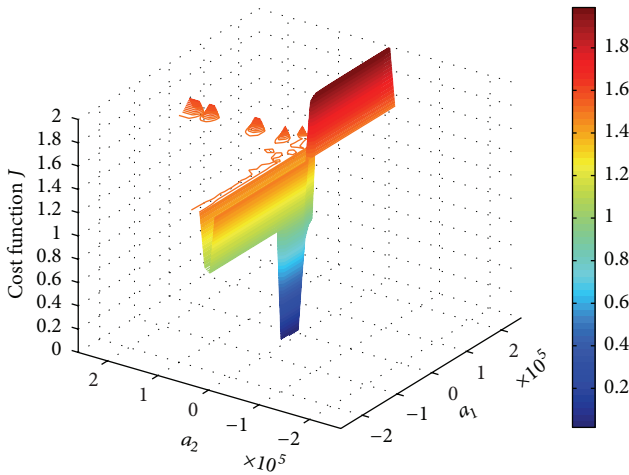
FIGURE 13: Visualisation of the multiobjective cost function J over a_1 and a_2.

—— Theoretical lower and upper area bounds
—— Without hardware opt. (mean of 25% best)
+ Without hardware opt. (best)
—— With hardware opt. (mean of 25% best)
+ With hardware opt. (best)

FIGURE 14: Chip area for predefined coefficients with and without multiobjective optimisation for hardware efficiency (fixed-point) as presented in Table 5. Limit bars indicate the theoretical minimum and maximum area requirements.

but significantly varying hardware costs due to the different amounts of set bits in the coefficients. The uncertainty in hardware cost lies between a factor of 2 and 10 depending on the number format considered. Introducing an additional hardware cost objective allows for significant reduction of this uncertainty. Consequently, using a multiobjective cost function taking the number of set bits into account allows for a much more reliable design process guaranteeing identification of hardware-efficient filter implementations.

We have shown partial visualisations of the cost function. While no general insights can be derived from these minimal projections, it is interesting to observe the change in appearance with modifications to the cost function J. Figure 10 shows the BER as a function of filter coefficients a_1 and a_2 while all other scaling values and coefficients are kept fixed at the values of the DE algorithm's solution. The plot shows that for the depicted partial design space, the constraints for a good solution (low BER) are abs(a_2) being close to zero and a_1 being negative. The exact value of a_1 is of little relevance. Extending the objective function by additional criteria (see (21)) changes the situation significantly. Figure 13 shows the

multiobjective cost function J over filter coefficients a_1 and a_2 while all other scaling values and coefficients are kept fixed at the values of the DE algorithm's final solution. The additional criteria have further constrained the acceptable value of a_1 to the interval $0, \ldots, -0.5$.

Filter structures are expensive in terms of chip area, especially when implemented with high precision. It is of major interest to identify the most suitable number format (fixed-point, floating-point; precision) and to minimise the power consumption by suitable choice of coefficients. Comparing Figures 12(a) and 12(b) shows that the fixed-point filter's BER deteriorates much faster with decreased precision than the floating-point filter's BER (13 bit versus 9 bit precision). One can also observe that the deviation from the red line is much

more prominent in the fixed-point case. Typically, floating point arithmetic is considered more costly than fixed-point. Our experiments show that, from a system perspective, the difference in chip area for otherwise comparable system is not so clear. Floating-point arithmetic requires more area per bit precision than fixed-point arithmetic. It requires, however, less precision to achieve a specific BER. Given that our floating-point implementation is far from optimal, the chip area per bit error can be considered roughly equivalent.

10. Conclusion

DE can sample the huge time domain design space of a communication system with a 6th-order receiving filter including bit-true BER simulation using Matlab/Mex/MPFR in $31.38\,\text{s} \cdot 1000\,\text{generations} = 8\,\text{h}\,43\,\text{min}$ using standard hardware (single core). Given that this design space exploration is performed offline, the time required is acceptable. Each identified filter coefficient set is already quantised. The cost function is therefore accurate and the filter directly implementable.

Using DE as an exploration tool for the huge discrete design space of digital receiver filters allows for interesting insights. We have demonstrated two, namely, that (1) receiving filters with magnitude responses deviating significantly from the matched filter's magnitude response can outperform standard filter design techniques relying on specification in the frequency domain and that (2) from a system perspective, fixed- and floating-point IIR implementations have roughly comparable cost.

Both findings are in contrast to current practice in filter design for communication systems. We therefore mandate further BER-guided exploration of communication system's discrete filter design space.

11. Future Work

We have chosen to investigate communication systems without intersymbol interference (ISI). This typically is the case in low-rate communication systems. It would be interesting to investigate how systems with intersymbol interference could benefit from the implicit filter specification as described in our work.

We have shown that implicit filter specification through system BER specification and system simulation can result in filter designs with significantly different magnitude responses than conventional filter specifications typically used for communication systems. This shows the importance of taking into consideration nonlinear effects, rendering the matched-filter assumption void. We have only considered the most basic nonlinear effects, namely, an AWGN channel, BER calculation in time domain, and the finite-precision effects of digital filter implementations. Many more opportunities for a more accurate system model exist [15]. It would be worthwhile exploring further nonlinear effects and their respective impact on filter design. Furthermore, indoor as well as multipath channel models would make the simulation results more relevant for practical applications.

Differential Evolution has become a widely used tool since its inception almost 20 years ago. We have chosen to implement DE as originally described in [2] as its performance was sufficient for our purpose. It would be worth exploring state-of-the-art DE implementations [19], especially integrating automatic/dynamic schemes for parameter (population size, F, λ) selection. Reducing optimisation time through parallel DE would be another fruitful direction for future work. Not all DE schemes, however, lend themselves equally well to efficient parallelisation [35].

References

[1] A. Oppenheim and R. Schafer, *Discrete-Time Signal Processing*, Prentice Hall Signal Processing Series, Pearson Education, Upper Saddle River, NJ, USA, 2009.

[2] R. Storn and K. Price, "*Differential evolution*-a simple and efficient heuristic for global optimization over continuous spaces," *Journal of Global Optimization*, vol. 11, no. 4, pp. 341–359, 1997.

[3] J.-J. Shyu and Y.-C. Lin, "Design of finite-wordlength IIR digital filters in the time/spatial domain," in *Proceedings of the 1995 IEEE International Symposium on Circuits and Systems (ISCAS '95)*, vol. 3, pp. 2027–2030, May 1995.

[4] R. Storn, "Designing nonstandard filters with *Differential evolution*," *IEEE Signal Processing Magazine*, vol. 22, no. 1, pp. 103–106, 2005.

[5] R. Storn, "System design by constraint adaptation and *Differential evolution*," *IEEE Transactions on Evolutionary Computation*, vol. 3, no. 1, pp. 22–34, 1999.

[6] G. Ramos and J. J. López, "Filter design method for loudspeaker equalization based on IIR parametric filters," *Journal of the Audio Engineering Society*, vol. 54, no. 12, pp. 1162–1178, 2006.

[7] M. Haseyama and D. Matsuura, "A filter coefficient quantization method with genetic algorithm, including simulated annealing," *IEEE Signal Processing Letters*, vol. 13, no. 4, pp. 189–192, 2006.

[8] Y. Yang and X. Yu, "Cooperative coevolutionary genetic algorithm for digital IIR filter design," *IEEE Transactions on Industrial Electronics*, vol. 54, no. 3, pp. 1311–1318, 2007.

[9] M. Nilsson, M. Dahl, and I. Claesson, "Digital filter design of IIR filters using real valued genetic algorithm," in *Proceedings of the 2nd WSEAS International Conference on Electronics, Control and Signal Processing (ICECS '03)*, pp. 3:1–3:6, World Scientific and Engineering Academy and Society (WSEAS), Stevens Point, Wis, USA, 2003.

[10] N. Karaboga, "Digital IIR filter design using *Differential evolution* algorithm," *EURASIP Journal on Advances in Signal Processing*, vol. 7, no. 7, pp. 1269–1276, 2005.

[11] B. Luitel and G. K. Venayagamoorthy, "*Differential evolution* particle swarm optimization for digital filter design," in *Proceedings of the IEEE Congress on Evolutionary Computation (CEC '08)*, IEEE World Congress on Computational Intelligence, pp. 3954–3961, June 2008.

[12] K.-S. Tang, K. F. Man, S. Kwong, and Z. F. Liu, "Design and optimization of IIR filter structure using hierarchical genetic algorithms," *IEEE Transactions on Industrial Electronics*, vol. 45, no. 3, pp. 481–487, 1998.

[13] S. A. Hashemi and B. Nowrouzian, "A novel finite-wordlength particle swarm optimization technique for FRM IIR digital

filters," in *Proceedings of the IEEE International Symposium of Circuits and Systems (ISCAS '11)*, pp. 2745–2748, May 2011.

[14] C. Dai, W. Chen, and Y. Zhu, "Seeker optimization algorithm for digital IIR filter design," *IEEE Transactions on Industrial Electronics*, vol. 57, no. 5, pp. 1710–1718, 2010.

[15] T. Stücke, N. Christoffers, R. Kokozinski, and S. Kolnsberg, "BER optimization for micro power receivers using quick and accurate system simulation," in *Proceedings of the 14th IST Mobile & Wireless Communications Summit*, June 2005.

[16] A. Hjorungnes, P. S. R. Diniz, and M. L. R. de Campos, "Jointly minimum BER transmitter and receiver FIR MIMO filters for binary signal vectors," *IEEE Transactions on Signal Processing*, vol. 52, no. 4, pp. 1021–1036, 2004.

[17] K. V. Price, R. M. Storn, and J. A. Lampinen, *Differential Evolution-A Practical Approach to Global Optimization*, Springer, New York, NY, USA, 2005.

[18] U. K. Chakraborty, *Advances in Differential Evolution*, Springer, New York, NY, USA, 2008.

[19] S. Das and P. N. Suganthan, "*Differential evolution*: a survey of the State-of-the-Art," *IEEE Transactions on Evolutionary Computation*, vol. 15, no. 1, pp. 4–31, 2011.

[20] W. Zhu, J.-A. Fang, Y. Tang, W. Zhang, and W. Du, "Digital IIR filters design using *Differential evolution* algorithm with a controllable probabilistic population size," *PLoS ONE*, vol. 7, no. 7, Article ID e40549, 2012.

[21] S.-T. Pan, "Evolutionary computation on programmable robust IIR filter Pole-Placement design," *IEEE Transactions on Instrumentation and Measurement*, vol. 60, no. 4, pp. 1469–1479, 2011.

[22] D. Zaharie, "Influence of crossover on the behavior of *Differential evolution* algorithms," *Applied Soft Computing*, vol. 9, no. 3, pp. 1126–1138, 2009.

[23] B. Widrow and I. Kollár, *Quantization Noise: Roundoff Error in Digital Computation, Signal Processing, Control, and Communications*, Cambridge University Press, Cambridge, UK, 2008.

[24] A. Cox, S. Sankaranarayanan, and B.-Y. Chang, "A bit too precise? Bounded verification of quantized digital filters," in *Tools and Algorithms for the Construction and Analysis of Systems*, C. Flanagan and B. König, Eds., vol. 7214 of *Lecture Notes in Computer Science*, pp. 33–47, Springer, Berlin, Germany, 2012.

[25] H. Kar, "Asymptotic stability of fixed-point state-space digital filters with combinations of quantization and overflow nonlinearities," *Signal Processing*, vol. 91, no. 11, pp. 2667–2670, 2011.

[26] J. Proakis, *Digital Communications*, McGraw-Hill Series in Electrical and Computer Engineering, McGraw-Hill, New York, NY, USA, 2001.

[27] M. F. Quelhas and A. Petraglia, "On the design of IIR digital filter using linearized equation systems," in *Proceedings of IEEE International Symposium on Circuits and Systems (ISCAS '10)*, pp. 2702–2705, June 2010.

[28] A. Eletri, E. Salem, A. Zerek, and S. Elgandus, "Effect of coefficient quantization on the frequency response of an IIR digital filter by using software," in *Proceedings of the 7th International Multi-Conference on Systems, Signals and Devices (SSD '10)*, pp. 1–6, June 2010.

[29] Y. Zhao, J. Zhou, X. Zhou, and G. Sobelman, "General lattice wave digital filter with phase compensation scheme," in *Proceedings of the IEEE 9th International Conference on ASIC (ASICON '11)*, pp. 220–223, October 2011.

[30] C. Huang, Z. Xu, G. Li, H. Xu, and L. Chang, "An improved lattice IIR digital filter structure," in *Proceedings of the 8th International Conference on Information, Communications and Signal Processing (ICICS '11)*, pp. 1–5, December 2011.

[31] B. W. Bomar, *Finite Wordlength Effects*, CRC Press, New York, NY, USA, 2009.

[32] S. Luke, *Essentials of Metaheuristics*, Lulu Press, Raleigh, NC, USA, 2009.

[33] The MathWorks, "Compile MEX-function from C/C++ or Fortran source code," 2012, http://www.mathworks.de/de/help/matlab/ref/mex.html.

[34] MPFR, "The GNU MPFR library," 2012, http://www.mpfr.org/ .

[35] D. K. Tasoulis, N. G. Pavlidis, V. P. Plagianakos, and M. N. Vrahatis, "Parallel *Differential evolution*," in *Proceedings of the IEEE Congress on Evolutionary Computation (CEC '04)*, vol. 2, pp. 2023–2029, June 2004.

Modeling and Identification of Ultra-Wideband Analog Multipliers

Andreas Pedross-Engel, *Student Member, IEEE*, Hermann Schumacher, *Member, IEEE*,
and Klaus Witrisal, *Member, IEEE*

Abstract—Analog multipliers are employed in many applications. In conventional RF front-ends, for example, they are widely used for frequency conversion tasks. In noncoherent energy detectors or transmitted-reference front-ends, they multiply the (broadband) input signals by themselves to achieve a down-conversion. Unfortunately, there exist no ideal hardware realizations of such devices, hence they inevitably create undesired signal content at their output. To be able to deal with these effects or correct for them, we need to be able to model and identify realistic RF multipliers. This work proposes and validates a multiple-input single-output Wiener-Hammerstein model for ultra-wideband analog multipliers. The structure of the proposed model gives insight in the distortions created and it provides the possibility to study the realistic behavior of systems involving those multipliers, e.g. the influence of undesired nonlinear signal content. A comparison of the model performance is shown with respect to measurements and Agilent ADS circuit simulations.

Index Terms—MISO, mixers, model identification, multipliers, nonlinear, UWB, Wiener-Hammerstein

I. Introduction

The multiplication of signals is a fundamental algebraic concept that is extensively used in signal processing and communications. Its mathematical properties are well studied and understood. In fact almost all signal processing concepts utilize this basic operator, no matter if analog or digital, continuous- or discrete-time. The need for devices to perform the multiplication operation is tremendous, e.g. for digital filtering, Fourier transformation of signals, energy detection, auto- and crosscorrelation. Therefore, a lot of work has been put into studying analog and digital hardware realizations of this mathematical operation.

An important example of analog multipliers are frequency conversion mixers, which are extensively used in RF front-ends [1]. Mixers are used to change the center frequency of bandlimited signals by multiplying the input signal $x(t)$ by a
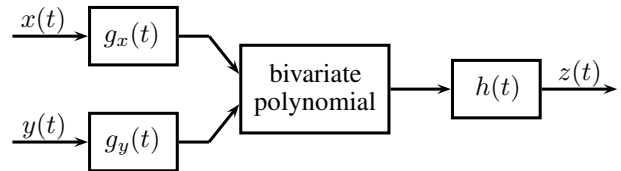
Fig. 1. Wiener-Hammerstein system model consisting of input filters $g_x(t)$ and $g_y(t)$, an output filter $h(t)$, and a bivariate polynomial as static nonlinearity.

single-tone signal[1], e.g.

$$z(t) = \mathcal{M}\left\{x(t), A\cos(2\pi ft + \phi)\right\}, \qquad (1)$$

where f is the difference between the center frequencies of the input signal $x(t)$ and the desired output signal $z(t)$, A is an amplitude, ϕ is some phase offset, and $\mathcal{M}\left\{\cdot, \cdot\right\}$ represents the multiplication operator

$$\mathcal{M}\left\{x(t), y(t)\right\} = x(t) \cdot y(t). \qquad (2)$$

Hence, such devices are commonly designed for the purpose of frequency shifting only. For analysis of this operation, the mixer can be considered as a single-input single-output (SISO) system, exploiting the fact that one mixer input signal is considered to be known, e.g. a single-tone signal $A\cos(2\pi ft+\phi)$. This assumption leads to mixer characteristics which can be obtained from single-tone and two-tone measurements of the device, e.g. conversion gains and third-order intercept-points (IP3) [1].

However, these narrowband characteristics cannot give a reasonable description of the input-output behavior of a mixer when used as a non-narrowband analog multiplier, e.g. for multiplying two ultra-wideband (UWB) signals in UWB receiver systems. In particular energy detectors [2] and auto-correlation receivers [3] are noncoherent receivers [4] that are based on multipliers. Hence, multipliers play a crucial role in their performance, e.g. in mitigation of narrowband interference [5]–[7] or synchronization [8]. Multipliers are also used in alternative UWB approaches as compressed sensing [9], [10] or hybrid matched filter correlation receivers [11] for which their influence on the receiver performance needs to be analyzed. In [12], for example, it was shown that analog

[1]The authors want to note, that in real mixer applications $x(t)$ gets "switched" by the signal of a local oscillator, so the input signal gets rather multiplied with a rectangular function $y(t) = A\mathrm{sign}\left(\cos(2\pi ft + \phi)\right)$ instead of a single-tone. But for illustration of the concept of frequency shifting, we prefer to consider the ideal case of multiplication of $x(t)$ with a single sinusoidal signal.

Fig. 2. Circuit model of the UWB mixer designed by Ulm University consisting of two active single-ended-to-differential converter input stages (baluns), biasing, a four-quadrant Gilbert cell multiplier, and an output buffer.

multipliers create undesired signal content, which have an impact on the system performance of a noncoherent UWB receiver [13]. These undesired signal components cause self-interference due to nonlinearities of higher order, which results in a degradation of the signal-to-interference-and-noise ratio of the test statistic and hence in a degradation of the bit-error rate. These effects can only be modeled using UWB models.

In general, Volterra system models [14], [15] are often used to model nonlinear RF devices [16]. An example is shown in [17], where a Volterra system model with a periodic kernel is proposed. Such a kernel is suitable to model the frequency-conversion behavior of a mixer. It was shown that the proposed model can reconstruct metrics like transconductance or third-order intermodulation (IM3). The big drawback of Volterra systems is that they may consist of kernels of high dimensionality, which are hard to identify and which do not give insight into the operation of the devices per se.

Wiener-Hammerstein systems are a subclass of Volterra system models [18] which give better intuition about the device operation. In [19], [20] identification methods for Wiener-Hammerstein systems [15] are proposed, with the drawback that they cover SISO systems only. On the other hand, [21] shows an approach to identify multiple-input multiple-output (MIMO) Wiener and MIMO Hammerstein systems, but not their concatenations: Wiener-Hammerstein or Hammerstein-Wiener systems.

In [22] a multiple-input single-output (MISO) Wiener-Hammerstein model and a dedicated recursive identification method is presented. This model consists of parallel SISO Wiener-Hammerstein models for each input signal, while the MISO model output is the sum of the partial SISO model outputs. Although this model gives good insight into the system behavior, it cannot model multiplicative cross terms of the input signals, which is crucial for modeling analog multipliers.

This paper proposes a MISO Wiener-Hammerstein system model consisting of input and output filters and a bivariate polynomial kernel (cf. Fig. 1) that can model accurately ultra-wideband analog multipliers. The model is flexible and, due to its structure, it gives insight in the behavior of such devices. E.g. in [12], the influence of undesired signal content on system performance metrics was shown. Performance degradations have been explained using the proposed Wiener-Hammerstein system model. A method is proposed which facilitates easy and accurate identification of the model parameters. It is shown that the proposed model reaches the accuracy of Agilent ADS circuit simulations but with less computational effort. The model allows to study the nonideal behavior of systems caused by analog multipliers, e.g. the influence of undesired signal content.

In [12] the authors introduced another method to perform identification of the model parameters on Agilent ADS simulations. The Wiener-Hammerstein input filters were estimated using intermediate signals of the circuit-level simulation, which are normally not accessible in real hardware. In contrast, the newly proposed approach is able to identify real hardware multipliers based on measurements.

The paper is organized as follows. In Section II, the MISO Wiener-Hammerstein model for ultra-wideband analog multipliers is introduced. The theory of how to identify its parameters is addressed in Section III. Verification and performance evaluation of the model are shown in Section IV, followed by conclusions.

II. SIGNAL MODEL OF NONIDEAL MULTIPLIERS

To study the UWB behavior of multipliers, exemplarily a UWB mixer (see Fig. 2) designed by Ulm University was investigated [23], [24]. This mixer was designed to perform a multiplication operation for a UWB correlation receiver [25] that supports the full UWB frequency range from 3.1 GHz

to 10.6 GHz defined by the FCC [26]. It has been manufactured using Telefunken Semiconductor's Si/SiGe2 HBT technology [27] and consists of two active single-ended-to-differential converter input stages (baluns), biasing circuitry, a four-quadrant Gilbert cell multiplier, and an output buffer stage with a lowpass filter.

Gilbert cell multipliers do have, for the bipolar case, an input-output relationship given as [23]

$$z(t) = I_\mathrm{T}\tanh\left(\frac{x(t)}{2V_\mathrm{T}}\right)\tanh\left(\frac{y(t)}{2V_\mathrm{T}}\right), \qquad (3)$$

where I_T is the total emitter bias current, V_T is the thermal voltage, $x(t)$ and $y(t)$ are two input voltage signals, and $z(t)$ is an output current signal. This topology is known to approximate the ideal multiplication operation sufficiently well for low input levels, due to the approximately linear working points of the tanh functions [28].

Unfortunately, typical Gilbert cell mixers consist of additional circuitry as the aforementioned single-ended-to-differential converters, the output buffer stage, and some biasing circuitry. These auxiliaries introduce distortions to the output signal. These are are not modeled by (3), neither are parasitic effects as e.g. memory effects due to parasitic capacitors or current leakage. Therefore, a more generic approach is proposed.

A possible way is to express the tanh function using Taylor-expansion [29], which is given as

$$\tanh(x) = \sum_{n=1}^{\infty}\frac{2^{2n}\left(2^{2n}-1\right)}{(2n)!}\mathrm{B}_{2n}x^{2n-1}, \qquad (4)$$

with B_{2n} being the $2n$-th Bernoulli number. Comparing (4) with (3) and having the auxiliaries in mind, it seems possible to describe the static nonlinearity of the system using a bivariate polynomial.

In addition, linear time-invariant filters need to be considered at the input and the output stages, which do not exist in an ideal multiplier. A nonideal multiplication of two independent signals $x(t)$ and $y(t)$ can hence be modeled as

$$\mathcal{M}\left\{x(t),y(t)\right\} = h(t)*$$
$$\left[\sum_{u=0}^{U}\sum_{v=0}^{u}c_{u-v,v}\left(g_x(t)*x(t)\right)^{u-v}\left(g_y(t)*y(t)\right)^{v}\right], \quad (5)$$

which represents a Wiener-Hammerstein system with U being the maximum order of a static bivariate polynomial nonlinearity, $*$ representing the convolution operator, $g_x(t)$ and $g_y(t)$ being impulse responses of linear time-invariant input filters, respectively, $h(t)$ being the impulse response of a linear time-invariant output filter, and $\{c_{u-v,v}\}$ being the coefficients of the polynomial. These coefficients can be used to derive signal metrics and to investigate the influence of output distortions on a considered application [12]. The coefficient $c_{1,1}$ represents a constant gain of the desired ideal multiplication term, $c_{0,0}$ gives the constant DC bias, and $c_{2,0}$, $c_{0,2}$ represent the gains of the squared filtered input signals. In Fig. 3, a multiplier model of order $U = 3$ is illustrated.
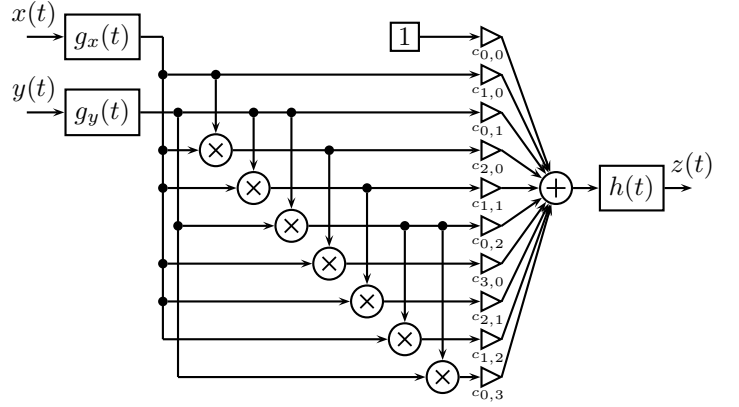
Fig. 3. A nonideal multiplier system $z(t) = \mathcal{M}\left\{x(t),y(t)\right\}$ of order $U = 3$ consists of two input and one output filters, and seven ideal multipliers and gains, which model the static bivariate nonlinearity.

III. MODEL IDENTIFICATION

To identify the system model of the analog multiplier given in (5), an approach with two steps is proposed. The first step is to identify the filters $g_x(t)$, $g_y(t)$, and $h(t)$, respectively. The second step is to estimate the polynomial coefficients $\{c_{u-v,v}\}$ using these identified filters.

A. Filter Identification

A way to identify the input and output filters of a given analog multiplier is to excite the device with two different single-tones, e.g. $x(t) = A_x\cos\left(2\pi f_x t + \phi_x\right)$ and $y(t) = A_y\cos\left(2\pi f_y t + \phi_y\right)$. It is assumed that the multiplier has negligible undesired output components for small input signals, hence the signal term which is represented by $c_{1,1}$ is predominant. The output $z(t)$ of the device is thus given as

$$z(t) \approx \Re\left\{\frac{1}{2}c_{1,1}A_xA_y e^{j2\pi(f_x+f_y)t}e^{j(\phi_x+\phi_y)}\right.$$
$$\times G_x(f_x)G_y(f_y)H(f_x+f_y)\}$$
$$+\Re\left\{\frac{1}{2}c_{1,1}A_xA_y e^{j2\pi(f_x-f_y)t}e^{j(\phi_x-\phi_y)}\right.$$
$$\times G_x(f_x)G_y^*(f_y)H(f_x-f_y)\}, \qquad (6)$$

which represents two single-tones at frequencies $|f_x + f_y|$ and $|f_x - f_y|$, respectively, where $G_x(f)$, $G_y(f)$, $H(f)$ are the frequency responses of the input and output filters, $G_y^*(f)$ represents the complex conjugate of $G_y(f)$, and $\Re\{a\}$ denotes to the real part of $a \in \mathbb{C}$. It can be seen that both tones exhibit complex gains which contain those frequency responses at certain frequencies. The complex amplitude of the signal with the difference frequency[2] $|f_x - f_y|$ is given as

$$\alpha\left(f_x,f_y\right) = \frac{1}{2}c_{1,1}A_xA_y e^{j(\phi_x-\phi_y)}$$
$$\times G_x(f_x)G_y^*(f_y)H(f_x-f_y), \qquad (7)$$

---

[2]For simplicity, the method is shown using the difference frequency $|f_x - f_y|$ only. The method can easily be expanded to support the sum frequency $|f_x + f_y|$ too.

which can be easily measured, e.g. by sampling the input and output signals and performing a discrete Fourier transform (DFT) to get the complex amplitudes of these tones.

If these measurements are done in an equidistant two-dimensional input frequency sweep, equidistant samples of the frequency responses of the filters can be obtained. N^2 measurements are taken, where $N = \frac{f_{\text{up}} - f_{\text{low}}}{\Delta f} + 1 \in \mathbb{Z}$ is the number of the frequencies within the desired input frequency range $[f_{\text{low}}, f_{\text{up}}]$ at a spacing of Δf. We define the vector

$$\boldsymbol{\sigma} = [f_{\text{low}}, f_{\text{low}} + \Delta f, f_{\text{low}} + 2\Delta f, \ldots, f_{\text{up}}]^T \qquad (8)$$

of input frequencies[3]. The vector $\boldsymbol{\rho}$ of output frequencies is then given as

$$\boldsymbol{\rho} = [0, \Delta f, 2\Delta f, \ldots, (N-1)\Delta f]^T. \qquad (9)$$

1) Magnitude Responses: The magnitude responses can be obtained by taking the absolute value and the logarithm of (7) to get a linear relation,

$$\log|\alpha(f_x, f_y)| = \log|\tfrac{1}{2}c_{1,1}| + \log|A_x A_y| \\ + \log|G_x(f_x)| + \log|G_y(f_y)| + \log|H(|f_x - f_y|)|. \quad (10)$$

We formulate the linear system of equations

$$\boldsymbol{\alpha} = \mathbf{P}\mathbf{m} + \boldsymbol{\xi} + \boldsymbol{\nu}, \qquad (11)$$

where $\boldsymbol{\alpha}$ is the measurement vector with elements

$$[\boldsymbol{\alpha}]_{k+(l-1)N} = \log|\alpha([\boldsymbol{\sigma}]_k, [\boldsymbol{\sigma}]_l)|, \qquad (12)$$

$k, l = 1, 2, \ldots, N$, and $\boldsymbol{\nu}$ represents any errors in the measurements or model, e.g. nonlinear terms of higher order or nonlinear memory which are not modeled, and measurement noise. The vector $\boldsymbol{\xi}$ corrects for the measured input amplitudes. Its elements are given as

$$[\boldsymbol{\xi}]_{k+(l-1)N} = \log|A_x([\boldsymbol{\sigma}]_k, [\boldsymbol{\sigma}]_l) A_y([\boldsymbol{\sigma}]_k, [\boldsymbol{\sigma}]_l)|, \quad (13)$$

where the possible dependency of the input signal amplitude on measurement point (k, l) is explicitly shown. The vector $\mathbf{m}$ is the concatenation of the sampled logarithmic magnitude responses given as

$$\mathbf{m} = \left[\log|\mathbf{g}_x|^T, \log|\mathbf{g}_y|^T, \log|\mathbf{h}|^T, \log|\tfrac{1}{2}c_{1,1}|\right]^T, \quad (14)$$

whose elements are $[\mathbf{g}_x]_i = G_x([\boldsymbol{\sigma}]_i)$, $[\mathbf{g}_y]_i = G_y([\boldsymbol{\sigma}]_i)$, and $[\mathbf{h}]_i = H([\boldsymbol{\rho}]_i)$, $i = 1, \ldots, N$. The matrix $\mathbf{P}$ is an indicator matrix, which is defined as

$$\mathbf{P} = [\mathbf{P}_1 \ \mathbf{P}_2 \ \mathbf{P}_3 \ \mathbf{1}_{N^2}], \qquad (15)$$

---

[3]Note that the input frequencies can be chosen differently, e.g. variable frequency spacings or frequency regions can be covered. The output frequency vector depends on the input frequency vectors. The choice by the authors was to show a simple example.

where $\mathbf{1}_{N^2}$ is an all-ones vector with N^2 elements, and

$$[\mathbf{P}_1]_{k+(l-1)N,i} = \begin{cases} 1 & , \text{for } [\boldsymbol{\sigma}]_k = [\boldsymbol{\sigma}]_i \\ 0 & , \text{otherwise} \end{cases} \qquad (16)$$

$$[\mathbf{P}_2]_{k+(l-1)N,i} = \begin{cases} 1 & , \text{for } [\boldsymbol{\sigma}]_l = [\boldsymbol{\sigma}]_i \\ 0 & , \text{otherwise} \end{cases} \qquad (17)$$

$$[\mathbf{P}_3]_{k+(l-1)N,i} = \begin{cases} 1 & , \text{for } |[\boldsymbol{\sigma}]_k - [\boldsymbol{\sigma}]_l| = [\boldsymbol{\rho}]_i \neq 0 \\ 2 & , \text{for } |[\boldsymbol{\sigma}]_k - [\boldsymbol{\sigma}]_l| = 0 \\ 0 & , \text{otherwise} \end{cases} \qquad (18)$$

where $k, l, i = 1, 2, \ldots, N$. Note that $\mathbf{P}$ needs to have a full rank, hence $N \geq 4$.

Using this data model, the magnitude response can be estimated in a least-squares sense using

$$\hat{\mathbf{m}} = \mathbf{P}^\dagger(\boldsymbol{\alpha} - \boldsymbol{\xi}), \qquad (19)$$

where $\mathbf{P}^\dagger$ represents the Moore-Penrose pseudo inverse of $\mathbf{P}$. For a valid least-squares solution, the matrix $\mathbf{P}$ needs to be full rank and uncorrelated with the error $\boldsymbol{\nu}$ [30]. Measurements have shown (see Section IV), that these assumptions are fulfilled[4].

2) Phase Responses: The phase responses can be estimated in a similar way. The phase of the output signal $z(t)$ is given (cf. (7)) as

$$\angle\alpha(f_x, f_y) = (\phi_x - \phi_y) \\ + \angle G_x(f_x) - \angle G_y(f_y) + \angle H(|f_x - f_y|). \quad (20)$$

The elements of the measured phase vector $\boldsymbol{\beta}$ are defined as

$$[\boldsymbol{\beta}]_{k+(l-1)N} = \angle\alpha([\boldsymbol{\sigma}]_k, [\boldsymbol{\sigma}]_l), \qquad (21)$$

hence

$$\boldsymbol{\beta} = \mathbf{Q}\boldsymbol{\psi} + \boldsymbol{\zeta} + \boldsymbol{\nu}, \qquad (22)$$

where $\boldsymbol{\nu}$ represents any errors in the measurements or model which have the same causes as in (11). The vector $\boldsymbol{\zeta}$, with elements

$$[\boldsymbol{\zeta}]_{k+(l-1)N} = (\phi_x([\boldsymbol{\sigma}]_k, [\boldsymbol{\sigma}]_l) - \phi_y([\boldsymbol{\sigma}]_k, [\boldsymbol{\sigma}]_l)), \quad (23)$$

corrects for the measured input phases. The indicator matrix $\mathbf{Q}$, which is full rank for $N \geq 4$, is

$$\mathbf{Q} = [\mathbf{P}_1 \ \mathbf{P}_2 \ \mathbf{P}_3]. \qquad (24)$$

Finally the estimate of the phase response vectors

$$\boldsymbol{\psi} = \left[\angle\mathbf{g}_x^T, -\angle\mathbf{g}_y^T, \angle\mathbf{h}^T\right]^T \qquad (25)$$

is obtained in a least-square sense as

$$\hat{\boldsymbol{\psi}} = \mathbf{Q}^\dagger(\boldsymbol{\beta} - \boldsymbol{\zeta}). \qquad (26)$$

The matrix $\mathbf{Q}$ needs to be full rank and uncorrelated with the error $\boldsymbol{\nu}$ to obtain a valid least-squares solution [30].

---

[4]For the identification using measurements, the power of the error $\boldsymbol{\nu}$ was found to be -30.7 dB below the power of the dependent variable vector $\boldsymbol{\alpha} - \boldsymbol{\xi}$. For the identification using ADS, the power of $\boldsymbol{\nu}$ was found to be -28.5 dB below the power of the dependent variable vector. The corresponding correlation coefficients are 0.1452 for the identification using measurements and 0.1382 for the identification using ADS. These numbers suggest, that $\boldsymbol{\nu}$ is uncorrelated to $\mathbf{P}$
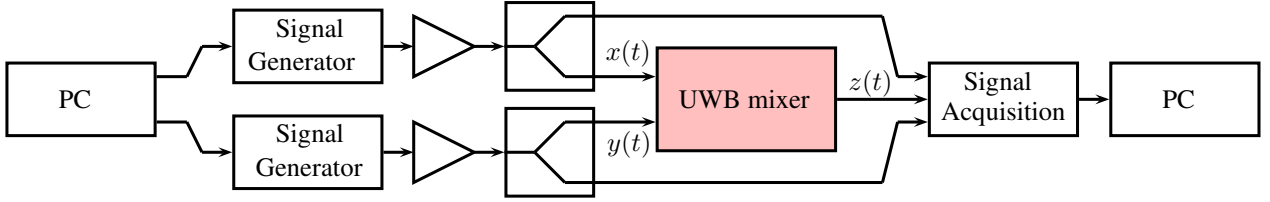
Fig. 4. Measurement setup for mixer identification.

3) Equivalent IIR Filter Modeling: To model the input and output filters, the estimated magnitude and phase responses can be used to find equivalent discrete-time IIR filters, e.g. utilizing metaheuristic algorithms [31]–[33]. The used cost function can be chosen, e.g. as the weighted sum of squared differences from the given sampled target frequency responses. To avoid ambiguities due to gain exchange between the filters and the bivariate polynomial coefficients, the filters should be normalized to a passband gain of one. Effects like exchange of group delay between the input and output filters do not play a crucial role due to the fact that the identification method does identify the phase response of the input and output filters. Phase ambiguities are resolved by fitting the IIR filter models. Note that the measurement setup needs to be calibrated to ensure that any delays induced by the measurement setup are removed.

B. Polynomial Coefficients Identification

To estimate the coefficients $\{c_{u-v,v}\}$ of the bivariate polynomial kernel of the system model, the device has to be excited with signals which fit into its input frequency region and have a given amplitude distribution. The amplitude distribution can be seen as a weighting of the estimation: an amplitude interval with a higher probability mass is modeled more accurately than an amplitude interval with a lower probability mass. The amplitude distribution should hence depend on the signals of the application under consideration, just like the input frequency range[5].

Segments of length L of the sampled input signals are stored in vectors $\mathbf{x}$ and $\mathbf{y}$, respectively. These signals need to be filtered with discrete-time equivalents of the identified input filters $\hat{g}_x(t)$ and $\hat{g}_y(t)$, respectively. The filtered input signals $\hat{\mathbf{x}}$ and $\hat{\mathbf{y}}$ are thus given as

$$\hat{\mathbf{x}} = \hat{\mathbf{G}}_x \mathbf{x} \tag{27}$$
$$\hat{\mathbf{y}} = \hat{\mathbf{G}}_y \mathbf{y}, \tag{28}$$

with $\hat{\mathbf{G}}_x$ and $\hat{\mathbf{G}}_y$ being the Toeplitz matrices of the discrete-time equivalents of $\hat{g}_x(t)$ and $\hat{g}_y(t)$.

The sampled device output vector $\mathbf{z}$ is then

$$\mathbf{z} = \hat{\mathbf{X}}\mathbf{c} + \boldsymbol{\nu}, \tag{29}$$

where

$$\mathbf{c} = [c_{0,0}, c_{1,0}, c_{0,1}, c_{2,0}, c_{1,1}, c_{0,2}, \dots]^T \tag{30}$$

represents the vector of polynomial coefficients. The vector $\boldsymbol{\nu}$ represents the measurement noise, and $\hat{\mathbf{X}}$ is given as

$$\hat{\mathbf{X}} = \hat{\mathbf{H}} \left[\mathbf{1}_M, \hat{\mathbf{x}}, \hat{\mathbf{y}}, \hat{\mathbf{x}}^2, (\hat{\mathbf{x}} \odot \hat{\mathbf{y}}), \hat{\mathbf{y}}^2, \dots \right] \tag{31}$$

where $\hat{\mathbf{H}}$ is the Toeplitz matrix of the discrete-time equivalent of $\hat{h}(t)$, $\odot$ represents the element-wise multiplication and the exponentiation represents an element-wise exponentiation of the vector elements[6]. Note that L needs to be chosen to ensure that $\hat{\mathbf{X}}$ has full rank.

The polynomial coefficient vector can finally be estimated in a least-square sense using

$$\hat{\mathbf{c}} = \hat{\mathbf{X}}^\dagger \mathbf{z}. \tag{32}$$

IV. MODEL VERIFICATION

The verification of the model is performed using the aforementioned UWB mixer designed by Ulm University. The device consists of a bare mixer die which has been bonded onto a printed circuit board (PCB). The signal inputs and the output are AC coupled with a capacitors of 100 pF. For comparison, the proposed identification methods are also evaluated using an Agilent ADS circuit-level model of that UWB mixer circuit.

A. Model Performance

A metric to evaluate the performance of the system identification is the normalized mean square error (NMSE) of the system model output $\mathbf{z}$ passed through an application-specific target filter $T(f)$ represented by its discrete-time equivalent Toeplitz matrix $\mathbf{T}$. This filter extracts the frequency range of interest. The NMSE is thus defined as

$$\mathrm{NMSE} = \mathrm{E}\left\{\frac{\left(\mathbf{Tz} - \mathbf{T}\hat{\mathbf{X}}\hat{\mathbf{c}}\right)^T \left(\mathbf{Tz} - \mathbf{T}\hat{\mathbf{X}}\hat{\mathbf{c}}\right)}{\mathbf{z}^T \mathbf{T}^T \mathbf{Tz}}\right\}, \tag{33}$$

where $\mathrm{E}\{\cdot\}$ represents the expectation operator.

In this work, $T(f)$ was chosen to be a Bessel filter of order 6 with cut-off frequency of 91.9 MHz. It approximates a sliding window integrator [34] for a noncoherent multichannel autocorrelation UWB receiver [13], [35].

[5]It is possible to use other signals than the desired signals of the application under consideration. However, only an estimation with the desired signal amplitude distribution will lead to minimal modeling errors.

[6]We assume that the Toeplitz matrices $\hat{\mathbf{G}}_x$, $\hat{\mathbf{G}}_y$, and $\hat{\mathbf{H}}$ are designed such that transient effects at the signal boundaries are avoided.
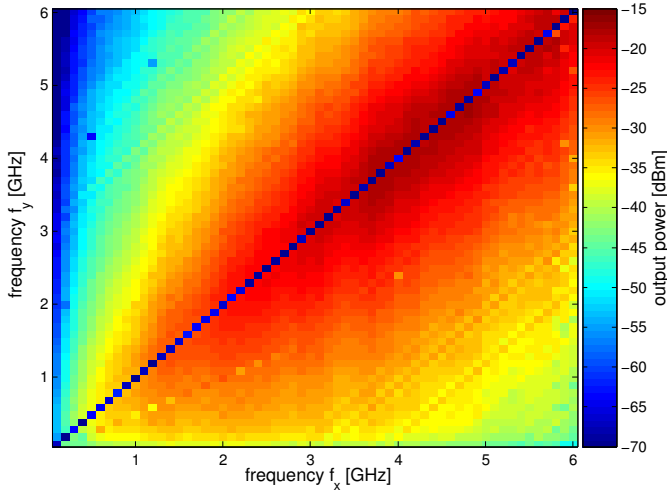
Fig. 5. Magnitude response of two dimensional frequency sweep measurements. Each grid point represents the output power of the output single-tone at a frequency of $|f_x - f_y|$, where f_x and f_y are frequencies of the input single-tones.

Fig. 6. Input and output filter magnitude responses of the system model fitted to the measurement and to the ADS circuit model simulation.

B. Measurement Setup

The measurement setup is depicted in Fig. 4. To estimate the frequency responses, a two dimensional frequency sweep from 100 MHz to 6 GHz with a Δf of 100 MHz was performed using an Agilent E8267C signal generator and a Rohde&Schwarz ZVA24 network analyzer. The single-tones $x(t) = A_x \cos(2\pi f_x t + \phi_x)$ and $y(t) = A_y \cos(2\pi f_y t + \phi_y)$ generated by the signal generators got amplified, and after power splitting had a power of -20 dBm at the input ports of the mixer. The input and output signals were sampled at a rate of 20 GHz using an Agilent Infiniium 54855A scope. To obtain the magnitude and phase of the input tones and of the desired output tone $A_z \cos(2\pi|f_x - f_y|t + \phi_z)$, a DFT was performed[7]. The DFT has the advantage, that it mitigates all undesired frequencies. It was observed from those measurements that such components have negligible power, which validates the assumption from Section III-A that an ideal multiplier can be assumed for the filter identification step. The signal powers of the desired output single-tones of the two-dimensional frequency sweep measurements, hence $|A_z(f_x, f_y)|^2$, are shown in Fig. 5. Each grid point represents the signal power of the output tone at a frequency of $|f_x - f_y|$, where f_x and f_y are frequencies of the input single-tones.

To estimate the polynomial coefficients the two input ports of the device were excited with application-specific, uncorrelated signals. For this measurement, multicarrier UWB pulses [13], [34] were used. These pulses are root-raised-cosine pulses with $\beta = 0.5$, which are truncated at the first zero-crossings. The length of these pulses is 10.6 ns. An additional zero-guard interval of 5 ns—to minimize inter-symbol-interference—results in a symbol period of 16 ns. The bandwidth of this signal is 1.75 GHz with a center frequency of 4 GHz, comprising seven non-overlapping subcarriers spaced by 250 MHz. The pulses were generated using the Tektronix

---

[7]Sample rate, signal frequencies and sample lengths need to be chosen properly to avoid leakage effects of the DFT.

AWG7102 arbitrary waveform generator with a sampling rate of 10 GHz. Due to the fact that the Tektronix AWG7102 does not have a sufficient output lowpass filter to avoid an image signal of the desired one, the excitation signal shows additional frequency components from 5.125 GHz to 6.875 GHz. These image signals are accounted for in the coefficient estimation procedure. The input power to the mixer ports was -20 dBm, which is sufficient to drive the mixer at times into saturation due to a peak-to-average-power ration (PAPR) of the UWB signals of 18 dB. The input and output signals were again sampled using the Agilent Infiniium 54855A scope at a sampling rate of 20 GHz.

C. Model Parameter Estimation

Fig. 6 shows the magnitude responses of the estimated filters (cf. Section III-A1) obtained from the measurement. For comparison, the estimated filter magnitude responses are also shown for the ADS circuit model.

It can be seen that the estimated output filters $\hat{H}_{\mathrm{meas.}}(f)$, $\hat{H}_{\mathrm{ADS}}(f)$ and the input filters $\hat{G}_{x,\mathrm{meas.}}(f)$, $\hat{G}_{x,\mathrm{ADS}}(f)$ are very similar to one another. They differ in the region of interest (from DC to 2 GHz for $\hat{H}_{\mathrm{meas.}}(f)$ and $\hat{H}_{\mathrm{ADS}}(f)$ and from 3.125 GHz to 4.875 GHz for $\hat{G}_{x,\mathrm{ADS}}(f)$ and $\hat{G}_{x,\mathrm{meas.}}(f)$) up to 1.3 dB and 1.6 dB, respectively. The input filters $\hat{G}_{y,\mathrm{meas.}}(f)$ and $\hat{G}_{y,\mathrm{ADS}}(f)$ do differ up to 18.9 dB on the shown frequency range, but 0.6 dB in the region of interest. The differences between the ADS system model and the measurement system model might be caused by parasitic effects that are not modeled by the ADS circuit-model, but which certainly exist in the hardware mixer.

To model the input and output filters, the magnitude responses of the estimated filters (cf. Section III-A1) were used to find equivalent discrete-time minimum-phase IIR filters, utilizing a differential evolution algorithm [36]. The used cost function was chosen as the weighted sum of squared differences from the given sampled target magnitude response. The filter order of $G_x(f)$, $G_y(f)$, and $H(f)$ was set to two.
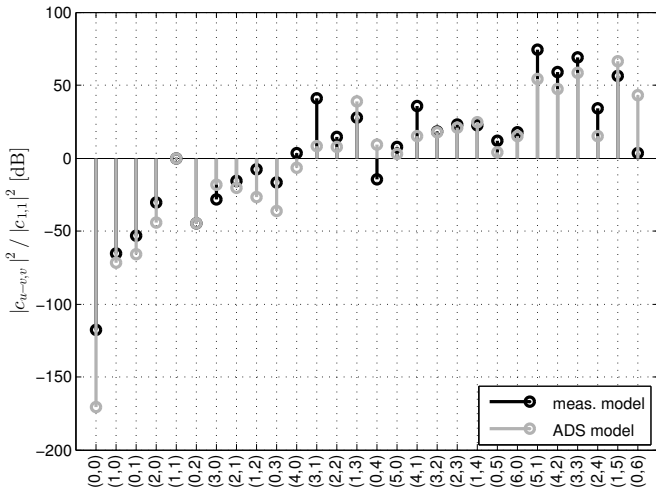
Fig. 7. Polynomial coefficients $\{c_{u-v,v}\}$ of the system models fitted to the measurement and to the ADS simulation, respectively. The coefficients are normalized to the desired signal coefficient $c_{1,1}$. The pair (a, b) represents the respective polynomial coefficient $c_{a,b}$.

Fig. 9. Frequency domain output signals of the measurement-fitted system model in comparison to the measurement and the model error.

Fig. 8. Time domain output signals of the nonideal multiplier system model in comparison to the measurement, the output signal of the ADS circuit model, and the system model fitted onto the ADS circuit model.
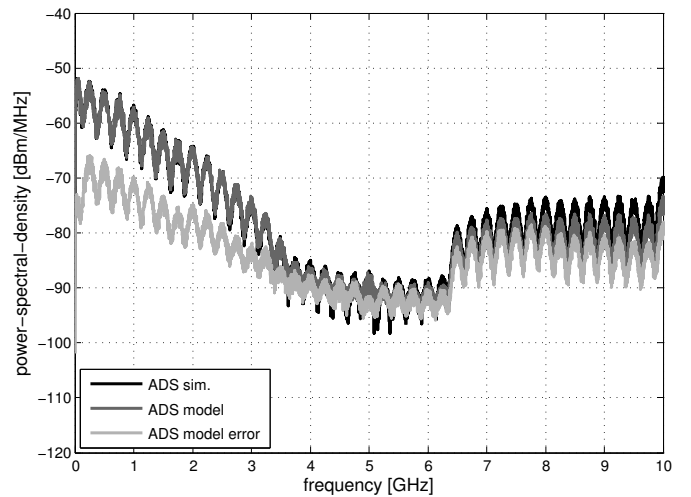
Fig. 10. Frequency domain output signals of the ADS-simulation-fitted system model in comparison to the ADS circuit model and the model error.

The obtained filters were taken to identify the polynomial coefficients. The order of the bivariate polynomial was chosen to minimize the NMSE. For the given application it was found to be six. In Fig. 7, the estimated polynomial coefficients $\{c_{u-v,v}\}$ are depicted for the measurement system model and the ADS system model. It can be seen that both sets of coefficients are similar, however, some coefficients differ. The maximal difference is 52.9 dB for $c_{0,0}$, but at very low magnitude. The average difference is 6.6 dB. Also these differences between the ADS system model and the measurement system model might be caused by parasitic effects.

The time and frequency domain representations of the output signal are shown in Figs. 8 - 10. The model output signal is compared with the measured output signal, the ADS simulation output, and the system model output matched to the ADS simulation.

In the time domain, it can be seen that the output waveforms are similar. In the frequency domain it can be seen that all signals have a similar power-spectral-density (PSD) in the range from DC up to about 3 GHz. In Fig. 9 and Fig. 10 also the PSDs of the model errors are depicted. The power of the measurement-fitted model error is -30.5 dBm and -38.5 dBm for the ADS-simulation-fitted model, respectively. (For comparison, the output power of the measurement and the ADS simulation is -24.3 dBm and -26.0 dBm, respectively.) For frequencies higher than 3 GHz, the PSDs deviate but are rather small compared to the lower frequency region. The strong attenuation of the measured output signal at frequencies higher than 6 GHz is due to the strong lowpass filter of the scope. The signal content within the frequency band from 3.125 GHz to 6.875 GHz in the measured output signal resembles the signal which is fed into the mixer and may hence be crosstalk from the inputs, e.g. it may be induced by the PCB or may be current
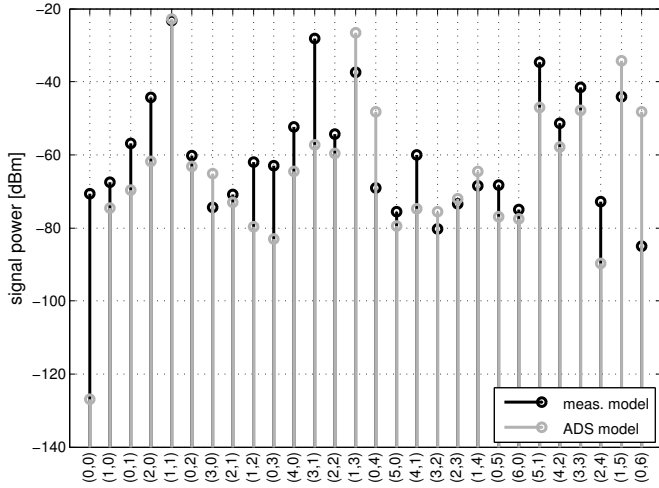
Fig. 11. Power of the nonlinear signal with the respective coefficients $\{c_{u-v,v}\}$ of the system model fitted to the measurement and the system model fitted to the ADS simulation. The pair (a,b) represents its respective nonlinear coefficient $c_{a,b}$.

leakage through the mixer. This crosstalk is not modeled in the proposed multiplier model and can thus not be identified and reconstructed using that particular model. However, the crosstalk and current leakage might be identified separately after subtracting the measurement-fitted model output from the sampled measurement output. Alternatively, the model could be extended to support nonlinear memory as in [18], thus representing a Volterra system model instead of a Wiener-Hammerstein system model.

The NMSE of the measurement-fitted model compared to the measurement is -11.5 dB, the NMSE of the ADS simulation compared to the measurement is -5.1 dB, and the NMSE of the ADS-simulation-fitted model compared to the ADS simulation output is -21.1 dB. These values are obtained using a training set of 750 pulses to estimate the polynomial coefficients and a validation set of 750 pulses to perform the NMSE computation. The noise level of the measurement is about -47.6 dBm, hence 17.1 dB less than the measurement-fitted model error. These values confirm that the fit of the proposed system model works very well. They show that the proposed system model is more accurate than the ADS circuit model simulation for the given application, due to the fact that the ADS circuit model does not model parasitic effects. Nonlinear memory effects, which are not considered in the system model, might cause the increased NMSE of the measurement-fitted model with respect to the ADS-fitted one.

In Fig. 11, the output power of the individual nonlinear signal parts is depicted. This representation gives intuition about the structure of the output signal and which terms are dominant or which can be neglected for further analysis. It can be seen that the desired signal with $c_{1,1}$ has the highest power of about -24 dBm. Also the signal parts of fourth order with coefficients $c_{3,1}$ and $c_{1,3}$ show significant powers. It also can be seen, although the coefficients seem to be very similar for the ADS model and the measurement model, that the power of some nonlinear signal parts differ more than 30 dB, on

average 5.6 dB.

V. CONCLUSION

This paper proposes a Wiener-Hammerstein system model for ultra-wideband analog multipliers. The model consists of input and output filters and a static bivariate polynomial nonlinearity. Due to its structure, it gives insight into distortions created by analog multipliers. Methods to identify the input and output filters and the polynomial coefficients were derived. It has been shown that these methods yield a system model which can reconstruct the measured output signal of a UWB mixer with an NMSE of -11.5 dB. A respective ADS circuit simulation showed an NMSE of just -5.1 dB. The proposed system can model the realistic behavior of an ultra-wideband analog multiplier and gives the possibility to study the degradation of the performance of a considered application caused by undesired signal content. For system simulations, the model gives the possibility to change the polynomial coefficients or the filters for studying the impact on system performance metrics. Typical values of these parameters can be determined from existing multiplier devices. Finally, the model can replace extensive and time-consuming ADS circuit simulations for system validations.

ACKNOWLEDGMENT

REFERENCES

[1] B. Razavi, *RF Microelectronics*. Pearson Education, 2012.

[2] A. Gerosa, S. Soldà, A. Bevilacqua, D. Vogrig, and A. Neviani, "An energy-detector for noncoherent impulse-radio UWB receivers," *IEEE Transactions on Circuits and Systems I: Regular Papers*, vol. 56, no. 5, pp. 1030–1040, 2009.

[3] L. Stoica, A. Rabbachin, and I. Oppermann, "Impulse radio based non-coherent UWB transceiver architectures - an example," in *IEEE International Conference on Ultra-Wideband*, 2006, pp. 483–488.

[4] K. Witrisal, G. Leus, G. Janssen, M. Pausini, F. Troesch, T. Zasowski, and J. Romme, "Noncoherent ultra-wideband systems," *IEEE Signal Processing Magazine*, vol. 26, no. 4, pp. 48–66, July 2009.

[5] H.-U. Dehner, H. Jakel, D. Burgkhardt, and F. Jondral, "The Teager-Kaiser energy operator in presence of multiple narrowband interference," *IEEE Communications Letters*, vol. 14, no. 8, pp. 716–718, 2010.

[6] A. Rabbachin, T. Quek, P. Pinto, I. Oppermann, and M. Win, "Non-coherent UWB communication in the presence of multiple narrowband interferers," *IEEE Transactions on Wireless Communications*, vol. 9, no. 11, pp. 3365–3379, 2010.

[7] T. Q. Quek, M. Z. Win, and D. Dardari, "Unified analysis of UWB transmitted-reference schemes in the presence of narrowband interference," *IEEE Transactions on Wireless Communications*, vol. 6, no. 6, pp. 2126–2139, 2007.

[8] L. Zwirello, C. Heine, X. Li, and T. Zwick, "An UWB correlation receiver for performance assessment of synchronization algorithms," in *IEEE International Conference on Ultra-Wideband*, Sept. 2011, pp. 210–214.

[9] L. Lampe and K. Witrisal, "Challenges and recent advances in IR-UWB system design," in *IEEE International Symposium on Circuits and Systems*, May 2010, pp. 3288–3291.

[10] A. Oka and L. Lampe, "A compressed sensing receiver for bursty communication with UWB impulse radio," in *IEEE International Conference on Ultra-Wideband*, Sept. 2009, pp. 279–284.

[11] F. Tufvesson, S. Gezici, and A. Molisch, "Ultra-wideband communications using hybrid matched filter correlation receivers," *IEEE Transactions on Wireless Communications*, vol. 5, no. 11, pp. 3119–3129, 2006.

[12] A. Pedross and K. Witrisal, "Analysis of nonideal multipliers for multichannel autocorrelation UWB receivers," in *2012 IEEE International Conference on Ultra-Wideband*, Sept. 2012, pp. 140 – 144.

[13] K. Witrisal, "Noncoherent autocorrelation detection of orthogonal multicarrier UWB signals," in *2008 IEEE International Conference on Ultra-Wideband*, vol. 2, Sept. 2008, pp. 161–164.

[14] M. Schetzen, *The Volterra & Wiener Theories of Nonlinear Systems*. Krieger Publishing Company, 2006.

[15] V. J. Mathews and G. L. Sicuranza, *Polynomial Signal Processing*. John Wiley & Sons, Inc., 2000.

[16] P. Li and L. Pileggi, "Efficient per-nonlinearity distortion analysis for analog and RF circuits," *IEEE Transactions on Computer-Aided Design of Integrated Circuits and Systems*, vol. 22, pp. 1297–1309, 2003.

[17] G. Theodoratos, A. Vasilopoulos, G. Vitzilaios, and Y. Papananos, "Calculating distortion in active CMOS mixers using Volterra series," in *2006 IEEE International Symposium on Circuits and Systems*, 2006.

[18] D. Morgan, Z. Ma, J. Kim, M. Zierdt, and J. Pastalan, "A generalized memory polynomial model for digital predistortion of RF power amplifiers," *IEEE Transactions on Signal Processing*, vol. 54, no. 10, pp. 3852–3860, 2006.

[19] S. Billings and S. Y. Fakhouri, "Identification of a class of nonlinear systems using correlation analysis," *Proceedings of the Institution of Electrical Engineers*, vol. 125, no. 7, pp. 691–697, 1978.

[20] J. Paduart, L. Lauwers, R. Pintelon, and J. Schoukens, "Identification of a Wiener–Hammerstein system using the polynomial nonlinear state space approach," *Control Engineering Practice*, vol. 20, no. 11, pp. 1133–1139, 2012. [Online]. Available: http://www.sciencedirect.com/science/article/pii/S0967066112001281

[21] F. Ikhouane and F. Giri, "A unified approach for the identification of SISO/MIMO Wiener and Hammerstein systems," in *16th IFAC Symposium on System Identification*, July 2012, pp. 2–6.

[22] M. Boutayeb and M. Darouach, "Recursive identification method for MISO Wiener-Hammerstein model," *IEEE Transactions on Automatic Control*, vol. 40, no. 2, pp. 287–291, 1995.

[23] J. Dederer, *Si/SiGe HBT ICs for Impulse Ultra-Wideband (I-UWB) Communications and Sensing*. Cuvillier Verlag, 2009.

[24] J. Dederer, B. Schleicher, F. De Andrade Tabarani Santos, A. Trasser, and H. Schumacher, "FCC compliant 3.1-10.6 GHz UWB pulse radar system using correlation detection," in *2007 IEEE/MTT-S International Microwave Symposium*, June 2007, pp. 1471 –1474.

[25] J. Dederer, B. Schleicher, A. Trasser, T. Feger, and H. Schumacher, "A fully monolithic 3.1-10.6 GHz UWB Si/SiGe HBT Impulse-UWB correlation receiver," in *2008 IEEE International Conference on Ultra-Wideband*, vol. 1, Sept. 2008, pp. 33 –36.

[26] Federal Communications Commission (FCC), "Revision of part 15 of the commission's rules regarding ultra-wideband transmission systems," Federal Communications Commission (FCC), Tech. Rep., 2002, first Report and Order, ET Docket 98-153, FCC 02-48; Adopted: February 2002; Released: April 2002.

[27] A. Schüppen, J. Berntgen, P. Maier, M. Tortschanoff, W. Kraus, and M. Averweg, "An 80 GHz SiGe production technology," *III-Vs Review*, vol. 14, no. 6, pp. 42 – 46, 2001. [Online]. Available: http://www.sciencedirect.com/science/article/pii/S0961129001805305

[28] B. Gilbert, "A precise four-quadrant multiplier with subnanosecond response," *IEEE Journal of Solid-State Circuits*, vol. 3, no. 4, pp. 365–373, Dec. 1968.

[29] M. Abramowitz and I. A. Stegun, *Handbook of Mathematical Functions with Formulas, Graphs, and Mathematical Tables*. Dover Publications Inc., 1964.

[30] F. Hayashi, *Econometrics*. Princeton Univ Press, 2000.

[31] S. Luke, *Essentials of Metaheuristics*, 2nd ed. Lulu, 2013, available for free at http://cs.gmu.edu/~sean/book/metaheuristics/.

[32] R. Pintelon and J. Schoukens, *System Identification: A Frequency Domain Approach*. IEEE Press, 2001.

[33] L. Ljung, *System Identification: Theory for the User*, 2nd ed. Prentice Hall, 1999.

[34] A. Pedross and K. Witrisal, "Sliding window integrator approximations for multichannel autocorrelation UWB receivers," in *2012 IEEE International Symposium on Circuits and Systems*, May 2012, pp. 2537–2540.

[35] P. Meissner and K. Witrisal, "Analysis of a noncoherent UWB receiver for multichannel signals," in *2010 IEEE 71st Vehicular Technology Conference (VTC 2010-Spring)*, May 2010, pp. 1–5.

[36] A. Melzer, A. Pedross, and M. Mücke, "Holistic biquadratic IIR filter design for communication systems using differential evolution," *Journal of Electrical and Computer Engineering, Special Issue on Hardware Implementation of Digital Signal Processing Algorithms*, vol. 2013, March 2013.